Electrodynamics in Deformable Solids for Electromagnetic Forming

Electrodynamics in Deformable Solids for Electromagnetic Forming

PROEFSCHRIFT

ter verkrijging van de graad van doctor
aan de Technische Universiteit Delft,
op gezag van de Rector Magnificus prof.dr.ir. J.T. Fokkema,
in het openbaar te verdedigen ten overstaan van een commissie,
door het College voor Promoties aangewezen,
op maandag 6 oktober 2003 om 13:00 uur

door

Teodora-Emilia MOTOAŞCĂ

inginer
Universitatea "Transilvania" din Brasov
geboren te Brasov, Roemenië

Printed in The Netherlands

To my parents and my dear Roger

for their steady support and understanding

Motto: *"Victory belongs to the most persevering"*

Contents

Chapter 1

Introduction

This chapter presents a detailed introduction into the subject of electromagnetic forming with a section dedicated to the history of electromagnetic forming.

1.1 History and importance of electromagnetic forming

When electricity was first introduced, man discovered the effects of strong electromagnetic fields on conducting bodies: the conducting bodies can be moved and deformed. Caused by electromagnetic force, both effects (motion and deformation) have been studied for their positive and negative aspects, ever since the first electrical machine was designed and brought into operation.

During operation of electrical machines the electromagnetic force produces sometimes, besides the desired motion, the undesired deformation of some parts of the electrical machines. On the other hand, in other applications a certain deformation is the desired effect of electromagnetic force, while the motion is only a secondary effect, accompanying the deformation. One such procedure is the electromagnetic forming, a high-velocity forming process aiming at the shaping of conducting objects (the so-called workpieces) in strong electromagnetic fields.

Even though electromagnetic forming was already known in the early 20-th century, the subject has not been studied extensively since application at an industrial level was not possible due to many technical limitations. Due

Figure 1.1:   Examples of beverage cans that may be made with electro-
               magnetic forming methods [courtesy of Corus, IJmuiden,
               The Netherlands].

to the lack of high-performance components and materials (e.g. fast high-
voltage switches, good insulation materials, etc.) required for building an
operational electromagnetic forming system, this technology was left aside for
decades, notwithstanding its promise. In addition, the lack of fast computers
to perform the required complicated numerical modelling, also contributed to
this situation.

In Fig. 1.1, some examples of hollow cylindrical objects are shown that
may be made with the aid of electromagnetic forming methods.

The electromagnetic forming system has many advantages that make it
an attractive alternative to conventional forming systems (hydraulic, mechanic,
etc.) or even to other high-velocity forming systems (explosive gas, low/high
explosive, electrohydraulic).

In conventional forming systems the typical deformation velocity is in the
order of 0.1 m/s, while it can reach a few hundred meters per second in all high-
velocity forming systems, including electromagnetic forming systems. It means
that the object (workpiece) is deformed rapidly, in the order of microseconds.

As opposed to most conventional forming systems, during electromag-
netic forming, there is no mechanical contact with the workpiece. Because no
mechanical contact is required, lubricants are not needed and the process is
"clean". Since the energy transfer is established through the electromagnetic
field, the electromagnetic forming process can be carried out in air (or even

vacuum), while in other high-velocity forming systems a liquid (e.g. electrohy-draulic system or some explosive systems) or a gas (e.g. some other explosive systems) is required as energy transfer medium. The pressure exerted on the workpiece is almost uniform in electromagnetic forming and the force is exerted in each interior and surface point of the workpiece. Unstrained workpieces can be deformed by nearly a 100 % without failure, because the formability limits increase during electromagnetic forming due to high deformation velocity, while in conventional forming systems, the same materials fail at 20 - 40 % deformation.

The principal advantage of electromagnetic forming is its controllability and repeatability, as most of the high-velocity procedures, while the required equipment is relatively simple. In electromagnetic forming systems, the deformation takes place at room temperature and the temperature rise within the forming system is comparatively small. It means that heat distortions of workpieces, frequently occurring in conventional forming systems, are theoretically avoided and also the workpiece handling is simplified.

Besides many advantages, electromagnetic forming has also some disadvantages: it needs special safety precautions (high voltage of operation) and the required equipment is still expensive and physically large. In practice, its application is restricted to rather simple shapes (unless forming dies are used, see later), and there are size limitations for workpieces to be shaped.

During the last few decades, an increasing need to produce high-strength components more economically than by conventional forming caused renewed interest in electromagnetic forming. Moreover, semiconductor high-voltage switches became available to replace the rather maintenance prone, expensive high voltage switches. For a better understanding and design of the electromagnetic forming process, and for better application of this high-velocity forming procedure, an accurate theoretical model is needed. Such a model is not trivial at all, since it requires knowledge of electromagnetics, mechanics and thermodynamics. In particular, in electromagnetic forming a full model of the elastic and the plastic deformation of workpieces is desired. Hence it is useful to develop a consistent analytical model of the electrodynamics in deformable media.

1.2 Description of electromagnetic forming

Electromagnetic forming requires the generation of a strong, transient electromagnetic field. The field is located in the air gap between a forming coil (work
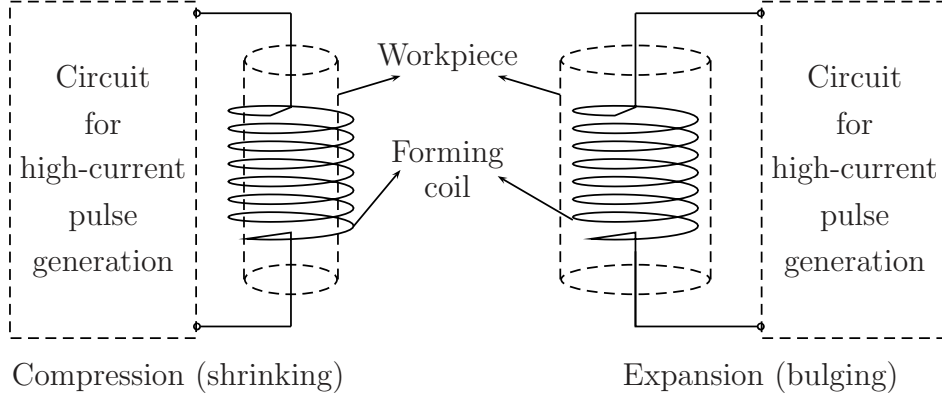
Figure 1.2:   Typical electromagnetic forming systems for hollow circular
                    cylindrical objects.

coil) and a metallic object to be shaped (workpiece). A high-current pulse
produced by a dedicated circuit, see Fig. 1.2, is passed through the forming
coil in order to generate the electromagnetic field in the air gap and in the
workpiece. This electromagnetic field will induce an eddy current in the work-
piece opposite to the initial current pulse. As a consequence, intense repulsive
forces between the forming coil and the workpiece are developed, causing the
workpiece to move and deform rapidly, first elastically and finally plastically.
Consequently, if the repulsive forces are large enough, the workpiece will have
a permanent deformation when motion ends. The shape of this permanent de-
formation is influenced by the presence of forming dies. When forming dies are
used, the workpiece is pushed against them and the final shape of the workpiece
can be quite complex. Without forming dies, the workpiece deforms freely and
its final shape depends on a large number of parameters of the process.

      Until now (see literature review in Section 1.4) only flat workpieces (metal
sheets) and hollow cylindrical workpieces (metal tubes) have been used in elec-
tromagnetic forming processes. The workpieces have been made from non-
magnetic, conducting materials as aluminum, silver, brass, etc. or from soft
magnetic, conducting materials as low-carbon mild steel.

      A typical electromagnetic forming system for shaping hollow cylindrical
objects consists of a circuit for high-current pulse generation and a solenoidal
forming coil, as in Fig. 1.2. The current pulse obtained from the circuit for
high-current pulse generation is in the order of 100 kA with a pulse rise-time in
the order of 10 μs. The energy that will be released within the forming system is
in the order of 100 kJ. Theoretically, within the same electromagnetic forming

system two types of deformations can be obtained: compression (shrinking) and expansion (bulging) of hollow circular cylindrical workpieces. When the workpiece is placed inside the forming coil, as in the left side of Fig. 1.2, the workpiece is subjected to compression (shrinking) and its diameter decreases during the deformation process. During this deformation process, the forming coil is subjected to expansion (bulging). When the workpiece is placed outside the forming coil, as in the right side of Fig. 1.2, the workpiece is subjected to expansion (bulging) and its diameter increases during the deformation process, while the forming coil is subjected to compression (shrinking).

By compression, expansion, or even by a combination of both, final shapes as the ones shown in Fig. 1.1 can be obtained, with a typical electromagnetic forming system for shaping hollow cylindrical objects as in Fig. 1.2, . In order to get more insight into the electromagnetic forming process that can lead to such shapes, we will investigate the electromagnetic forming of hollow circular cylindrical objects in detail.

1.3 Statement of the problem

The main goal is to calculate the spatial and temporal behavior of a conducting, electromagnetically stationary and mechanically deformable hollow circular cylinder (the workpiece) subjected to an intense transient electromagnetic field. Let us look carefully at some aspects of the problem.

First of all, the spatial and temporal behavior has to be investigated. This means that the evolution in time of all parameters that characterize the deformation process should be investigated.

Secondly, the workpiece may be made of magnetic or non-magnetic highly conducting material. In our present situation the deformation of the matter is due to the electromagnetic force density. Deformation will occur both in magnetic and non-magnetic media. The literature on electromagnetic force distribution in magnetic media is confusing because various contradicting expressions have been reported for the electromagnetic force density in magnetic materials. So, for magnetic materials this issue should be carefully analyzed.

Thirdly, the workpiece is assumed to be electromagnetically stationary. With regard to the electromagnetic field inside the deformable matter, one must distinguish between stationary matter and moving matter. The electromagnetic field equations have simple expressions for stationary matter, but they become more complicated if the matter is moving with constant particle

velocity. The electromagnetic field equations are even more complicated for accelerated motion of matter because additional forces of inertia will act on each particle of the matter. Although there are many phenomena related to the motion of the matter, the particle velocity of the material will be much smaller than the velocity of the electromagnetic field, i.e., the light speed. In this case it is sufficient that only stationary matter is considered in the analysis of the electromagnetic field.

1.4   Brief literature review

Apart from the papers that dealt explicitly with electromagnetic forming, many papers investigated other subjects related with electromagnetic forming, such as the generation of high-strength magnetic fields, electrodynamics in moving media, hyperplasticity, high-velocity deformation of solids, etc. Since the number of published papers in the above-mentioned fields is very large, only some significant papers dealing explicitly with electromagnetic forming will be discussed here.

The experiments of P. Kapitza in the 1920s were indicated by many authors as the beginning of electromagnetic forming. Kapitza achieved magnetic field strengths sufficient to deform massive solid conductors. In his view, electromagnetic forming was merely a negative consequence of strong electromagnetic fields in designing electrical machines.

Some more interest was shown in electromagnetic forming in the 1950s and early 1960s when the first rudimentary models began to emerge due to the intensive development of aeronautical engineering. As mentioned by Langlois [108] in 1958, Convair, a division of General Dynamics in San Diego, was assigned the task to develop production applications for the use of electromagnetic forces. The very simple theoretical model of the phenomena described by Langlois [108] was later improved by Birdsall *et al.* [20]. Shortly after, the first commercial electromagnetic forming machine was produced in 1962, as mentioned in the first comprehensive monograph of high-velocity forming of metals [29], which is partially dedicated to electromagnetic forming. A later edition of the same monograph [30] presents electromagnetic forming in an improved manner.

Many papers on electromagnetic forming were written during the late 1960s and early 1970s and it seems that the interest regarding this subject dwindled since then. Baines *et al.* [9] presented a theoretical model of the phenomena together with the experimental verification of it. In this work the

properties and the geometry of both the forming coil and the workpiece were assumed to be time-invariant; this simple model showed poor agreement with the experiments. Important contributions were made by Lal [105, 106], who identified three phases in the electromagnetic forming process, each of them with specific equations derived from energy considerations. In these phases the time-changing parameters were taken into account. Together with an extensive theory, experimental results were presented. Jansen [96] did not present a very extensive theory, but reported a large number of experimental results instead.

Later, Fluerasu discussed the electromagnetic forming of a hollow circular cylindrical, conducting object in some papers [62, 63, 64]. Other authors, as Bendjima *et al.* [16, 17] and Azzouz *et al.* [7], referred to the experimental results of Fluerasu for validation of their numerical results. A model of the electromagnetic forming process was presented by Al-Hassani [3]. In this work, a single equivalent circuit was derived from the two coupled circuits representing the forming coil and the workpiece, respectively. In the same period, Moon and Pao [133], and Moon and Chattopahyay [134] presented a consistent theory, supported by experiments only for the case of flat workpieces made of ferromagnetic material.

A large number of Russian papers dealt with electromagnetic forming in the 1960s and 1970s. A short paper by Boichenko *et al.* [24] briefly presented the equipment for electromagnetic forming, together with advantages, disadvantages and some practical problems of electromagnetic forming. In the same period a book by Winkler [189] was published, which included a monograph about high-velocity forming of metals, containing an extensive part dedicated to electromagnetic forming with comparisons of methods used by other authors.

In the late 1970s and 1980s only a few papers about electromagnetic forming were published. We can mention the work of King *et al.* [100], dealing extensively with the material behavior during electromagnetic forming, and the work of Sasu [160], who presented the operation of magnetoforming machines in terms of nonlinear electric circuit analysis.

In the late 1980s, a few French authors showed an interest in electromagnetic forming. Rioux *et al.* [152] proposed the use of an inductance for energy storage, instead of the classical capacitor bank that all previous authors used both for the theory and in the experiments. No experimental results were given to validate this type of energy storage. In the same year, the works of other authors – Baccino *et al.* [8], Charlier *et al.* [35], Dormeval [54], Galizzi and Colombe [68], Guillot [77], Rioux and Rioux-Damidau [153], and Schley [163] – about various aspects related to electromagnetic forming were presented in

the same issue of a journal.

In the 1990s, as the computing resources progressed, the electromagnetic forming process could be simulated better. This progress has been followed by a large number of papers dealing with numerical simulations of electromagnetic forming. In papers by Bendjima *et al.* [16, 17], Azzouz *et al.* [7], and Meriched and Feliachi [132], numerical results obtained with a finite-element method using simplified models of the process were presented and compared with the experimental ones obtained years before by Fluerasu. The numerical results showed quite a good agreement with the experimental ones.

Other authors used simplified models of the fundamental processes because they were only interested in the behavior of the material during electromagnetic forming. Here, with an impressive number of experimental results, we can mention Takatsu [181], Murata [140], Hwang [92], Daehn [45], Tamhane [182], Fenton [61], Zhang [191] and Hashimoto [81]. Often, the method of calculation is not presented and only results obtained for different materials are presented and compared. Besides, a large number of Japanese papers exists that has not been translated.

To describe a typical forming system, the quantities and symbols of Appendix A will be used throughout this thesis. As an overview, the characteristic parameters of the configurations described in the mentioned literature are given in Appendix B.

From this brief literature overview we may conclude that no definitive consistent model of the electromagnetic forming process has been developed yet. So, a model that takes into account the processes as they occur during electromagnetic forming is still needed in order to be able to gain a better understanding of electromagnetic forming and to use it more efficiently in designing new machines, as part of a new technology in e.g. the food packaging industry.

1.5   Outline of the thesis

In Chapter 2, we present a general theory about the electromechanical force densities associated with pulsed electromagnetic fields in piecewise homogeneous, isotropic, linear media with conductive losses. This issue is strongly related to electromagnetic forming because subsequently we will assume that these force densities act as source densities in the elastodynamic equations and in the corresponding boundary conditions. These equations and boundary

conditions govern the elastic and anelastic motion of deformable matter. We show in this chapter that the conductivity and the gradients in permittivity and permeability lead to volume force densities, while jump discontinuities in permeability lead to surface force densities.

In Chapter 3, we present a general overview of all parameters that describe the specific electromagnetic forming process that will be considered in this thesis, along with an extensive discussion about some modeling issues relating to these parameters. These modeling issues refer to some simplifications and approximations that have been used to develop a comprehensive analytical model of the electromagnetic forming process. Further, the actual structure of this thesis follows the principal steps shown in Fig. 1.3.

In Chapter 4, the calculation of the transient diffusive electromagnetic field in cylindrical configurations modeling the electromagnetic forming system for compression and for expansion of hollow circular cylindrical objects is presented. The configurations consist of a hollow cylindrical domain with a high electrical conductivity placed inside (for compression) or outside (for expan-
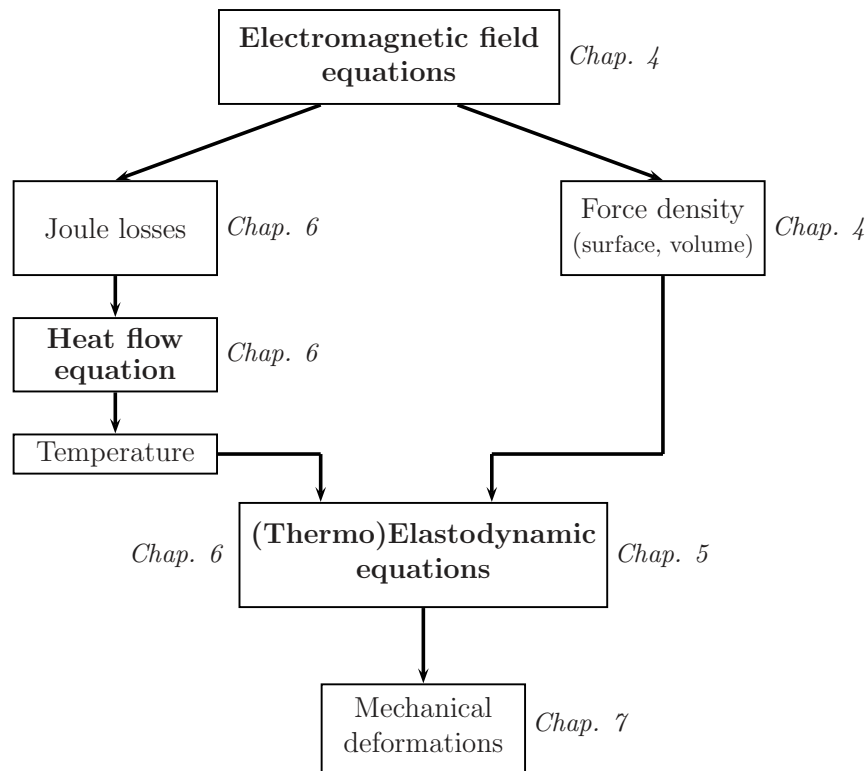
Figure 1.3: Principal steps followed in the analysis.

sion) of a cylindrical sheet antenna carrying a given electric current per unit length. The configuration is assumed to have infinite length and to be axially symmetric. Some particular cases related to this configuration are presented in detail and for them numerical results are given.

Further, Chapter 5 presents the calculation of the elastodynamic field in the hollow cylindrical domain with a high electrical conductivity, presented in Chapter 3. This cylindrical configuration is locally excited by the electromagnetic force density calculated in Chapter 4. The elastodynamic behavior of the hollow cylindrical domain with high electrical conductivity (workpiece) is described for the plane strain case and some numerical results for the electromagnetic compression and for electromagnetic expansion of hollow circular cylindrical objects are presented.

The results obtained in Chapter 4 for the transient diffusive electromagnetic field are used in Chapter 6 to analyze the evolution of the temperature in the workpiece due to dissipation of electromagnetic energy during in the forming process. Further, the influence of temperature effects are taken into account in the thermoelastic strains for computing the resulting thermoelastic field in Chapter 6, in the same configurations as the ones considered in Chapter 5.

In Chapter 7, we calculate the plastic deformations obtained in electromagnetic compression and in electromagnetic expansion of hollow circular cylindrical objects. The cylindrical configuration is locally excited by the electromagnetic force density calculated in Chapter 4. The plastic deformations are discussed for the plane strain case as in Chapter 5, and for this case numerical results are presented for an inelastic-perfectly plastic material.

In Chapter 8, the design of a set-up for an experimental investigation of electromagnetic forming of steel beverage cans, as well as the results of a set of experiments are discussed. Our original plan was to design a simple experimental demonstrator to validate the chosen theoretical model for electromagnetic forming with all its assumptions and approximations. Various attempts have been made to find the appropriate high-voltage equipment (capacitor, switch, measurement devices) needed for the experimental verification. In 2001, Corus Research Development and Technology approached us for a cooperation to realize such a demonstrator in their research facilities in IJmuiden. In the original plan for the experimental set-up there was also room for experimental validation. In the subsequent period, several designs for experimental set-ups have been realized. In that process there came an increasing focus from Corus on doing experiments on hardened (strengthened) thin steel beverage cans only.

For this reasons an approximate approach will be discussed in Chapter 8. Finally, Corus supported a limited set of experiments carried out at the KEMA High Voltage Laboratory in Arnhem.

In Chapter 9, we present some steps that may lead to the improvement of the simplified model developed in the previous chapters. In all previous chapters, a model has been developed based on the assumption that the geometry and the parameters that characterize the forming system are time, temperature and deformation invariant. This is not the case in a real forming system, so the changes induced by temperature rise, by deformation in the geometry and parameters of the configuration are described in Chapter 9. Since the analysis of all parts of the forming system is too complex, only the forming coil and the workpiece we are investigated. The other parts of the forming system are assumed to be invariant as properties and behavior. All influences are integrated in a complex model. New variables are introduced in the presented model to make it more realistic. These steps may complicate the numerical solution of the problem, but if done in an iterative way they will give a more realistic view of electromagnetic forming. Thus, with a more complex model we will get more realistic numerical results and it is possible to obtain a better accordance between the numerical simulations and the experimental results.

In Chapter 10 we present some conclusions drawn from the analysis of the proposed problem. The advantages and disadvantages of electromagnetic forming as presented in Chapter 3 are reconsidered based on the practical experience. Some ideas for future research on electrodynamics in deformable media are also given.

Chapter 2

Electromechanical force densities

In this chapter the electromechanical force densities associated with pulsed electromagnetic fields in piecewise homogeneous, isotropic, linear media with conductive losses are discussed in the context of their application in a process of shaping metal objects. The various assumptions will be discussed. The conductivity and the gradients in permittivity and in permeability lead to volume force densities. Jump discontinuities in permittivity and permeability lead to surface force densities. These force densities are assumed to act as volume (body) source densities in the elastodynamic equations and as surface source densities in the corresponding boundary conditions. These equations and boundary conditions govern the elastic and anelastic motion of deformable matter.

2.1 Introduction

The present chapter discusses the expressions for electromechanical volume and surface forces associated with pulsed electromagnetic fields in electromagnetic forming systems. The literature pertaining to forces in electromagnetic bodies is not only vast but also controversial. An extensive review on more fundamental aspects has been given by Penfield and Haus [144] while the expressions of the force distribution in magnetized material have been discussed by many other authors like Carpenter [32, 33], Byrne [31], Carter [34] and Reyne *et al.* [151]. The question of why, after all this time, there is difference of opinion

regarding the distribution of force in electromagnetic bodies is partly answered by Penfield and Haus [144]. According to this book, the answer to this question can only be found in a complete description of the physical system involved. We quote: *the complete physical system can be viewed as consisting of three mutually coupled subsystems: a mechanical subsystem describing the mechanics of the moving material masses; an electromagnetic subsystem describing the dynamics of the electromagnetic fields; and a thermodynamic subsystem taking into account the internal energy and the generation of heat and its flow. Theses three subsystems are mutually coupled and together completely describe the system under consideration.* This interdisciplinary combination of continuum mechanics, electromagnetics, thermodynamics, and even special relativity makes the problem difficult to study.

However, for the engineering application of electromagnetic forming where materials bodies are shaped in intense, pulsed electromagnetic fields, a number of observations and assumptions can be made. The force expression that follows from the general theory contains certain terms that are too small to be of engineering importance. In view of this, we make the following assumptions:

1. The materials involved are electrically and magnetically linear and simple. Nonlinear effects and piezo-electric, magneto-electric and magneto-elastic effects are considered to be higher-order effects and are neglected.

2. The deformation velocities $|\boldsymbol{v}| = v$ of all points in the material body are supposed to be small in comparison with the velocity of light c. In electromagnetic forming the particle deformation velocities are typically in the order of $v \approx 100 - 500$ m/s. Thus, terms of first and higher order in (v/c) may be neglected.

With this discussion, these assumptions and the theory of Penfield and Haus [144] in mind, the simplified physical system for deriving force densities in electromagnetic forming devices consists of an electromagnetic system and a mechanical system only, coupled through electromechanical force densities.

For the derivation of the distributed electromechanical force in this simplified system, roughly speaking two approaches can be followed:

1. Microscopic model approach

This approach starts with the expression for the Lorentz force in vacuum and the assumption of an underlying microscopic model for matter, e.g. Amperian-current model or the magnetic-charge model for elementary magnetic dipoles.

Through spatial averaging techniques expressions for the macroscopic electromechanical forces can be derived. This approach may be compared with the derivation of Maxwell's equations from their microscopic counterparts, see [186].

2. Macroscopic model approach

Here the force that impressed, external currents and charges exert on the electromagnetic field in the configuration follows from a balance of electromagnetic momentum. Most of the standard considerations on the subject focus on the relevant forces in (quasi-)static electric and magnetic fields, see e.g. Stratton [177], Moon [135], Fano [58], Penfield and Haus [144], or on the case of continuously differentiable spatial variations in the constitutive properties, see e.g. Stratton [177] and Landau [107]. The present approach has been suggested by A.T. de Hoop, author of [50], and by H. Blok, author of [22].

In this chapter we follow the macroscopic approach along the line of analysis presented by Stratton [177]. His analysis will be extended to the case of piecewise (in)homogeneous, isotropic media, thus allowing for interfaces across which the constitutive parameters jump by finite amounts. We will show that finite gradients in permittivity and permeability lead to distributed volume forces and interface conditions lead to distributed surface forces. The pulsed field behavior introduces a distributed volume force that is associated with the time derivative of the electromagnetic momentum of the field.

As final result of the discussion below it will be conjectured that, in mechanically deformable matter, the electromagnetic volume currents and surface currents cause impressed external mechanical volume forces and surface forces, respectively, and thus lead to an elastodynamic wave field in the relevant medium. The mechanical stress associated with wave motion then determines the amount of mechanical deformation that the medium undergoes.

2.2   Configuration and its electromagnetic field

We consider in this chapter a simple configuration consisting of a pulsed current loop with external current density $\boldsymbol{J}^{ext}(\boldsymbol{r},t)$ and external charge density $\boldsymbol{\rho}^{ext}(\boldsymbol{r},t)$ that irradiates a smooth inhomogeneous, isotropic object with constitutive parameters $\{\varepsilon,\sigma,\mu\}$ located in vacuum as shown in Fig. 2.1.
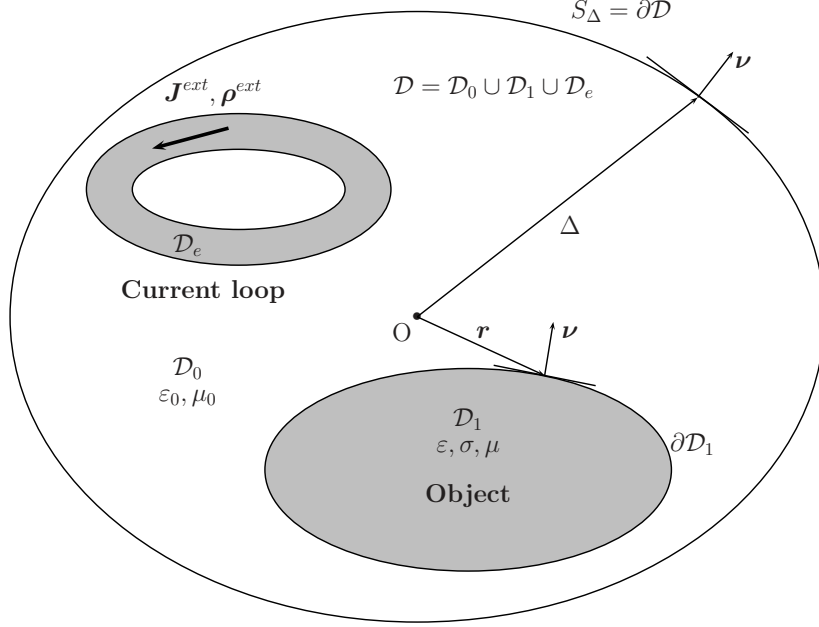
Figure 2.1:   A pulsed current loop with $\boldsymbol{J}^{ext}$ and ρ^{ext} in a vacuum do-
main $\mathcal{D}_0$ irradiates an inhomogeneous, isotropic object $\mathcal{D}_1$.
$\mathcal{D}_0$ is exterior to the source domain $\mathcal{D}_e$ and the object do-
main $\mathcal{D}_1$. The domain $\mathcal{D} = \mathcal{D}_0 \cup \mathcal{D}_1 \cup \mathcal{D}_e$ has the boundary
$\partial\mathcal{D}$.

The electromagnetic field equations are given by

$$\boldsymbol{\nabla}\times\boldsymbol{H} - \varepsilon\partial_t\boldsymbol{E} - \sigma\boldsymbol{E} = \boldsymbol{J}^{ext}, \tag{2.1}$$

$$\boldsymbol{\nabla}\times\boldsymbol{E} + \mu\partial_t\boldsymbol{H} = 0. \tag{2.2}$$

The compatibility relations are

$$\boldsymbol{\nabla}\cdot(\varepsilon\partial_t\boldsymbol{E} + \sigma\boldsymbol{E}) = -\boldsymbol{\nabla}\cdot\boldsymbol{J}^{ext}, \tag{2.3}$$

$$\boldsymbol{\nabla}\cdot(\mu\partial_t\boldsymbol{H}) = 0. \tag{2.4}$$

Further we introduce

$$\rho^{ext} = -\int_{t'=0}^{t} \boldsymbol{\nabla}\cdot\boldsymbol{J}^{ext}\, \mathrm{d}t', \tag{2.5}$$

as volume density of external electric charge. Across a source-free interface
of jump discontinuity in ε, μ and σ, the field quantities satisfy the continuity

conditions

$$\boldsymbol{\nu} \times \boldsymbol{H} = \text{continuous across interface,} \tag{2.6}$$

$$\boldsymbol{\nu} \times \boldsymbol{E} = \text{continuous across interface,} \tag{2.7}$$

and

$$\boldsymbol{\nu} \cdot (\varepsilon \partial_t \boldsymbol{E} + \sigma \boldsymbol{E}) = \text{continuous across interface,} \tag{2.8}$$

$$\boldsymbol{\nu} \cdot (\mu \partial_t \boldsymbol{H}) = \text{continuous across interface,} \tag{2.9}$$

where $\boldsymbol{\nu}$ is the normal vector of the interface.

2.3 Electromechanical volume forces and surface forces in the configuration

We take as physical interpretation that the volume source densities of external currents and electric charges in domain $\mathcal{D}_e$ exert on the field the volume force, cf. Stratton [177]

$$\boldsymbol{F}_V^{ext} = \int_{\mathcal{D}} \boldsymbol{f}_V^{ext} \ \mathrm{d}V = - \int_{\mathcal{D}} [\rho^{ext} \boldsymbol{E} + \boldsymbol{J}^{ext} \times \boldsymbol{B}] \ \mathrm{d}V. \tag{2.10}$$

To arrive at an expression that shows how the electromagnetic field transmits this force to other parts of the configuration (e.g. outside $\mathcal{D}_e$ in Fig. 2.1), we use Eqs. (2.1) - (2.5), then apply some transformations and end up with the expression

$$\boldsymbol{F}_V^{ext} = \int_{\mathcal{D}} [\rho^{ind} \boldsymbol{E} + \sigma \boldsymbol{E} \times \mu \boldsymbol{H} - \frac{1}{2} (\boldsymbol{\nabla} \varepsilon)(\boldsymbol{E} \cdot \boldsymbol{E}) - \frac{1}{2} (\boldsymbol{\nabla} \mu)(\boldsymbol{H} \cdot \boldsymbol{H})$$
$$+ \partial_t (\varepsilon \boldsymbol{E} \times \mu \boldsymbol{H})] \ \mathrm{d}V + \int_{\mathcal{D}} \boldsymbol{\nabla} \cdot \mathcal{T}^M \ \mathrm{d}A. \tag{2.11}$$

In Eq. (2.11) we have

$$\rho^{ind} = - \int_{t'=0}^{t} \boldsymbol{\nabla} \cdot \boldsymbol{J}^{ind} \, \mathrm{d}t', \tag{2.12}$$

where

$$\boldsymbol{J}^{ind} = \sigma \boldsymbol{E}. \tag{2.13}$$
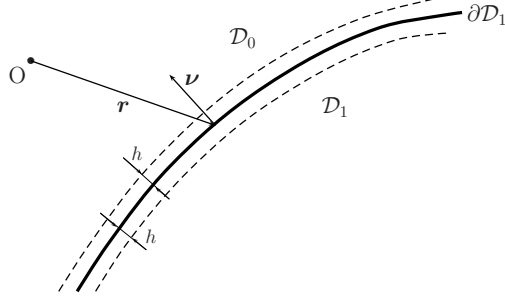
Figure 2.2: Detail of the boundary of the material object $\mathcal{D}_1$ in Fig. 2.1.

which is the volume density of induced electric current. Further,

$$\mathcal{T}^M = \frac{1}{2}\varepsilon(\boldsymbol{E}\cdot\boldsymbol{E})\,\mathcal{I} - \varepsilon\boldsymbol{E}\boldsymbol{E} + \frac{1}{2}\mu(\boldsymbol{H}\cdot\boldsymbol{H})\,\mathcal{I} - \mu\boldsymbol{H}\boldsymbol{H}, \qquad (2.14)$$

is the Maxwell stress tensor with $\mathcal{I}$ the unit tensor of rank two. Using Gauss' divergence theorem, the last term of Eq. (2.11) can be rewritten as

$$\int_{\mathcal{D}} \boldsymbol{\nabla}\cdot\mathcal{T}^M \ \mathrm{d}A = \int_{\partial\mathcal{D}} \boldsymbol{\nu}\cdot\mathcal{T}^M \ \mathrm{d}A + \int_{\partial\mathcal{D}_1} \boldsymbol{f}_S^M \ \mathrm{d}A, \qquad (2.15)$$

where

$$\boldsymbol{f}_S^M = -\lim_{h\downarrow 0}[\boldsymbol{\nu}\cdot\mathcal{T}^M(\boldsymbol{r}+h\boldsymbol{\nu}) - \boldsymbol{\nu}\cdot\mathcal{T}^M(\boldsymbol{r}-h\boldsymbol{\nu})], \quad r\in\partial\mathcal{D}_1, \qquad (2.16)$$

see Fig. (2.2). The results presented in Eqs. (2.11) and (2.15) can be rewritten as

$$\boldsymbol{F}_V^{ext} = \boldsymbol{F}_V^{ind} + \boldsymbol{F}_V^{grad} + \boldsymbol{F}_S^M + \boldsymbol{F}_S^{M;\infty} + \partial_t\boldsymbol{G}. \qquad (2.17)$$

In this expression,

$$\boldsymbol{F}_V^{ind} = \int_{\mathcal{D}} \boldsymbol{f}_V^{ind} \ \mathrm{d}V = \int_{\mathcal{D}} (\rho_e^{ind}\boldsymbol{E} + \sigma\boldsymbol{E}\times\mu\boldsymbol{H}) \ \mathrm{d}V \qquad (2.18)$$

is the volume force that the electromagnetic field exerts on the induced volume density of electric current,

$$\boldsymbol{F}_V^{grad} = \int_{\mathcal{D}} \boldsymbol{f}_V^{grad} \ \mathrm{d}V = \int_{\mathcal{D}} [-\frac{1}{2}(\boldsymbol{\nabla}\varepsilon)(\boldsymbol{E}\cdot\boldsymbol{E}) - \frac{1}{2}(\boldsymbol{\nabla}\mu)(\boldsymbol{H}\cdot\boldsymbol{H})] \ \mathrm{d}V \qquad (2.19)$$

is the volume force that the field exerts on gradients of permittivity and permeability. Further,

$$\boldsymbol{F}_S^M = \int_{\partial\mathcal{D}_1} \boldsymbol{f}_S^M \ \mathrm{d}A \qquad (2.20)$$

is a force due to a jump in the Maxwell stress tensor at the boundary of $\mathcal{D}_1$. This jump is conjectured to act as a surface force at $\partial\mathcal{D}_1$ for the elastodynamic wavefield in the configuration. At the boundary of $\mathcal{D}$ a force is exerted that equals

$$\boldsymbol{F}_S^{M,\infty} = \lim_{\Delta\to\infty} \int_{S_\Delta} \boldsymbol{f}_S^{M,\infty} \ \mathrm{d}A = \lim_{\Delta\to\infty} \int_{S_\Delta} \boldsymbol{\nu}\cdot\mathcal{T}^M \ \mathrm{d}A. \tag{2.21}$$

For its interpretation take for $\mathcal{D}$ the ball $\mathcal{B} = \{\boldsymbol{r} \in R^3; 0 < |\boldsymbol{r}| < \Delta\}$ of radius Δ and center at the origin. In the far-field region, the behavior of the field radiated by the sources in $\mathcal{D}_e$ guarantees that $\boldsymbol{F}_S^{M,\infty}$ exists as $\Delta \to \infty$. Similarly also $\partial_t \boldsymbol{G}$ exists as $\Delta \to \infty$. The corresponding term $\boldsymbol{\nu}\cdot\mathcal{T}^M$ can be interpreted as the "radiation pressure" that the field, by carrying its momentum from the exciting sources to S_Δ, exerts on the "sphere at infinity". Note that exerting this pressure is compatible with the property that this sphere absorbs the power radiated to it. This radiation pressure is irreversibly lost to the electromagnetic momentum.

Finally,

$$\boldsymbol{G} = \int_{\mathcal{D}} \boldsymbol{g} \ \mathrm{d}V = \int_{\mathcal{D}} (\varepsilon\boldsymbol{E}\times\mu\boldsymbol{H}) \ \mathrm{d}V, \tag{2.22}$$

is the electromagnetic momentum carried by the field.

We can now try to deduce from this result to which extent the different terms will contribute to the mechanical deformation of the materials present in $\mathcal{D}_1$. With the interpretation of the radiation pressure on the sphere at infinity in mind, also the terms $\boldsymbol{F}_V^{ind}$ and $\boldsymbol{F}_V^{grad}$ have the structure of an irreversible loss of momentum. It is noted that, when no matter is present in $\mathcal{D}_1$, both terms will vanish. As a consequence

$$\boldsymbol{f}_V^{ind} = \sigma\boldsymbol{E}\times\mu\boldsymbol{H} \qquad \text{in } \mathcal{D}_1, \tag{2.23}$$

and

$$\boldsymbol{f}_V^{grad} = -\frac{1}{2}\boldsymbol{\nabla}\varepsilon(\boldsymbol{E}\cdot\boldsymbol{E}) - \frac{1}{2}\boldsymbol{\nabla}\mu(\boldsymbol{H}\cdot\boldsymbol{H}) \qquad \text{in } \mathcal{D}_1, \tag{2.24}$$

can be conjectured to be the driving volume source densities of body force in the elastodynamic field equations that govern the behavior of dynamic stress and particle velocity in mechanically deformable matter.

With these interpretations *the balance of electromagnetic momentum* for the configuration in Fig. 2.1 is obtained as

$$\boldsymbol{F}_V^{ext} = \boldsymbol{F}_V^{ind} + \boldsymbol{F}_V^{grad} + \boldsymbol{F}_S^M + \boldsymbol{F}_S^{M,\infty} + \partial_t\boldsymbol{G}, \tag{2.25}$$

in which the various terms are defined and discussed above. So far, we have only used the physical interpretation of the terms $\rho^{ext}\boldsymbol{E}$ and $\boldsymbol{J}^{ext}\times\mu\boldsymbol{H}$ in $-\boldsymbol{F}_V^{ext}$ as the force that the electromagnetic field exerts on external electric charges and currents, the validity of Maxwell's electromagnetic field equations and the axiom that, as a consequence of the principle

$$action = - \ reaction,$$

the quantity $+\boldsymbol{F}_V^{ext}$ is the force that the impressed currents and accompanying charges exert on the field.

2.4 Electromechanical volume and surface force densities in a homogeneous, magnetic object located in vacuum

From the discussion in Section 2.3 we observe that in a homogeneous, highly conducting magnetic object with medium parameters σ, μ located in vacuum the volume density of induced charge ρ_e^{ind} vanishes and we find

$$\boldsymbol{f}_V^{ind} = \sigma\boldsymbol{E}\times\mu\boldsymbol{H} \qquad \text{in } \mathcal{D}_1, \tag{2.26}$$

$$\boldsymbol{f}_V^{grad} = 0 \qquad \text{in } \mathcal{D}_1. \tag{2.27}$$

Since in the electromechanical system for electromagnetic forming, the electromagnetic field may be considered transient diffusive, the derivative with respect to time of the electromagnetic momentum is always negligibly small in comparison to other terms in the balance of electromagnetic momentum. To conclude, the force exerted on $\mathcal{D}_1$ is in the present case

$$\boldsymbol{F}_V^{ext} = \boldsymbol{F}_V^{ind} + \boldsymbol{F}_S^{M}. \tag{2.28}$$

In this case, the volume density of force $\boldsymbol{f}_V^{ext}$ inside $\mathcal{D}_1$ is given by

$$\boldsymbol{f}_V^{ext} = \boldsymbol{f}_V^{ind} = \sigma\mu(\boldsymbol{E}\times\boldsymbol{H}), \tag{2.29}$$

while the surface density of force at $\partial\mathcal{D}_1$, follows immediately from Eqs. (2.15) and (2.16).

2.5 Elastodynamic wave motion generated by volume forces and surface forces in a perfectly elastic, homogeneous, isotropic solid

Here the subscript notation and summation convention will be used. The elastodynamic wavefield is characterized by its tensorial dynamic stress $\tau_{p,q} = \tau_{p,q}(\boldsymbol{r}, t)$, together with its vectorial particle velocity $v_r = v_r(\boldsymbol{r}, t)$. These quantities satisfy the equation of motion

$$\partial_p \tau_{p,k} - \rho_m \partial_t v_k = -f_{V;k}^{ext}, \tag{2.30}$$

in which $\rho_m = \rho_m(\boldsymbol{r})$ is the volume density of mass of the medium, and the constitutive equation

$$\tau_{p,q} = C_{p,q,i,j} e_{i,j}, \tag{2.31}$$

in which $C_{p,q,i,j}$ is the elastic stiffness tensor and $e_{i,j} = e_{j,i}$ is the strain. The latter quantity satisfies the strain-displacement relation

$$e_{i,j} = \frac{1}{2}(\partial_i u_j + \partial_j u_i), \tag{2.32}$$

in which u_j is the particle displacement. The relation between particle velocity and particle displacement is

$$v_r = \partial_t u_r. \tag{2.33}$$

In an isotropic material we have

$$C_{p,q,i,j} = \lambda_L \delta_{p,q} \delta_{i,j} + \mu_L (\delta_{p,i} \delta_{q,j} + \delta_{p,j} \delta_{q,i}), \tag{2.34}$$

in which λ_L and μ_L are the Lamé coefficients of the medium.
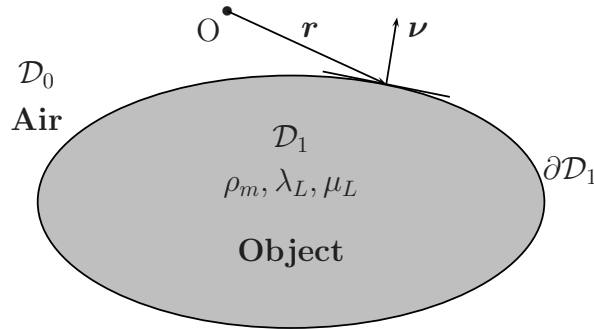
Figure 2.3: Object $\mathcal{D}_1$ with elastic properties ρ_m, λ_L, μ_L.

Combination of Eqs. (2.31) - (2.34) results in the deformation rate equation

$$\partial_t \tau_{p,q} = \lambda_L (\partial_r v_r) \delta_{p,q} + \mu_L (\partial_p v_q + \partial_q v_p). \qquad (2.35)$$

Across the surface discontinuity in elastodynamic properties $\partial \mathcal{D}_1$, the boundary conditions are

$$\lim_{h \downarrow 0} [\nu_p \tau_{p,k}(\boldsymbol{r} + h\boldsymbol{\nu}) - \nu_p \tau_{p,k}(\boldsymbol{r} - h\boldsymbol{\nu})] = -f_{S;k}^{ext} \qquad \text{on } \partial \mathcal{D}_1 \qquad (2.36)$$

and

$$[v_r]_{0 \uparrow \downarrow 1} = 0 \qquad \text{on } \partial \mathcal{D}_1. \qquad (2.37)$$

The surface density of force $f_{S;k}^{ext}$ in Eq. (2.36) follows from Eqs. (2.15) and (2.16).

2.6   Conclusions

In the discussion above, based on the extensive discussions with A.T. de Hoop, author of [50], and with H. Blok, author of [22], it has been conjectured that in the presence of mechanically deformable matter the electromagnetic volume and surface currents in the balance of electromagnetic momentum act as impressed external mechanical volume and surface forces, respectively, and thus generate an elastodynamic wave field in the object.

From the discussion in this chapter we have seen that the simplified physical system for deriving force densities in electromagnetic forming techniques consists of an electromagnetic system and a mechanical system that are only coupled through the electromagnetic force densities. The role of the fields in an electromagnetic forming system is depicted in Fig. 2.4. In this chapter we have only discussed the linear, elastodynamic deformation. The nonlinear, plastic deformation indicated in Fig. 2.4 will be discussed in Chapter 7.
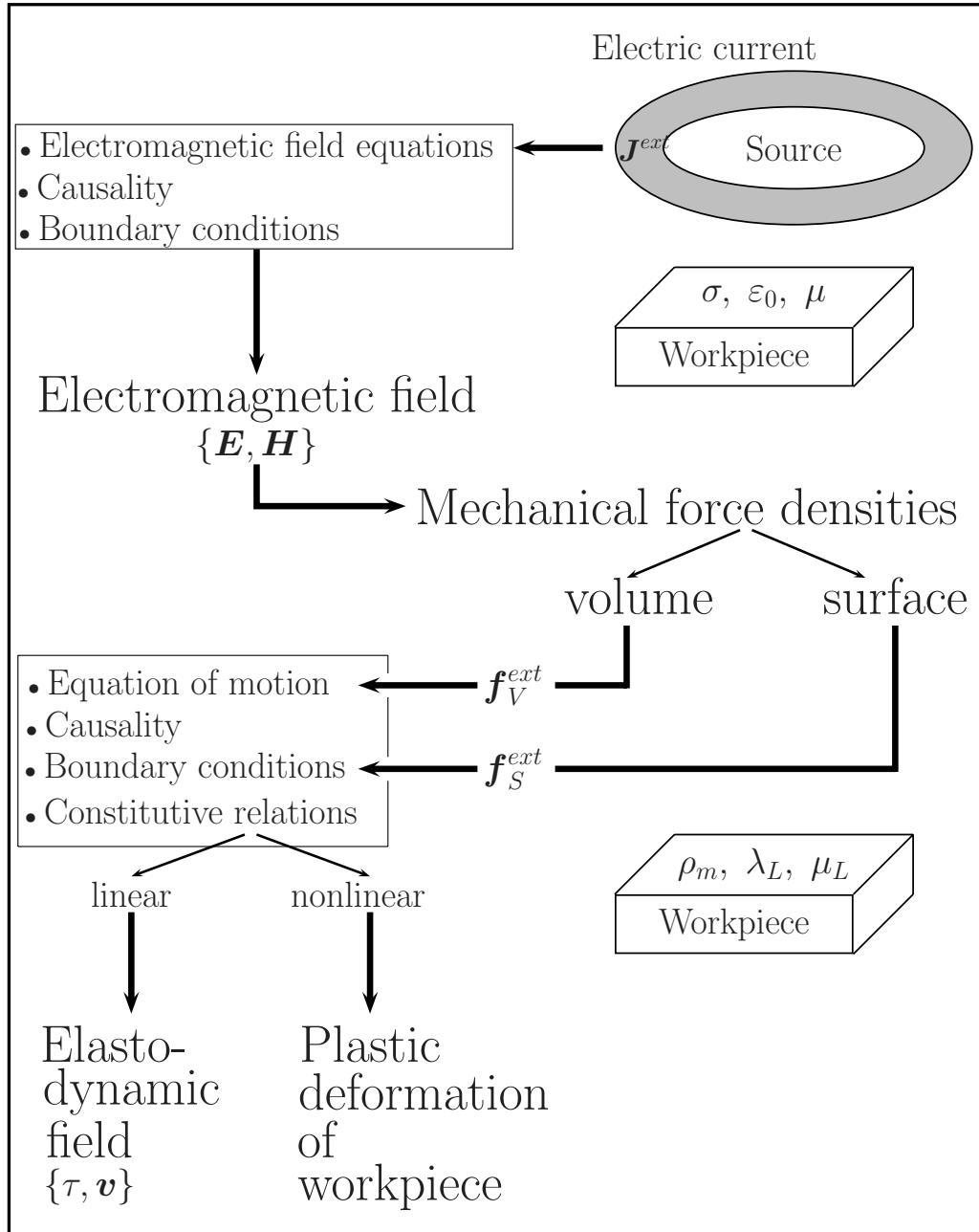
Figure 2.4: Role of fields in electromagnetic forming.

Chapter 3

Modelling issues for electromagnetic forming

This chapter presents the simplifications and the approximations that have been used to develop a comprehensive analytical model of the electromagnetic forming process of hollow circular cylindrical objects made of highly conducting material.

3.1 Real configuration and justification of the approximations

The theoretical model to be developed in this work applies both to electromagnetic compression and to electromagnetic expansion of hollow circular cylindrical objects made of conducting material. The electromagnetic force densities involved are calculated in different ways for electromagnetic compression and for electromagnetic expansion. When electromagnetic force densities inside the workpiece are known, the theoretical model developed from Chapter 5 onwards may be applied for the electromagnetic forming in a practical configuration as the one shown in Fig. 3.1.

In this thesis, we will give numerical results both for the theoretical model of electromagnetic forming and for the experimental model of electromagnetic expansion. In order to show the application of the theoretical model for both types of deformation, two possible electromagnetic forming systems will be further discussed.
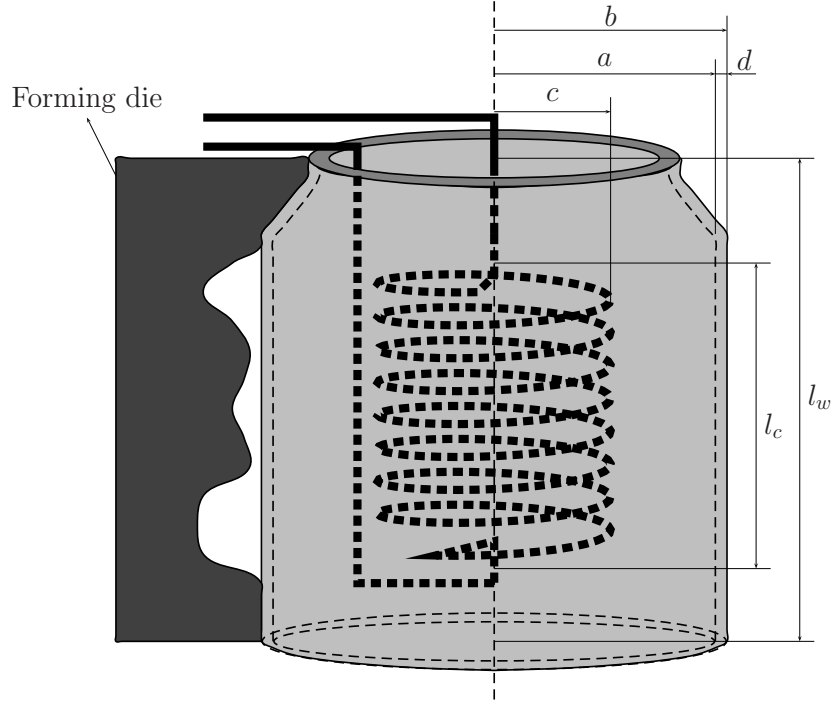
Figure 3.1: Real configuration to be modelled for expansion (bulging).

In order to keep the model mathematically as simple as possible, we will make some approximations and simplifications related to geometry, parameters and fields. Each of them is explained in detail in this chapter. Some of these approximations have been used only in the early stages of the model development. Then, during further steps towards a more realistic model of electromagnetic forming, some of the approximations and simplifications prove to be no longer necessary.

3.2   Equivalent network model

The circuit for high-current pulse generation shown in Fig. 1.2 consists mainly of a capacitor bank, a high-voltage, high-current switch and possibly a clamp diode. The electromagnetic forming systems for compression and for expansion of hollow circular cylindrical workpieces are the ones shown in Figs. 3.2 and 3.3, respectively. These forming systems in Figs. 3.2 and 3.3 may be modelled in first approximation as simple electric circuits. For the calculation of the equivalent electric circuit elements, the geometry and the material properties of each component of the electromagnetic forming systems are required. We
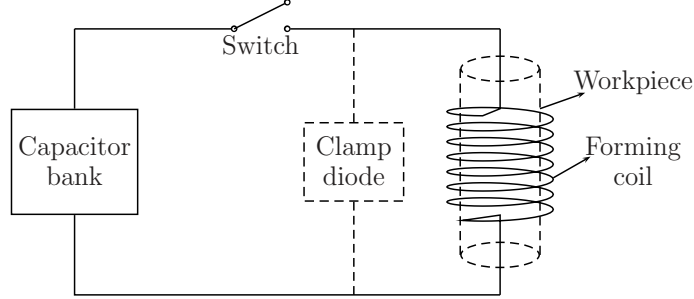
Figure 3.2:   Electromagnetic forming system for compression (shrink-ing) of hollow cylindrical workpieces.
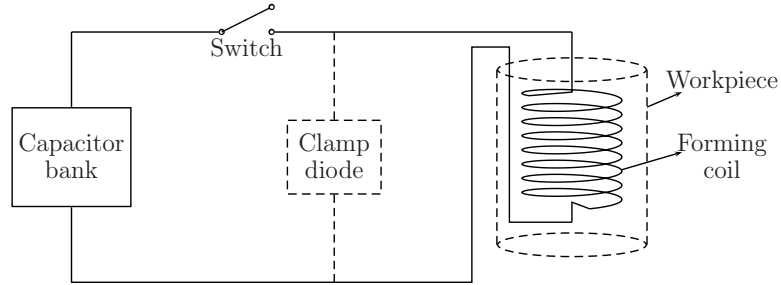
Figure 3.3:   Electromagnetic forming system for expansion (bulging) of hollow cylindrical workpieces.

have chosen here to model both forming systems with the same network model.

In the chosen network model, the capacitor bank is equivalent to a capacitor C, while the forming coil and the workpiece are modelled as two RL-series circuits, coupled via their mutual inductance. The clamp diode is modelled as a resistance, while the other parts of the forming system, before and after the clamp diode, are modelled as RL-series circuits. The network model of a typical electromagnetic forming system is shown in Fig. 3.4. In this network model, we use the following quantities and symbols:

C − capacitance of the capacitor bank,

V_0 − charge voltage of the capacitor bank,

R_{ext} − equivalent resistance of components before the clamp diode,

L_{ext} − equivalent inductance of components before the clamp diode,

R_{diode} − equivalent resistance of the clamp diode,

R_{int} − equivalent resistance of components after the clamp diode,

L_{int} − equivalent inductance of components after the clamp diode,
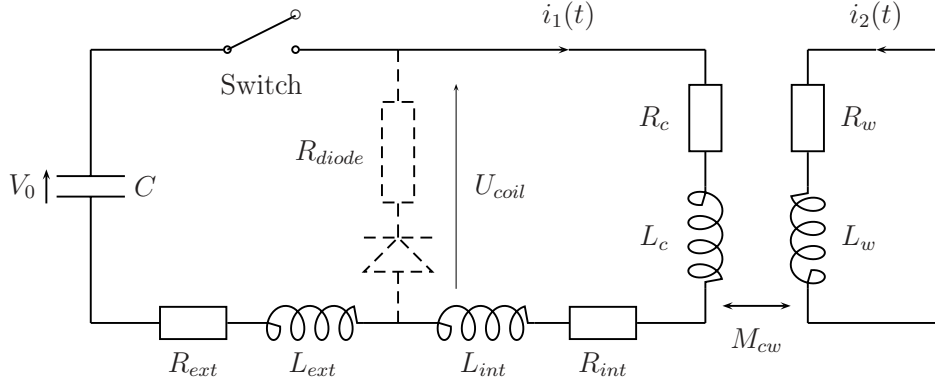
Figure 3.4: The equivalent network model of an electromagnetic forming system.

$$R_c - \text{resistance of the forming coil,}$$
$$L_c - \text{self-inductance of the forming coil,}$$
$$R_w - \text{resistance of the workpiece,}$$
$$L_w - \text{self-inductance of the workpiece,}$$
$$M_{cw} - \text{mutual inductance between the coil and the workpiece.}$$

When the switch in Fig. 3.4 is closed, the discharge of the capacitor bank creates a current pulse $i_1(t)$ in the forming coil. This current generates an electromagnetic field inside the workpiece. This field will further induce an eddy current $i_2(t)$ in the workpiece. As a consequence of the interaction between the electromagnetic field and the induced current, an electromagnetic force is developed, causing the workpiece to deform rapidly, first elastically and finally plastically.

The currents $i_1(t)$ and $i_2(t)$ are used as preliminary quantities in the later models of electromagnetic forming. This is why their shapes and specific time intervals are important for the electromagnetic forming process.

Depending on the values of the circuit elements, when the clamp diode is not present, both currents $i_1(t)$ and $i_2(t)$ may be underdamped, critically damped or overdamped. In the literature, the current pulses are in most cases assumed to be underdamped. It has been mentioned that, for an underdamped current pulse $i_2(t)$, the plastic deformation of the workpiece takes place only in the first cycle of the current pulse, while in the next cycles only elastic deformations of the workpiece may occur. During the entire process, the workpiece is subjected to only one type of deformation, either compression or expansion.

(a)

(b)
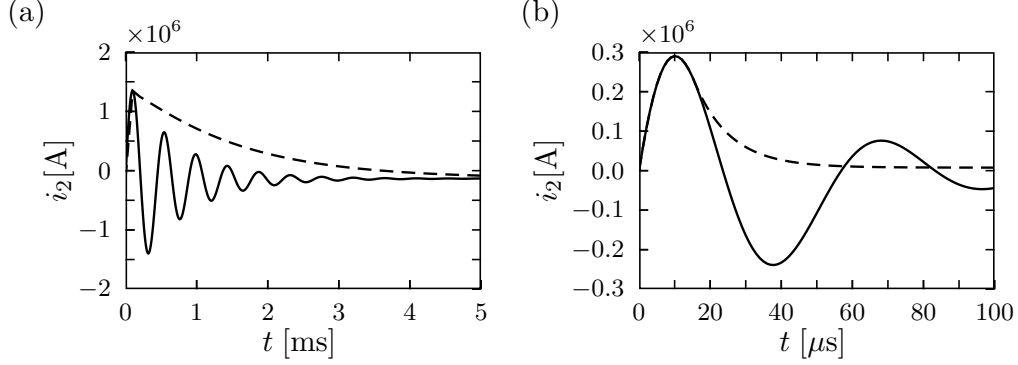
Figure 3.5:   Examples of currents in the workpiece $i_2(t)$ for electromag-
netic compression (a) and electromagnetic expansion (b)
from network model with (dashed line) and without (solid
line) a clamp diode.

In most practical applications, in which no clamp diode is present in the
circuit, the obtained currents $i_1(t)$ and $i_2(t)$ are underdamped. In Fig. 3.5,
some examples of currents $i_2(t)$ that may be obtained in the electromagnetic
forming systems described in Appendix C.1 and C.2 are shown.

The underdamped, critically damped or overdamped currents $i_1(t)$ and
$i_2(t)$, obtained in typical electromagnetic systems, are shifted in time, with
respect to each other. When $i_1(t)$ and $i_2(t)$ are underdamped currents, it is
possible that the forming coil designed for a type of application (compression or
expansion) to be subjected alternatively to compression and expansion causing
it to collapse when not well-dimensioned. When $i_1(t)$ and $i_2(t)$ are damped
currents, the forming coil will be subjected only to one type of deformation,
namely expansion in forming systems designed for compression of workpieces
and compression in forming systems designed for expansion of workpieces. It
means that the mechanical strength requirements for the forming coil may be
reduced if damped current pulses $i_1(t)$ and $i_2(t)$ are used in electromagnetic
forming.

If $i_1(t)$ and $i_2(t)$ are underdamped currents, they can be converted into
damped current pulses using a clamp diode. In the present case, the effect of
this diode may be approximated by a resistance R that satisfies

$$R = \infty \qquad \text{if} \quad u_{coil} > 0 \qquad \text{(inactive diode)}, \qquad (3.1)$$
$$R = R_{diode} \quad \text{if} \quad u_{coil} < 0 \qquad \text{(active diode)}. \qquad (3.2)$$

When a clamp diode is present, the currents $i_1(t)$ and $i_2(t)$ are always damped
and they are calculated in two stages, before and after the clamp diode comes

into operation. In the first stage, the diode is inactive and the currents $i_1^I(t)$ and $i_2^I(t)$ are calculated from the coupled circuit equations

$$(R_{ext} + R_{int} + R_c)i_1^I + (L_{ext} + L_{int} + L_c)\frac{\mathrm{d}i_1^I}{\mathrm{d}t} - M_{cw}\frac{\mathrm{d}i_2^I}{\mathrm{d}t} = V_0 - \frac{1}{C}\int_0^t i_1^I \,\mathrm{d}t, \tag{3.3}$$

$$R_w i_2^I + L_w \frac{\mathrm{d}i_2^I}{\mathrm{d}t} - M_{cw}\frac{\mathrm{d}i_1^I}{\mathrm{d}t} = 0. \tag{3.4}$$

The clamp diode comes into action when the voltage across the forming coil u_{coil} becomes zero. This time instant will be called the crossover time t_{cross}

$$u_{coil}(t_{cross}) = V_0 - \frac{1}{C}\int_0^{t_{cross}} i_1^I \,\mathrm{d}t - R_{ext}i_1^I - L_{ext}\frac{\mathrm{d}i_1^I}{\mathrm{d}t} = 0. \tag{3.5}$$

In the second stage, the diode is active and the currents i_1^{II} and i_2^{II} are calculated from the coupled circuit equations

$$(R_{int} + R_c)i_1^{II} + (L_{int} + L_c)\frac{\mathrm{d}i_1^{II}}{\mathrm{d}t} - M_{cw}\frac{\mathrm{d}i_2^{II}}{\mathrm{d}t} = 0, \tag{3.6}$$

$$R_w i_2^{II} + L_w \frac{\mathrm{d}i_2^{II}}{\mathrm{d}t} - M_{cw}\frac{\mathrm{d}i_1^{II}}{\mathrm{d}t} = 0. \tag{3.7}$$

The currents $i_1(t)$ and $i_2(t)$ can then be written as,

$$i_1(t) = \left\{ \begin{array}{ll} i_1^I(t), & t < t_{cross} \\ i_1^{II}(t), & t > t_{cross} \end{array} \right. , \tag{3.8}$$

$$i_2(t) = \left\{ \begin{array}{ll} i_2^I(t), & t < t_{cross} \\ i_2^{II}(t), & t > t_{cross} \end{array} \right. . \tag{3.9}$$

If there is no clamp diode in the forming circuit, the currents $i_1(t)$ and $i_2(t)$ are calculated from Eqs. (3.3) - (3.4) and both $i_1(t)$ and $i_2(t)$ are oscillating currents, shifted in time with respect to each other, in the underdamped case.

During the real forming process, the parameters of the network model will be time-dependent, because they depend on the geometry of the circuit and this geometry will change when deformation takes place. Some changes in the values of these parameters may also be brought by temperature changes.

In order to be able to calculate the worst case for a possible experimental set-up, in the above procedure we have assumed that all elements in the network model are time invariant. Their values have been calculated using the initial geometry and properties of the electromagnetic forming system. In the further steps towards a more realistic model the dependencies on time, temperature and deformation will gradually be taken into account, see Chapter 9.

3.3 Simplifications of the geometry of the configuration

In the beginning, the changes in geometry due to deformation and due to temperature rise are not taken into account in the electromagnetic field calculations presented in Chapter 4. Later on, as a more realistic model is developed, the changes in geometry of the configurations at a given moment are the input for recalculating the electromagnetic field at the next instant of time. The linear dimensions, the surface area and volume of the configurations in electromagnetic forming are affected not only by deformation, but also by the temperature rise in the forming system. If the temperature rise is small, its influence on geometry of the configurations may be neglected. This assumption is used in early stages of the model, while in Chapter 6 and in Chapter 9, the changes in geometry due to temperature rise are discussed.

Thus, as primary assumptions, there are no changes in the geometry of the configurations due to deformation or to temperature rise. Now we will analyze the main dimensions of the invariant geometry of the configurations to be solved.

1. Length of the forming coil and the workpiece

Both for compression and expansion of hollow circular cylindrical workpieces, the configuration shows axial symmetry. If a cylindrical coordinate system is used, the position in the configurations is specified by the coordinates $\{r, \varphi, z\}$ with respect to a reference frame with an origin $\mathcal{O}$ and three perpendicular
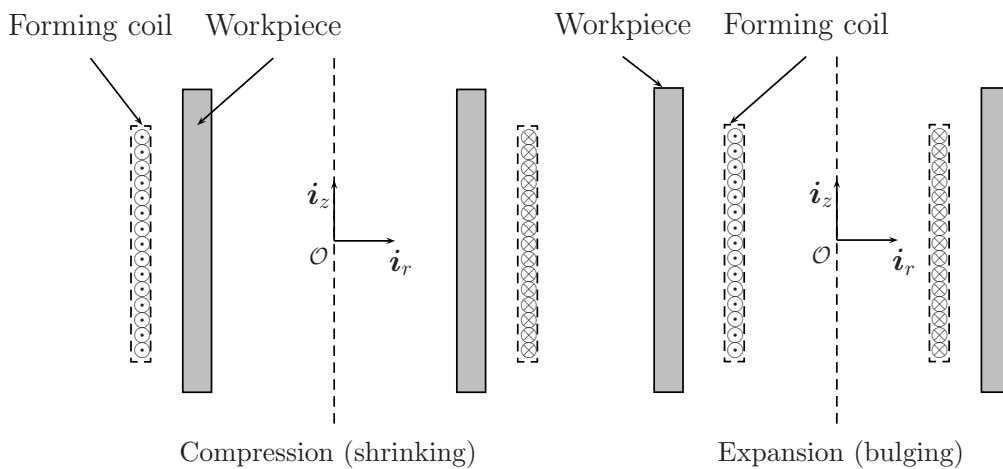
Figure 3.6: Longitudinal section of the forming coil and the workpiece.
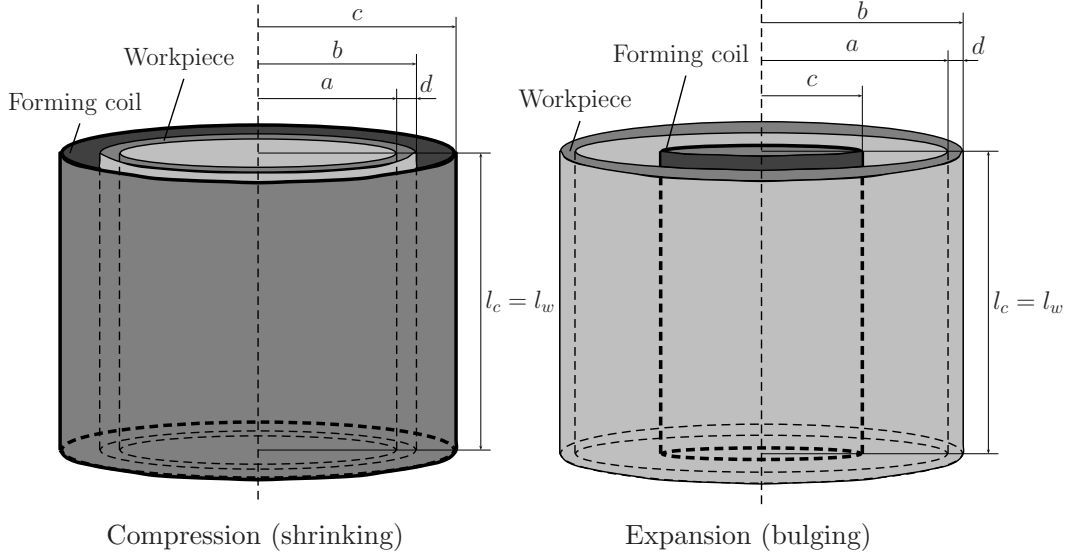
Figure 3.7:   Model configurations; no end effects are assumed to occur
               in the electromagnetic field.

base vectors $\{\boldsymbol{i}_r, \boldsymbol{i}_\varphi, \boldsymbol{i}_z\}$ of unit length. The $z-$axis is the axis of symmetry of the configurations. The configurations only depend on the two coordinates $\{r, z\}$, as presented in Fig. 3.6.

The intention is to develop a simple but accurate analytical model for both compression and expansion, avoiding the problems related to modeling the end points of the forming coil and the workpiece. This may be achieved by considering infinitely long configurations. A finite vertical section of such a model is representative for the real configuration in electromagnetic forming. So, the simplified configurations to be considered are the ones presented in Fig. 3.7.

In both cases, the electric current in the forming coil flows in the φ-direction, so the induced magnetic field in the workpiece will be directed in the z-direction, and the induced electric current is directed in the opposite φ-direction. The electromagnetic force density in the workpiece will be directed radially inwards in case of compression and radially outwards in case of expansion.

2. Thickness of the forming coil and the workpiece

The cross sections of real configurations to be modelled are presented in Fig. 3.8. A plastic tube is used in both configurations to support the windings of the
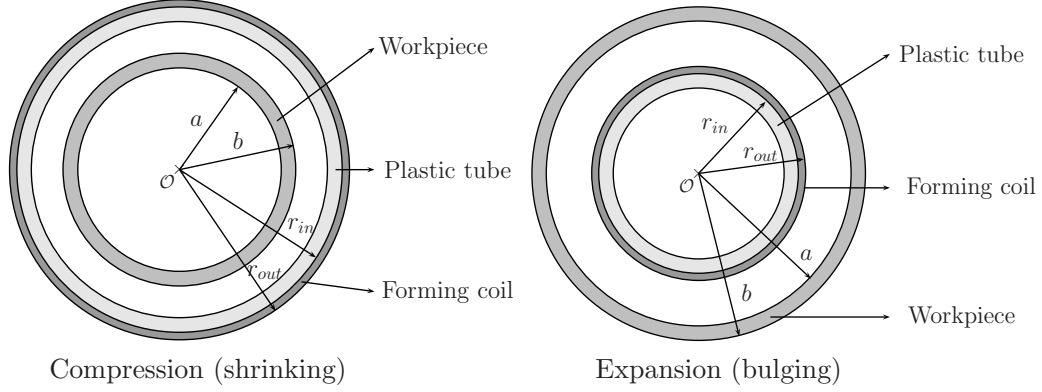
Figure 3.8: Cross section of the forming coil and the workpiece.

forming coil. It has no influence on model development and it is treated as having properties similar to the air contained in the air-gap in between forming coil and workpiece. Both configurations can be divided into five cylindrical subdomains.

In case of compression, the cylindrical subdomains are:

$$r \in [0, a) - \text{the inner space of the workpiece,}$$
$$r \in [a, b] - \text{the workpiece,}$$
$$r \in (b, r_{in}) - \text{the air gap in between the workpiece and the forming coil,}$$
$$r \in [r_{in}, r_{out}] - \text{the forming coil,}$$
$$r \in (r_{out}, \infty) - \text{the space outside the forming coil.}$$

In case of expansion, the subdomains are:

$$r \in [0, r_{in}) - \text{the inner space of the forming coil,}$$
$$r \in [r_{in}, r_{out}] - \text{the forming coil,}$$
$$r \in (r_{out}, a) - \text{the air gap in between the workpiece and the forming coil,}$$
$$r \in [a, b] - \text{the workpiece,}$$
$$r \in (b, \infty) - \text{the space outside the workpiece.}$$

Now, for both configurations it is illustrating to mention the range of variation for the thicknesses of the cylindrical layers with finite thickness, thus namely the workpiece, the forming coil and the air gap in between them. The thickness of the workpieces that have been used in the electromagnetic forming processes in the literature, as presented in Appendix B, is in the order of a few mm, with an air gap in between the forming coil and the workpiece in the range of 1–5

mm. The mean radius of the forming coil is in the range of 10–50 mm and its windings are usually made of a round conductor with a diameter of 1–3 mm. The ratio between the mean radius of the coil and its thickness is so small that the forming coil can be simulated by an infinitely thin sheet antenna.

3.4 Approximations for the parameters of the configuration

A large number of material parameters characterize the electromagnetic forming process. Of course, all parts of the electromagnetic forming system play a role in the forming process, but here only the parameters related to the forming coil and the workpiece are investigated. First of all we study the electromagnetic, elastic and thermal properties of the materials in the electromagnetic forming system. Secondly, we look at other parameters that influence the network model of the electromagnetic forming system.

1. Electromagnetic properties of the materials

The electrical properties of a material are described by its conductivity and its permittivity, while its magnetic properties are described by its permeability and its hysteresis loss.

The electromagnetic forming process is applied only to workpieces made of highly conductive materials as aluminum, copper, silver, brass and mild steel, which have conductivities in the order of 10^7 S/m (see Appendix B). The forming coil is made of a copper conductor or another highly conducting material. In electromagnetic fields that vary relatively slowly over time, the permittivity of the highly conductive materials is almost equal to the permeability of vacuum, $\varepsilon_0 = 8.854 \cdot 10^{-12}$ F/m.

All the above-mentioned materials, except for low-carbon mild steel, are non-magnetic, with a permeability equal to that of vacuum, $\mu_0 = 4\pi \cdot 10^{-7}$ H/m. In the analytical model, when a linear magnetic material has been considered, we assume that the saturation regime is not reached and that the material shows a constant magnetic permeability $\mu = 100\ \mu_0$. When the experimental validation of a model for electromagnetic forming of very thin steel beverage cans is discussed, we assume that the saturation regime is reached very quickly and after that even the mild steel might be considered a magnetic material having $\mu = \mu_0$. For all the considered materials, the hysteresis losses are neglected.

In general, the electromagnetic properties of materials strongly depend on the temperature, but in the early stages of the model the electromagnetic properties are assumed to be temperature and time invariant. In the later stages of the model, when the temperature in the configuration can be calculated at all time instants, only a linear variation of the electrical properties with temperature is used. The newly calculated electrical properties at a certain time instant are used as input for the model to be used at subsequent instants of time.

Note that the coefficients in the linear temperature dependence will remain constant only if there are no significant changes in the geometry of the material. These kind of changes will be investigated in Chapter 6.

2. Elastoplastic properties of the materials

The elastoplastic properties of a material can be described by its mass density, Young's modulus, Poisson's ratio, Lamé's coefficients, yield strength, ultimate tensile strength, rupture stress and maximum elongation or maximum strain. Besides, various non-linear models of stress-strain relations in the plastic deformation region use specific coefficients to account for the temperature rise and for the deformation velocity.

The elastoplastic properties of materials are mostly given as experimental data of the material and depend on the working methods (annealing, heat treatments etc.). The influence of the deformation velocity on the elastoplastic properties is taken into account via the model of elastoplastic behaviour.

The temperature rise has a certain influence on the elastoplastic properties of materials, since each material has its own so-called critical temperature, T_{cr}, obtained at the intersection of the curves of yielding and fracture, but the influence of temperature on the elastoplastic properties is not taken into account in early stages of the model. The influence of temperature rise on the elastoplastic properties of materials is only considered in Chapter 9.

In the literature related to electromagnetic forming, all authors assume that the mass density of the materials is constant. The assumption of invariant mass density is also used in the model presented here. In reality, the mass density changes with temperature, but for a large temperature range these changes are negligible, as it will be shown in Chapter 9. There exists a dependence of mass density on deformation state, but this dependence is neglected.

3. Thermal properties of the materials

The thermal properties of a material can be described by its specific heat and

thermal conductivity. Both properties change with temperature in a reasonably linear manner, but these changes are not taken into account in the development of the model.

4. Elements of the equivalent network model

The values of the elements of the equivalent network model corresponding to the forming coil and the workpiece change because, during the forming process, the geometry and the properties of workpiece and forming coil change. We have assumed that the values of the elements of the network model are constant, calculated with the geometry of the system in the initial state, so

$$R_w = \pi(a + b)/(\sigma_w l_w d), \tag{3.10}$$

$$L_w = \pi \mu_w (a + b)^2/(4l_w), \tag{3.11}$$

$$R_c = 2\pi c l_c/(\sigma_c g\, h), \tag{3.12}$$

$$L_c = \pi \mu_c c^2 n^2 l_c, \tag{3.13}$$

$$k_c = (c/r_{mean})^2, \tag{3.14}$$

$$M_{cw} = k_c (L_c L_w)^{1/2}. \tag{3.15}$$

The actual values of the elements of the equivalent network model may easily be calculated at each instant of time and temperature level, based on the actual geometry and material properties of the forming system.

3.5   Approximations for the fields in the configuration

The fields to be investigated in this thesis are the fields in the workpiece, namely the electromagnetic, elastic, temperature and thermoelastic fields.

1. Electromagnetic field in the workpiece

If in a medium the dielectric properties dominate, the electromagnetic field is wavelike in nature and the electric displacement current yields a much larger contribution to the magnetic field than the conduction current. If, on the other hand, the conductive properties dominate, the electromagnetic field is diffusive in nature and the conduction current yields a much larger contribution to the magnetic field than the electric displacement current. In our case all workpieces are made of highly conducting materials i.e., the conductive properties dominate and the transient electromagnetic field is considered diffusive in nature.

2. Elastic field in the workpiece

The source of the elastic field in the workpiece is the electromagnetic force density due to the transient electromagnetic field in the workpiece. Solving the elastic field equations will yield the components of the stress and the displacement in the workpiece.

In the literature related to electromagnetic forming, the source of the dynamic elastic or plastic field is the electromagnetic pressure exerted on the outside of the workpiece. This electromagnetic pressure accounts for the total electromagnetic force exerted at all points inside the workpiece. The approach presented in this thesis describes the electromagnetic forming process with regard to the motion of each particle inside the workpiece, motion that is generated by the electromagnetic volume force density and by the electromagnetic surface force density existent at each point of the workpiece. Difficulties are encountered when calculating the plastic deformations, since the models are mostly empirical and non-unique.

3. Temperature field in the workpiece

The temperature field in the configuration is calculated, since it may possibly influence the whole deformation process. Such temperature calculations have not been investigated in detail in the literature related to electromagnetic forming, but they shown to be important for the process of electromagnetic forming.

The thermoelastic field in the workpiece is basically calculated in the same way as the elastic field and it involves the introduction of a temperature-dependent term in the elastic field equations.

Chapter 4

Electromagnetic description of the problem

This chapter presents the calculation of the transient diffusive electromagnetic field in cylindrical configurations related to typical electromagnetic forming systems, as presented in the previous chapters. In particular, the electromagnetic force density is calculated from the diffusive electromagnetic field components. Numerical results are given for some particular cases related to these forming systems.

4.1 Configuration of the electromagnetic problem

The configurations in which the diffusive electromagnetic field will be calculated are presented in Fig. 4.1. These configurations model the case of electromagnetic compression and electromagnetic expansion, respectively.

The position in the configuration is specified by the cylindrical coordinates $\{r, \varphi, z\}$. The time coordinate is t.

Both configurations can be divided into four cylindrical subdomains, since in Section 3.3, the forming coil was assimilated with an infinitely thin sheet antenna. In case of compression, the cylindrical subdomains are: the inner space of the workpiece with $r \in [0, a)$, the workpiece domain $\mathcal{D}$ with $r \in [a, b]$, the air gap in between the workpiece and the forming coil with $r \in (b, c)$ and the space outside the forming coil with $r \in (c, \infty)$. In case of expansion, the subdomains are: the inner space of the forming coil with $r \in [0, c)$,
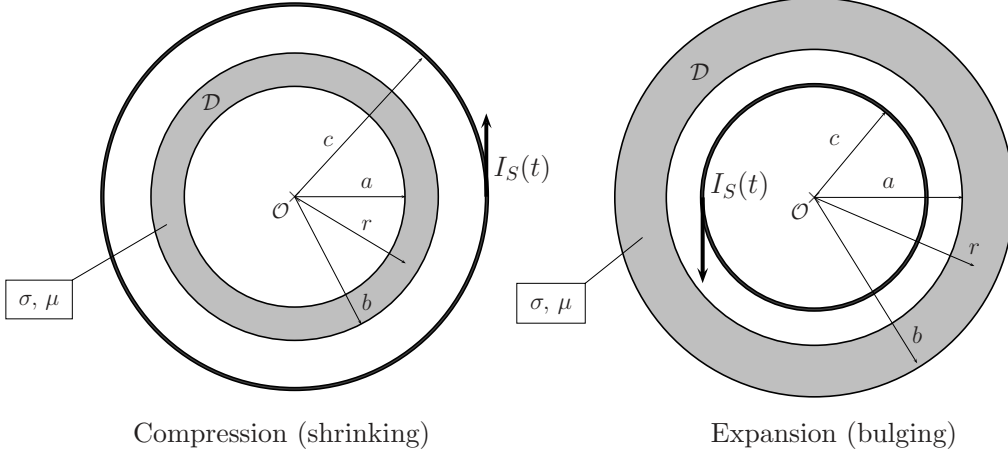
Figure 4.1:   Cross section of the cylindrical configurations for the cal-
culation of diffusive electromagnetic field.

the air gap in between the workpiece and the forming coil with $r \in (c, a)$, the
workpiece domain $\mathcal{D}$ with $r \in [a, b]$ and the space outside the workpiece with
$r \in (b, \infty)$.

The medium of the workpiece is homogeneous, linear, time invariant,
locally and instantaneously reacting and isotropic in its electromagnetic be-
havior, with permeability μ and electrical conductivity σ. The other media
are assumed to be vacuum with permeability μ_0 and zero conductivity. The
configuration is excited by a single sheet antenna, located at radial position
$r = c$, carrying an electric current in the positive φ-direction. This sheet an-
tenna models the infinitesimally thin forming coil in the real electromagnetic
forming system. The configuration under investigation is assumed to have infi-
nite length in the z-direction. This fact, combined with the axial symmetry of
the configuration, gives that all quantities related to this configuration depend
on the radius r and time t, only.

4.2   Diffusive field equations and boundary conditions

The electromagnetic field quantities in each domain of the configuration are
the electric field strength $\boldsymbol{E}$ and the magnetic field strength $\boldsymbol{H}$. In the domain
of the workpiece $\mathcal{D}$, these field quantities satisfy the diffusive electromagnetic

field equations

$$\nabla \times \boldsymbol{H} - \sigma \boldsymbol{E} = \boldsymbol{0}, \tag{4.1}$$
$$\nabla \times \boldsymbol{E} + \mu \partial_t \boldsymbol{H} = \boldsymbol{0}. \tag{4.2}$$

In the cylindrical sheet at $r = c$, an electric current $I_S(t)$ per unit length along the z-direction is present. The electromagnetic field is causally related to the action of this electric-current source.

The given source generates a one-dimensional, r-dependent field of which only $E_\varphi = E_\varphi(r,t)$ and $H_z = H_z(r,t)$ differ from zero. These field components satisfy the diffusive electromagnetic field equations

$$\partial_r H_z + \sigma E_\varphi = 0, \quad \text{for} \ \ a < r < b, \tag{4.3}$$
$$\frac{1}{r}\partial_r(r E_\varphi) + \mu \partial_t H_z = 0, \quad \text{for} \ \ a < r < b. \tag{4.4}$$

The simplest way to construct solutions to Eqs. (4.3) and (4.4) that satisfy the proper boundary and excitation conditions and ensure causality is to use the Laplace transformation with respect to time. To illustrate the notation, let

$$\hat{I}_S(s) = \boldsymbol{\mathsf{L}}_t^s I_S(t) = \int_{t=0^-}^{\infty} \exp(-s\,t) I_S(t)\,\mathrm{d}t, \tag{4.5}$$

where it has been assumed that the electric current source starts to act at the instant $t = 0$. The complex transform parameter s (in linear system theory also denoted as *the complex frequency*) is taken in the right half of the complex s-plane. For the class of bounded functions $I_S(t)$ this is sufficient to guarantee a one-to-one correspondence between a causal time function and its Laplace transform. Under the transformation it turns out that $\boldsymbol{\mathsf{L}}_t^s \partial_t \to s$, while

$$\hat{I}_S(s)\exp(-s\,t_0) = \boldsymbol{\mathsf{L}}_t^s I_S(t - t_0), \quad \text{for any real } t_0 \geq 0. \tag{4.6}$$

The Laplace transformed quantities are denoted with a hat symbol and we omit the explicit s-dependence in our notation. When we take the limit

$$s \to \mathrm{j}\omega, \tag{4.7}$$

we end up with the Fourier transformed quantities, where j is the imaginary unit and $\omega = 2\pi f$ is the radial frequency, while f denotes the frequency of operation. In our numerical work, we use the FFT (Fast Fourier Transform) to compute the pertaining Fourier transforms.

In the conductive domain $\mathcal{D}$ of the workpiece, the application of the Laplace transform to the electromagnetic field equations Eqs. (4.3) and (4.4) leads to

$$\partial_r \hat{H}_z + \sigma \hat{E}_\varphi = 0, \quad \text{for } a < r < b, \tag{4.8}$$

$$\frac{1}{r}\partial_r(r\hat{E}_\varphi) + s\mu\hat{H}_z = 0, \quad \text{for } a < r < b. \tag{4.9}$$

From the above system of equations, the diffusion equation is obtained as

$$\partial_r^2 \hat{H}_z + \frac{1}{r}\partial_r \hat{H}_z - \gamma^2 \hat{H}_z = 0, \tag{4.10}$$

where $\gamma = \sqrt{s\sigma\mu}$. The components of the electromagnetic diffusive field are obtained as

$$\hat{H}_z = \hat{I}_S \left[A \frac{I_0(\gamma r)}{I_0(\gamma a)} + B \frac{K_0(\gamma r)}{K_0(\gamma a)} \right], \tag{4.11}$$

$$\hat{E}_\varphi = -Z\hat{I}_S \left[A \frac{I_1(\gamma r)}{I_0(\gamma a)} - B \frac{K_1(\gamma r)}{K_0(\gamma a)} \right], \tag{4.12}$$

where $I_{0,1}(\gamma r)$ and $K_{0,1}(\gamma r)$ are the modified Bessel function of the first and second kind, respectively, and we have introduced the impedance

$$Z = \sqrt{s\mu/\sigma}. \tag{4.13}$$

The constants A and B have to be determined from the conditions that the electric field E_φ and the magnetic field H_z are continuous through the interfaces with the inner vacuum domains.

In the vacuum domains, we have zero conductivity and the following quasi-static equations hold

$$\partial_r \hat{H}_z = 0, \tag{4.14}$$

$$\frac{1}{r}\partial_r(r\hat{E}_\varphi) + s\mu_0\hat{H}_z = 0. \tag{4.15}$$

The first equation, Eq. (4.14), indicates that in a vacuum domain $\partial_r \hat{H}_z = 0$, and as a consequence the magnetic field is constant. At infinity, $\hat{H}_z$ is zero, while at the position of the electric current sheet the magnetic field $\hat{H}_z$ makes a jump with amplitude $\hat{I}_S$. The second equation, Eq. (4.15), shows that the electric field $\hat{E}_\varphi$ is a linear combination of the functions r and $1/r$.

Analysis for compression

In the inner vacuum domain $r < a$, the components of the electromagnetic field are obtained as

$$\hat{H}_z = \hat{I}_S C, \tag{4.16}$$

$$\hat{E}_\varphi = -\frac{1}{2}\left(\frac{\mu_0}{\mu}\right)\gamma Z \hat{I}_S C r. \tag{4.17}$$

Using the continuity conditions for the magnetic and electric fields at $r = a$, and the excitation condition that the magnetic field at $r = b$ is equal to $\hat{I}_S$, we obtain the following system of equations

$$A + B = C,$$

$$A\frac{I_1(\gamma a)}{I_0(\gamma a)} - B\frac{K_1(\gamma a)}{K_0(\gamma a)} = \eta a\, C, \tag{4.18}$$

$$A\frac{I_0(\gamma b)}{I_0(\gamma a)} + B\frac{K_0(\gamma b)}{K_0(\gamma a)} = 1,$$

where

$$\eta = \frac{1}{2}\left(\frac{\mu_0}{\mu}\right)\gamma. \tag{4.19}$$

The solution of this system of equations is

$$A = \frac{I_0(\gamma a)\left[K_1(\gamma a)+\eta a K_0(\gamma a)\right]}{I_0(\gamma b)\left[K_1(\gamma a)+\eta a K_0(\gamma a)\right] + K_0(\gamma b)\left[I_1(\gamma a)-\eta a I_0(\gamma a)\right]}, \tag{4.20}$$

$$B = \frac{K_0(\gamma a)\left[I_1(\gamma a)-\eta a I_0(\gamma a)\right]}{I_0(\gamma b)\left[K_1(\gamma a)+\eta a K_0(\gamma a)\right] + K_0(\gamma b)\left[I_1(\gamma a)-\eta a I_0(\gamma a)\right]}, \tag{4.21}$$

$$C = \frac{1/(\gamma a)}{I_0(\gamma b)\left[K_1(\gamma a)+\eta a K_0(\gamma a)\right] + K_0(\gamma b)\left[I_1(\gamma a)-\eta a I_0(\gamma a)\right]}. \tag{4.22}$$

Substituting the expressions for the constants A, B and C in the diffusive field expressions, we arrive at

$$\hat{H}_z = \hat{I}_S \frac{1/(\gamma a)}{I_0(\gamma b)\left[K_1(\gamma a)+\eta a K_0(\gamma a)\right] + K_0(\gamma b)\left[I_1(\gamma a)-\eta a I_0(\gamma a)\right]}, \tag{4.23}$$

$$\hat{E}_\varphi = -Z\hat{I}_S \frac{\eta r/(\gamma a)}{I_0(\gamma b)\left[K_1(\gamma a)+\eta a K_0(\gamma a)\right] + K_0(\gamma b)\left[I_1(\gamma a)-\eta a I_0(\gamma a)\right]}, \tag{4.24}$$

when $r \in [0, a)$, and

$$\hat{H}_z = \hat{I}_S \frac{I_0(\gamma r)\left[K_1(\gamma a)+\eta a K_0(\gamma a)\right] + K_0(\gamma r)\left[I_1(\gamma a)-\eta a I_0(\gamma a)\right]}{I_0(\gamma b)\left[K_1(\gamma a)+\eta a K_0(\gamma a)\right] + K_0(\gamma b)\left[I_1(\gamma a)-\eta a I_0(\gamma a)\right]}, \tag{4.25}$$

$$\hat{E}_\varphi = -Z\hat{I}_S \frac{I_1(\gamma r)\left[K_1(\gamma a)+\eta a K_0(\gamma a)\right] - K_1(\gamma r)\left[I_1(\gamma a)-\eta a I_0(\gamma a)\right]}{I_0(\gamma b)\left[K_1(\gamma a)+\eta a K_0(\gamma a)\right] + K_0(\gamma b)\left[I_1(\gamma a)-\eta a I_0(\gamma a)\right]}, \tag{4.26}$$

in the cylindrical domain corresponding to the workpiece $r \in [a, b]$.

Further, in the cylindrical domain corresponding to the air-gap in between the forming coil and the workpiece $r \in (b, c]$, we obtain

$$\hat{H}_z = \hat{I}_S, \tag{4.27}$$

$$\hat{E}_\varphi = \hat{E}_\varphi(b)\frac{b}{r} - Z\hat{I}_S\eta\, b\left(\frac{r}{b} - \frac{b}{r}\right), \tag{4.28}$$

and in the cylindrical domain corresponding to surrounding medium $r \in (c, \infty)$,

$$\hat{H}_z = 0, \tag{4.29}$$

$$\hat{E}_\varphi = \hat{E}_\varphi(b)\frac{b}{r} - Z\hat{I}_S\eta\, b\left(\frac{c}{b} - \frac{b}{c}\right)\frac{c}{r}. \tag{4.30}$$

Analysis for expansion

For the case of expansion we will consider only the case that the electric-current sheet coincides with the inner boundary of the workpiece ($c = a$). Using the excitation condition that the magnetic field at $r = a$ is equal to $\hat{I}_S$ and the continuity conditions for the magnetic and electric fields at $r = b$, we obtain the following system of equations

$$
\begin{aligned}
A + B &= C - 1, \\
A\frac{I_1(\gamma a)}{I_0(\gamma a)} - B\frac{K_1(\gamma a)}{K_0(\gamma a)} &= \eta\, a\, C, \\
A\frac{I_0(\gamma b)}{I_0(\gamma a)} + B\frac{K_0(\gamma b)}{K_0(\gamma a)} &= 0.
\end{aligned}
\tag{4.31}
$$

After solving this system of equations, the electromagnetic field expressions are obtained in a similar way as in the case of compression. We suffice with the presentation of the solutions of the above system of equations,

$$A = \gamma\, a\, I_0(\gamma a)\left[\eta\, a\, K_0(\gamma a)\, C + K_1(\gamma a)(C - 1)\right], \tag{4.32}$$

$$B = \gamma\, a\, K_0(\gamma a)\left[-\eta\, a\, I_0(\gamma a)\, C + I_1(\gamma a)(C - 1)\right], \tag{4.33}$$

$$C = \frac{I_0(\gamma b)K_1(\gamma a) + K_0(\gamma b)I_1(\gamma a)}{I_0(\gamma b)\left[K_1(\gamma a) + \eta a K_0(\gamma a)\right] + K_0(\gamma b)\left[I_1(\gamma a) - \eta a I_0(\gamma a)\right]}. \tag{4.34}$$

4.3   Electromagnetic force density

In Chapter 2, the general theory regarding the electromagnetic force in material media has been presented. Taking into account the remarks in Section 2.4, the application of Eq. (2.29) for the given cylindrical configuration gives

$$f_r^V(r,t) = \sigma \mu E_\varphi(r,t) H_z(r,t), \tag{4.35}$$

for $r \in [a,b]$, thus in the cylindrical domain representing the workpiece. The electromagnetic surface force density on the upper boundary $r = b$ of the workpiece is, according to Eq. (2.16)

$$f_r^S(b,t) = -\frac{1}{2}\left(\mu_0 \lim_{r \downarrow b}[H_z(r,t)]^2 - \mu \lim_{r \uparrow b}[H_z(r,t)]^2\right), \tag{4.36}$$

while on the lower boundary $r = a$ of the workpiece we have

$$f_r^S(a,t) = -\frac{1}{2}\left(\mu \lim_{r \downarrow a}[H_z(r,t)]^2 - \mu_0 \lim_{r \uparrow a}[H_z(r,t)]^2\right). \tag{4.37}$$

All the quantities in the right-hand side of Eqs. (4.35) - (4.37) are already known for the whole time-interval of investigation and within the whole configuration. The electromagnetic volume force density and the electromagnetic surface force density can then be calculated very easily. In view of the continuity of the magnetic field strength at the boundaries $r = a$ and $r = b$, the surface force expressions in Eqs. (4.36) - (4.37) reduce to

$$f_r^S(b,t) = \frac{1}{2}(\mu - \mu_0)\left[H_z(b,t)\right]^2, \tag{4.38}$$

while on the lower boundary a of the workpiece we have

$$f_r^S(a,t) = \frac{1}{2}(\mu_0 - \mu)\left[H_z(a,t)\right]^2. \tag{4.39}$$

For non-magnetic workpieces, the surface force densities are zero, while for magnetic workpieces, they have non-zero values.

The electromagnetic volume force density in the cylindrical domain representing the workpiece may be calculated either in the time domain as

$$f_r^V(r,t) = \sigma \mu E_\varphi(r,t) H_z(r,t), \tag{4.40}$$

or in the frequency domain as

$$\hat{f}_r^V(r,\omega) = \frac{\sigma \mu}{2\pi} \int_{\omega'=-\infty}^{\infty} \hat{E}_\varphi(r,\omega-\omega') \hat{H}_z(r,\omega')\, \mathrm{d}\omega'. \tag{4.41}$$

4.4   Numerical results

In this section, we present some numerical results for typical electromagnetic forming systems designed for compression and for expansion of hollow circular cylindrical workpieces. First, we will present numerical results for electromagnetic compression and then one example for electromagnetic expansion.

The following types of workpieces subjected to electromagnetic compression are investigated:

- a non-magnetic $(\mu = \mu_0)$ thick workpiece with an inner radius $r = a = 20$ mm and an outer radius $r = b = 22$ mm,

- a hypothetical magnetic $(\mu = 100 \, \mu_0)$ thick workpiece with an inner radius $r = a = 20$ mm and an outer radius $r = b = 22$ mm,

- a non-magnetic $(\mu = \mu_0)$ thin workpiece with an inner radius $r = a = 20$ mm and an outer radius $r = b = 20.2$ mm.

In all these cases, the cylindrical current sheet is located at $r = c = 24$ mm and the electrical conductivity of the workpiece is $\sigma = 3.6 \cdot 10^7$ S/m.

For electromagnetic expansion, only a non-magnetic $(\mu = \mu_0)$ thick workpiece with an inner radius $r = a = 20$ mm and an outer radius $r = b = 22$ mm is considered. In this case, the electrical conductivity of the workpiece is $\sigma = 3.6 \cdot 10^7$ S/m and the cylindrical current sheet is located at $r = c = 20$ mm.

In our following examples, we have considered that the current per unit length $I_S(t)$ flowing in the sheet antenna has been determined from the network model, where a clamp diode with $R_{diode} = 0$ is present. The current per unit length $I_S(t)$ is the current $i_2(t)/l_w$, see Chapter 3 and Appendix C.

Spatial distribution of the electromagnetic field for compression

In order to obtain some physical insight in the spatial dependence of the electromagnetic quantities, we present the electromagnetic field quantities for a relatively low frequency, $f = 1$ kHz, and for a relatively high frequency, $f = 100$ kHz in a non-magnetic $(\mu = \mu_0)$ thick $(b - a = 2$ mm) workpiece.

The spatial distributions of the magnetic field strength and of the electric field strength are presented in Figs. 4.2 and 4.3. Note that the results are normalized with respect to the electric current $\hat{I}_S$. For high-frequency, as expected, we observe the large decay of the electromagnetic fields in the negative radial direction inside the conductive workpiece.
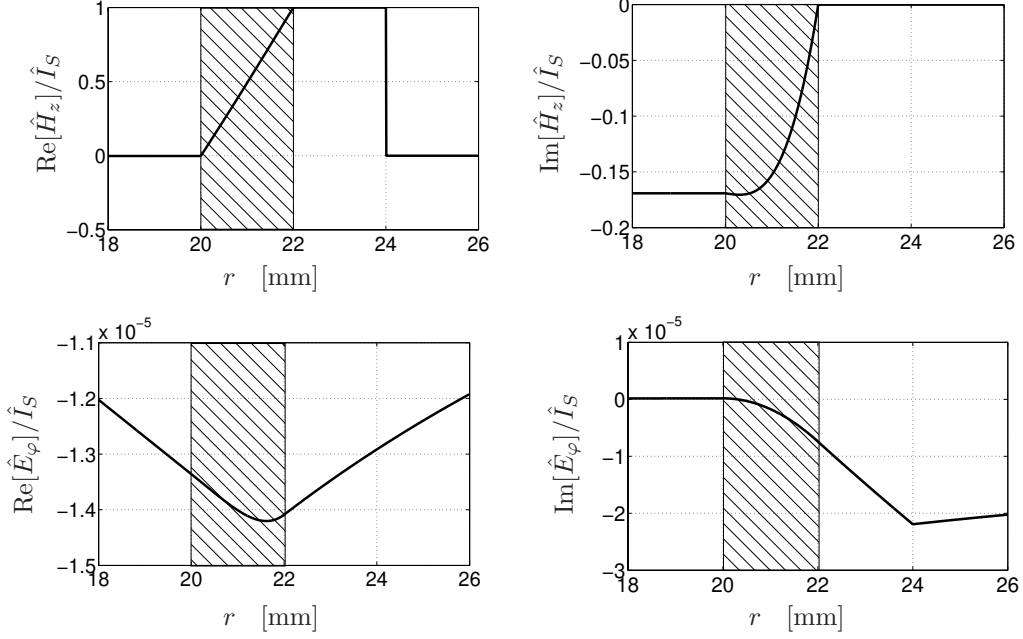
Figure 4.2:   Real and imaginary part of the magnetic field strength
              and of the electric field strength as a function of po-
              sition at $f = 1$ kHz for a non-magnetic $(\mu = \mu_0)$ thick
              $(b - a = 2$ mm$)$ workpiece subjected to compression.

Further, we have computed the results for the magnetic $(\mu = 100\,\mu_0)$
thick $(b - a = 2$ mm$)$ workpiece. It appears that the results at the frequency
$f = 1$ kHz are very similar to the ones of the non-magnetic case at $f = 100$ kHz.

The reason is that for the parameters considered, the diffusion coeffi-
cient γ, wherein the frequency parameter s and the permeability μ occur as a
product, has the same value in both these cases.

Also the impedance Z, wherein the frequency parameter s and the per-
meability μ occur also as a product, has the same value in both these cases.
The only difference is that the parameter η is not the same, but the factor
behind this value is very small.
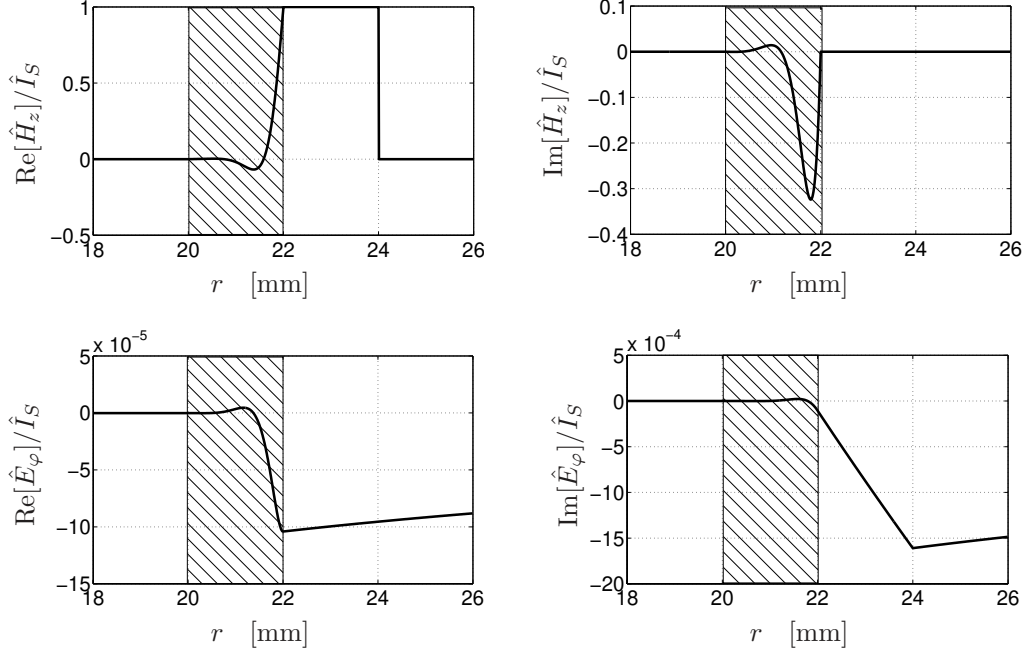
Figure 4.3:   Real and imaginary part of the magnetic field strength
               and of the electric field strength as a function of posi-
               tion at $f = 100$ kHz for a non-magnetic $(\mu = \mu_0)$ thick
               $(b - a = 2$ mm) workpiece subjected to compression.

Non-magnetic thick workpiece in compression

In the left-top plot of Fig. 4.4, the current per unit length in the sheet antenna
in the time domain $I_S(t)$ is presented, while its frequency domain counterpart
$|\hat{I}_S(f)|$ is presented in the right-top plot of this figure. In the left-bottom plot
of this figure, the electromagnetic volume force density at the upper boundary
$r = b$ of the workpiece is presented, both in the time domain (left-bottom plot)
and in the frequency domain (right-bottom plot).

In the time domain, the electromagnetic volume force density f_r^V decays
more rapidly than the current per unit length $I_S(t)$ in the sheet antenna. In
fact, it contains higher frequency components that can also be observed from
its frequency spectrum. Although the dominant part of the electromagnetic
force density f_r^V is negative, there is an extended time interval where the
electromagnetic volume force density is positive.
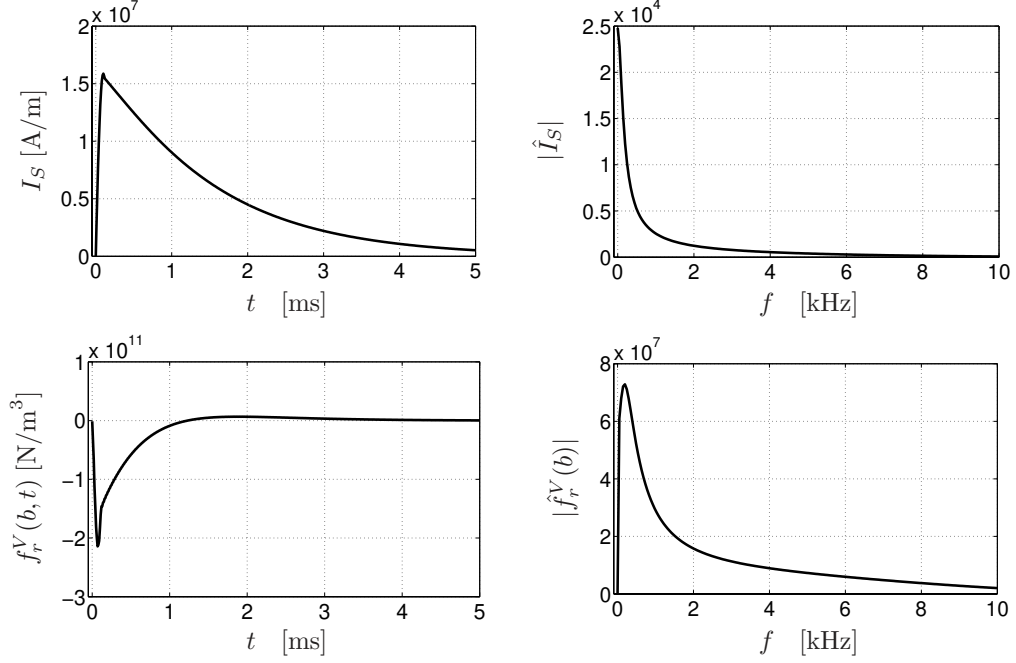
Figure 4.4: Electric current per unit length in the sheet antenna I_S and electromagnetic volume force density f_r^V at $r = b$ in the time domain (*left*) and in the frequency domain (*right*), for a non-magnetic ($\mu = \mu_0$) thick ($b-a = 2$ mm) workpiece subjected to compression.

The positive values of the electromagnetic volume force density are negligible as compared with the maximum value of the electromagnetic volume force density f_r^V of about $-2 \cdot 10^{11}$ N/m^3.

Further, in Fig. 4.5, the space-time evolution of the electromagnetic volume force density in the cylindrical domain $r \in [a, b]$ of the workpiece is presented.

For the relatively thick workpiece with $b - a = 2$ mm, that has been chosen in this case, the presented figures show that the electromagnetic volume force density has large values at small time instants and near the interface closest to the sheet antenna and it decays rapidly in time and in space.

Figure 4.5:   Electromagnetic volume force density f_r^V in space-time do-
main for a non-magnetic $(\mu = \mu_0)$ thick $(b - a = 2$ mm$)$
workpiece subjected to compression.

Figure 4.6:   Normalized electromagnetic volume force density at $r = b$ in the time domain (*left*) and in the frequency domain (*right*) for a non-magnetic ($\mu = \mu_0$) thick workpiece (dashed lines) and for a magnetic ($\mu = 100\,\mu_0$) thick workpiece (solid lines) subjected to compression.

Magnetic thick workpiece in compression

The electromagnetic volume force density at the upper interface $r = b$ of the cylindrical domain representing the workpiece has been calculated for a workpiece made of a hypothetical linear magnetic material ($\mu = 100\,\mu_0$). The thickness of the workpiece is $b - a = 2$ mm. The results in the time domain and in the frequency are presented in Fig. 4.6 as solid lines.

For comparison, the results for a non-magnetic workpiece have been given as the dashed lines, and all results are normalized with $(\mu/\mu_0)^{-3/2}$, since from their expressions it directly follows that the absolute values of the electromagnetic force density in a magnetic material are $(\mu/\mu_0)^{3/2}$ times larger than the ones obtained in a non-magnetic material. We observe that the time domain results are roughly the same, although in the magnetic workpiece, the electromagnetic volume force density decays to zero more rapidly than in a non-magnetic one.

In Fig. 4.7, the evolution of the electromagnetic force density in the space-time domain both for a non-magnetic and for a magnetic workpiece is presented. For the magnetic workpiece, significant (non-zero) results of the electromagnetic volume force density are obtained only for a small part of the workpiece, i.e. only for a cylindrical domain located near the outer boundary $r = b$ facing the electric current sheet.
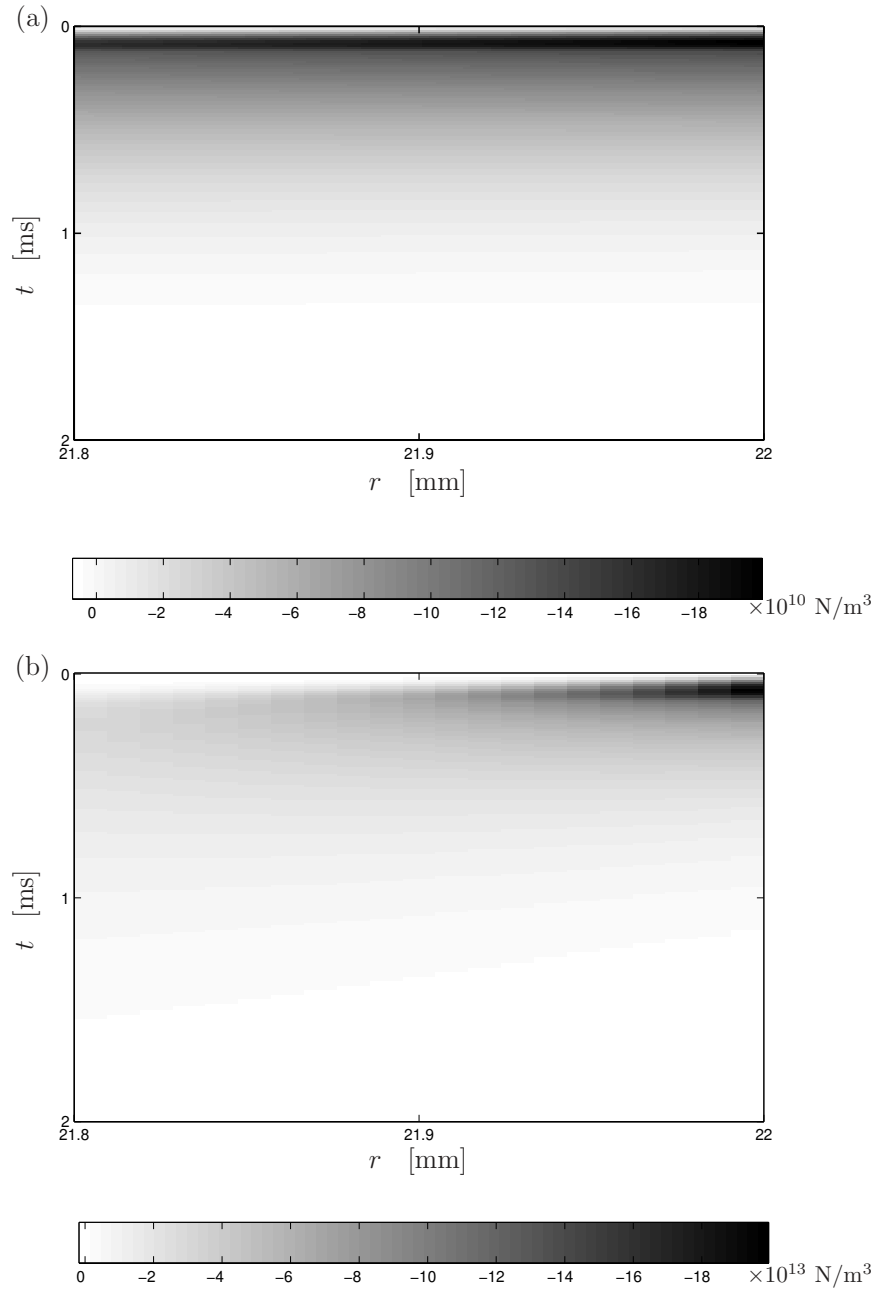
Figure 4.7:   Normalized   electromagnetic   volume   force   density
$(\mu/\mu_0)^{-\frac{3}{2}} f_r^V$ in space-time domain for a non-magnetic
$(\mu = \mu_0)$ thick $(b - a = 2 \text{ mm})$ workpiece (a) and for a
magnetic $(\mu = 100\,\mu_0)$ thick $(b - a = 2 \text{ mm})$ workpiece (b)
subjected to compression.

Figure 4.8: Electromagnetic surface force density f_r^S at $r = a$ (*left*) and at $r = b$ (*right*) in the time domain for a magnetic ($\mu = 100\,\mu_0$) thick ($b - a = 2$ mm) workpiece subjected to compression.

Therefore, we have presented the space-time evolution of the electromagnetic force density only for a small part (21.8 mm $< r <$ 22 mm) of the workpiece. Comparing the results for the magnetic and the non-magnetic workpieces, we observe indeed the large decay of the electromagnetic force density in the negative radial direction of the magnetic workpiece, together with a different decay in time.

In case of a magnetic workpiece, there exists also an electromagnetic surface force density on both sides of the workpiece, calculated as in Section 4.3. The time-domain results for the electromagnetic surface force density are presented in Fig. 4.8, for $r = a$ (left) and $r = b$ (right).

As expected, on the upper boundary $r = b$ closest to the sheet antenna, the absolute values of the electromagnetic surface force density are larger than the ones of the electromagnetic surface force density on the lower boundary $r = a$.

Non-magnetic thin workpiece in compression

The electromagnetic volume force density has been computed also for a non-magnetic ($\mu = \mu_0$), thin ($b - a = 0.2$ mm) workpiece, using the same current pulse as for the previous numerical results. In Fig. 4.9, the electromagnetic volume forces in the space-time domain for a non-magnetic thick ($b - a = 2$ mm) and for a non-magnetic thin ($b - a = 0.2$ mm) workpiece are presented.
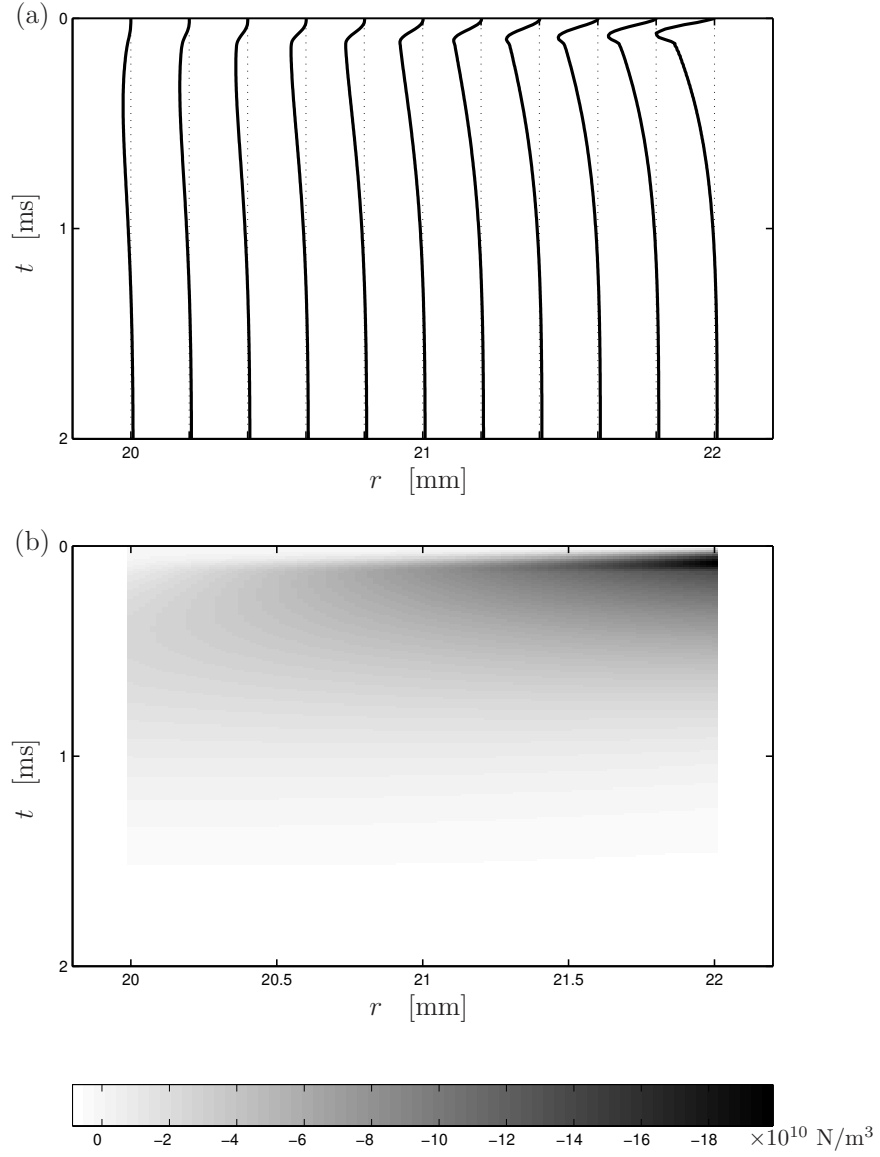
Figure 4.9:   Electromagnetic volume force density f_r^V in space-time
              domain for a non-magnetic ($\mu = \mu_0$) thick ($b - a = 2$
              mm) workpiece (a) and for a non-magnetic ($\mu = \mu_0$) thin
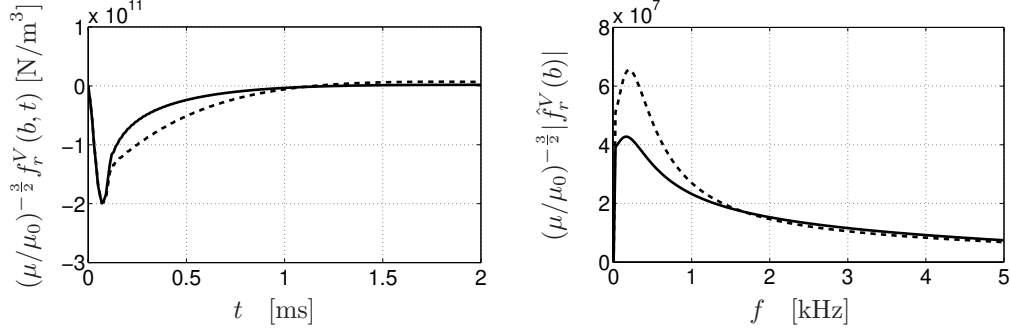   ($b - a = 0.2$ mm) workpiece (b) subjected to compression.
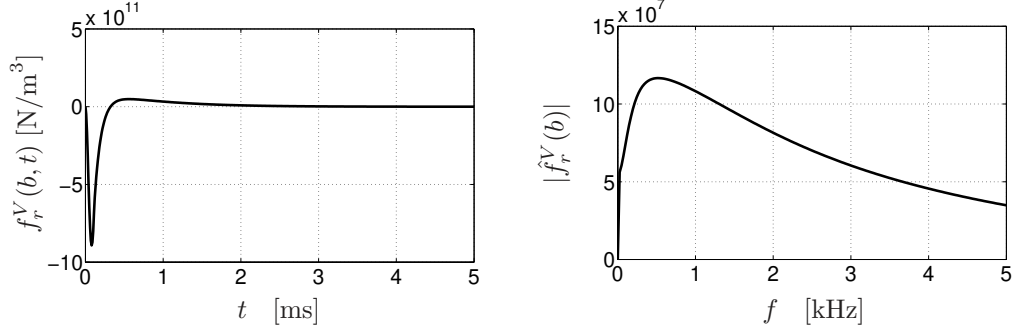
Figure 4.10: Electromagnetic volume force density f_r^V at $r = b$ in the time domain (*left*) and in the frequency domain (*right*) for a non-magnetic ($\mu = \mu_0$) thin ($b - a = 0.2$ mm) workpiece subjected to compression.

In the non-magnetic thin workpiece, the maximum electromagnetic volume force density is roughly four times larger than in the thick workpiece, decreases slower in the radial direction, and is more concentrated in a smaller time window. It seems to penetrate better in the thin workpiece than in the thick workpiece. When we investigate the results for the electromagnetic volume force density at the upper interface $r = b$, as presented in Fig. 4.10, and compare them with the results of Fig. 4.4 for a non-magnetic thick workpiece, we notice that at $r = b$ the width of the electromagnetic force density pulse already at the starting point is much smaller in a thin workpiece than in a thick workpiece; this means that it has a much wider frequency content, which is also clearly visible when we compare their frequency spectra.

Non-magnetic thick workpiece in expansion

The electromagnetic volume force density has been also computed also for a non-magnetic ($\mu = \mu_0$) thick ($b - a = 0.2$ mm) workpiece subjected to expansion, using the same current pulse as for the previous numerical results. In Fig. 4.11, the electromagnetic volume forces in the space-time domain for a non-magnetic ($\mu = \mu_0$) thick ($b - a = 2$ mm) subjected to compression and to expansion are presented.

For expansion, as expected the electromagnetic volume force density has positive values, with a larger amplitude near the interface closest to the source. In both cases of compression and expansion, the electromagnetic force density
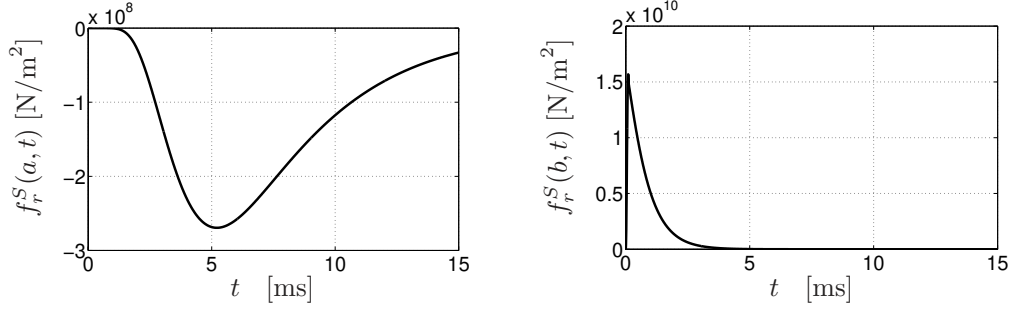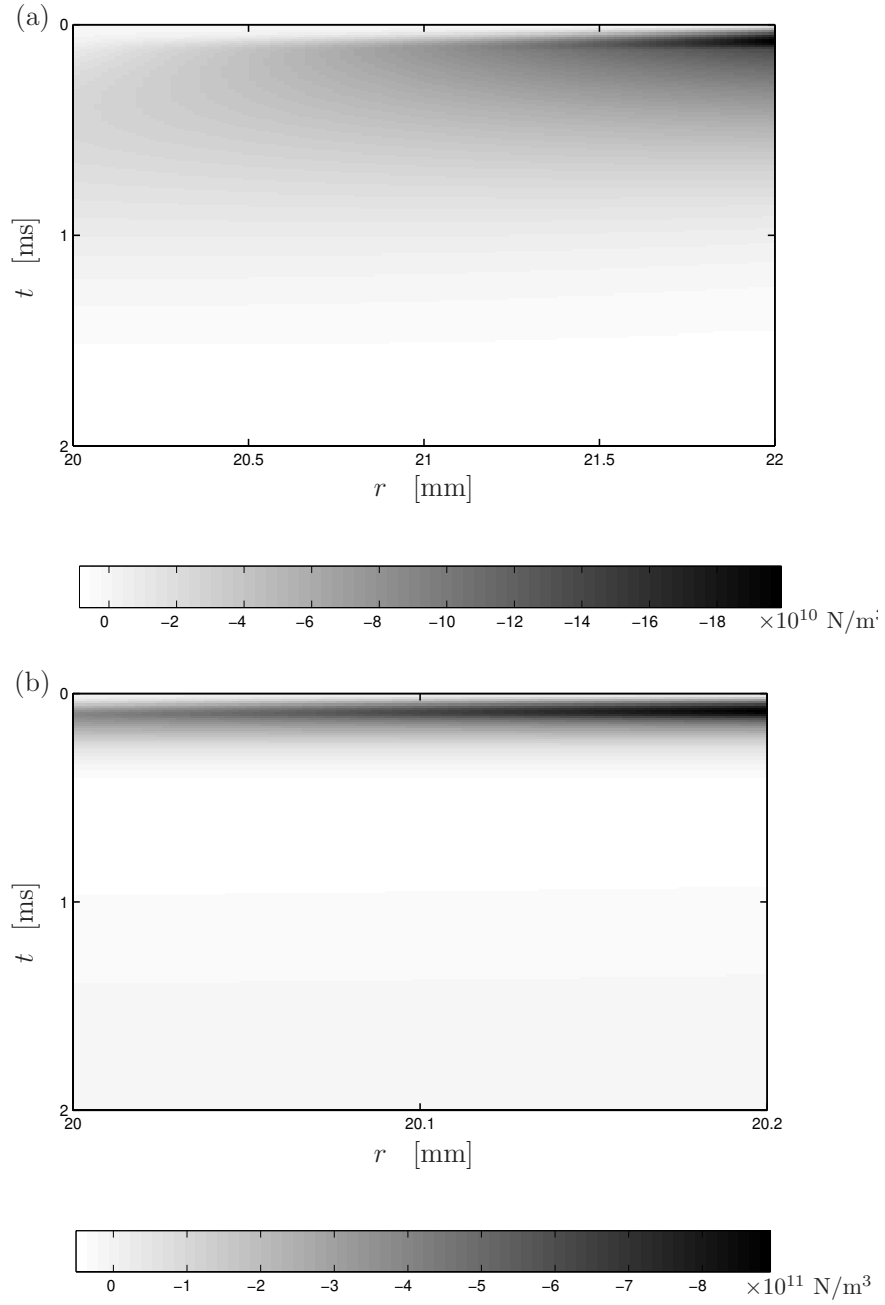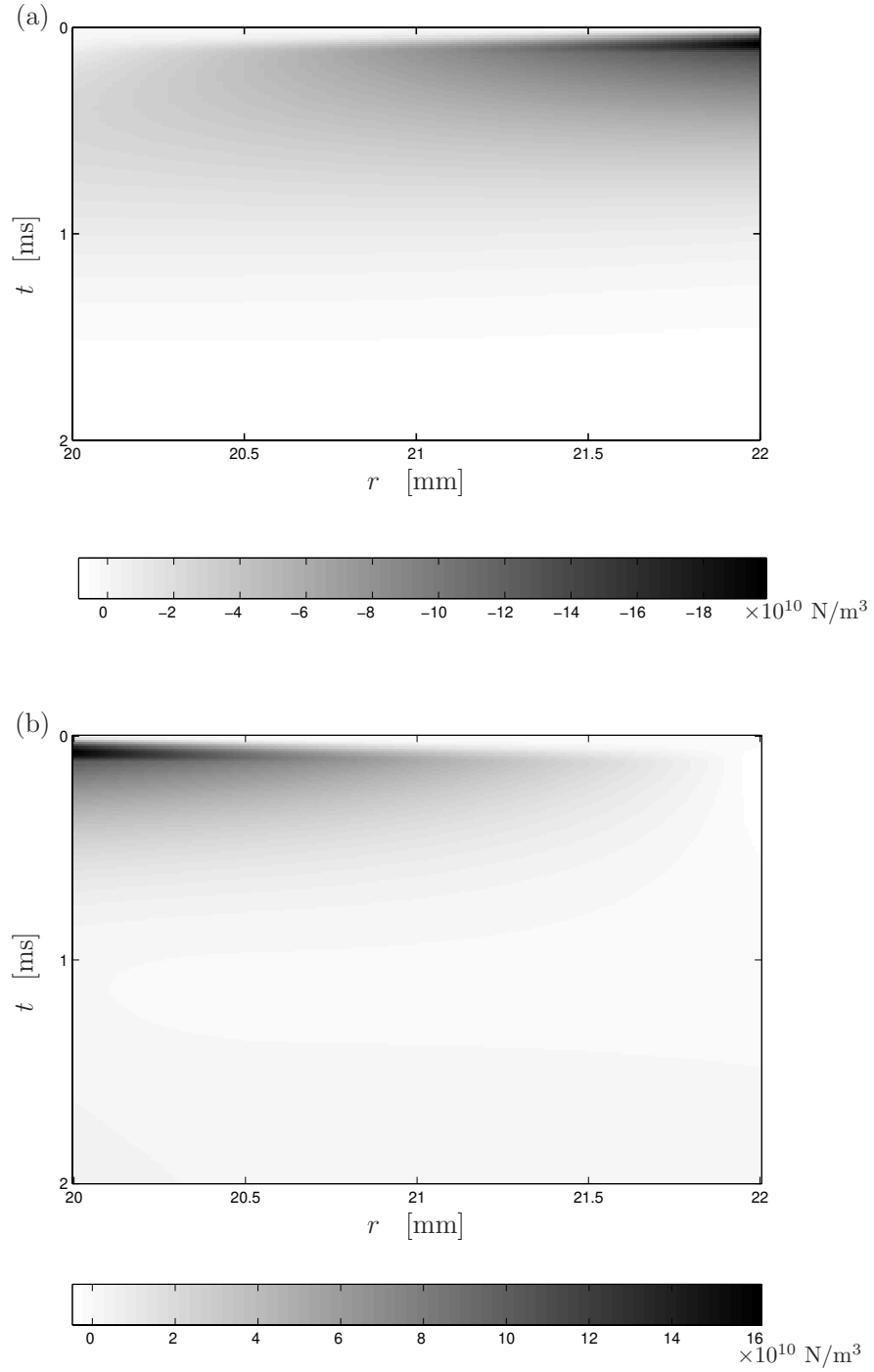
Figure 4.11: Electromagnetic volume force density f_r^V in space-time domain for a non-magnetic ($\mu = \mu_0$) thick ($b{-}a = 2$ mm) workpiece subjected to compression (a) and to expansion (b).

reaches its maximum after a very short interval of time and near to the interface closest to the source of electromagnetic field. We notice also that the electromagnetic force densities in compression are larger in absolute values than the electromagnetic force densities in expansion, due to the different configurations in which the electromagnetic field is calculated. For compression the electromagnetic field penetrates from outside towards inside the workpiece at it gets more concentrated, while for compression the electromagnetic field penetrates from inside towards outside and it gets more dissipated.

4.5   Conclusions

In this chapter, the transient diffusive electromagnetic field in cylindrical configurations related to electromagnetic compression and electromagnetic expansion has been calculated. The configurations consisted of a hollow cylindrical domain with a high electrical conductivity representing the workpiece placed inside (for compression) or outside (for expansion) of a cylindrical sheet antenna carrying a given electric current per unit length representing the forming coil. The configurations have been assumed to have infinite length and to be axially symmetric.

Is has been also assumed that the displacement current may be neglected and the diffusive field equations may be applied in the conducting cylindrical domain. Further, in the domains containing air with zero electrical conductivity σ, the static field equations have been applied.

The electromagnetic field components and electromagnetic volume force have been computed in the frequency domain for compression. For sufficiently low frequencies, in the highly conductive cylindrical domain, the electromagnetic field components have almost a linear dependence as function of the radial position. As frequency increases, the components of the electromagnetic field have no longer this linear dependence in the highly conductive cylindrical domain, and the electromagnetic field is concentrated near the upper interface, i.e. near the interface closest to the sheet antenna.

The electromagnetic volume force has been computed for compression in the highly conducting domain for two types of materials, one non-magnetic ($\mu = \mu_0$) and one linear magnetic ($\mu = 100\,\mu_0$). The values of the electromagnetic volume force density are much larger in a magnetic material than in a non-magnetic one. The numerical results showed also that, in both cases, the electromagnetic force density decays rapidly in time and space. For the magnetic material, the electromagnetic surface force density has also been cal-

culated. Its values are much smaller that the integrated value of the electromagnetic volume force density over the thickness of the highly conducting domain.

Then, the electromagnetic volume force has been calculated for a very thin highly-conductive cylindrical domain subjected to compression. The thickness of this domain has been assumed to be one tenth of the thickness considered in the previous numerical results. The comparison of the results for the electromagnetic volume force density in the space-time domain showed than in a thin cylindrical domain the values of the force density are roughly four times larger that in the thick cylindrical domain. Anyhow, in both cases the electromagnetic volume force density decreases rapidly in time and space.

Finally, the electromagnetic volume force has been calculated in a nonmagnetic ($\mu = \mu_0$) thick highly conducting domain, subjected to expansion. The results showed that the electromagnetic volume force is concentrated near the lower interface, thus near the interface closest to the sheet antenna. In a similar manner as for compression, the electromagnetic force density decays rapidly in time and space, and their absolute values are slightly smaller in absolute value than the ones obtained for compression.

In the literature related to electromagnetic forming, see [9, 105, 62, 3, 111, 189, 191], an equivalent pressure calculated with the use of the Maxwell stress tensor is used for the calculation of radial displacements. This formula uses only the values of the magnetic field at the upper and lower boundaries of the cylindrical domain, as they have been calculated with our model. In our case, we will use the electromagnetic volume forces and the electromagnetic surface forces for the calculation of the radial displacement in the next chapter. Further we will compare the results with the ones obtained with the model using equivalent surface forces (pressure).

Chapter 5

Elastodynamic description of the problem

This chapter presents the calculation of the transient elastic field in a cylindrical workpiece subjected to electromagnetic compression and to electromagnetic expansion, as presented in Chapter 3. The cylindrical configuration is locally excited by the electromagnetic volume force and surface force densities calculated in Chapter 4.

The elastodynamic behavior of the workpiece is described for the plane strain case, in the assumption of a linear elastic behavior of the material for the whole time interval of analysis. Numerical results corresponding to this case are presented both for compression and for expansion.

5.1   Configuration of the elastodynamic problem

The configuration in which the elastic field is to be determined models both the case of electromagnetic compression and electromagnetic expansion, and it is presented in Fig. 5.1. The position in the configuration is specified by the coordinates $\{r, \varphi, z\}$ with respect to the reference frame with the origin $\mathcal{O}$ and the three mutually perpendicular vectors $\{\boldsymbol{i}_r, \boldsymbol{i}_\varphi, \boldsymbol{i}_z\}$ of unit length each. In the indicated order, the base vectors form a right-handed system.

From Chapter 2 we see that the source that excites the elastic field is the electromagnetic volume force density $\boldsymbol{f}_V^{ext} = \boldsymbol{f}^V = f_r^V \boldsymbol{i}_r + f_\varphi^V \boldsymbol{i}_\varphi + f_z^V \boldsymbol{i}_z$, together with the electromagnetic surface force density $\boldsymbol{f}_S^{ext} = \boldsymbol{f}^S = f_r^S \boldsymbol{i}_r + f_\varphi^S \boldsymbol{i}_\varphi + f_z^S \boldsymbol{i}_z$.
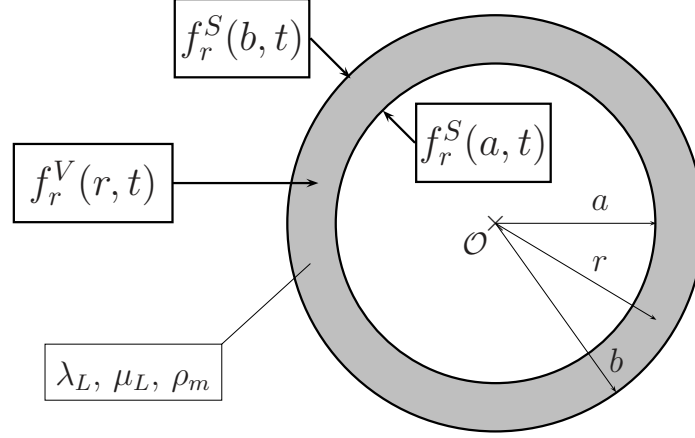
Figure 5.1:   Cross section of the cylindrical configuration for the calcu-
lation of elastodynamic field that has as source the known
electromagnetic force densities.

As shown in the previous chapter, only the radial components of these force
densities are non-zero, i.e. only $f_r^V \neq 0$ and $f_r^S \neq 0$. Their values are known
for the whole configuration and in the whole time interval of calculation.

5.2   Elastic field equations and boundary conditions

In a cylindrical coordinate system, the components of the stress, strain and par-
ticle displacement are $\{\tau_{rr},\ \tau_{\varphi\varphi},\ \tau_{zz},\ \tau_{r\varphi},\ \tau_{\varphi z},\ \tau_{zr}\}$, $\{e_{rr},\ e_{\varphi\varphi},\ e_{zz},\ e_{r\varphi},\ e_{\varphi z},\ e_{zr}\}$
and $\{u_r,\ u_\varphi,\ u_z\}$, respectively. With these components, the equations of mo-
tion are, see [56, 184]

$$\partial_r\tau_{rr} + \frac{1}{r}\,\partial_\varphi\tau_{r\varphi} + \partial_z\tau_{rz} + \frac{1}{r}(\tau_{rr} - \tau_{\varphi\varphi}) - \rho_m\partial_t^2 u_r = -f_r^V, \qquad (5.1)$$

$$\partial_r\tau_{r\varphi} + \frac{1}{r}\,\partial_\varphi\tau_{\varphi\varphi} + \partial_z\tau_{\varphi z} + \frac{2}{r}\,\tau_{r\varphi} - \rho_m\partial_t^2 u_\varphi = 0, \qquad (5.2)$$

$$\partial_r\tau_{rz} + \frac{1}{r}\,\partial_\varphi\tau_{\varphi z} + \partial_z\tau_{zz} + \frac{1}{r}\,\tau_{rz} - \rho_m\partial_t^2 u_z = 0. \qquad (5.3)$$

In the same coordinate system, the components of the strain are defined as

$$e_{rr} = \partial_r u_r, \qquad (5.4)$$

$$e_{\varphi\varphi} = r^{-1}(\partial_\varphi u_\varphi + u_r), \qquad (5.5)$$

$$e_{zz} = \partial_z u_z, \qquad (5.6)$$

$$e_{r\varphi} = \frac{1}{2}\left(r^{-1}\partial_\varphi u_r + \partial_r u_\varphi - r^{-1}u_\varphi\right), \tag{5.7}$$

$$e_{\varphi z} = \frac{1}{2}\left(\partial_z u_\varphi + r^{-1}\partial_\varphi u_z\right), \tag{5.8}$$

$$e_{rz} = \frac{1}{2}(\partial_r u_z + \partial_z u_r). \tag{5.9}$$

Since the workpiece has been assumed homogeneous and isotropic, the constitutive relations are given by

$$\tau_{rr} = (\lambda_L + 2\mu_L)e_{rr} + \lambda_L e_{\varphi\varphi} + \lambda_L e_{zz}, \tag{5.10}$$
$$\tau_{\varphi\varphi} = \lambda_L e_{rr} + (\lambda_L + 2\mu_L)e_{\varphi\varphi} + \lambda_L e_{zz}, \tag{5.11}$$
$$\tau_{zz} = \lambda_L e_{rr} + \lambda_L e_{\varphi\varphi} + (\lambda_L + 2\mu_L)e_{zz}, \tag{5.12}$$
$$\tau_{r\varphi} = 2\mu_L e_{r\varphi}, \tag{5.13}$$
$$\tau_{\varphi z} = 2\mu_L e_{\varphi z}, \tag{5.14}$$
$$\tau_{rz} = 2\mu_L e_{rz}. \tag{5.15}$$

In the modelled cylindrical configuration with infinite length, we will assume that the stresses and strains are uniform along the length of the workpiece. This assumption, combined with the rotational symmetry of the configuration gives that all elements of the stress, strain and particle displacement are functions only of the radius and time, and all ∂_φ and ∂_z operators result in zero. Moreover, $u_\varphi = 0$. The radial displacement u_r and the longitudinal displacement u_z will be further analyzed.

There exists no radial stress within the air, so the boundary conditions to be applied at $r = a$ and $r = b$, are

$$\lim_{r\downarrow a} \tau_{rr}(r,t) = -f_r^S(a,t), \qquad \lim_{r\uparrow b} \tau_{rr}(r,t) = f_r^S(b,t), \tag{5.16}$$

respectively. In our cylindrical configuration with infinite length two particular cases related to elastic field may be distinguished: the plane stress case and the plane strain case.

The plane stress case models a tube with free ends, thus the longitudinal displacement u_z is allowed and the longitudinal stress is assumed to be zero, $\tau_{zz} = 0$. Though there is a longitudinal displacement u_z, the infinite length of the configuration does not allow the calculation of the longitudinal displacement u_z.

The plane strain case models a tube with fixed ends, thus the longitudinal displacement u_z is zero, and further the longitudinal strain e_{zz} is also zero. The infinite length of our model can deal with this case. Moreover, the case $u_z = 0$

characterize the practical situation in which the finite workpiece is clamped at the ends. Therefore, we will solve Eq. (5.1) for the case of plane strain.

In the case of plane strain ($e_{zz} = 0$), the relevant non-zero strains for the configuration under consideration are

$$e_{rr} = \partial_r u_r, \tag{5.17}$$

$$e_{\varphi\varphi} = r^{-1} u_r. \tag{5.18}$$

When these expressions are substituted into Eqs. (5.10) - (5.12) we get

$$\tau_{rr} = (\lambda_L + 2\mu_L)\partial_r u_r + \lambda_L r^{-1} u_r, \tag{5.19}$$

$$\tau_{\varphi\varphi} = \lambda_L e_{rr} + (\lambda_L + 2\mu_L)r^{-1} u_r, \tag{5.20}$$

$$\tau_{zz} = \lambda_L e_{rr} + \lambda_L r^{-1} u_r. \tag{5.21}$$

After substitution of Eqs. (5.19) and (5.20) into Eq. (5.1), it becomes

$$\partial_r^2 u_r + \frac{1}{r}\,\partial_r u_r - \frac{1}{r^2}\,u_r - \frac{1}{c_P^2}\partial_t^2 u_r = -\frac{1}{\lambda_L + 2\mu_L}\,f_r^V, \tag{5.22}$$

where

$$c_P = \left(\frac{\lambda_L + 2\mu_L}{\rho_m}\right)^{1/2} \tag{5.23}$$

is the compressional or P-wave speed.

The simplest way to construct solutions to Eq. (5.22) that satisfy the proper boundary and excitation conditions and ensure causality is to use the Laplace transformation with respect to time. As in Chapter 4, we take $s \to j\omega$, where $\omega = 2\pi f$ is the radial frequency, while f denotes the frequency of operation. In our numerical work, we use the FFT (Fast Fourier Transform) to compute the pertaining Fourier transforms.

After the application of the Laplace transformation with $s \to j\omega$, the non-zero components of the strain tensor and of the stress tensor are written as

$$\hat{e}_{rr} = \partial_r \hat{u}_r, \tag{5.24}$$

$$\hat{e}_{\varphi\varphi} = r^{-1} \hat{u}_r, \tag{5.25}$$

and correspondingly,

$$\hat{\tau}_{rr} = (\lambda_L + 2\mu_L)\partial_r \hat{u}_r + \lambda_L r^{-1} \hat{u}_r, \tag{5.26}$$

$$\hat{\tau}_{\varphi\varphi} = \lambda_L \partial_r \hat{u}_r + (\lambda_L + 2\mu_L)r^{-1} \hat{u}_r, \tag{5.27}$$

$$\hat{\tau}_{zz} = \lambda_L \partial_r \hat{u}_r + \lambda_L r^{-1} \hat{u}_r, \tag{5.28}$$

Further, the application of the same transform to Eq. (5.22) leads to

$$\partial_r^2 \hat{u}_r + \frac{1}{r}\,\partial_r \hat{u}_r - \frac{1}{r^2}\,\hat{u}_r + k^2 \hat{u}_r = -\frac{1}{\lambda_L + 2\mu_L}\,\hat{f}_r^V. \tag{5.29}$$

where $k = \omega/c_P$ is the wavenumber. We may write the total solution of Eq. (5.29) as

$$\hat{u}_r(r) = \hat{u}_r^{part}(r) + \hat{u}_r^{gen}(r), \tag{5.30}$$

where $\hat{u}_r^{part}(r)$ denotes the particular solution of Eq. (5.29) and $\hat{u}_r^{gen}(r)$ denotes the general solution of the homogeneous form of Eq. (5.29).

Particular solution $\hat{u}_r^{part}(r)$

We may construct the particular solution $\hat{u}_r^{part}(r)$ using the Green's function $\hat{G}(r, r')$ as follows,

$$\hat{u}_r^{part}(r) = \frac{1}{\lambda_L + 2\mu_L} \int_{r'=a}^{b} \hat{G}(r, r') \hat{f}_r^V(r') r'\, \mathrm{d}r', \tag{5.31}$$

where $\hat{G}(r, r')$ is the solution of equation

$$\frac{1}{r}\,\partial_r(r\partial_r \hat{G}) + \left(k^2 - \frac{1}{r^2}\right)\hat{G} = -\frac{1}{r'}\,\delta(r - r'). \tag{5.32}$$

In an unbounded domain with a cylindrical source placed at $r = r'$, we may write the solution of Eq. (5.32) as

$$\hat{G}(r, r') = \begin{cases} A\,J_1(kr)Y_1(kr'), & \text{for } r < r', \\[2ex] B\,Y_1(kr)J_1(kr'), & \text{for } r > r', \end{cases} \tag{5.33}$$

where $J_1(kr)$ and $Y_1(kr)$ are the Bessel function of the first and second kind, respectively. The coefficients A and B are calculated from the continuity condition at $r = r'$, i.e.,

$$\lim_{r\downarrow r'} \hat{G} - \lim_{r\uparrow r'} \hat{G} = 0, \tag{5.34}$$

together with the excitation condition at $r = r'$, i.e.,

$$\lim_{r\downarrow r'} r\partial_r \hat{G} - \lim_{r\uparrow r'} r\partial_r \hat{G} = -1. \tag{5.35}$$

From these conditions, we obtain $A = B = -\pi/2$ and then

$$\hat{G}(r, r') = \begin{cases} -\dfrac{\pi}{2} J_1(kr) Y_1(kr'), & \text{for } r \leq r', \\[4mm] -\dfrac{\pi}{2} Y_1(kr) J_1(kr'), & \text{for } r \geq r'. \end{cases} \tag{5.36}$$

In our further analysis we need also the radial derivative of the particular solution. This is obtained as

$$\partial_r \hat{u}_r^{part}(r) = \frac{1}{\lambda_L + 2\mu_L} \int_{r'=a}^{b} \partial_r \hat{G}(r, r') \hat{f}_r^V(r') r' \, \mathrm{d}r', \tag{5.37}$$

where

$$\partial_r \hat{G}(r, r') = \begin{cases} -\dfrac{\pi}{2} [k J_0(kr) - r^{-1} J_1(kr)] Y_1(kr'), & \text{for } r < r', \\[4mm] -\dfrac{\pi k}{4} [Y_0(kr) J_1(kr) + J_0(kr) Y_1(kr)] + \dfrac{\pi}{2r} Y_1(kr) J_1(kr), \\ & \text{for } r = r', \\[4mm] -\dfrac{\pi}{2} [k Y_0(kr) - r^{-1} Y_1(kr)] J_1(kr'), & \text{for } r > r'. \end{cases} \tag{5.38}$$

A special case for the calculation of the elastodynamic field is $k \to 0$ ($f \to 0$). The time-domain correspondent of this case is $t \to \infty$ and the quasistatic elastic field is obtained. When $k \to 0$, Eqs. (5.36) and (5.38) become

$$\lim_{k \to 0} \hat{G}(r, r') = \begin{cases} \dfrac{r}{2r'}, & \text{for } r \leq r', \\[4mm] \dfrac{r'}{2r}, & \text{for } r \geq r', \end{cases} \tag{5.39}$$

and

$$\lim_{k \to 0} \partial_r \hat{G}(r, r') = \begin{cases} \dfrac{1}{2r'}, & \text{for } r < r', \\[4mm] 0, & \text{for } r = r', \\[4mm] -\dfrac{r'}{2r^2}, & \text{for } r > r', \end{cases} \tag{5.40}$$

respectively. Until here, since all quantities in Eqs. (5.31) and (5.37) are known, we have calculated the particular solution $\hat{u}_r^{part}(r)$ and its radial derivative

$\partial_r \hat{u}_r^{part}(r)$ as functions of the radius r. Thus, we also have the values of the particular solution and its radial derivative at the boundaries $r = a$ and $r = b$ of the cylindrical domain representing the workpiece.

General solution $\hat{u}_r^{gen}(r)$

The general solution $\hat{u}_r^{part}(r)$ of the homogeneous form of Eq. (5.29) is given by

$$\hat{u}_r^{gen}(r) = C\, J_1(kr) + D\, Y_1(kr), \tag{5.41}$$

where the coefficients C and D are obtained from the boundary conditions

$$\lim_{r\downarrow a} \hat{\tau}_{rr} = -\hat{f}_r^S(a), \tag{5.42}$$

$$\lim_{r\uparrow b} \hat{\tau}_{rr} = \hat{f}_r^S(b), \tag{5.43}$$

with $\hat{\tau}_{rr}$ from Eq. (5.26). Similar to Eq. (5.30), we write $\hat{\tau}_{rr}$ as

$$\hat{\tau}_{rr}(r) = \hat{\tau}_{rr}^{part}(r) + \hat{\tau}_{rr}^{gen}(r), \tag{5.44}$$

where

$$\hat{\tau}_{rr}^{part}(r) = (\lambda_L + 2\mu_L)\partial_r \hat{u}_r^{part} + \lambda_L r^{-1}\hat{u}_r^{part}, \tag{5.45}$$

and

$$\hat{\tau}_{rr}^{gen}(r) = C\, M(kr) + D\, N(kr), \tag{5.46}$$

with

$$M(kr) = k(\lambda_L + 2\mu_L)J_0(kr) - \frac{2\mu_L}{r}J_1(kr), \tag{5.47}$$

$$N(kr) = k(\lambda_L + 2\mu_L)Y_0(kr) - \frac{2\mu_L}{r}Y_1(kr). \tag{5.48}$$

From Eqs. (5.42) - (5.43) we obtain the following system of equations in matrix form

$$\begin{pmatrix} M(ka) & N(ka) \\ M(kb) & N(kb) \end{pmatrix} \begin{pmatrix} C \\ D \end{pmatrix} = \begin{pmatrix} h(a) \\ h(b) \end{pmatrix}, \tag{5.49}$$

where the elements of the known vector are given by

$$h(a) = -\hat{f}_r^S(a) - \hat{\tau}_{rr}^{part}(a), \tag{5.50}$$

$$h(b) = \hat{f}_r^S(b) - \hat{\tau}_{rr}^{part}(b). \tag{5.51}$$

Thus, the coefficients C and D may be calculated as

$$C = \frac{N(kb)h(a) - N(ka)h(b)}{M(ka)N(kb) - N(ka)M(kb)}, \tag{5.52}$$

$$D = \frac{-M(kb)h(a) + M(ka)h(b)}{M(ka)N(kb) - N(ka)M(kb)}. \tag{5.53}$$

Hence, the solution for $\hat{u}_r$ is obtained as

$$\hat{u}_r(r) = \hat{u}_r^{part}(r) + J_1(kr)\frac{N(kb)h(a) - N(ka)h(b)}{M(ka)N(kb) - N(ka)M(kb)}$$
$$+ Y_1(kr)\frac{-M(kb)h(a) + M(ka)h(b)}{M(ka)N(kb) - N(ka)M(kb)}. \tag{5.54}$$

When $k \to 0$, thus for the calculation of the quasistatic elastic field, the general solution in Eq. (5.41) may be written as

$$\hat{u}_r^{gen}(r) = C\,r + D\,\frac{1}{r}. \tag{5.55}$$

Similar with the procedure presented above, we get

$$\hat{\tau}_{rr}^{gen}(r) = 2(\lambda_L + \mu_L)\,C - 2\mu_L\frac{1}{r^2}\,D. \tag{5.56}$$

The coefficients C and D are obtained from the application of the boundary conditions in Eqs. (5.42) - (5.43). This procedure yields the following system of equations

$$2(\lambda_L + \mu_L)\,C - 2\mu_L\frac{1}{a^2}\,D = h(a), \tag{5.57}$$

$$2(\lambda_L + \mu_L)\,C - 2\mu_L\frac{1}{b^2} = h(b), \tag{5.58}$$

where the functions $h(a)$ and $h(b)$ have been defined in Eqs. (5.50) - (5.51). The coefficients C and D are

$$C = \frac{a^2h(a) - b^2h(b)}{2(\lambda_L + \mu_L)(a^2 - b^2)}, \tag{5.59}$$

$$D = \frac{a^2b^2[h(a) - h(b)]}{2\mu_L(a^2 - b^2)}. \tag{5.60}$$

Hence, for $f \to 0$, the solution for $\hat{u}_r$ is obtained as

$$\hat{u}_r(r) = \hat{u}_r^{part}(r) + r\frac{a^2h(a) - b^2h(b)}{2(\lambda_L + \mu_L)(a^2 - b^2)} + \frac{1}{r}\frac{a^2b^2[h(a) - h(b)]}{2\mu_L(a^2 - b^2)}. \tag{5.61}$$

Now, all non-zero components of the strain and stress tensor may be calculated in the frequency domain, in accordance to Eqs. (5.24) - (5.28). The results may then be transformed back to the time-domain using an inverse FFT.

5.3 The method of equivalent surface forces

In the literature related to electromagnetic forming, see [9, 105, 62, 3, 111, 189, 191], the present problem is dealt with the use of an equivalent surface force (pressure) accounting for the total electromagnetic force exerted on the workpiece during the deformation process.

Although in the literature relating to electromagnetic forming, the elastic field is not dealt with into detail, while in some papers the elastic deformations are neglected, we may deduce from their treatment of the problem that the present method can be used for the calculation of the elastodynamic field if we take these equivalent surface forces as external sources.

Thus, the electromagnetic force density f_r^V in the right-hand side of Eq. (5.1) is assumed to be zero and we have to solve the following equation of motion

$$\partial_r^2 u_r + \frac{1}{r}\,\partial_r u_r - \frac{1}{r^2}\,u_r - \frac{1}{c_P^2}\partial_t^2 u_r = 0, \tag{5.62}$$

supplemented with boundary conditions.

Due to the existence of the equivalent surface forces that act at the boundaries of the workpiece, the boundary conditions to be applied are different from the ones in Eq. (5.16). The new boundary conditions to be applied result from the fact that the total electromagnetic force acting on the workpiece is replaced by an equivalent electromagnetic surface force, calculated with the Maxwell stress-tensor formula.

Therefore, two equivalent surface forces act on the workpiece,

$$\boldsymbol{f}^{S;eq}(b,t) = \lim_{r\downarrow b} -\boldsymbol{i}_r \cdot \mathcal{T}^M = -\frac{1}{2}\mu_0\,[H_z(b,t)]^2\,\boldsymbol{i}_r, \tag{5.63}$$

so

$$f_r^{S;eq}(b,t) = -\frac{1}{2}\mu_0\,[H_z(b,t)]^2 \tag{5.64}$$

at the outer boundary $r = b$, and

$$\boldsymbol{f}^{S;eq}(a,t) = \lim_{r\uparrow a} \boldsymbol{i}_r \cdot \mathcal{T}^M = \frac{1}{2}\mu_0\,[H_z(a,t)]^2\,\boldsymbol{i}_r, \tag{5.65}$$

so

$$f_r^{S;eq}(a,t) = \frac{1}{2}\mu_0\,[H_z(a,t)]^2 \tag{5.66}$$

at the inner boundary $r = a$. These surface forces are opposite to each other, as shown by their signs. Thus, the boundary conditions in Eq. (5.16) become

$$\lim_{r \downarrow a} \tau_{rr}(r, t) = -f_r^{S;eq}(a, t), \tag{5.67}$$

$$\lim_{r \uparrow b} \tau_{rr}(r, t) = f_r^{S;eq}(b, t). \tag{5.68}$$

Theory of perfectly conducting shells

If the workpiece is assumed to be perfectly conducting ($\sigma \to \infty$), for electromagnetic compression we will have $H_z(a, t) = 0$ and $H_z(b, t) = I_S$, while for electromagnetic expansion we will have $H_z(a, t) = I_S$ and $H_z(b, t) = 0$.

So, the surface forces acting on the workpiece in electromagnetic compression are

$$f_r^{S;eq}(b, t) = -\frac{1}{2}\mu_0 I_S^2, \tag{5.69}$$

$$f_r^{S;eq}(a, t) = 0, \tag{5.70}$$

while the surface forces acting on the workpiece in electromagnetic expansion are

$$f_r^{S;eq}(b, t) = 0, \tag{5.71}$$

$$f_r^{S;eq}(a, t) = \frac{1}{2}\mu_0 I_S^2. \tag{5.72}$$

In the next section we will use the method of equivalent surface forces as presented in Eqs. (5.62) - (5.67), to compare the numerical results with the ones obtained with our theory, while in Chapter 8, the thin-shell model for electromagnetic expansion will be presented in detail.

5.4   Numerical results

In this section, we present some numerical results for typical electromagnetic forming systems designed for compression and for expansion of hollow circular cylindrical workpieces.

The following types of workpieces subjected to electromagnetic compression are investigated:

- a non-magnetic $(\mu = \mu_0)$ thick workpiece with an inner radius $r = a = 20$ mm and an outer radius $r = b = 22$ mm,

- a hypothetical magnetic $(\mu = 100\,\mu_0)$ thick workpiece with an inner radius $r = a = 20$ mm and an outer radius $r = b = 22$ mm,

- a non-magnetic $(\mu = \mu_0)$ thin workpiece with an inner radius $r = a = 20$ mm and an outer radius $r = b = 20.2$ mm.

For electromagnetic expansion, only a non-magnetic $(\mu = \mu_0)$ thick workpiece with an inner radius $r = a = 20$ mm and an outer radius $r = b = 22$ mm is considered.

In all these cases the workpiece has the same elastic properties and it is assumed that it has a linear elastic behavior within the whole range of stresses and strains. The workpiece has a mass density $\rho_m = 2.7 \cdot 10^3$ kg/m^3 and Lamé coefficients of elasticity $\lambda_L = 17 \cdot 10^{10}$ N/m^2 and $\mu_L = 8 \cdot 10^{10}$ N/m^2, see Appendix C.1.

In order to adapt to the notation widely used in the classical theory of elastic field, only for the numerical results, we will denote the normal stresses in the workpiece by $\sigma_r = \tau_{rr}$, $\sigma_\varphi = \tau_{\varphi\varphi}$, $\sigma_z = \tau_{zz}$ and the normal strains in the workpiece by $\varepsilon_r = e_{rr}$, $\varepsilon_\varphi = e_{\varphi\varphi}$, $\varepsilon_z = e_{zz}$. Their expressions in the time-domain are

$$\varepsilon_r = \partial_r u_r, \tag{5.73}$$

$$\varepsilon_\varphi = r^{-1} u_r, \tag{5.74}$$

$$\sigma_r = (\lambda_L + 2\mu_L)\varepsilon_r + \lambda_L \varepsilon_\varphi + \lambda_L \varepsilon_z, \tag{5.75}$$

$$\sigma_\varphi = \lambda_L \varepsilon_r + (\lambda_L + 2\mu_L)\varepsilon_\varphi + \lambda_L \varepsilon_z, \tag{5.76}$$

$$\sigma_z = \lambda_L \varepsilon_r + \lambda_L \varepsilon_\varphi + (\lambda_L + 2\mu_L)\varepsilon_z. \tag{5.77}$$

For each case, the temporal evolution of the elastic field components at the inner radius $r = a$ will be presented. For the most important components of the elastic field, i.e. the radial displacement u_r and the tangential stress τ_φ the space-time evolutions have been calculated. These results will be compared with the corresponding results obtained with the application of Eqs. (5.67) and (5.68) from the method of equivalent surface forces presented in Section 5.3.

Non-magnetic thick workpiece in compression

In Fig. 5.2, the components of the elastic field at $r = a$ in a non-magnetic $(\mu = \mu_0)$ thick $(b - a = 2$ mm) workpiece subjected to compression are presented. As the problem is almost quasi-static, the radial displacement is most

Figure 5.2:   Elastic field components at $r = a$ in the time domain for
               a non-magnetic ($\mu = \mu_0$) thick ($b - a = 2$ mm) workpiece
               subjected to compression.

of the time negative and its shape is very similar to the one of the electromag-
netic volume force density at the same radial position.

     With the chosen elastic properties of the material the values of the radial
displacement are very small, and these values yield very small radial and tan-
gential strains, ε_r and ε_φ, respectively. The tangential stress σ_φ has the largest
values from all the stress components, while the radial stress σ_r is very small
and can be neglected. The longitudinal stress σ_z has negative values that are
about three times smaller than the values of the tangential stress.

Figure 5.3: Radial displacement u_r in space-time domain, calculated with the present theory (a) and with the method of equivalent surface forces (b), for a non-magnetic ($\mu = \mu_0$) thick ($b - a = 2$ mm) workpiece subjected to compression.

Figure 5.4:   Tangential stress σ_φ in space-time domain, calculated with the present theory (a) and with the method of equivalent surface forces (b), for a non-magnetic ($\mu = \mu_0$) thick ($b - a = 2$ mm) workpiece subjected to compression.

The space-time evolution of the radial displacement u_r, presented in Fig. 5.3, has been calculated using the theory presented in Section 5.2 and with the method of equivalent surface forces presented in Section 5.3. Both methods are used to obtain the space-time evolution of the tangential stress σ_φ in Fig. 5.4.

From our simulations we have observed that the radial displacement at $r = b$ is slightly smaller than the radial displacement at $r = a$, results that confirm the fact that during the electromagnetic compression the workpiece becomes thicker. The radial displacement in Fig. 5.3 (a) and (b) has similar maximum values, and their space-time evolution is almost the same. A similar behavior is noticed in Fig. 5.4 (a) and (b).

In order to have a better picture of the real differences between the results obtained with the two methods, in Fig. 5.5 we present the temporal evolution of the radial displacement and of the tangential stress at the inner boundary

Figure 5.5: Radial displacement u_r and tangential stress σ_φ in time domain at $r = a$ (upper graphs) and $r = b$ (lower graphs), calculated with the present theory (solid lines) and with the method of equivalent surface forces (dashed lines), for a non-magnetic ($\mu = \mu_0$) thick ($b - a = 2$ mm) workpiece subjected to compression.

$r = a$ and at the outer boundary $r = b$ of the workpiece. We notice that both methods yield similar results.

Magnetic thick workpiece in compression

In Fig. 5.6, the components of the elastic field at $r = a$ in a magnetic ($\mu = 100\,\mu_0$) thick ($b - a = 2$ mm) workpiece are presented. For the magnetic workpiece, most field components are in the same order of magnitude as the corresponding components in the non-magnetic thick workpiece.
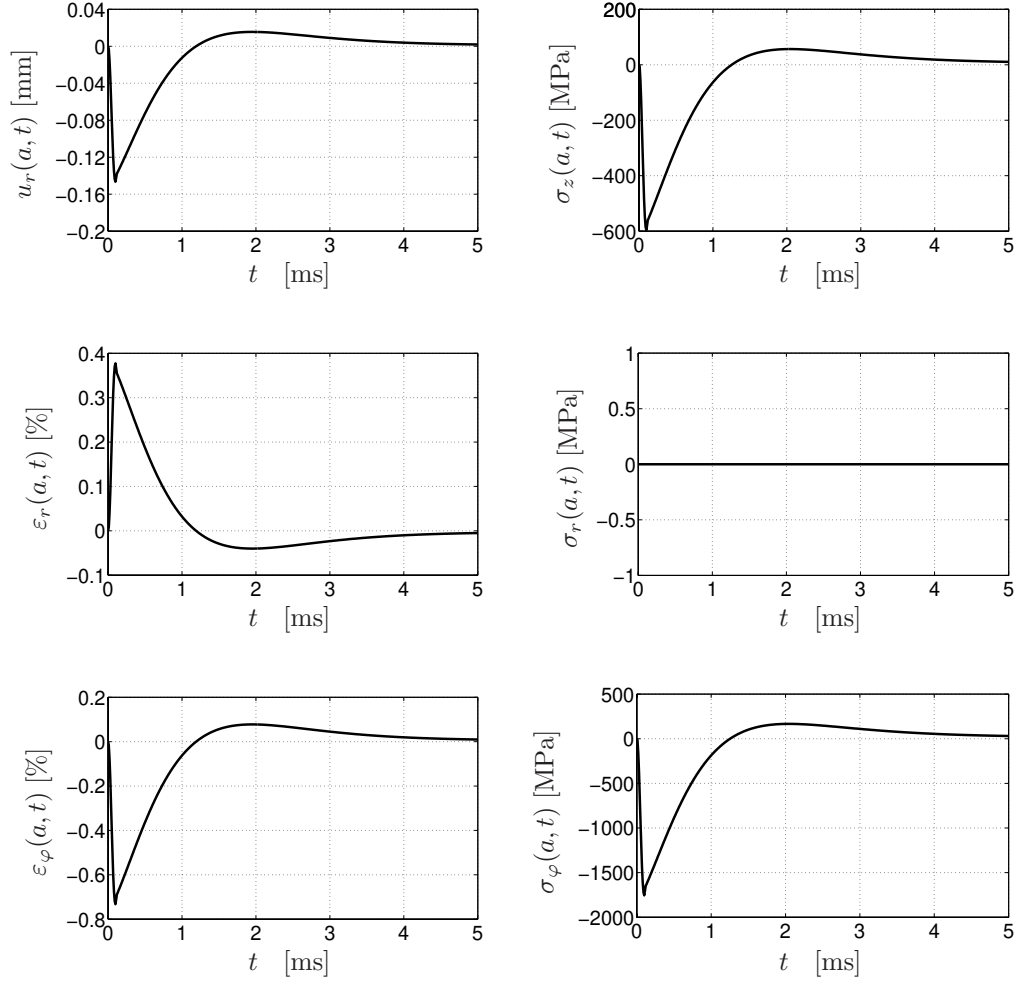

Figure 5.6:   Elastic field components at $r = a$ in the time domain for a magnetic ($\mu = 100\,\mu_0$) thick ($b - a = 2$ mm) workpiece subjected to compression.

The radial strain σ_r is not zero, since at the boundaries electromagnetic surface forces are present. These electromagnetic surface forces are used in the boundary conditions of Eq. (5.16) for the calculation of the elastic field.

The values of the radial stress σ_r are small as compared with the values of the tangential stress σ_φ. The longitudinal stress σ_z is negative and about three times smaller than the tangential stress σ_φ.

Further, in Figs. 5.7 and 5.8 we present the space-time evolution of the radial displacement and of the tangential stress σ_φ, when calculated with the presented theory and with the method of equivalent surface forces.

The maximum values of the radial displacement u_r when calculated with our method are about four times larger than the corresponding values calculated with the method of equivalent surface forces, see Fig. 5.7 (a) and (b) and their space-time evolution is very different. The same observation is valid for the tangential stress in Fig. 5.8 (a) and (b).

In order to have a better picture of the real differences between the results obtained with the two methods, in Fig. 5.9 we present the temporal evolution of the radial displacement and of the tangential stress at the inner boundary $r = a$ and at the outer boundary $r = b$ of the workpiece.

We notice that the radial displacement u_r has negative values when calculated with both methods, though the values calculated with our method are about four times larger than with the method of equivalent surface forces.

For the tangential stress σ_φ at the inner boundary $r = a$ of the workpiece, the same observation is valid, while at the outer boundary $r = b$ of the workpiece the two methods give results that differ very much from each other. The method of equivalent surface forces gives at the outer boundary $r = b$ a tangential stress σ_φ that has the same behavior as the one at the upper boundary.

Our method gives a tangential stress that has a different behavior that the similar tangential stress at the inner boundary, due to the existence of surface force that are taking into account the magnetic nature of the workpiece. Because these surface forces are negligible at the boundary $r = a$, their influence on the tangential stress behavior is very small, while at the outer boundary $r = b$, the surface forces are very large and it has a considerable influence on the behavior of the tangential stress.
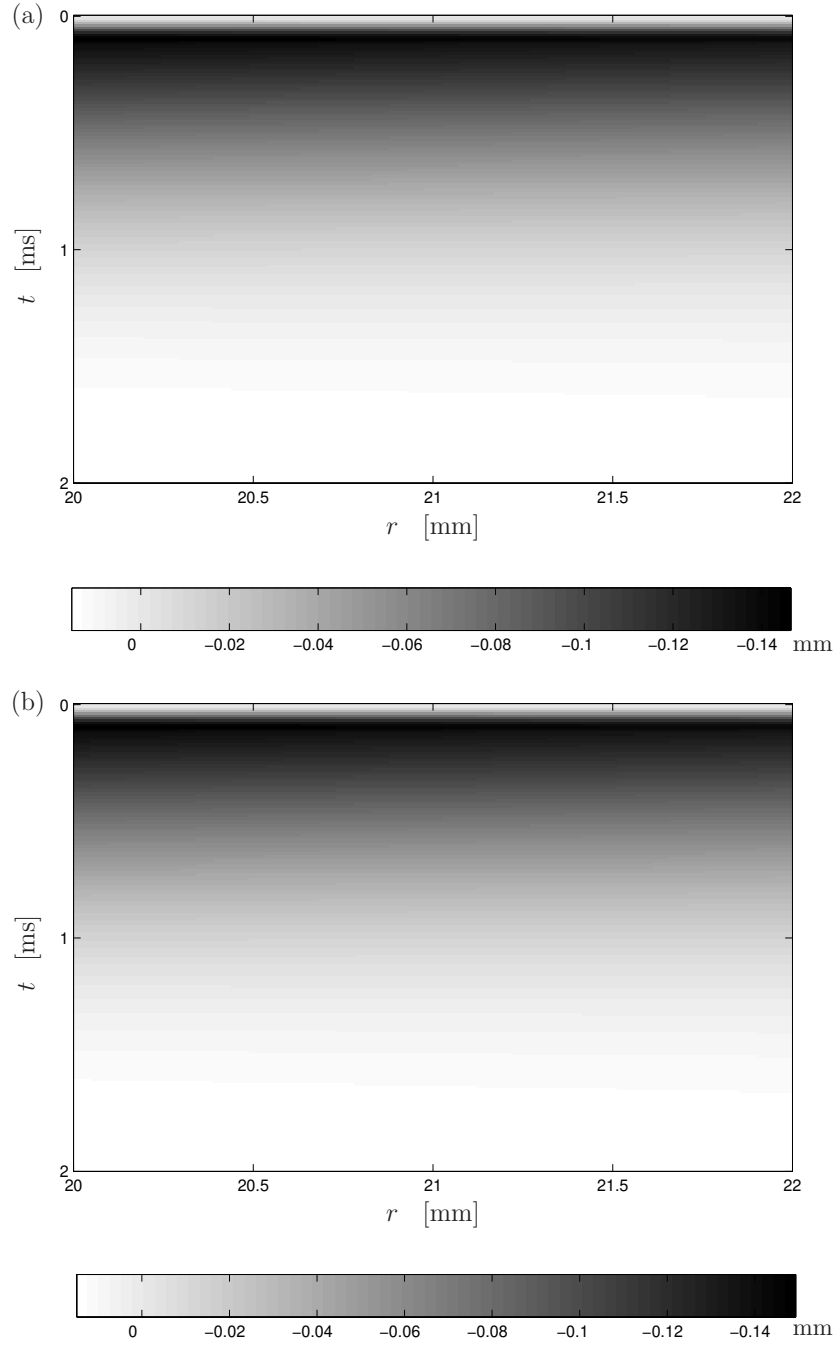
Figure 5.7:   Radial displacement u_r in space-time domain, calculated with the present theory (a) and with the method of equivalent surface forces (b), for a magnetic ($\mu = 100\,\mu_0$) thick ($b - a = 2$ mm) workpiece subjected to compression.
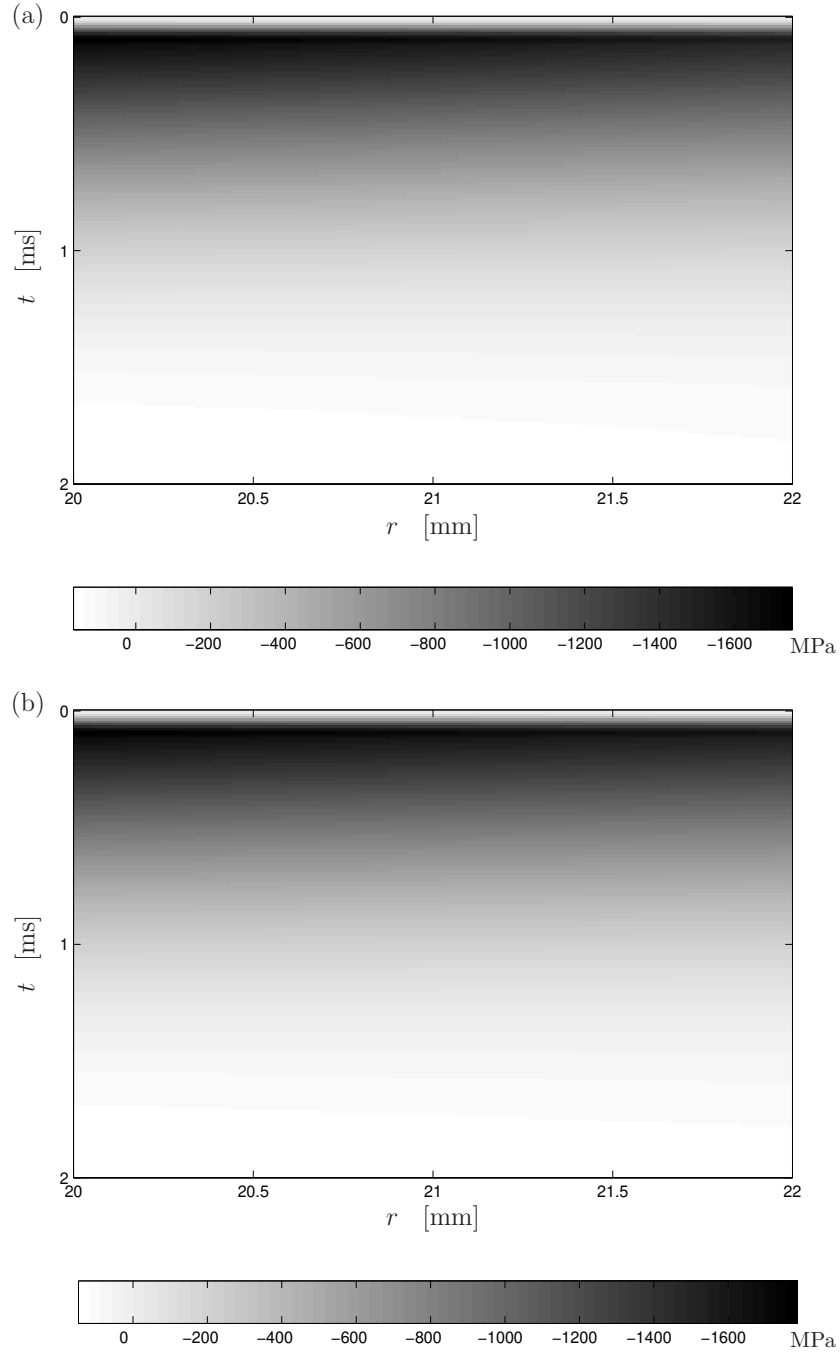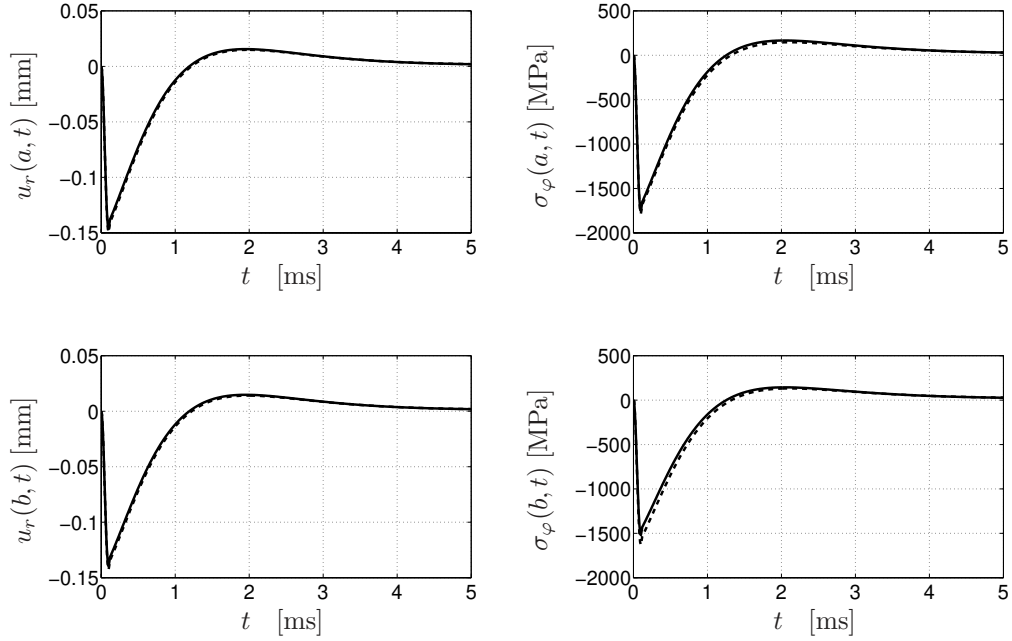
Figure 5.8:   Tangential stress σ_φ in space-time domain, calculated with the present theory (a) and with the method of equivalent surface forces (b), for a magnetic $(\mu = 100\,\mu_0)$ thick $(b - a = 2\text{ mm})$ workpiece subjected to compression.

Figure 5.9:   Radial displacement u_r and tangential stress σ_φ at $r = a$
               (upper graphs) and $r = b$ (lower graphs) in time domain,
               calculated with the present theory (solid lines) and with
               the method of equivalent surface forces (dashed lines), for
               a magnetic $(\mu = 100\,\mu_0)$ thick $(b - a = 2\text{ mm})$ workpiece
               subjected to compression.

Non-magnetic thin workpiece in compression

In Fig. 5.10, the components of the elastic field at $r = a$ in a non-magnetic
$(\mu = \mu_0)$ thin $(b - a = 0.2\text{ mm})$ workpiece are presented. The radial displace-
ment is small, but it is about 10 times larger than for the thick non-magnetic
workpiece. Again, because there are no electromagnetic surface forces acting
on the workpiece, the radial stress is very small and it can be neglected in
further calculations.

In Figs. 5.11 and 5.12 we present the space-time evolution of the ra-
dial displacement and of the tangential stress σ_φ, when calculated with the
presented theory, with the method of equivalent surface forces, and with the
theory of perfectly conducting thin shells.
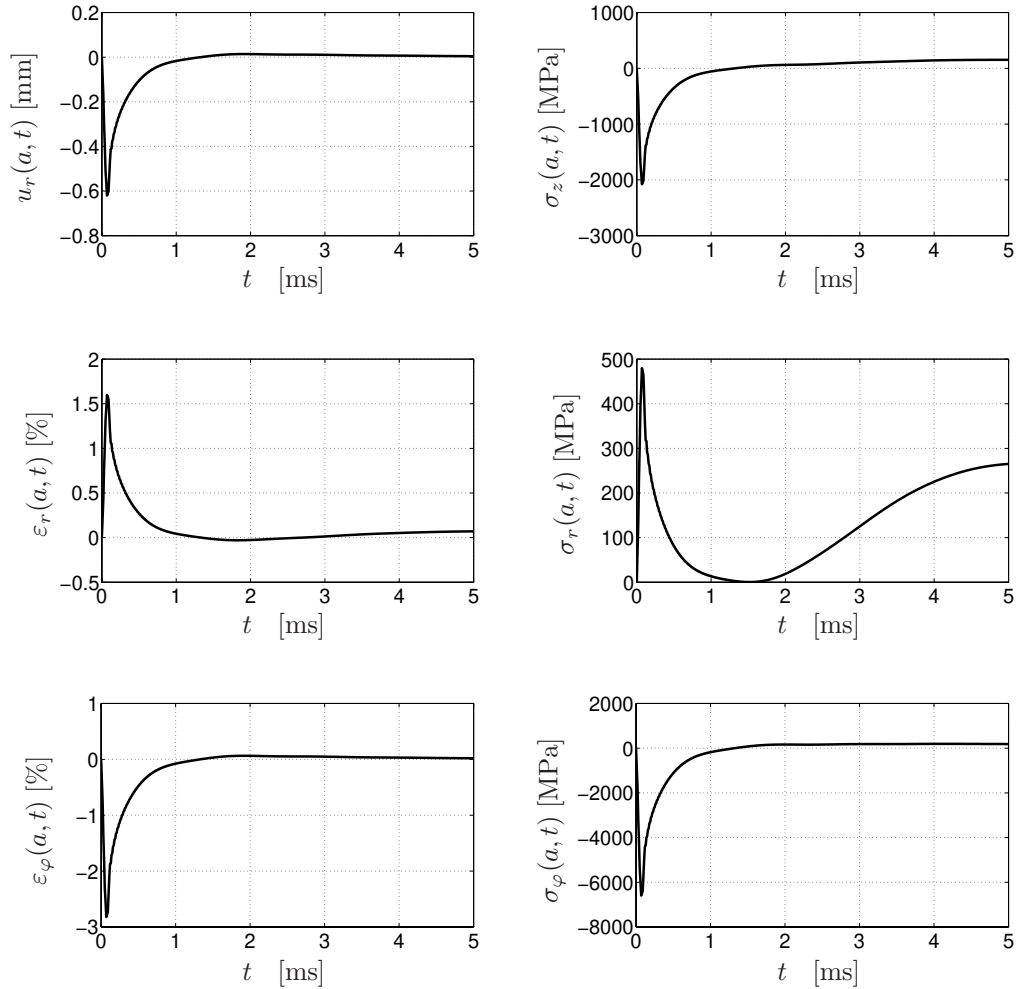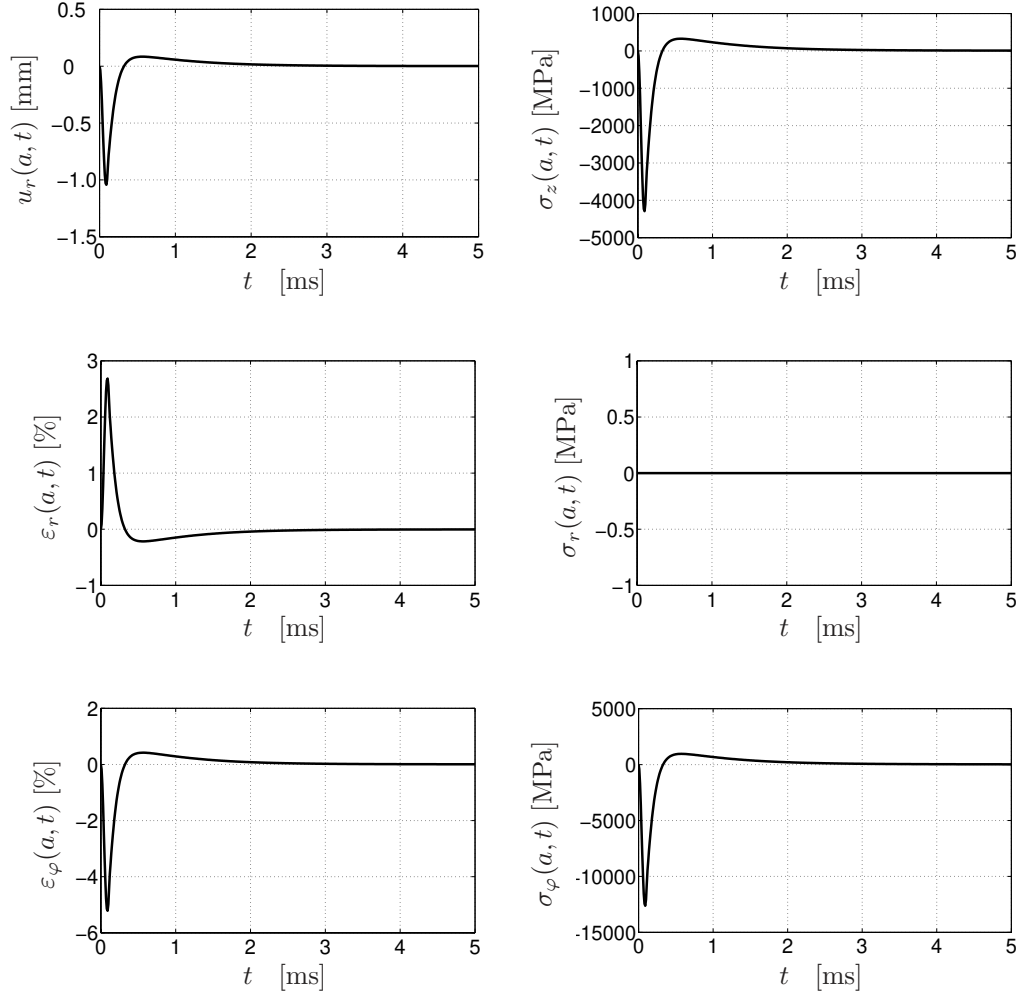
Figure 5.10:   Elastic field components at $r = a$ in the time domain for
               a non-magnetic ($\mu = \mu_0$) thin ($b - a = 0.2$ mm) workpiece
               subjected to compression.

The values of the radial displacement u_r when calculated with our method
are the same with the corresponding values calculated with the method of
equivalent surface forces, see Fig. 5.11 (a) and (b). The same observation is
valid for the tangential stress in Fig. 5.12 (a) and (b).

In order to have a better picture of the real differences between the
results obtained with these two methods, in Fig. 5.13 we present the temporal
evolution of the radial displacement u_r and of the tangential stress σ_φ at the
inner boundary $r = a$ and at the outer boundary $r = b$ of the workpiece.
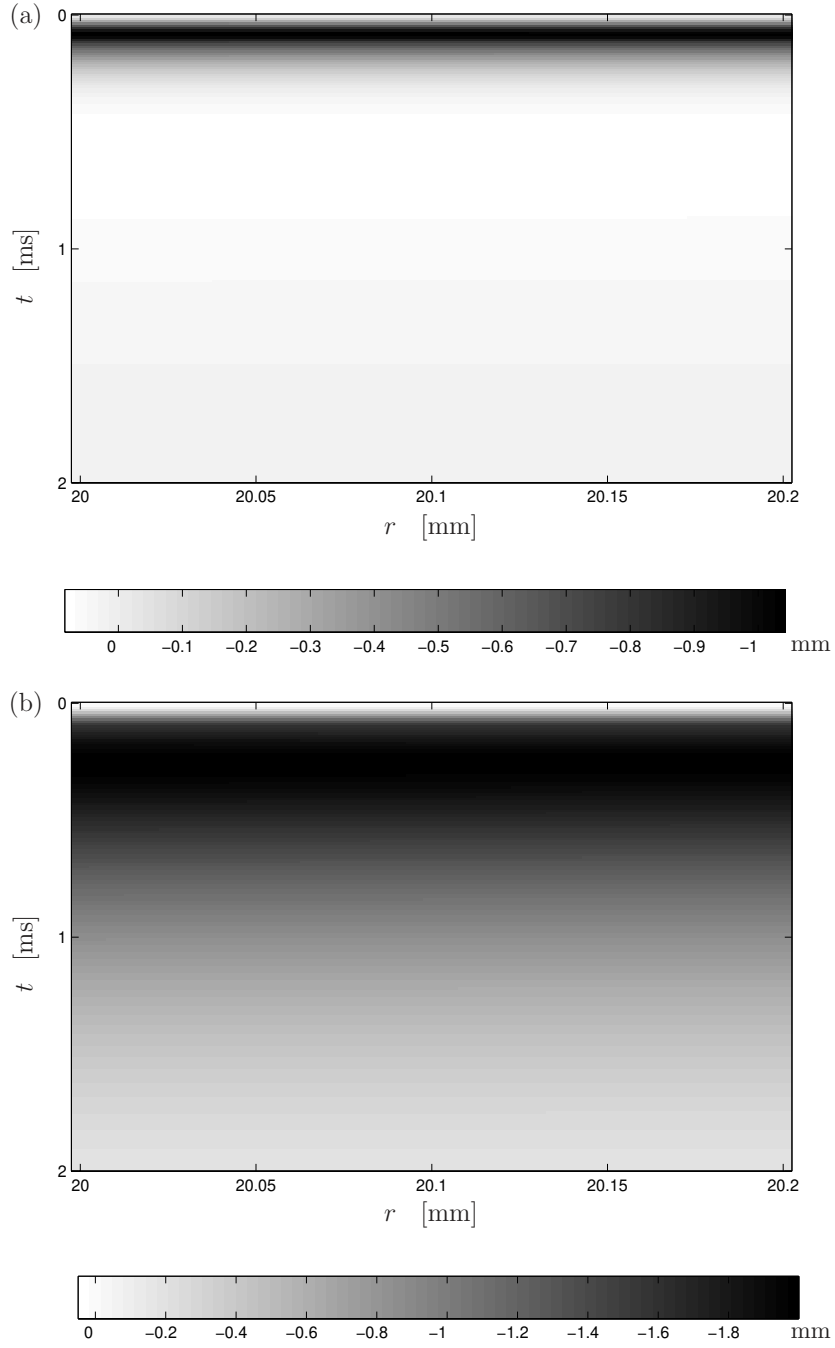
Figure 5.11: Radial displacement u_r in space-time domain, calculated
with the present theory (a) and with the method of equiv-
alent surface forces (b) for a non-magnetic ($\mu = \mu_0$) thin
($b - a = 0.2$ mm) workpiece subjected to compression.

(a)

(b)
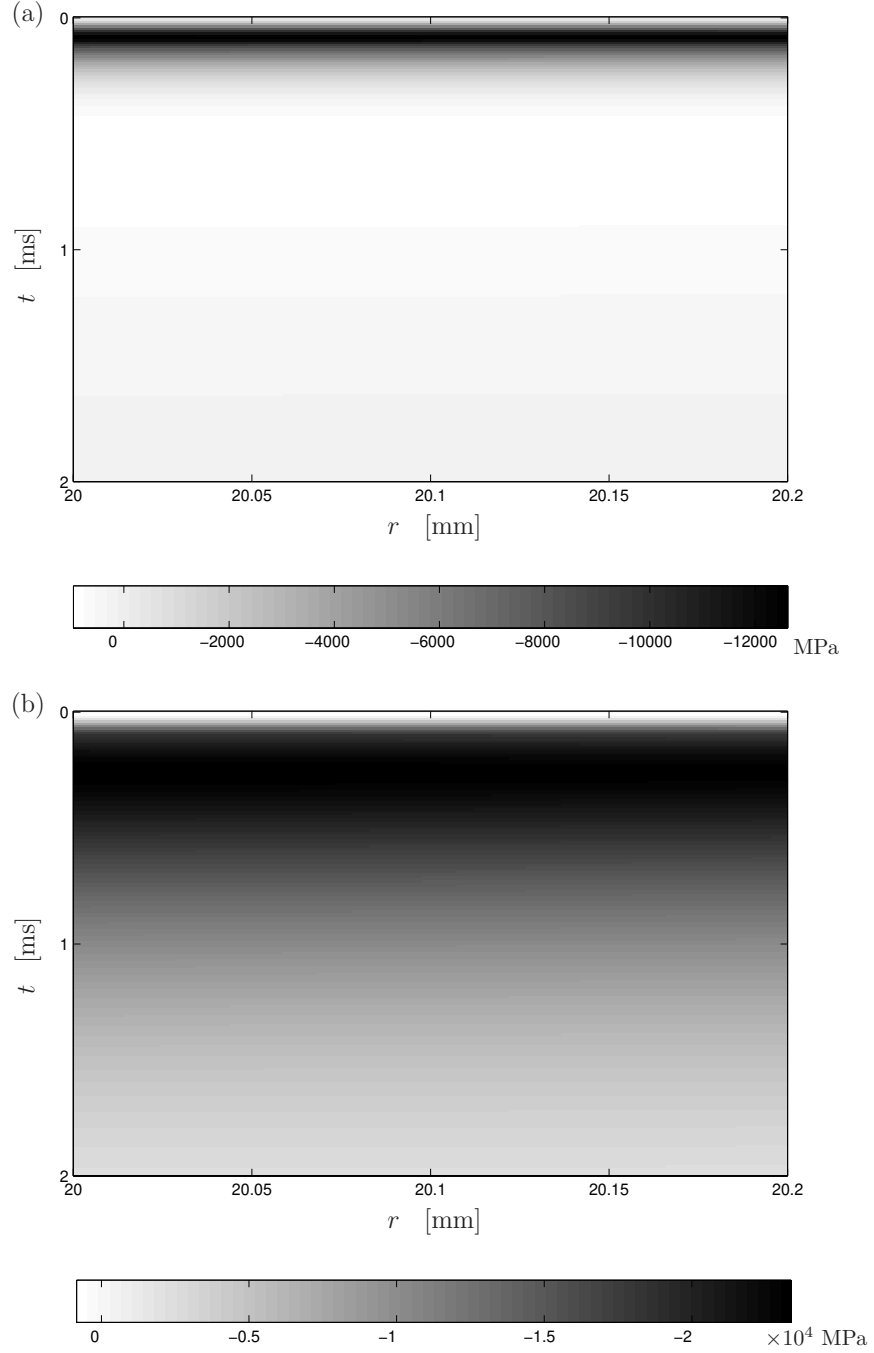
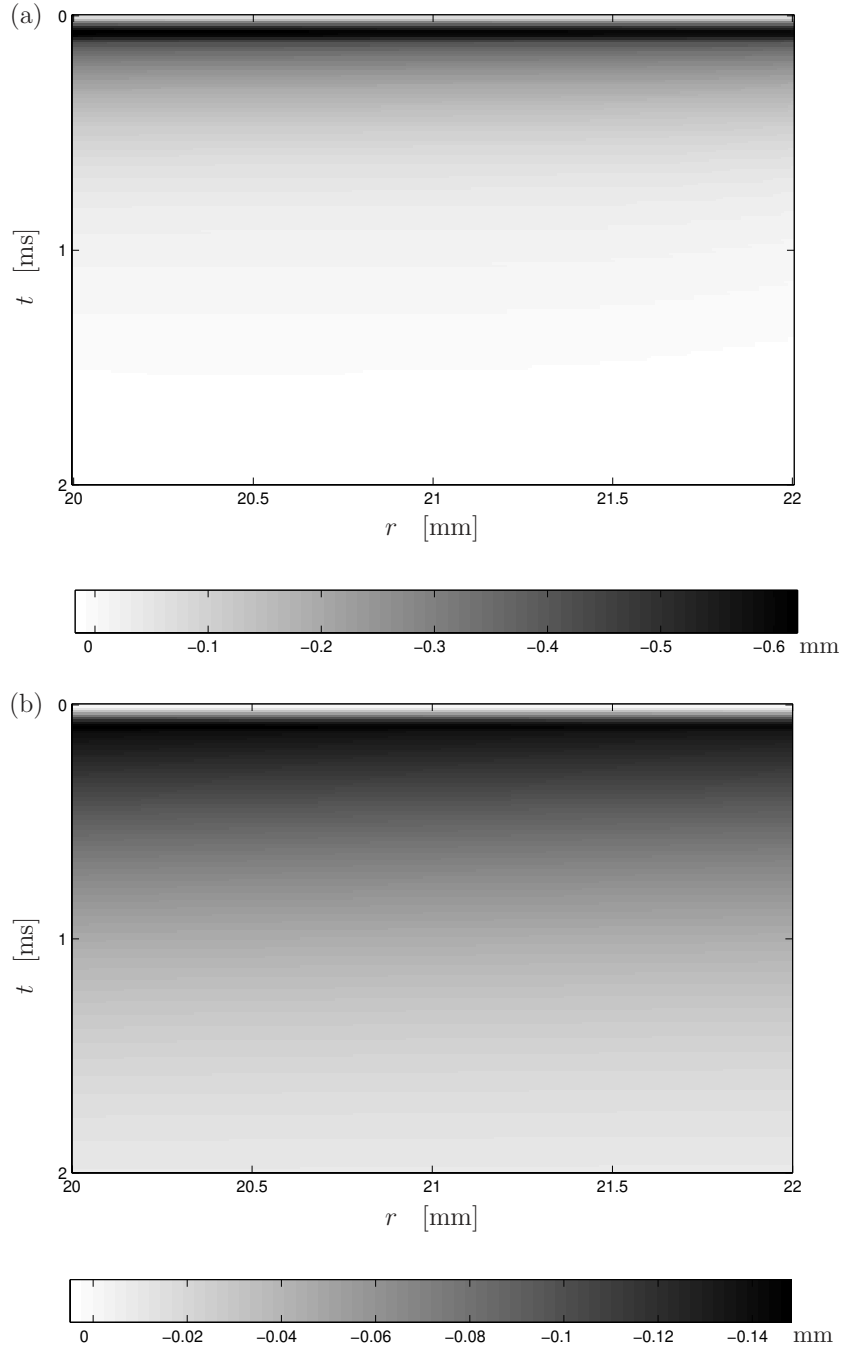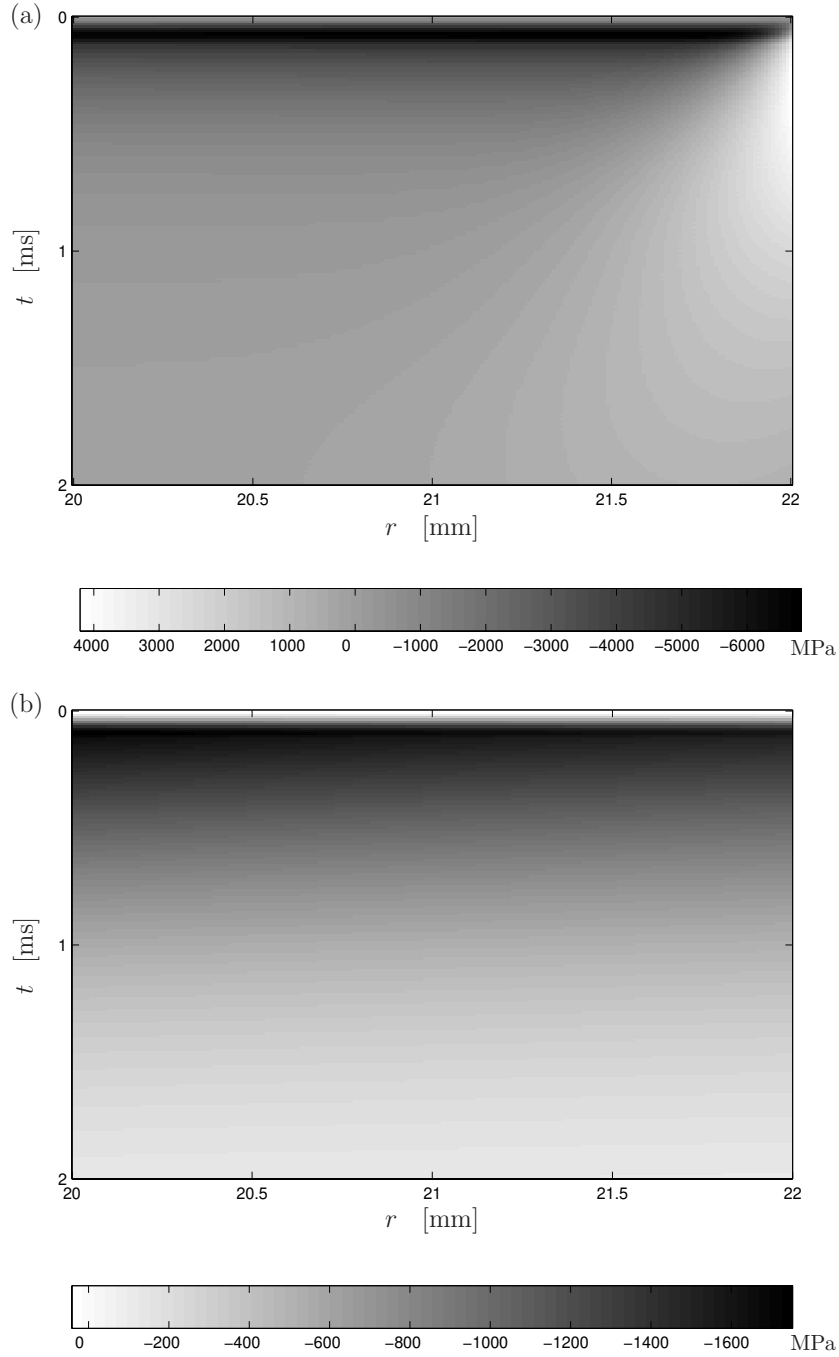Figure 5.12:   Tangential stress σ_φ in space-time domain , calculated with the present theory (a) and with the method of equivalent surface forces (b) for a non-magnetic ($\mu = \mu_0$) thin ($b - a = 0.2$ mm) workpiece subjected to compression.

Figure 5.13: Radial displacement u_r and tangential stress σ_φ at $r = a$ (upper graphs) and $r = b$ (lower graphs), calculated with the present theory (solid lines) and with the theory of perfectly conducting shells (dotted lines), for a non-magnetic ($\mu = \mu_0$) thin ($b - a = 0.2$ mm) workpiece subjected to compression.

There is no difference in the results obtained with the two methods, solid and dashed lines in Fig. 5.13, respectively. In addition, we present also the results obtained with the theory of perfectly conducting thin shells, using Eqs. (5.69) - (5.70), dotted lines in Fig. 5.13. When theory of perfectly conducting shells is used, the maximum values of the radial displacement u_r are larger than the ones obtained with our theory and with the method of equivalent surface forces, at the boundaries of the workpiece.

Non-magnetic thick workpiece in expansion

In Fig. 5.14, the components of the elastic field at $r = a$ in a non-magnetic ($\mu = \mu_0$) thick ($b - a = 2$ mm) workpiece subjected to expansion are presented. As the problem is almost quasi-static, the radial displacement is most of the time positive and its shape is very similar to the one of the electromagnetic volume force density at the same radial position.
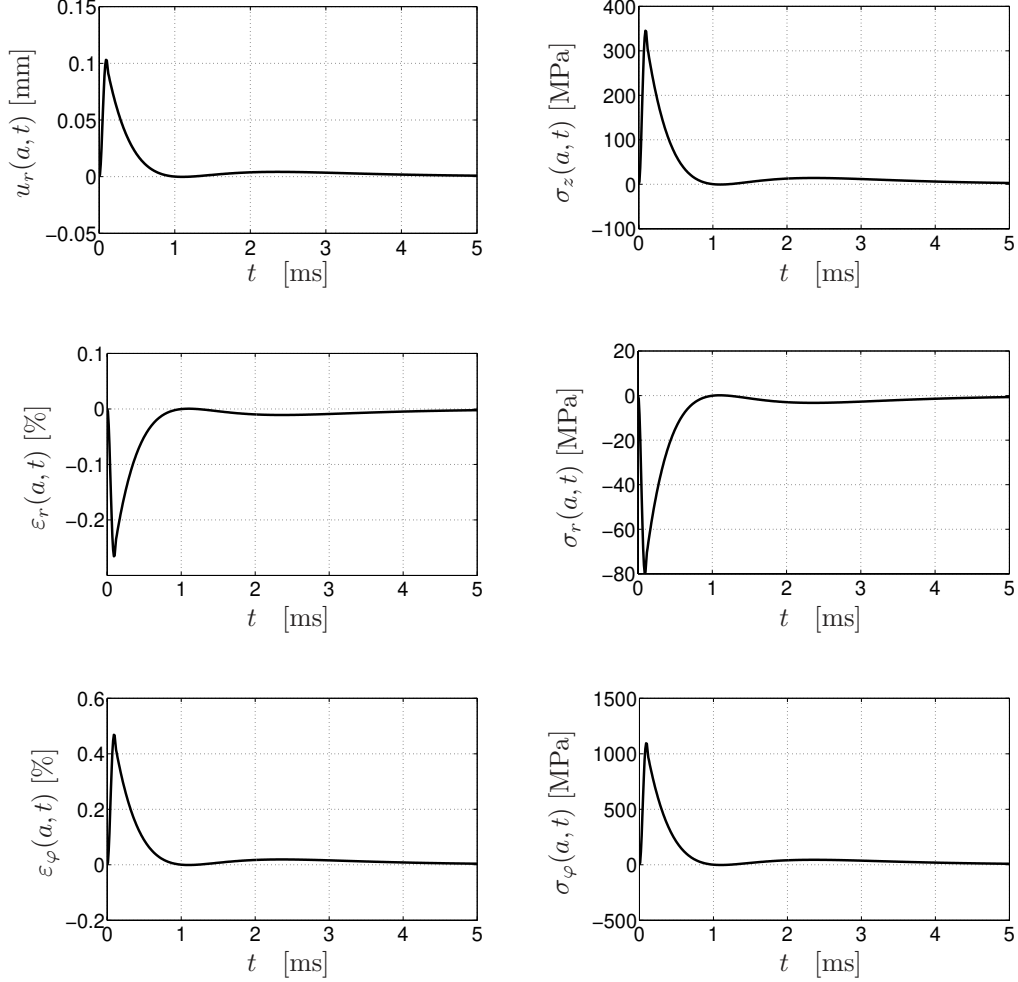
Figure 5.14:   Elastic field components at $r = a$ in the time domain for a non-magnetic ($\mu = \mu_0$) thick ($b - a = 2$ mm) workpiece subjected to expansion.

With the chosen elastic properties of the material the values of the radial displacement are very small, and these values yield very small radial and tangential strains, ε_r and ε_φ, respectively. The tangential stress σ_φ has the largest values from all the stress components, while the radial stress σ_r is very small and can be neglected. The longitudinal stress σ_z has negative values that are about three times smaller than the values of the tangential stress.

The space-time evolution of the radial displacement u_r, presented in Fig. 5.15, has been calculated using the theory presented in Section 5.2 and with the method of equivalent surface forces presented in Section 5.3.
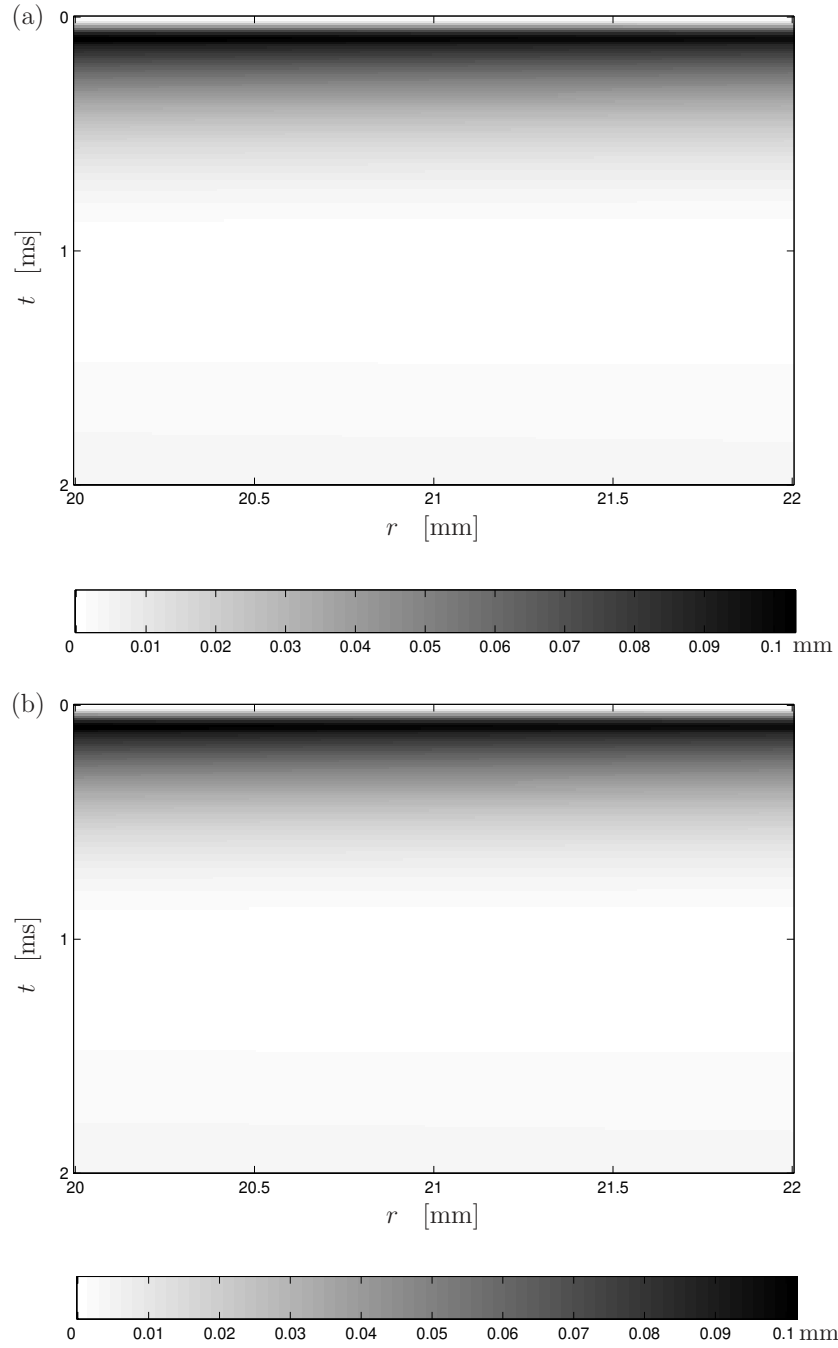
Figure 5.15:   Radial displacement u_r in space-time domain, calculated with the present theory (a) and with the method of equivalent surface forces (b), for a non-magnetic ($\mu = \mu_0$) thick ($b - a = 2$ mm) workpiece subjected to expansion.
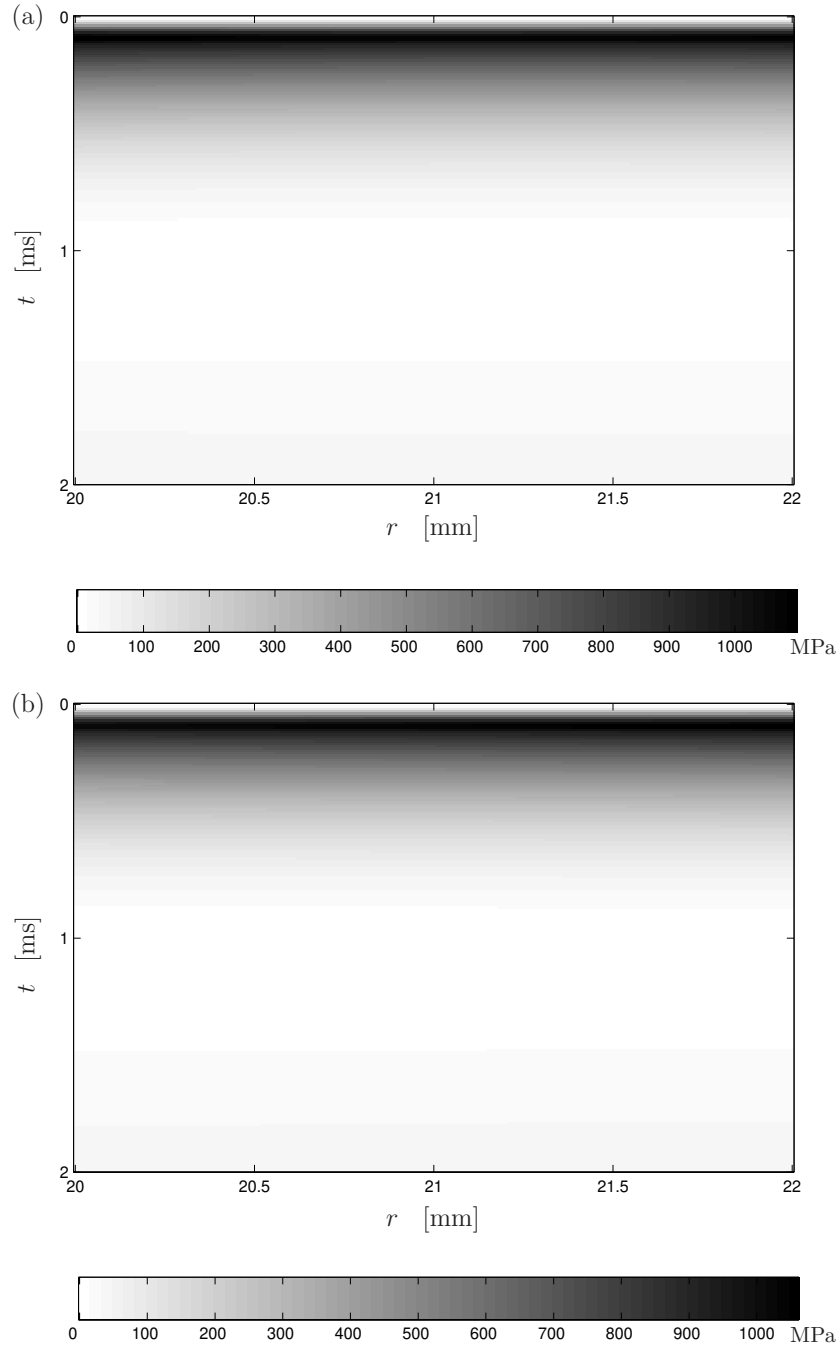
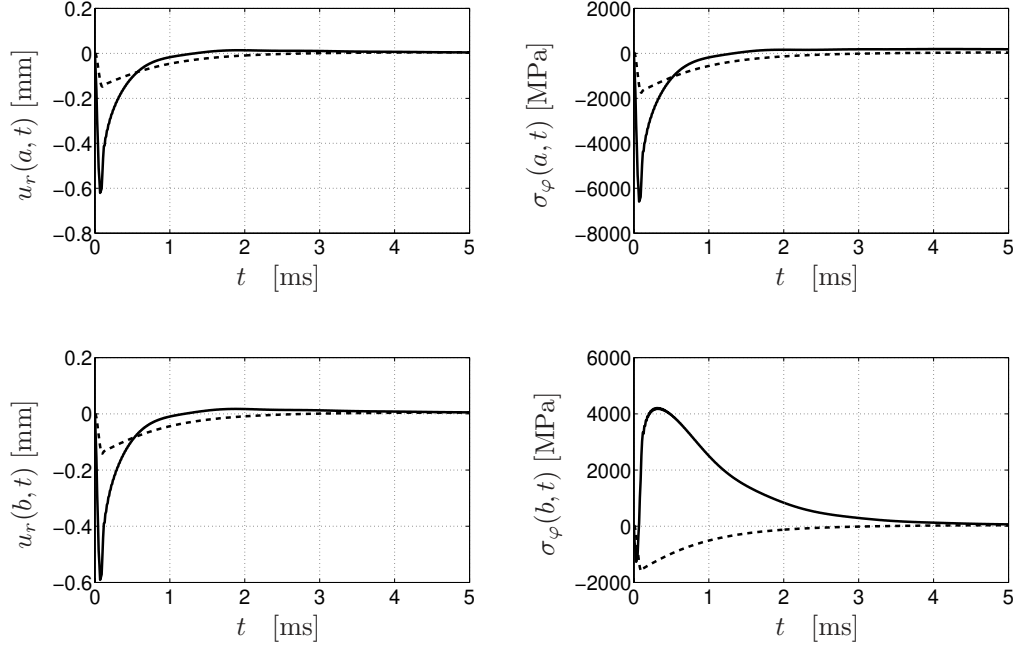Figure 5.16: Tangential stress σ_φ in space-time domain, calculated with the present theory (a) and with the method of equivalent surface forces (b), for a non-magnetic ($\mu = \mu_0$) thick ($b - a = 2$ mm) workpiece subjected to expansion.

Both methods are used to obtain the space-time evolution of the tangential stress σ_φ in Fig. 5.16. From our simulations we have observed that the radial displacement at $r = b$ is slightly smaller than the radial displacement at $r = a$, results that confirm the fact that during the electromagnetic expansion the workpiece becomes thinner. The radial displacement u_r in Fig. 5.15 (a) and (b) has similar maximum values, and their space-time evolution is almost the same. A similar behavior is noticed in Fig. 5.16 (a) and (b).

In order to have a better picture of the real differences between the results obtained with the two methods, in Fig. 5.17 we present the temporal evolution of the radial displacement and of the tangential stress at the inner boundary $r = a$ and at the outer boundary $r = b$ of the workpiece. We notice that the two methods give similar results at the boundaries of the workpiece.

For all three types of workpieces subjected to compression, the longitudinal stress σ_z has negative values, smaller than the values of the tangential
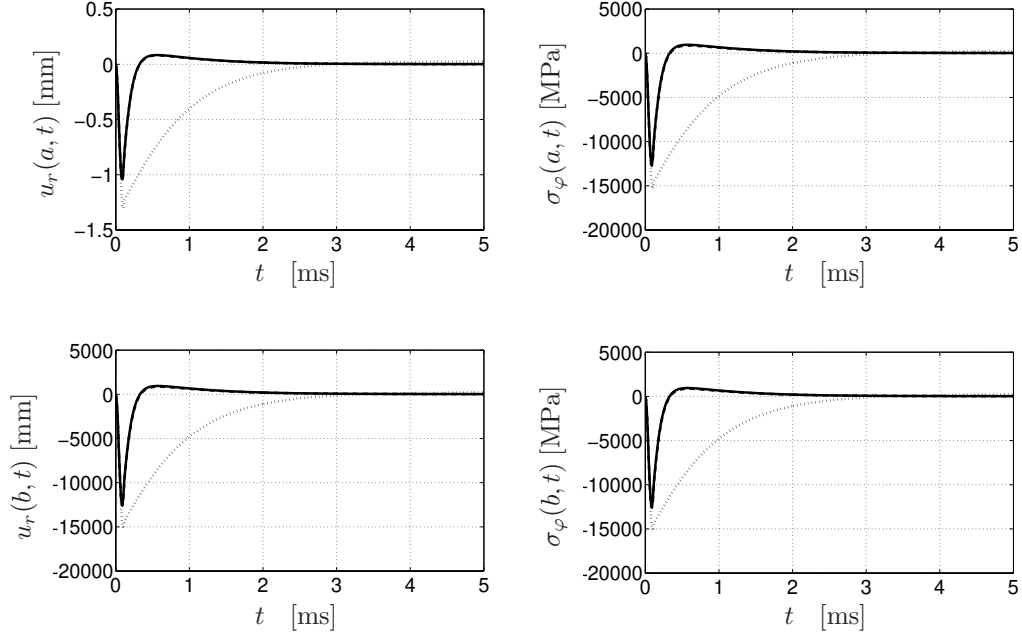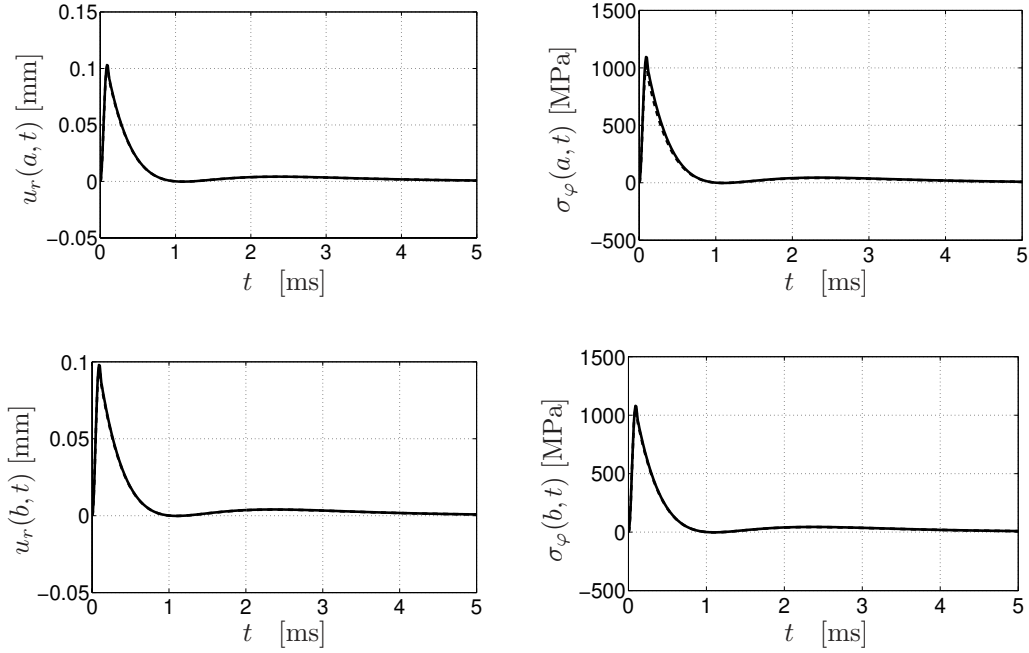

Figure 5.17: Radial displacement u_r and tangential stress σ_φ at $r = a$ (upper graphs) and $r = b$ (lower graphs) in the time domain, calculated with the present theory (solid lines) and with the method of equivalent surface forces (dashed lines), for a non-magnetic ($\mu = \mu_0$) thick ($b - a = 2$ mm) workpiece subjected to expansion.

stress σ_φ, but still they cannot be neglected. The presence of the negative longitudinal stress in electromagnetic compression shows that at the ends a longitudinal force acts on the workpiece and it acts in the sense of preventing the length of the workpiece to increase.

However, for the workpiece subjected to expansion, the longitudinal stress σ_z has positive values, smaller than the values of the tangential stress σ_φ, but still they cannot be neglected. The presence of the positive longitudinal stress in electromagnetic compression shows that at the ends a longitudinal force acts on the workpiece and it acts in the sense of preventing the length of the workpiece to decrease.

For our case of workpieces of infinite length these two effects avoid supplementary problems. When finite workpieces are used in the same plane strain case a supplementary force should be exerted along the workpiece to compensate the effect of the tangential stress σ_φ, e.g. by clamping the ends of the workpiece.

5.5 Conclusions

The elastic field in a circular cylindrical workpiece subjected to electromagnetic compression and to electromagnetic expansion has been determined, where the electromagnetic volume and surface force densities calculated in the previous chapter have been the external sources of this field. The solution of the equation of radial motion has been found as the sum of the general solution of the homogeneous equation of motion and the particular solution of the non-homogeneous equation of motion. The particular solution has been calculated using a source type of integral representation.

The numerical results obtained for the elastic field in the cylindrical configuration show that the particle radial displacement u_r has small values for all workpieces, in the order of 0.1 – 1 mm even at the moment where it has reached its maximum values. The radial displacement is slightly larger at the inner boundary $r = a$ of the workpiece than at the outer boundary $r = b$, in absolute value, both for compression and for expansion. It means that the workpiece becomes slightly thicker during the electromagnetic compression, and it becomes thinner during electromagnetic expansion. For all workpieces, the radial stress σ_r has small, negligible values, except for the magnetic workpiece.

The results obtained with the method of equivalent surface forces differ

from the results obtained with our theory, only for the case of a magnetic thick workpiece. For all non-magnetic workpieces the values obtained with these two methods are almost the same. For a non-magnetic thin workpiece, numerical results have been obtained also with the theory of perfectly conducting shells. These results are larger than the corresponding results obtained with out method. We may conclude, that for thin workpieces, our theory gives better results than the theory of perfectly conducting shells.

In electromagnetic forming we deal with an induced electrical current passing through a workpiece made of a material with very high electrical conductivity. This yields some heat production in the workpiece and thus to a temperature rise that, if it is considerable, may influence the evolution of the elastodynamic field in the workpiece. The effect of the temperature rise on the elastodynamic field will be analyzed in Chapter 6, together with the evolution of the temperature inside the workpiece.

We have focused in this chapter only on the linearized theory of elasticity, even though that for a given material the linearized theory of elasticity cannot be applied for the whole range of stresses and strains. When the stress reaches a so-called yield point, the material behavior is not linear and a non-linear theory has to be applied. This theory, together with the accompanying numerical results will be given in Chapter 7. In general, in a typical electromagnetic forming process, the time interval in which the workpiece shows an elastic behavior is limited to a few μs at the beginning of the process, before the onset of the plastic deformation. At the end of the elastic range, the deformations are very small as compared with the plastic ones to be obtained. That is the reason why most of the authors have neglected the elastic deformations described in this chapter.

Because of the motion and of the temperature changes of the workpiece during the electromagnetic forming, the parameters of the process changes at each time instant, thus an iterative model is required to deal with all changes at all time instants. In Chapter 9 we propose such an iterative method that takes into account the changes of the parameters during the deformation process.

Chapter 6

Temperature effects in electromagnetic forming

This chapter presents some calculations regarding temperature effects in an electromagnetic forming system. For simplicity, we will consider only the evolution of the temperature in the workpiece due to dissipation of electromagnetic energy during the forming process. Accounting for the temperature effects in the thermoelastic strains, the resulting thermoelastic field is then computed with the approach presented in Chapter 5.

6.1   Configuration of the temperature problem

The configuration in which the temperature field will be determined models the case of electromagnetic compression, and is presented in Fig. 6.1. The position in the configuration is specified by the coordinates $\{r, \varphi, z\}$ with respect to the reference frame with the origin $\mathcal{O}$ and the three mutually perpendicular vectors $\{\boldsymbol{i}_r, \boldsymbol{i}_\varphi, \boldsymbol{i}_z\}$ of unit length each. In the indicated order, the base vectors form a right-handed system.

The temperature distribution in the workpiece during the electromagnetic forming process depends on the heat exchange between the forming coil and the workpiece, and the dissipation of electromagnetic energy in the workpiece itself (Joule losses). This is altogether a complicated problem to solve. We expect that the major contribution to the temperature rise in the workpiece is due to the internal heat dissipation. So, in order to get an idea of the thermoelastic effects that correspond to such a rise, we have chosen for a
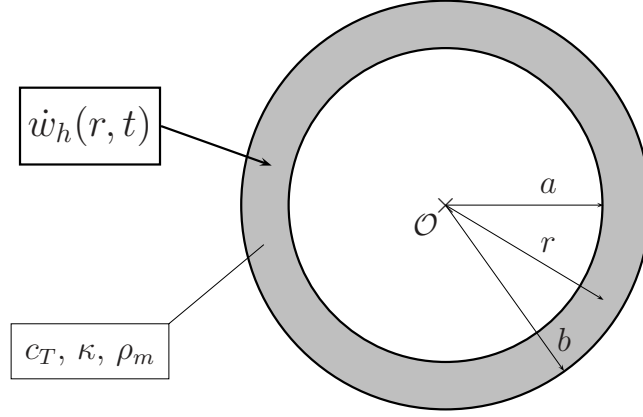
Figure 6.1:   Cross section of the cylindrical configuration for the calcu-
               lation of the temperature field that has as its source the
               known rate of heat dissipation.

model in which only the internal heat dissipation will be taken into account.
We will compute the temperature distribution in the workpiece, assuming that
the boundaries of the workpiece are insulated. The latter assumption might
lead to a somewhat too high temperature distribution, but that can partly
compensate the neglected transfer of heat from the forming coil.

The source that excites the temperature field is the rate of energy gen-
eration in the workpiece represented by the Joule losses inside the workpiece.
The Joule losses may be inferred from the known values of the electromagnetic
field components calculated in Chapter 4.

Once the temperature field is known, the corresponding thermoelastic
effects are introduced through additional thermoelastic strains that are pro-
portional to the product of the linear thermal expansion coefficient of the
workpiece and the temperature.

6.2 Temperature field equations and boundary con-
        ditions

In this section we investigate the heat conduction problem, i.e. the computation
of the temperature distribution in the workpiece as it results from the heat
generated in it through the dissipation of electromagnetic energy during the
forming process.

In a cylindrical coordinate system, the equations governing the thermal state of the workpiece, namely the equation of heat flow and the thermal conduction equation are written as

$$\frac{1}{r}\partial_r(rq_r) + \rho_m c_T \partial_t T = \dot{w}_h \tag{6.1}$$

and

$$q_r = -\kappa \partial_r T, \tag{6.2}$$

where T is the temperature, ρ_m is the mass density, c_T is the specific heat, κ is the thermal conductivity, and q_r is the heat flow density (heat flux) in the radial direction. The source term $\dot{w}_h$ in the right hand side of Eq. (6.1) represents the rate of volume density of the Joule losses in the workpiece

$$\dot{w}_h(r,t) = \sigma E_\varphi^2(r,t). \tag{6.3}$$

Combining Eqs. (6.1) and (6.2) results into

$$\partial_r^2 T + \frac{1}{r}\,\partial_r T - \frac{\rho_m c_T}{\kappa}\,\partial_t T = -\frac{1}{\kappa}\dot{w}_h. \tag{6.4}$$

This equation must be supplemented by the initial condition and the boundary conditions. The initial temperature within the whole configuration is T_0. For convenience we will from now on consider the temperature $T(r,t)$ in Eq. (6.4) to be $T(r,t) - T_0$. That means that the initial condition for the temperature will be

$$\lim_{t\downarrow 0} T(r,t) = 0. \tag{6.5}$$

There are many types of boundary conditions that may be applied, as discussed in Section 6.1. We have chosen here an insulated surface, thus the heat flux is zero at the boundaries, i.e. $q(r,t) = 0$ at $r = a$ and $r = a$. As a result, we then have as boundary conditions

$$\lim_{r\downarrow a} \partial_r T(r,t) = 0, \qquad \lim_{r\uparrow b} \partial_r T(r,t) = 0. \tag{6.6}$$

The simplest way to construct solutions to Eq. (6.4) that satisfy the proper boundary and excitation conditions and ensure causality is to use the Laplace transformation with respect to time. As in Chapter 4, we take $s \to j\omega$, where j is the imaginary unit and $\omega = 2\pi f$ is the radial frequency, while f denotes the frequency of operation. In our numerical work, we use the FFT (Fast Fourier Transform) to compute the pertaining Fourier transforms.

After the application of the Laplace transform, Eq. (6.4) becomes

$$\partial_r^2 \hat{T} + \frac{1}{r}\,\partial_r \hat{T} - \gamma^2 \hat{T} = -\frac{1}{\kappa}\hat{w}_h, \tag{6.7}$$

where $\gamma = \sqrt{s\rho_m c_T / \kappa}$.

We may write the total solution of Eq. (6.7) as

$$\hat{T}(r) = \hat{T}^{part}(r) + \hat{T}^{gen}(r), \tag{6.8}$$

where $\hat{T}^{part}(r)$ denotes the particular solution of Eq. (6.7) and $\hat{T}^{gen}(r)$ denotes the general solution of the homogeneous form of Eq. (6.7).

Particular solution $\hat{T}^{part}(r)$

We may construct the particular solution $\hat{T}^{part}(r)$ using the Green's function $\hat{G}(r, r')$ as it follows,

$$\hat{T}^{part}(r) = \frac{1}{\kappa}\int_{r'=a}^{b} \hat{G}(r, r')\hat{w}_r r'\,\mathrm{d}r', \tag{6.9}$$

where $\hat{G}(r, r')$ is the solution of equation

$$\frac{1}{r}\,\partial_r (r\partial_r \hat{G}) - \gamma^2 \hat{G} = -\frac{1}{r'}\,\delta(r - r'). \tag{6.10}$$

In an unbounded domain with a cylindrical source placed at $r = r'$, we may write the solution of Eq. (6.10) as

$$\hat{G}(r, r') = \begin{cases} A\,I_0(\gamma r)K_0(\gamma r'), & \text{for } r < r', \\[2mm] B\,K_0(\gamma r)I_0(\gamma r'), & \text{for } r > r', \end{cases} \tag{6.11}$$

where $I_0(\gamma r)$ and $K_0(\gamma r)$ are the modified Bessel function of the first and second kind, respectively. The coefficients A and B are calculated from the continuity condition at $r = r'$, i.e.,

$$\lim_{r\downarrow r'} \hat{G} - \lim_{r\uparrow r'} \hat{G} = 0, \tag{6.12}$$

together with the excitation condition at $r = r'$, i.e.,

$$\lim_{r\downarrow r'} r\partial_r \hat{G} - \lim_{r\uparrow r'} r\partial_r \hat{G} = -1. \tag{6.13}$$

From these conditions, we obtain $A = B = 1$ and then

$$\hat{G}(r, r') = \begin{cases} I_0(\gamma r)K_0(\gamma r'), & \text{for } r \leq r', \\ \\ K_0(\gamma r)I_0(\gamma r'), & \text{for } r \geq r'. \end{cases} \tag{6.14}$$

In our further analysis we need also the radial derivative of the particular solution. This is obtained as

$$\partial_r \hat{T}^{part}(r) = \frac{1}{\kappa} \int_{r'=a}^{b} \partial_r \hat{G}(r, r')\hat{w}_h(r')r' \, \mathrm{d}r', \tag{6.15}$$

where

$$\partial_r \hat{G}(r, r') = \begin{cases} \gamma I_1(\gamma r)K_0(\gamma r'), & \text{for } r < r', \\ \\ \frac{1}{2}\gamma[I_1(\gamma r)K_0(\gamma r) - K_1(\gamma r)I_0(\gamma r)], & \text{for } r = r', \\ \\ -\gamma K_1(\gamma r)I_0(\gamma r'), & \text{for } r > r'. \end{cases} \tag{6.16}$$

A special case in the calculation of the Green's function is represented by $\gamma \to 0$ ($f \to 0$). For this case, Eq. (6.16) becomes

$$\lim_{\gamma \to 0} \partial_r \hat{G}(r, r') = \begin{cases} 0, & \text{for } r < r', \\ \\ -\frac{1}{2r}, & \text{for } r = r', \\ \\ -\frac{1}{r}, & \text{for } r > r'. \end{cases} \tag{6.17}$$

For $\gamma \to 0$, the limit of Eq. (6.14) is ∞, and we have to find a way to evaluate the integral in Eq. (6.9). We notice that we can also calculate the integral

$$\gamma^2 \hat{T}^{part}(r) = \frac{1}{\kappa} \int_{r'=a}^{b} \gamma^2 \hat{G}(r, r')\hat{w}_h(r')r' \, \mathrm{d}r', \tag{6.18}$$

or

$$s\hat{T}^{part}(r) = \frac{1}{\rho_m c_T} \int_{r'=a}^{b} \gamma^2 \hat{G}(r, r')\hat{w}_h(r')r' \, \mathrm{d}r'. \tag{6.19}$$

The quantity $\hat{w}_h(r')$ at the right-hand side of the above equation is a known quantity in the frequency domain and $\gamma^2 \hat{G}(r, r')$ remains finite, so the integral

may easily be evaluated.. Its time-domain counterpart can be calculated using an inverse FFT. Further, taking into account that

$$\frac{1}{s}F(s) \to \int_{\tau=0}^{t} f(\tau)\,\mathrm{d}\tau, \tag{6.20}$$

we can calculate the time-domain counterpart of $\hat{T}^{part}(r)$ and then the values obtained can be transformed back to frequency domain.

Until here, since all quantities in Eq. (6.9) are known, we have calculated the particular solution $\hat{T}^{part}(r)$ and its radial derivative $\partial_r\hat{T}^{part}(r)$ as functions of the radius r. Thus, we also have the values of the particular solution and its radial derivative at the boundaries $r = a$ and $r = b$ of the cylindrical domain representing the workpiece.

General solution $\hat{T}^{gen}(r)$

The general solution $\hat{T}^{gen}(r)$ of the homogeneous form of Eq. (5.29) is given by

$$\hat{T}^{gen}(r) = C\,I_0(\gamma r) + D\,K_0(\gamma r), \tag{6.21}$$

where the coefficients C and D are obtained from the boundary conditions

$$\lim_{r\downarrow a}\partial_r\hat{T}^{gen} = -\partial_r\hat{T}^{part}(a), \tag{6.22}$$

$$\lim_{r\uparrow b}\partial_r\hat{T}^{gen} = -\partial_r\hat{T}^{part}(b), \tag{6.23}$$

with $\partial_r\hat{T}^{part}$ from Eq. (6.15).

From Eqs. (6.22) - (6.23) we obtain the following system of equations in matrix form

$$\left(\begin{array}{cc} \gamma I_1(\gamma a) & -\gamma K_1(\gamma a) \\ \gamma I_1(\gamma b) & -\gamma K_1(\gamma b) \end{array} \right) \left(\begin{array}{c} C \\ D \end{array} \right) = \left(\begin{array}{c} h(a) \\ h(b) \end{array} \right), \tag{6.24}$$

where the elements of the known vector are given by

$$h(a) = -\partial_r\hat{T}^{part}(a), \tag{6.25}$$

$$h(b) = -\partial_r\hat{T}^{part}(b). \tag{6.26}$$

Thus, the coefficients C and D may be calculated as

$$C = \frac{1}{\gamma}\frac{K_1(\gamma b)h(a) - K_1(\gamma a)h(b)}{I_1(\gamma a)K_1(\gamma b) - K_1(\gamma a)I_1(\gamma b)}, \tag{6.27}$$

$$D = \frac{1}{\gamma}\frac{I_1(\gamma b)h(a) - I_1(\gamma a)h(b)}{I_1(\gamma a)K_1(\gamma b) - K_1(\gamma a)I_1(\gamma b)}. \tag{6.28}$$

Hence, the solution for $\hat{T}$ is obtained as

$$\hat{T}(r) = \hat{T}^{part}(r) + I_0(\gamma r)\frac{1}{\gamma}\frac{K_1(\gamma b)h(a) - K_1(\gamma a)h(b)}{I_1(\gamma a)K_1(\gamma b) - K_1(\gamma a)I_1(\gamma b)}$$
$$+ K_0(\gamma r)\frac{1}{\gamma}\frac{I_1(\gamma b)h(a) - I_1(\gamma a)h(b)}{I_1(\gamma a)K_1(\gamma b) - K_1(\gamma a)I_1(\gamma b)}. \tag{6.29}$$

Further, for the calculation of the thermoelastic field we need also the radial derivative of $\hat{T}$, calculated as

$$\partial_r\hat{T}(r) = \partial_r\hat{T}^{part}(r) + I_1(\gamma r)\frac{K_1(\gamma b)h(a) - K_1(\gamma a)h(b)}{I_1(\gamma a)K_1(\gamma b) - K_1(\gamma a)I_1(\gamma b)}$$
$$- K_1(\gamma r)\frac{I_1(\gamma b)h(a) - I_1(\gamma a)h(b)}{I_1(\gamma a)K_1(\gamma b) - K_1(\gamma a)I_1(\gamma b)}. \tag{6.30}$$

The results for the temperature field may then be transformed back to time-domain using an inverse FFT.

Isothermal case for a thin workpiece

When the workpiece is very thin and we assume that it has the same temperature at every location, the calculation of the temperature field may be simplified since $q_r = 0$ in Eq. (6.2), and we then have from Eq. (6.1)

$$\hat{T}(r) = \frac{1}{\gamma^2 \kappa}\hat{w}_h. \tag{6.31}$$

Further, a first estimation of the temperature of the workpiece may be obtained using the approximation of Joule losses $\dot{w}_h$ in the workpiece with the network model

$$\dot{w}_h(t) = \frac{I_S^2(t)}{\sigma \ (b-a)^2}. \tag{6.32}$$

Since the Joule losses are totally converted into heat, in this case the actual temperature of the workpiece will be

$$T(t) = \frac{1}{\rho_m c_T \sigma (b-a)^2}\int_{\tau=0}^{t} I_S^2(\tau)\,\mathrm{d}\tau. \tag{6.33}$$

Since this temperature holds in the entire workpiece, the mean temperature $T_{mean}(t)$ of the workpiece equals

$$T_{mean}(t) = T(t). \tag{6.34}$$

6.3   Numerical results for the temperature field

In this section, we present some numerical results for typical electromagnetic forming systems designed for compression and for expansion of hollow circular cylindrical workpieces.

The following types of workpieces subjected to electromagnetic compression are investigated:

- a non-magnetic $(\mu = \mu_0)$ thick workpiece with an inner radius $r = a = 20$ mm and an outer radius $r = b = 22$ mm,

- a hypothetical magnetic $(\mu = 100\,\mu_0)$ thick workpiece with an inner radius $r = a = 20$ mm and an outer radius $r = b = 22$ mm,

- a non-magnetic $(\mu = \mu_0)$ thin workpiece with an inner radius $r = a = 20$ mm and an outer radius $r = b = 20.2$ mm.

For electromagnetic expansion, only a non-magnetic $(\mu = \mu_0)$ thick workpiece with an inner radius $r = a = 20$ mm and an outer radius $r = b = 22$ mm is considered.

In all these cases the workpiece has the same thermal properties, with a specific heat $c_T = 880$ J/(kg K), a thermal conductivity $\kappa = 190$ W/(m K) and a mass density $\rho_m = 2.7 \cdot 10^3$ kg/m^3, see Appendix C.1.

The temperature field in the space-time domain is presented for all the cases considered. Also, for each case the evolution in the time domain of the mean temperature is presented. The mean temperature in the workpiece has been calculated in two ways, as the average of the temperature field distribution over the thickness of the workpiece, and as the mean temperature in the absence of thermal conduction inside the workpiece. The latter approach is considered to be a good approximation for a thin workpiece.

In Figs. 6.2 and 6.3 we present the space-time evolution of the temperature and the temporal evolution of the mean temperature T_{mean}, respectively, in a non-magnetic thick workpiece subjected to compression. In Figs. 6.4 and 6.5 we present the space-time evolution of the temperature and the temporal evolution of the mean temperature T_{mean} in a magnetic thick workpiece subjected to compression, while in Figs. 6.6 and 6.7 we present the same quantities in a non-magnetic thin workpiece subjected to compression. Finally, in Figs. 6.8 and 6.9 we present the space-time evolution of the temperature and the temporal evolution of the mean temperature T_{mean}, respectively, in a non-magnetic thick workpiece subjected to compression.

Non-magnetic thick workpiece in compression
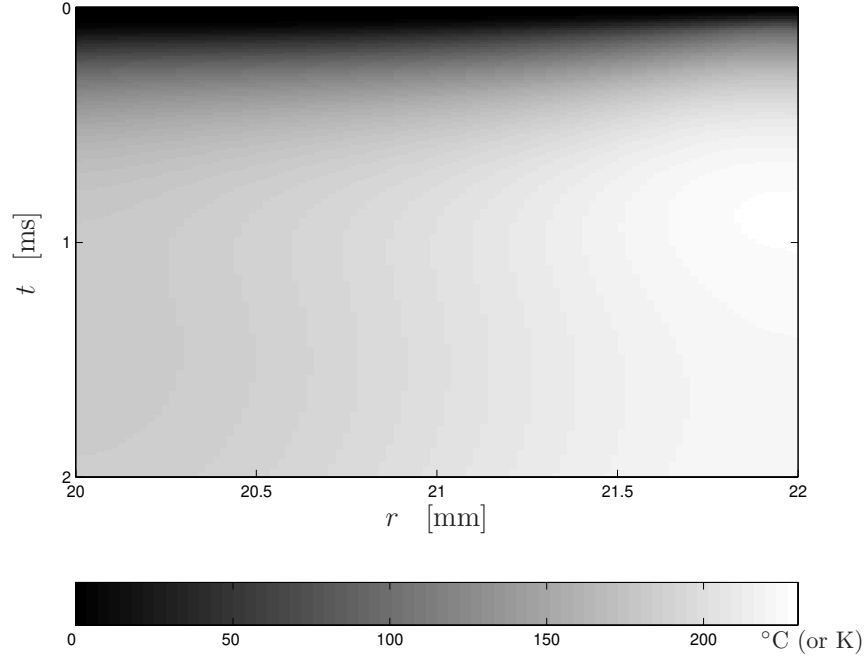
Figure 6.2: Temperature rise T in space-time domain for a non-magnetic $(\mu = \mu_0)$ thick $(b - a = 2$ mm$)$ workpiece subjected to compression.
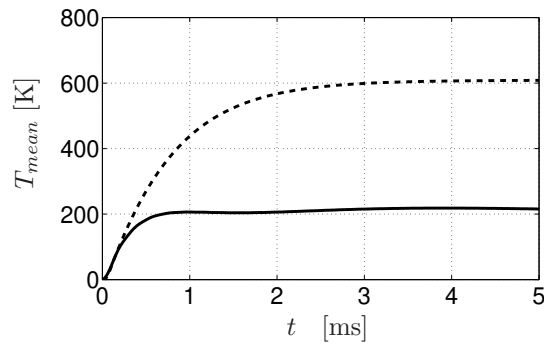
Figure 6.3: Mean temperature T_{mean} in the time domain, obtained from the exact results (solid lines) and obtained from neglecting thermal conduction (dashed lines) for a non-magnetic $(\mu = \mu_0)$ thick $(b - a = 2$ mm$)$ workpiece subjected to compression.

Magnetic thick workpiece in compression
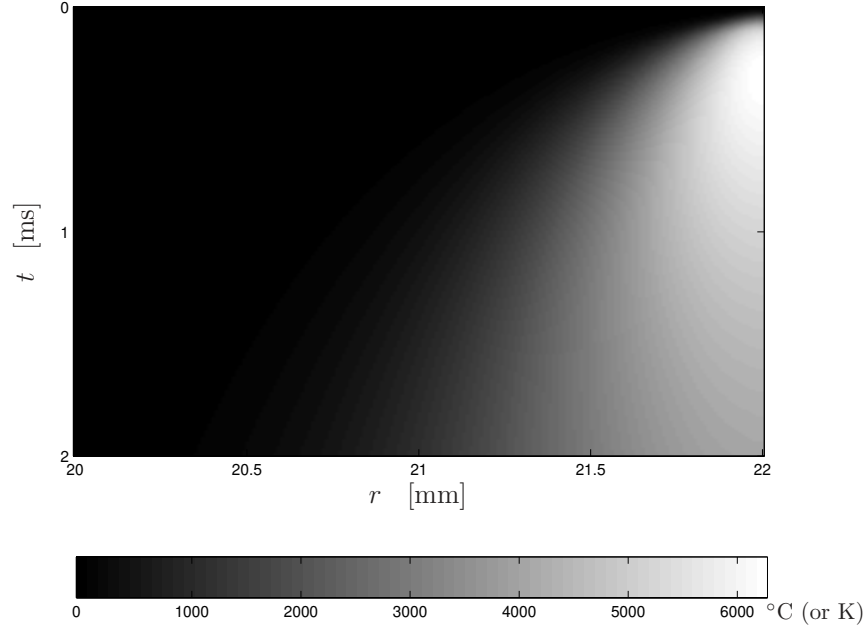
Figure 6.4:   Temperature rise T in space-time domain for a magnetic
               ($\mu = 100\,\mu_0$) thick ($b - a = 2$ mm) workpiece subjected to
               compression.
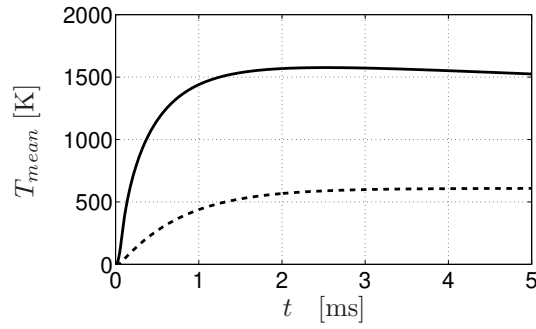
Figure 6.5:   Mean temperature T_{mean} in the time domain, obtained
               from the exact results (solid lines) and obtained from ne-
               glecting thermal conduction (dashed lines) for a magnetic
               ($\mu = 100\,\mu_0$) thick ($b - a = 2$ mm) workpiece subjected to
               compression.

Non-magnetic thin workpiece in compression
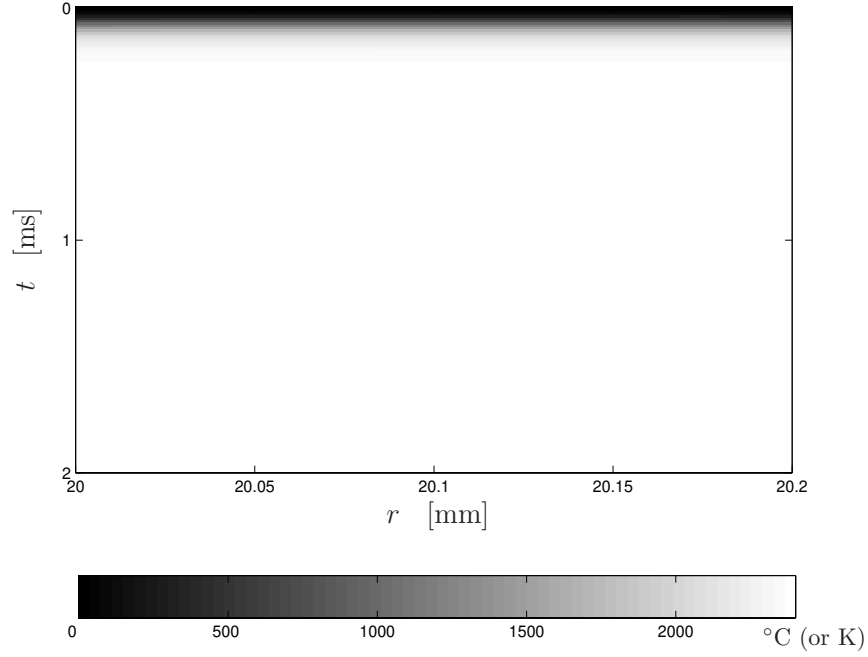
Figure 6.6: Temperature rise T in the space-time domain for a non-magnetic ($\mu = \mu_0$) thin ($b - a = 0.2$ mm) workpiece subjected to compression.
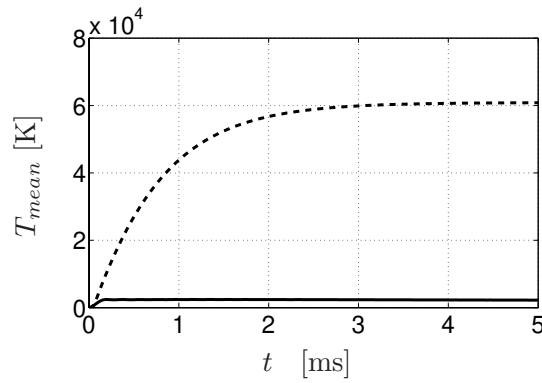
Figure 6.7: Mean temperature T_{mean} in the time domain, obtained from the exact results (solid lines) and obtained from neglecting thermal conduction (dashed lines) for a non-magnetic ($\mu = \mu_0$) thick ($b - a = 0.2$ mm) workpiece subjected to compression.

Non-magnetic thick workpiece in expansion
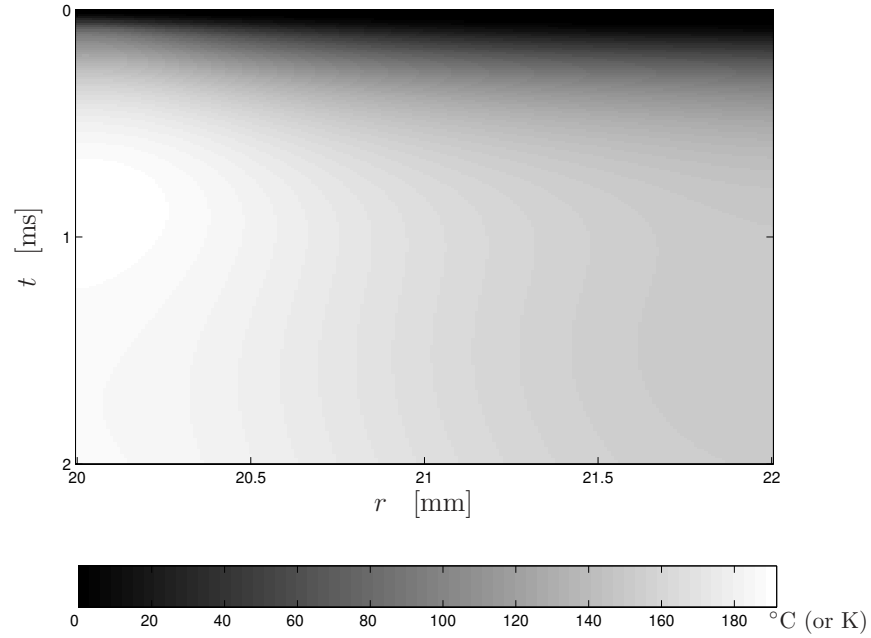
Figure 6.8: Temperature rise T in space-time domain for a non-magnetic ($\mu = \mu_0$) thick ($b - a = 2$ mm) workpiece subjected to expansion.
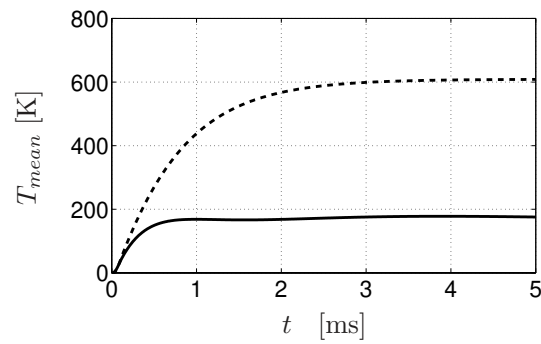
Figure 6.9: Mean temperature T_{mean} in the time domain, obtained from the exact results (solid lines) and obtained from neglecting thermal conduction (dashed lines) for a non-magnetic ($\mu = \mu_0$) thick ($b - a = 2$ mm) workpiece subjected to expansion.

We notice that in all considered cases, the temperature has large values. For the non-magnetic thick and the non-magnetic thin workpieces, the temperature rise reaches values at which the workpiece will melt. However, the calculated values do not take into account the heat exchange with the surrounding medium.

With the known evolution of temperature within the workpiece, the evolution of the thermoelastic field will be calculated in the next section.

6.4   The thermoelastic field in the workpiece

This section presents the calculation of the thermoelastic field in an infinite, hollow, cylindrical, conducting object. The configuration is locally excited by the electromagnetic volume and surface force densities calculated in Chapter 4, together with the temperature rise in the object, calculated in the first part of this chapter. The investigated configuration models both the case of electromagnetic compression and of electromagnetic expansion, and is presented in Fig. 6.10.

The equations of the dynamic thermoelastic field are the same as for the
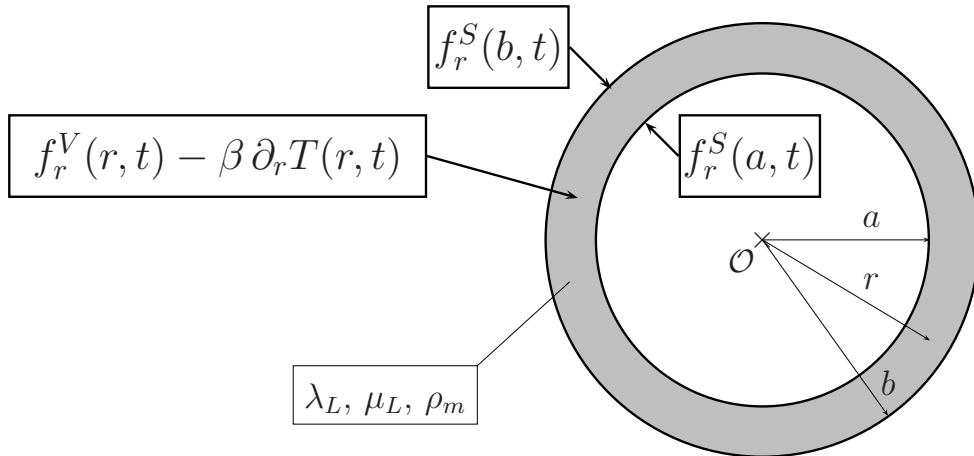
Figure 6.10:   Cross section of the cylindrical configuration for the calculation of the thermoelastic field that has as its source the known electromagnetic force densities and the known temperature rise.

elastic field in Section 5.2, see [93]

$$\partial_r \tau_{rr} + \frac{1}{r} \partial_\varphi \tau_{r\varphi} + \partial_z \tau_{rz} + \frac{1}{r}(\tau_{rr} - \tau_{\varphi\varphi}) - \rho_m \partial_t^2 u_r = -f_r^V, \qquad (6.35)$$

$$\partial_r \tau_{r\varphi} + \frac{1}{r} \partial_\varphi \tau_{\varphi\varphi} + \partial_z \tau_{\varphi z} + \frac{2}{r} \tau_{r\varphi} - \rho_m \partial_t^2 u_\varphi = 0, \qquad (6.36)$$

$$\partial_r \tau_{rz} + \frac{1}{r} \partial_\varphi \tau_{\varphi z} + \partial_z \tau_{zz} + \frac{1}{r} \tau_{rz} - \rho_m \partial_t^2 u_z = 0, \qquad (6.37)$$

together with the boundary conditions to be applied at $r = a$ and $r = b$,

$$\lim_{r \downarrow a} \tau_{rr}(r, t) = -f_r^S(a, t), \qquad\qquad \lim_{r \uparrow b} \tau_{rr}(r, t) = f_r^S(b, t). \qquad (6.38)$$

For the considered plane strain case, the non-zero thermoelastic normal strains are defined as

$$e_{rr} = \partial_r u_r, \qquad (6.39)$$

$$e_{\varphi\varphi} = r^{-1} u_r, \qquad (6.40)$$

while the constitutive relations, see [93] are

$$\tau_{rr} = (\lambda_L + 2\mu_L)e_{rr} + \lambda_L e_{\varphi\varphi} + \lambda_L e_{zz} - \beta T, \qquad (6.41)$$

$$\tau_{\varphi\varphi} = \lambda_L e_{rr} + (\lambda_L + 2\mu_L)e_{\varphi\varphi} + \lambda_L e_{zz} - \beta T, \qquad (6.42)$$

$$\tau_{zz} = \lambda_L e_{rr} + \lambda_L e_{\varphi\varphi} + (\lambda_L + 2\mu_L)e_{zz} - \beta T. \qquad (6.43)$$

where $\beta = \alpha_T(3\lambda_L + 2\mu_L)$ and α_T is the coefficient of linear thermal expansion of the workpiece, see [93]. We will focus here only on solving the equation of motion in the radial direction, obtained from Eq. (6.35) when applying the constitutive relations in Eqs. (6.41) - (6.42). The following equation of motion in the radial direction has to be solved

$$\partial_r^2 u_r + \frac{1}{r} \partial_r u_r - \frac{1}{r^2} u_r - \frac{1}{c_P^2} \partial_t^2 u_r = -\frac{1}{\lambda_L + 2\mu_L}(f_r^V - \beta \partial_r T). \qquad (6.44)$$

This equation can be solved in a similar manner as Eq. (5.22) since T is a known quantity, calculated as in Section 6.2.

After the application to Eq. (6.44) of the Laplace transform with $s \to j\omega$, we obtain

$$\partial_r^2 \hat{u}_r + \frac{1}{r} \partial_r \hat{u}_r - \frac{1}{r^2} \hat{u}_r + k^2 \hat{u}_r = -\frac{1}{\lambda_L + 2\mu_L}(\hat{f}_r^V - \beta \partial_r \hat{T}). \qquad (6.45)$$

where $k = \omega/c_P$ is the wavenumber and $\omega = 2\pi f$ is the radial frequency, while f denotes the frequency of operation. In our numerical work, we use the FFT (Fast Fourier Transform) to compute the pertaining Fourier transforms.

Similar to the method presented in the previous chapter, we may write the total solution of Eq. (6.45) as

$$\hat{u}_r(r) = \hat{u}_r^{part}(r) + \hat{u}_r^{gen}(r), \tag{6.46}$$

where $\hat{u}_r^{part}(r)$ denotes the particular solution of Eq. (6.45) and $\hat{u}_r^{gen}(r)$ denotes the general solution of the homogeneous form of Eq. (6.45).

Particular solution $\hat{u}_r^{part}(r)$

We may construct the particular solution $\hat{u}_r^{part}(r)$ using the Green's function $\hat{G}(r, r')$ as it follows,

$$\hat{u}_r^{part}(r) = \frac{1}{\lambda_L + 2\mu_L} \int_{r'=a}^b \hat{G}(r, r') \left[\hat{f}_r^V(r') - \beta \, \partial_r \hat{T}(r') \right] r' \, dr', \tag{6.47}$$

where $\hat{G}(r, r')$ is the same function as in Section 5.2.

General solution $\hat{u}_r^{gen}(r)$

The general solution $\hat{u}_r^{gen}(r)$ of the homogeneous form of Eq. (6.45) is given by

$$\hat{u}_r^{gen}(r) = C \, J_1(kr) + D \, Y_1(kr), \tag{6.48}$$

where the coefficients C and D are obtained from the boundary conditions

$$\lim_{r \downarrow a} \hat{\tau}_{rr} = -\hat{f}_r^S(a), \tag{6.49}$$

$$\lim_{r \uparrow b} \hat{\tau}_{rr} = \hat{f}_r^S(b), \tag{6.50}$$

with $\hat{\tau}_{rr}$ from Eq. (6.41). Similar to Eq. (6.46), we write $\hat{\tau}_{rr}$ as

$$\hat{\tau}_{rr}(r) = \hat{\tau}_{rr}^{part}(r) + \hat{\tau}_{rr}^{gen}(r), \tag{6.51}$$

where

$$\hat{\tau}_{rr}^{part}(r) = (\lambda_L + 2\mu_L)\partial_r \hat{u}_r^{part} + \lambda_L r^{-1} \hat{u}_r^{part} - \beta \hat{T}, \tag{6.52}$$

and

$$\hat{\tau}_{rr}^{gen}(r) = C \, M(kr) + D \, N(kr), \tag{6.53}$$

with

$$C = \frac{N(kb)h(a) - N(ka)h(b)}{M(ka)N(kb) - N(ka)M(kb)}, \qquad (6.54)$$

$$D = \frac{-M(kb)h(a) + M(ka)h(b)}{M(ka)N(kb) - N(ka)M(kb)}, \qquad (6.55)$$

and $M(kr)$ and $N(kr)$ as defined in Eqs. (5.47) and (5.48), respectively.

Hence, the solution for $\hat{u}_r$ is obtained as

$$\hat{u}_r(r) = \hat{u}_r^{part}(r) + J_1(kr)\frac{N(kb)h(a) - N(ka)h(b)}{M(ka)N(kb) - N(ka)M(kb)}$$
$$+ Y_1(kr)\frac{-M(kb)h(a) + M(ka)h(b)}{M(ka)N(kb) - N(ka)M(kb)}. \qquad (6.56)$$

with

$$h(a) = -\hat{f}_r^S(a) - \hat{\tau}_{rr}^{part}(a), \qquad (6.57)$$

$$h(b) = \hat{f}_r^S(b) - \hat{\tau}_{rr}^{part}(b). \qquad (6.58)$$

Now, all non-zero components of the strain and stress tensor may be calculated in the frequency domain, in accordance to Eqs. (5.24) - (5.28). The results may then be transformed back to time-domain using an inverse FFT.

6.5   Numerical results for the thermoelastic field

In this section, we present some numerical results for typical electromagnetic forming systems designed for compression and for expansion of hollow circular cylindrical workpieces. First, we will present numerical results for electromagnetic compression and then one example for electromagnetic expansion.

The following types of workpieces subjected to electromagnetic compression are investigated:

- a non-magnetic ($\mu = \mu_0$) thick workpiece with an inner radius $r = a = 20$ mm and an outer radius $r = b = 22$ mm,

- a hypothetical magnetic ($\mu = 100\,\mu_0$) thick workpiece with an inner radius $r = a = 20$ mm and an outer radius $r = b = 22$ mm,

- a non-magnetic ($\mu = \mu_0$) thin workpiece with an inner radius $r = a = 20$ mm and an outer radius $r = b = 20.2$ mm.

For electromagnetic expansion, only a non-magnetic ($\mu = \mu_0$) thick workpiece with an inner radius $r = a = 20$ mm and an outer radius $r = b = 22$ mm is considered.

In all these cases the workpiece has the same thermal properties, with a specific heat $c_T = 880$ J/(kg K), a thermal conductivity $\kappa = 190$ W/(m K) and a mass density $\rho_m = 2.7 \cdot 10^3$ kg/m^3, see Appendix C.1. The Lamé coefficients of elasticity are $\lambda_L = 17 \cdot 10^{10}$ N/m^2 and $\mu_L = 8 \cdot 10^{10}$ N/m^2 and the coefficient of linear thermal expansion is $\alpha_T = 12.6 \cdot 10^{-6}$ K^{-1}.

With the known evolution of the temperature within the workpiece, calculated in Section 6.3, the evolution of the thermoelastic field has been calculated for all the considered cases, using the method described in Section 6.4.

The non-zero components of the thermoelastic field, u_r, ε_r, ε_φ, σ_r, σ_φ and σ_z are presented in the time-domain at $r = a$. Similar with the previous chapter, for the most important components, i.e. the radial displacement u_r and the tangential stress τ_φ, the space-time evolutions have been calculated. These results will be compared with the corresponding results obtained in Section 5.4.

Non-magnetic thick workpiece in compression

In Fig. 6.11, the components of the thermoelastic field at $r = a$ in a non-magnetic ($\mu = \mu_0$) thick ($b - a = 2$ mm) workpiece subjected to compression are presented.

The values of the thermoelastic field components in Fig. 6.11 may be compared with the corresponding components of the elastic field in the same configuration in Fig. 5.2, in order to see the changes induced in the elastic field by the temperature rise in the configuration.

With the chosen elastic and thermal properties of the material, we notice that the influence of temperature rise on the elastic field components (except σ_r) is rather small in the beginning of the time interval of analysis (when $t < 0.1$ ms). In this time interval the temperature rise is small, thus the effect of the temperature terms in the thermoelastic field is small. Even though the temperature effect is small, for $t < 0.1$ ms the radial displacement $u_r(a, t)$ in Fig. 6.11 is still negative, but its absolute values are smaller than the corresponding values in Fig. 5.2. The radial displacement $u_r(a, t)$ in Fig. 6.11 has larger positive values than the radial displacement $u_r(a, t)$ in Fig. 5.2, and these larger positive values are reached after a shorter time interval.

Figure 6.11: Thermoelastic field components at $r = a$ in the time do-
main for a non-magnetic ($\mu = \mu_0$) thick ($b - a = 2$ mm)
workpiece subjected to compression.

For the considered case, the temperature rise in the workpiece yields an expansion of the workpiece, expansion that is in the same order of magnitude with the compression obtained for $t < 1$ ms. The intention of electromagnetic compression is to obtain only the compression of the workpiece, but due to the temperature rise we will obtain also an undesired expansion of the workpiece.

Therefore, in this case the temperature rise may be seen as a negative consequence that affects the deformation process. This negative effect disappears, however when the workpiece cools down.

Figure 6.12:   Radial displacement u_r (a) and tangential stress σ_φ (b) in space-time domain when temperature effects are taken into account, for a non-magnetic ($\mu = \mu_0$) thick ($b - a = 2$ mm) workpiece subjected to compression.

The temperature rise affects also the values of the strains ε_r and ε_φ in the same way as the radial displacement. The values of the tangential stress σ_φ in Fig. 6.11 are smaller than the corresponding values in Fig. 5.2. Due to the temperature rise in the workpiece, the values of radial stress σ_r in Fig. 6.11 are much larger than the corresponding negligible values in Fig. 5.2.

The absolute values of the radial stress σ_r in Fig. 6.11 are only about ten times smaller than the absolute values of the tangential stress σ_φ in the same figure, thus they cannot be neglected. The longitudinal stress σ_z has negative values that are about three times smaller than the values of the tangential stress σ_φ.

The space-time evolution of the radial displacement u_r, and of the tangential stress σ_φ as the most important components of the thermoelastic field are presented in Fig. 6.12 (a) and (b), respectively.

The radial displacement u_r in Fig. 6.12 (a) sooner reaches larger positive values than the radial displacement in Fig. 5.3. The absolute values of the negative radial displacement u_r in Fig. 6.12 (a) are slightly smaller than the corresponding values in Fig. 5.3. The values of the tangential stress σ_φ are almost similar in Fig. 6.12 (b) and in Fig. 5.4.

Magnetic thick workpiece in compression

In Fig. 6.13, the components of the thermoelastic field at $r = a$ in a magnetic ($\mu = 100\,\mu_0$) thick ($b - a = 2$ mm) workpiece subjected to compression are presented. The values of the thermoelastic field components in Fig. 6.13 may be compared with the corresponding components of the elastic field in the same configuration in Fig. 5.6, in order to see the changes induced in the elastic field by the temperature rise in the configuration.

The temperature effect on the radial displacement $u_r(a, t)$ is small at any time instant, see Fig. 6.13. It is still negative, but its absolute values are slightly smaller than the corresponding values in Fig. 5.6, in absolute value.

The temperature rise affects more the values of the strains ε_r and ε_φ. When temperature effects are taken into account, ε_r reaches very quickly negative values, while in simple elastic field calculation it had only positive values during the whole time interval of observation. The same remark is valid for the radial stress σ_r. When temperature effects are taken into account, ε_φ reaches very quickly positive values, while in simple elastic field calculation it had only negative values during the whole time interval of observation. The same remark is valid for the tangential stress σ_φ and for the longitudinal stress σ_z.
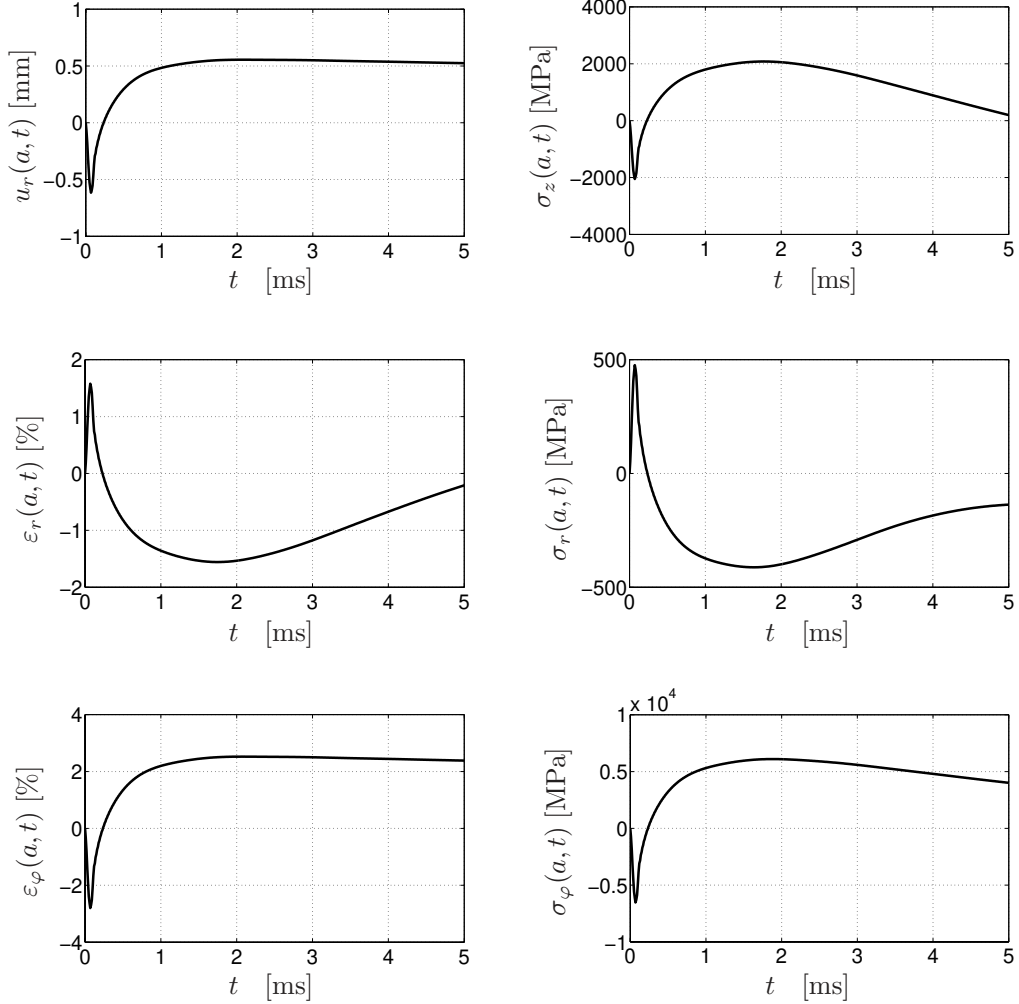
Figure 6.13: Thermoelastic field components at $r = a$ in the time domain for a magnetic ($\mu = 100\,\mu_0$) thick ($b - a = 2$ mm) workpiece subjected to compression.

The space-time evolution of the radial displacement u_r and of the tangential stress σ_φ as the most important components of the thermoelastic field are presented in Fig. 6.14 (a) and (b), respectively. The radial displacement u_r in Fig. 6.14 (a) reaches slightly larger positive values than the radial displacement in Fig. 5.7. The absolute values of the negative radial displacement u_r in Fig. 6.14 (a) are slightly smaller than the corresponding values in Fig. 5.7. The tangential stress σ_φ reaches large positive values, see Fig. 6.14 (b), while in Fig. 5.8 it had only negative values.

Figure 6.14: Radial displacement u_r (a) and tangential stress σ_φ (b) in space-time domain when temperature effects are taken into account, for a magnetic ($\mu = 100\,\mu_0$) thick ($b - a = 2$ mm) workpiece subjected to compression.

Non-magnetic thin workpiece in compression

In Fig. 6.15, the components of the thermoelastic field at $r = a$ for a non-magnetic ($\mu = 100\,\mu_0$) thin ($b - a = 0.2$ mm) workpiece subjected to compression are presented.

The values of the thermoelastic field components in Fig. 6.15 may be compared with the corresponding components of the elastic field in the same configuration in Fig. 5.10, in order to see the changes induced in the elastic field by the temperature rise in the configuration.
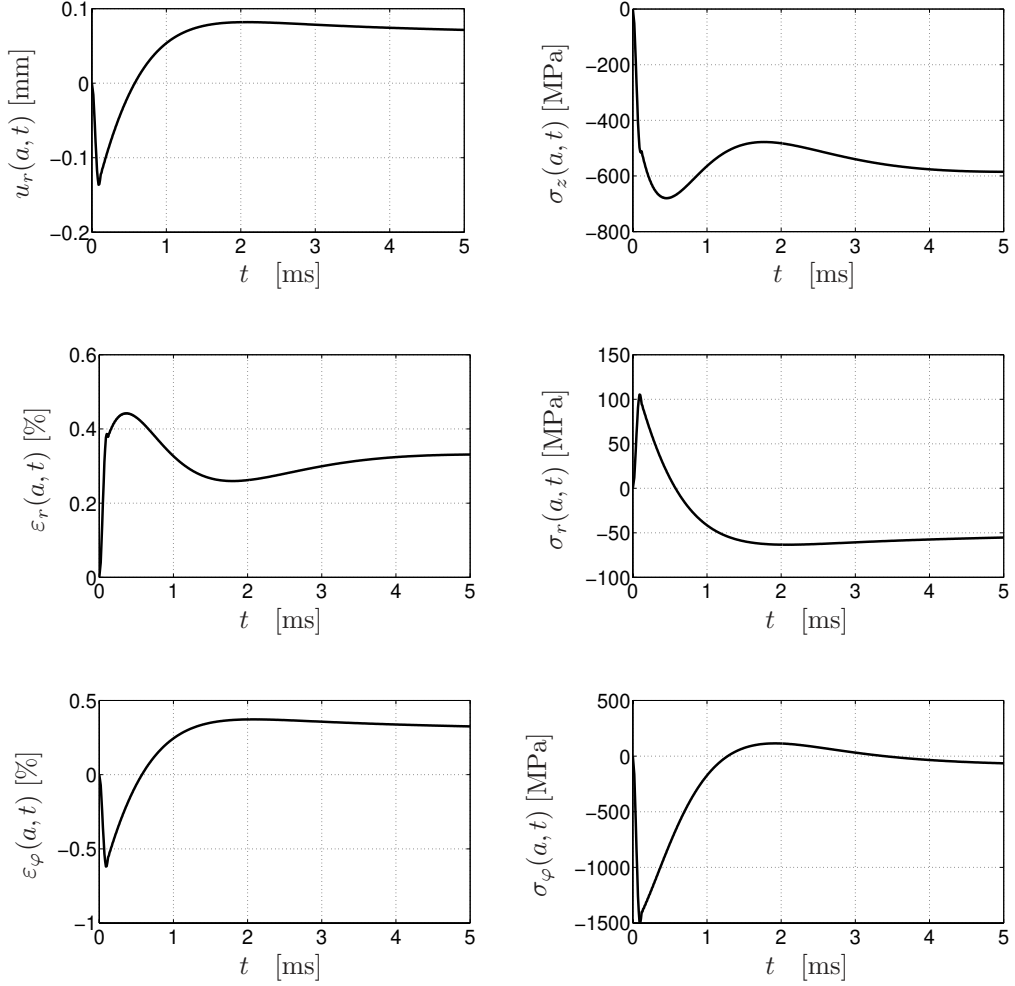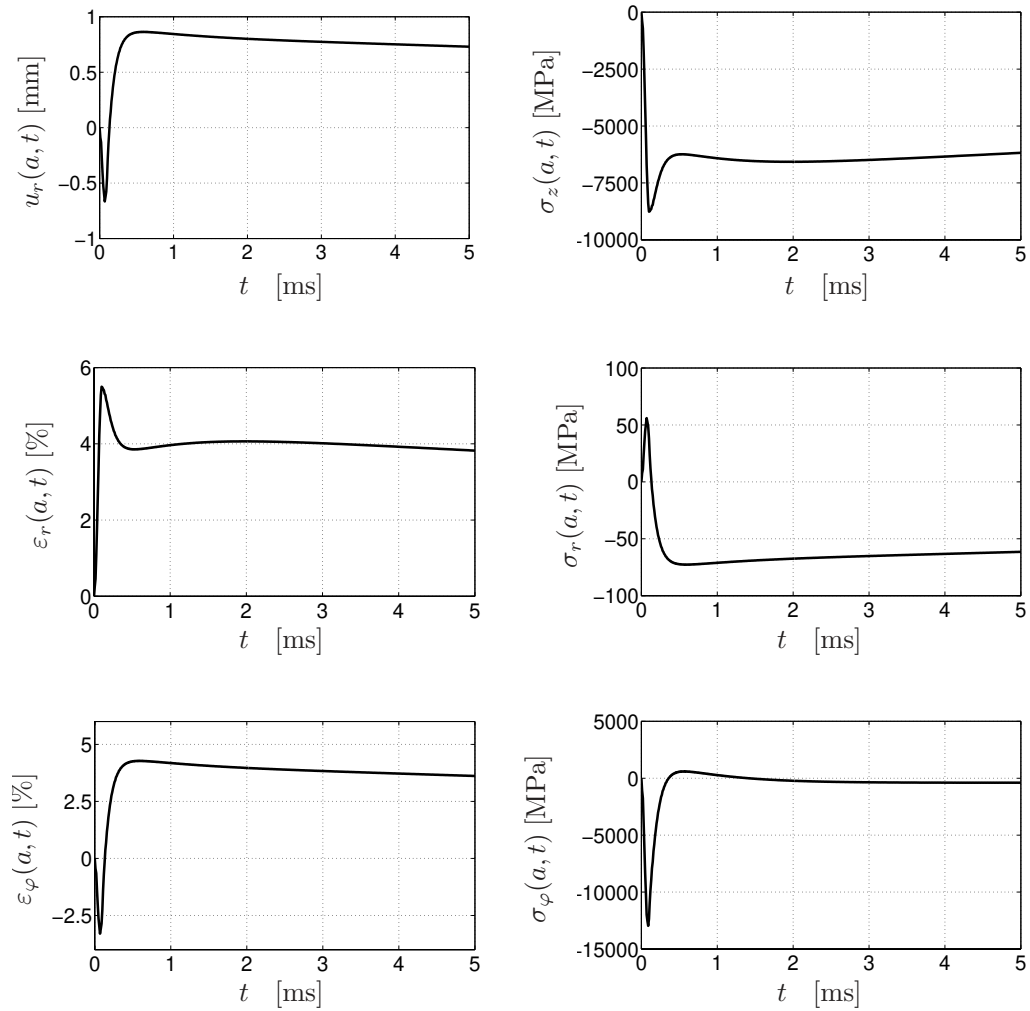

Figure 6.15: Thermoelastic field components at $r = a$ in the time domain for a non-magnetic ($\mu = 100\,\mu_0$) thin ($b - a = 0.2$ mm) workpiece subjected to compression.
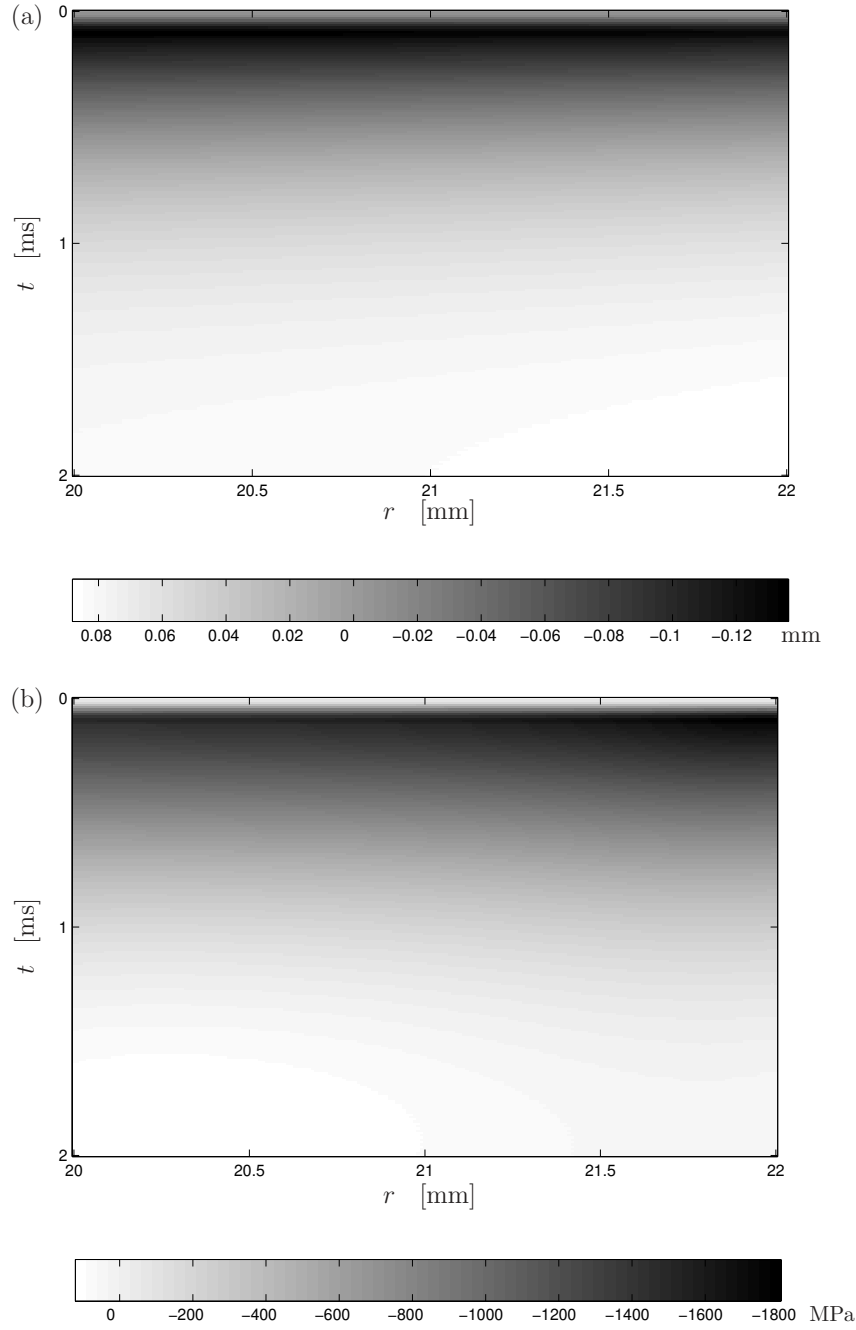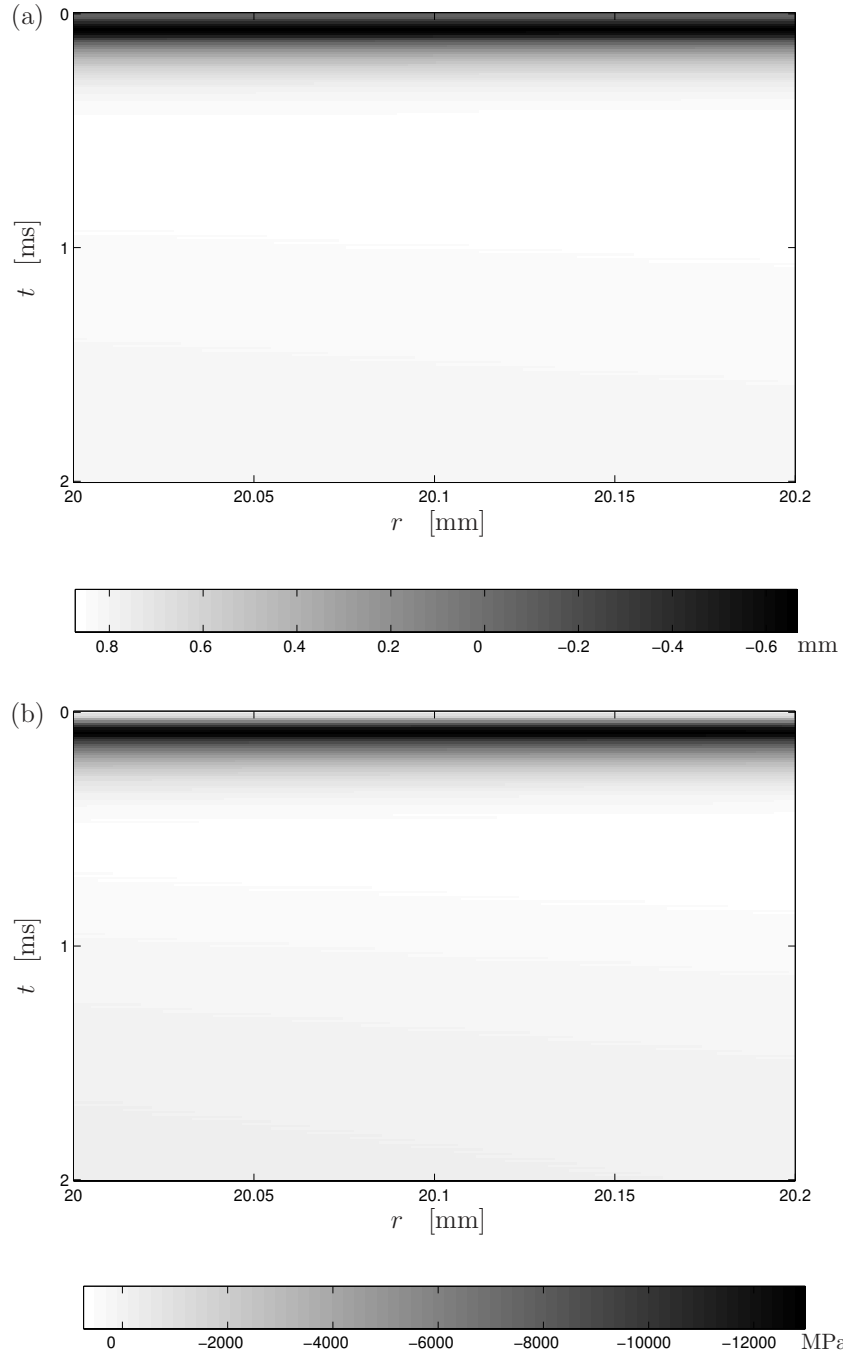
Figure 6.16:   Radial displacement u_r (a) and tangential stress σ_φ (b) in the space-time domain when temperature effects are taken into account, for a non-magnetic ($\mu = \mu_0$) thin ($b - a = 0.2$ mm) workpiece subjected to compression.

With the chosen elastic and thermal properties of the material, we notice that the influence of temperature rise on the elastic field components is large, because in the thin non-magnetic workpiece the temperature increases rapidly. The radial displacement has negative values for a very small interval of time and in absolute value they are about half of the corresponding values in Fig. 5.10. The values of the positive radial displacement in Fig. 6.15 are about two times larger than the values of the negative displacement in the same figure, while in Fig. 5.10 the positive radial displacement stays very small.

It means that the undesired expansion due to the temperature rise is much larger than the desired compression of the workpiece, thus again the temperature rise has negative consequences for the electromagnetic compression. The radial displacement is small, but its maximum positive values are about 10 times larger than the maximum positive values of the radial displacement for the thick non-magnetic workpiece.

The temperature rise affects also the values of the strains ε_r and ε_φ in the same way as the radial displacement. The values of the tangential stress σ_φ in Fig. 6.15 are almost similar to the corresponding values in Fig. 5.10. Due to the temperature rise in the workpiece, the radial stress σ_r in Fig. 6.15 are much larger than the corresponding negligible values in Fig. 5.10.

The space-time evolution of the radial displacement u_r, and of the tangential stress σ_φ are presented in Fig. 6.16 (a) and (b), respectively.

The radial displacement u_r in Fig. 6.16 (a) sooner reaches larger positive values than the radial displacement in Fig. 5.11. The absolute values of the negative radial displacement u_r in Fig. 6.12 (a) are about two times smaller than the corresponding values in Fig. 5.11, while the values of the tangential stress σ_φ are almost similar in Fig. 6.16 (b) and in Fig. 5.12.

Non-magnetic thick workpiece in expansion

In Fig. 6.11, the components of the thermoelastic field at $r = a$ in a non-magnetic ($\mu = \mu_0$) thick ($b - a = 2$ mm) workpiece subjected to expansion are presented.

The values of the thermoelastic field components in Fig. 6.17 may be compared with the corresponding components of the elastic field in the same configuration in Fig. 5.14, in order to see the changes induced in the elastic field by the temperature rise in the configuration.

With the chosen elastic and thermal properties of the material, we notice
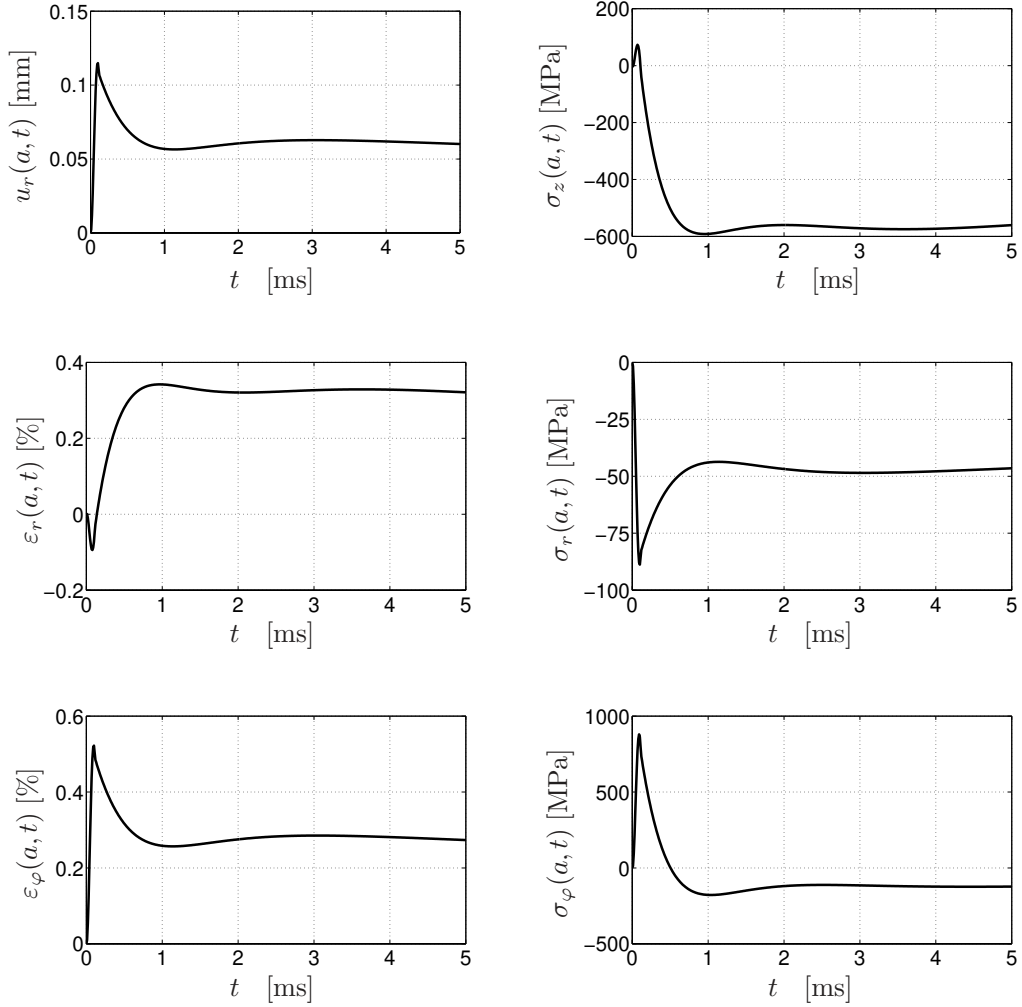
Figure 6.17:   Thermoelastic field components at $r = a$ in the time do-
main for a non-magnetic ($\mu = \mu_0$) thick ($b - a = 2$ mm)
workpiece subjected to expansion.

that the influence of temperature rise on the elastic field components is rather
small in the beginning of the time interval of analysis (when $t < 1$ ms). In
this time interval ($t < 1$ ms) the temperature rise is small, thus the effect of
the temperature terms in the thermoelastic field is small. Even though the
temperature effect is small, for $t < 1$ ms the radial displacement $u_r(a, t)$ in
Fig. 6.17 is positive and its values are slightly larger than the corresponding
values in Fig. 5.14.
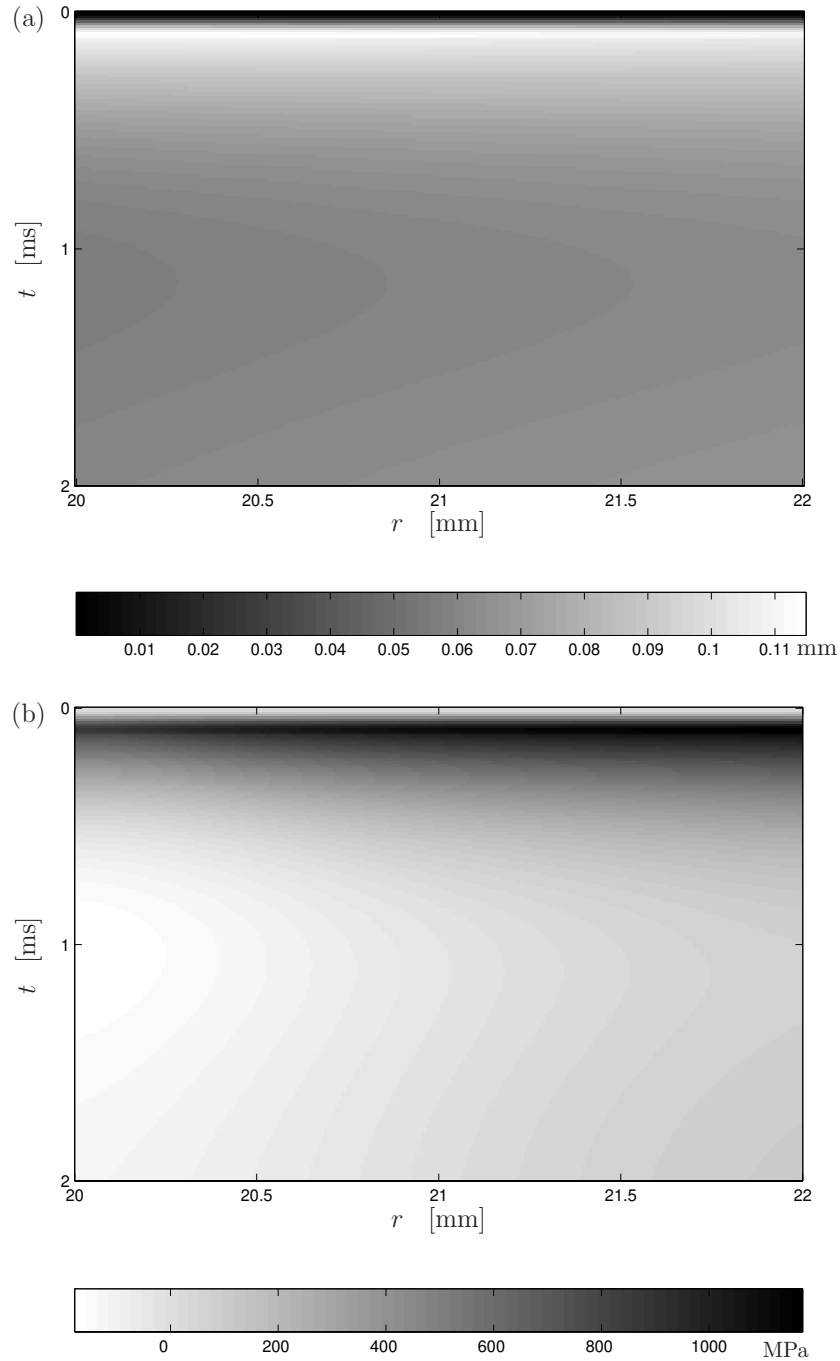
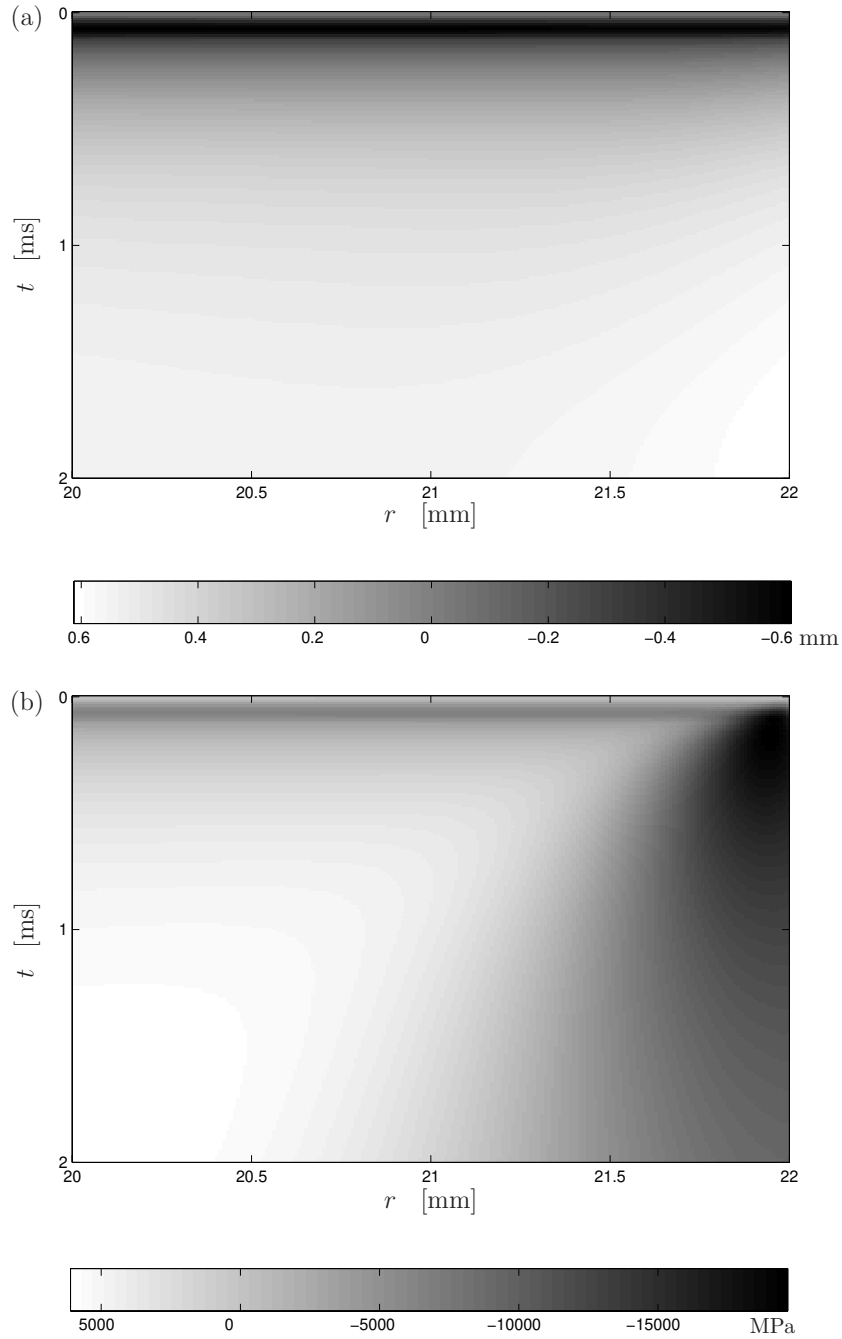Figure 6.18: Radial displacement u_r (a) and tangential stress σ_φ (b) in space-time domain when temperature effects are taken into account, for a non-magnetic ($\mu = \mu_0$) thick ($b - a = 2$ mm) workpiece subjected to expansion.

For the considered case, the temperature rise in the workpiece yields an supplementary expansion of the workpiece. Therefore, in this case the temperature rise may be seen as a positive consequence of the deformation process, even though it will disappear when the workpiece cools down.

The temperature rise affects more the values of the strains ε_r and ε_φ. When temperature effects are taken into account, ε_r reaches very quickly positive values, while in simple elastic field calculation it had only negative values during the whole time interval of observation.

The space-time evolution of the radial displacement u_r, and of the tangential stress σ_φ, as the most important components of the thermoelastic field are presented in Fig. 6.18 (a) and (b), respectively. The radial displacement u_r in Fig. 6.18 (a) reaches larger values than the radial displacement in Fig. 5.15. The values of the tangential stress σ_φ are almost similar in Fig. 6.18 (b) and in Fig. 5.16.

6.6   Conclusions

The temperature distribution in the circular cylindrical workpiece used in electromagnetic compression and electromagnetic compression has been determined, assuming an insulated workpiece. The temperature rise is due to the dissipation of electromagnetic energy, dissipation that is in fact the volume density of the Joule losses.

The solution of the equation of heat flow has been found as the sum of the general solution of the homogeneous equation of heat flow and the particular solution of the inhomogeneous equation of heat flow. The particular solution has been calculated using a source type of integral representation.

Then, the mean temperature of the workpiece has been calculated as the average over the thickness of the workpiece of the temperature distribution previously calculated. Alternatively, results for the mean temperature have been obtained. The numerical results have shown, however, that this simple formula is not useful since it leads to results that differ too much from the previously calculated results. This shows that it is necessary to base numerical temperature calculations on our exact theory.

The effects of the temperature rise on the components of the elastic field in our configuration also have been investigated. For the considered cases, the temperature rise has negative consequences for the electromagnetic compression, because in all cases a significant undesired expansion of the workpiece is

obtained, while in electromagnetic expansion the temperature rise has positive consequences because in all cases a supplementary expansion of the workpiece is obtained. However, both effects disappear when the workpiece cools down. Of course here a crude assumption is made, due to the fact that the temperature exchange with the forming coil and with the environment has been neglected.

When electromagnetic expansion of the workpiece is the aim of the process, the temperature rise may have positive consequences for the whole process, since an additional expansion due to the temperature rise is obtained during deformation process. Of course, we speak only about the elastic behavior of the material, with a linear stress-strain dependence. Some other possible effects of the temperature rise will be presented in Chapter 9.

Chapter 7

Elastoplastic description of the problem

This chapter presents the calculation of the plastic deformations in a cylindrical workpiece subjected to electromagnetic compression and to electromagnetic expansion, as presented in Chapter 3. The configuration considered is the same as the one in Chapter 5, and is excited by the electromagnetic force density calculated in Chapter 4. The elastoplastic behavior of the workpiece is described for the plane strain case using different models. Subsequently, the corresponding numerical results are given, both for compression and for expansion.

7.1   Configuration of the elastoplastic problem

The configuration in which the elastoplastic problem is to be solved models the case of electromagnetic compression and it is presented in Fig. 7.1. The position in the configuration is specified by the coordinates $\{r, \varphi, z\}$ with respect to the reference frame with the origin $\mathcal{O}$ and the three mutually perpendicular vectors $\{\boldsymbol{i}_r, \boldsymbol{i}_\varphi, \boldsymbol{i}_z\}$ of unit length each. In the indicated order, the base vectors form a right-handed system.

From Chapter 2 we see that the source that excites the elastoplastic field is the electromagnetic volume force density $\boldsymbol{f}_V^{ext} = \boldsymbol{f}^V = f_r^V \boldsymbol{i}_r + f_\varphi^V \boldsymbol{i}_\varphi + f_z^V \boldsymbol{i}_z$, together with the electromagnetic surface force density $\boldsymbol{f}_S^{ext} = \boldsymbol{f}^S = f_r^S \boldsymbol{i}_r + f_\varphi^S \boldsymbol{i}_\varphi + f_z^S \boldsymbol{i}_z$. As shown in Chapter 2, only the radial components of these force densities are non-zero, i.e. only $f_r^V \neq 0$ and $f_r^S \neq 0$. Their values are known
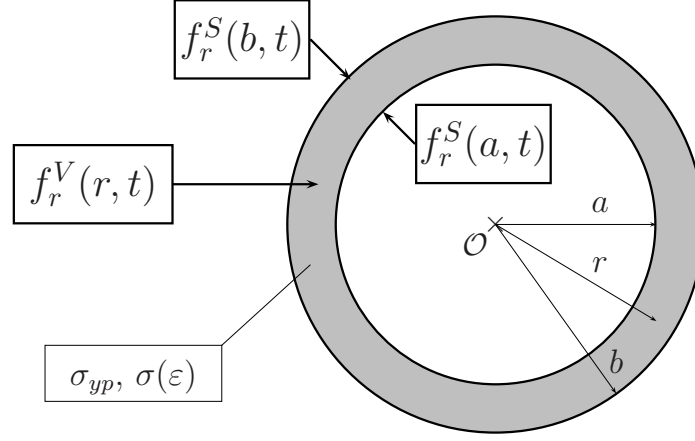
Figure 7.1:   Cross section of the cylindrical configuration for the calcu-
             lation of the elastoplastic field that has as its source the
             known electromagnetic force densities.

for the whole configuration and in the whole time interval of calculation.

In order to adapt to the notation widely used in the theory of quasistatic
elastic field, we will denote further by $\sigma_r = \tau_{rr}$, $\sigma_\varphi = \tau_{\varphi\varphi}$, $\sigma_z = \tau_{zz}$ as the nor-
mal stresses and the remaining components of the stress tensor as the shearing
stresses. Similarly, $\varepsilon_r = e_{rr}$, $\varepsilon_\varphi = e_{\varphi\varphi}$, $\varepsilon_z = e_{zz}$ are the normal strains and the
remaining components of the strain tensor as the shearing strains.

7.2   Models of the elastoplastic behavior

7.2.1   Introduction

From the quasistatic point of view, the constitutive stress-strain relations for
a certain material are described empirically using a simple *static stress-strain
diagram*. This diagram is obtained in a typical static tension test, where a
bar made of a solid material is subjected to quasi-static tensile straining, see
Fig. 7.2. When the tension tests are performed in a dynamic way, the nonlinear
stress-strain relation becomes more complex and involves the strain rate (or
deformation velocity) in a particular way.

Based on a typical static tensile test, an empirical stress-strain diagram
may be constructed. In fact, two different definitions of the stress can be
employed, resulting in two stress-strain curves for the same material. The two
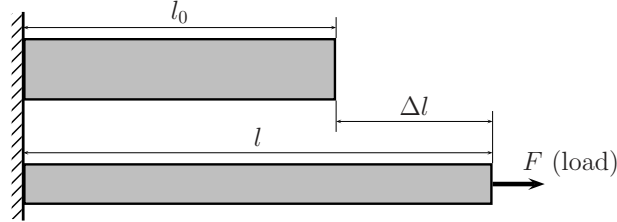
Figure 7.2: Simple tension test of a bar made of solid material.
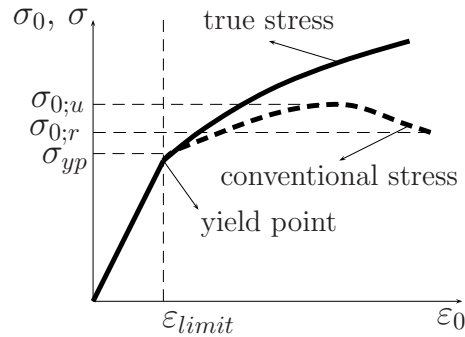
Figure 7.3: Typical static stress-strain diagram for a ductile material.

types of stress that are used are: the conventional (engineering) stress and the true stress. *The conventional normal stress σ_0 is defined as the ratio between load F and initial area of the transversal cross-section A_0 of the bar*, while *the true normal stress σ is defined as the ratio between load F and actual area A of the transversal cross-section of the bar*.

When constructed for a ductile material (a material that is capable of an appreciable amount of yielding or permanent plastic deformation before fracture), a typical static stress-strain diagram looks as in Fig. 7.3. In this diagram, for both types of stress, two regions are distinguished, namely *the elastic region* with a linear relation between stress and strain, and *the plastic region* with a non-linear relation between stress and strain. At the border between the two regions we find the yield point characterized by the yield stress σ_{yp}. After this point, larger deformations occur while the applied load F remains almost constant. The conventional stress shows a maximum called the ultimate tensile stress $\sigma_{0;u}$ and a lower value, called the rupture stress $\sigma_{0;r}$, where failure by rupture occurs.

In the elastic region, the conventional stress and the true stress are almost equal. In the plastic region, the conventional strain defined as the ratio between

elongation $\Delta l = l - l_0$ and initial length of the sample l_0,

$$\varepsilon_0 = \frac{1}{l_0} \int_{l_0}^{l} \mathrm{d}l = \frac{l - l_0}{l_0}, \tag{7.1}$$

is inadequate, see [184], and it is better to use the true strain ε that is defined as

$$\varepsilon = \int_{l_0}^{l} \frac{\mathrm{d}l}{l} = \ln(l/l_0) = \ln(1 + \varepsilon_0). \tag{7.2}$$

With the hypothesis of incompressibility of matter (constant volume), in the plastic region the relation between the true stress and conventional stress can be found as

$$\sigma = \sigma_0(1 + \varepsilon_0). \tag{7.3}$$

Most metals (including the ones used in electromagnetic forming) show a ductile behavior as in Fig. 7.3. The perfectly elastic behavior, i.e. the elastic region in Fig. 7.3, has been analyzed in detail in Chapters 5 and 6.

In the present chapter we will focus on the inelastic (plastic) behavior of materials characterized by a non-linear relation $\sigma = \sigma(\varepsilon)$. In the plastic region, the total deformation (total strain) of the material can be seen as the sum of the elastic and plastic deformation (elastic and plastic strain). It means that after a cycle of loading-unloading of the structure, the elastic deformation is recovered and the work done by stresses for the elastic deformation is zero, while the plastic deformation remains and the total work done by stresses results in the plastic (permanent) deformation.

7.2.2   Yield stress

Since in the elastic region and in the plastic region of an empirical stress-strain diagram different stress-strain relations apply, it is of great interest to determine the boundary between these two regions, i.e. the yield stress σ_{yp}. For a ductile material, as most of the metals are, three empirical theories for the calculation of the yield stress σ_{yp} exists, namely the theory of maximum shearing stress, the theory of maximum distortion energy and the theory of maximum octahedral stress, see [85, 75, 184]. All these theories are using the principal stresses in the material. For our circular cylindrical configuration with infinite length, the principal stresses are in fact the normal stresses σ_r, σ_φ and σ_z. The relation $|\sigma_\varphi| > |\sigma_z| > |\sigma_r|$ between the principal stresses is valid in our case.

1. The theory of maximum shearing stress

This theory is also called *the Tresca yield criterion* and it predicts that plastic deformation (yielding) starts when the maximum shearing stress σ_{max} in the material equals the maximum shearing stress $\sigma_{sh;yp} = 1/2\,\sigma_{yp}$ obtained from a simple tension test. In our case, the maximum shearing stress is calculated as

$$\sigma_{max} = \frac{1}{2}|\sigma_\varphi - \sigma_r| = \frac{1}{2}\sigma_{yp}. \tag{7.4}$$

2. The theory of maximum distortion energy

This theory is also called *the von Mises theory*, see [85, 75, 184] and it predicts that plastic deformation (yielding) occurs when, at any point in the body, the distortion energy per unit volume in a state of combined stress becomes equal to that associated with yielding in a simple tension test. This criterion has the following mathematical expression

$$(\sigma_r - \sigma_\varphi)^2 + (\sigma_\varphi - \sigma_z)^2 + (\sigma_z - \sigma_r)^2 = 2\,\sigma_{yp}^2. \tag{7.5}$$

3. The theory of octahedral shearing stress

This theory, see [184], is also called *the von Mises-Henky criterion* and it predicts that yielding occurs when the octahedral stress at a point achieves a particular value. With the octahedral stress defined as

$$\sigma_{oct} = \frac{1}{3}[(\sigma_r - \sigma_\varphi)^2 + (\sigma_\varphi - \sigma_z)^2 + (\sigma_z - \sigma_r)^2 + 6\,(\tau_{r\varphi}^2 + \tau_{\varphi z}^2 + \tau_{zr}^2)]^{1/2}, \tag{7.6}$$

the mathematical expression of this criterion is

$$\sigma_{oct} = \frac{\sqrt{2}}{3}\,\sigma_{yp}. \tag{7.7}$$

In our case, $\tau_{r\varphi} = \tau_{\varphi z} = \tau_{zr} = 0$ and the criterion described by Eq. (7.7) is similar to the one in Eq. (7.5). We see also that $\sqrt{2}/3$ in Eq.(7.7) is almost equal to $1/2$ in Eq. (7.4), thus the three strength theories are equivalent for our case.

7.2.3 Static elastoplastic behavior

As mentioned previously, the stress-strain diagram, which is obtained by experiments, gives information about the elastoplastic behavior of the tested

material. When the elastic deformations are neglected, the static stress-strain relation in ductile materials may be described in general as

$$\sigma_{stat}(\varepsilon) = K\varepsilon^n, \tag{7.8}$$

where K is the strength coefficient (e.g. $K = \sigma_{yp}$ for $n = 0$) and n is the strain-hardening index with values $0 \leq n < 1$. We notice that, with $K = E$ and $n = 1$, Eq. (7.8) becomes Hooke's law, valid in an elastic material.

In elastoplastic materials, the hypothesis of incompressibility of materials is valid. Based on this hypothesis an *effective stress* σ_{eff} and an *effective strain* ε_{eff} can be defined for each material. In our configuration, the effective stress is defined as

$$\sigma_{eff} = \frac{1}{\sqrt{2}} \left[(\sigma_r - \sigma_\varphi)^2 + (\sigma_\varphi - \sigma_z)^2 + (\sigma_z - \sigma_r)^2 \right]^{1/2}, \tag{7.9}$$

while the effective strain is defined as

$$\varepsilon_{eff} = \sqrt{\frac{2}{3}} \left[\varepsilon_r^2 + \varepsilon_\varphi^2 + \varepsilon_z^2 \right]^{1/2}. \tag{7.10}$$

The effective stress and the effective strain are always positive values. Based on these definitions, Eq. (7.8) may be extended on empirical basis to

$$\sigma_{stat}(\varepsilon_{eff}) = K\varepsilon_{eff}^n. \tag{7.11}$$

In Fig. 7.4 the typical static stress-strain diagrams for three types of elastoplastic materials are presented. In elastoplastic materials, the total strain in the plastic region is considered to be the sum of the elastic strain and the plastic strain

$$\varepsilon = \varepsilon^{(e)} + \varepsilon^{(p)}. \tag{7.12}$$

Here, because of a better match we choose to describe the elastoplastic behavior of materials as

$$\sigma_{stat}(\varepsilon) = \begin{cases} \varepsilon E, & \text{for } \varepsilon \leq \varepsilon_{limit} \;-\; \text{elastic range,} \\ A\,(B + \varepsilon)^\alpha, & \text{for } \varepsilon > \varepsilon_{limit} \;-\; \text{plastic range,} \end{cases} \tag{7.13}$$

where $\sigma_{yp} = \varepsilon_{limit}E$.

Thus, we choose to describe the static elastoplastic behavior of materials in Fig. 7.4 as

(a) perfectly plastic   (b) linear hardening   (c) exponential hardening
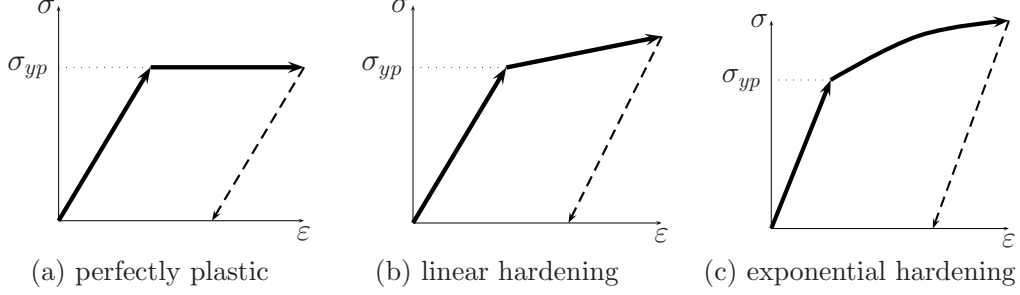
Figure 7.4: Typical stress-strain diagrams for elastoplastic materials.

- an elastic-perfectly plastic material (a) with

$$
\sigma_{stat}(\varepsilon) = \begin{cases} \varepsilon E, & \text{for } \varepsilon \leq \varepsilon_{limit} \; - \; \text{elastic range,} \\ \sigma_{yp}, & \text{for } \varepsilon > \varepsilon_{limit} \; - \; \text{plastic range,} \end{cases}
\tag{7.14}
$$

- an elastoplastic material with linear hardening (b) with

$$
\sigma_{stat}(\varepsilon) = \begin{cases} \varepsilon E, & \text{for } \varepsilon \leq \varepsilon_{limit} \; - \; \text{elastic range,} \\ \sigma_{yp} + A \, (B + \varepsilon), & \text{for } \varepsilon > \varepsilon_{limit} \; - \; \text{plastic range,} \end{cases}
\tag{7.15}
$$

- an elastoplastic material with exponential hardening (c) where

$$
\sigma_{stat}(\varepsilon) = \begin{cases} \varepsilon E, & \text{for } \varepsilon \leq \varepsilon_{limit} \; - \; \text{elastic range,} \\ \sigma_{yp} + A \, (B + \varepsilon)^{\alpha}, & \text{for } \varepsilon > \varepsilon_{limit} \; - \; \text{plastic range.} \end{cases}
\tag{7.16}
$$

If the structure is unloaded (dashed line in Fig. 7.4), the remaining strain is the plastic strain because the elastic strain is recovered. The elastic strain is very small and it may be neglected in further calculations. Thus, for the simplicity of notation, we may assume that in the plastic range $\varepsilon = \varepsilon^{(p)}$.

For the sake of simplicity, the pure plastic stresses and strains are going to be investigated first and then the elastoplastic stresses and strains.

7.2.4 Dynamic elastoplastic behavior

In general, we may write the complete stress-strain relation as

$$
\sigma = \sigma_{stat}(\varepsilon) + \sigma_{dyn}(\dot{\varepsilon}),
\tag{7.17}
$$

or

$$\sigma = \sigma_{stat}(\varepsilon) \cdot \sigma_{dyn}(\dot{\varepsilon}), \tag{7.18}$$

where $\sigma_{stat}(\varepsilon)$ is the static stress-strain relation and $\sigma_{dyn}(\dot{\varepsilon})$ is the dynamic stress-strain relation. Here, we will consider the additive form of the general stress-strain relation in Eq. (7.17).

For the dynamic behavior of the material, we choose on empirical grounds

$$\sigma_{dyn}(\dot{\varepsilon}) = \beta(\dot{\varepsilon})^{\gamma}, \qquad \text{for } \dot{\varepsilon} > 0. \tag{7.19}$$

7.3 Equations in the plastic region and boundary conditions

With the notations used in the theory of the quasi-static elastic field and taking into account the assumption of an infinitely long configuration with rotational symmetry, the relevant equation of motion to be solved is

$$\partial_r \sigma_r + \frac{1}{r}(\sigma_r - \sigma_\varphi) - \rho_m \partial_t^2 u_r = -f_r^V. \tag{7.20}$$

There exists no radial stress within the air, so the boundary conditions to be applied at $r = a$ and $r = b$, are

$$\lim_{r \downarrow a} \sigma_r(r,t) = -f_r^S(a,t), \qquad \lim_{r \uparrow b} \sigma_r(r,t) = f_r^S(b,t), \tag{7.21}$$

The normal components of the strain, see [184] and Eqs. (5.4) - (5.6), are

$$\varepsilon_r = \frac{1}{E_s}[\sigma_r - \frac{1}{2}(\sigma_\varphi + \sigma_z)] = \partial_r u_r, \tag{7.22}$$

$$\varepsilon_\varphi = \frac{1}{E_s}[\sigma_\varphi - \frac{1}{2}(\sigma_z + \sigma_r)] = r^{-1} u_r, \tag{7.23}$$

$$\varepsilon_z = \frac{1}{E_s}[\sigma_z - \frac{1}{2}(\sigma_r + \sigma_\varphi)] = 0, \tag{7.24}$$

where E_s is the modulus of plasticity (secant modulus), defined as

$$E_s = \frac{\sigma_{eff}}{\varepsilon_{eff}}. \tag{7.25}$$

(a) perfectly plastic   (b) linear hardening   (c) exponential hardening
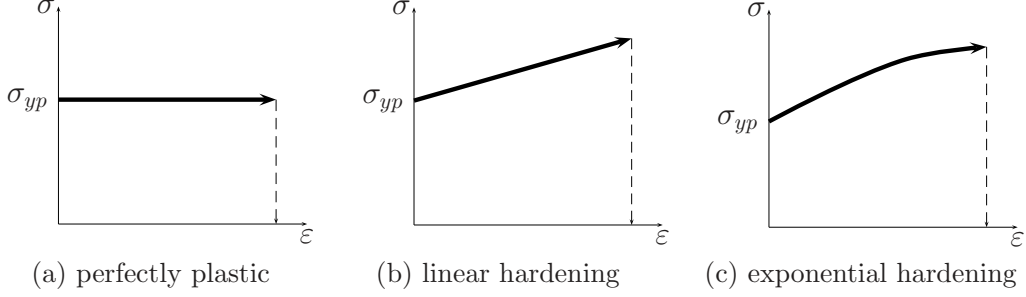
Figure 7.5: Typical stress-strain diagrams for inelastic materials.

All shear strains and shear stresses are zero for our configuration. The above equations are called the Henky's plastic stress-strain relations and follow from the total strain theory.

It has been shown that, in the plastic region, the hypothesis of incompressibility of matter holds for all materials, see [189]

$$\varepsilon_r + \varepsilon_\varphi + \varepsilon_z = 0, \tag{7.26}$$

and further

$$\partial_t \varepsilon_r + \partial_t \varepsilon_\varphi + \partial_t \varepsilon_z = 0. \tag{7.27}$$

The application of this condition to Eqs. (7.22) - (7.23) gives

$$\varepsilon_r = \frac{3}{4E_s}[\sigma_r - \sigma_\varphi], \tag{7.28}$$

$$\varepsilon_\varphi = \frac{3}{4E_s}[\sigma_\varphi - \sigma_r] = -\varepsilon_r. \tag{7.29}$$

Using these relations, the effective stress and effective strain are

$$\sigma_{\mathit{eff}} = \frac{\sqrt{3}}{2}|\sigma_\varphi - \sigma_r|, \tag{7.30}$$

$$\varepsilon_{\mathit{eff}} = \frac{2}{\sqrt{3}}|\varepsilon_\varphi| = \frac{2}{\sqrt{3}}|\varepsilon_r|. \tag{7.31}$$

In Fig. 7.5, three types of inelastic plastic materials are presented, corresponding to the elastoplastic ones described in Section 7.2.

In the next subsections we will solve Eq. (7.20) subjected to the boundary conditions in Eq. (7.21) for the case of a perfectly plastic material. Further, in Chapter 8 a more complex elastoplastic behaviour of the material will be considered.

For a perfectly plastic material we have $\sigma_{eff} = \sigma_{yp}$ at all instants of time and for the whole range of strains. For electromagnetic compression, we have $\sigma_r < 0, \sigma_\varphi < 0$ and $|\sigma_r| < |\sigma_\varphi|$. In this case Eq. (7.20) may be written as

$$\partial_r \sigma_r + \frac{1}{r} \left(\frac{2}{\sqrt{3}} \sigma_{eff} \right) - \rho_m \partial_t^2 u_r = -f_r^V. \tag{7.32}$$

For electromagnetic expansion, we have $\sigma_r > 0, \sigma_\varphi > 0$ and $|\sigma_r| < |\sigma_\varphi|$. In this case Eq. (7.20) may be written as

$$\partial_r \sigma_r - \frac{1}{r} \left(\frac{2}{\sqrt{3}} \sigma_{eff} \right) - \rho_m \partial_t^2 u_r = -f_r^V. \tag{7.33}$$

7.3.1 Dynamic equations in the plastic region

In electromagnetic forming, the deformation will take place with high velocity, thus the inertia term $\rho_m \partial_t^2 u_r$, that has been neglected in the quasi-static equation, has to be taken into account. Its value should be significant as compared with other terms in the equation of motion. We have then to solve Eq. (7.20), rewritten as

$$\partial_r \sigma_r + \frac{1}{r} \frac{2}{\sqrt{3}} \sigma_{eff} - \rho_m \partial_t v_r = -f_r^V, \tag{7.34}$$

where

$$v_r = \partial_t u_r = \partial_t r. \tag{7.35}$$

Within the assumptions of small deformations, the following relations are valid

$$\partial_t \varepsilon_r = \partial_r v_r, \tag{7.36}$$

$$\partial_t \varepsilon_\varphi = r^{-1} v_r. \tag{7.37}$$

When substituting these expressions in Eq. (7.27) we get

$$\partial_r v_r + \frac{1}{r} v_r = 0, \tag{7.38}$$

with the solution

$$v_r(r, t) = C(t) \frac{1}{r}. \tag{7.39}$$

It means that for each point inside the workpiece we have $r\, v_r(r,t) = C(t)$, thus also at $r = a$ and $r = b$. Then we have

$$r v_r(r, t) = a(t) v_r(a, t) = b(t) v_r(b, t) = r_i v_r(r_i, t), \tag{7.40}$$

where r_i is any point inside the workpiece, thus $r_i \in [a, b]$. It means that when the motion of a certain point of the workpiece is known, the motion of all the other points can easily be calculated from Eq. (7.40). Here, we choose to calculate first the motion of the inner radius $r = a$ of the workpiece, thus from Eq. (7.40) we have

$$v_r(r, t) = \frac{a(t)}{r} \, v_r(a, t), \tag{7.41}$$

where $r = r(t)$. We differentiate this equation with respect to time and we get

$$\partial_t v_r(r, t) = \frac{1}{r} v_r^2(a, t) + \frac{a(t)}{r} \partial_t v_r(a, t) - \frac{a^2(t)}{r^3} v_r^2(a, t). \tag{7.42}$$

The solution of Eq. (7.34) can be written as

$$\sigma_r = D(t) + \rho_m \int_a^r \partial_t v_r \, \mathrm{d}r - \frac{2}{\sqrt{3}} \int_a^r \frac{1}{r} \sigma_{\mathit{eff}} \, \mathrm{d}r - \int_a^r f_r^V \, \mathrm{d}r. \tag{7.43}$$

On this expression we apply the boundary condition at $r = a$ in Eq. (7.21) and we get

$$D(t) = -f_r^S(a, t). \tag{7.44}$$

Thus, Eq. (7.43) becomes

$$\sigma_r(r, t) = -f_r^S(a, t) + \rho_m \int_a^r \partial_t v_r \, \mathrm{d}r - \frac{2}{\sqrt{3}} \int_a^r \frac{1}{r} \sigma_{\mathit{eff}} \, \mathrm{d}r - \int_a^r f_r^V \, \mathrm{d}r. \tag{7.45}$$

On this equation we apply the boundary condition at $r = b$ in Eq. (7.21) and we get

$$f_r^S(b, t) = -f_r^S(a, t) + \rho_m \int_a^b \partial_t v_r \, \mathrm{d}r - \frac{2}{\sqrt{3}} \int_a^b \frac{1}{r} \sigma_{\mathit{eff}} \, \mathrm{d}r - \int_a^b f_r^V \, \mathrm{d}r. \tag{7.46}$$

When rearranging the terms of Eq. (7.46) and using Eq. (7.42), we finally end with the following differential equation in $v_r(a, t)$

$$\partial_t v_r(a, t) + v_r^2(a, t) \left[\frac{1}{a(t)} + \frac{a^2(t) - b^2(t)}{2a(t)b^2(t) \ln[b(t)/a(t)]} \right] =$$

$$= \frac{1}{\rho_m \, a(t) \ln[b(t)/a(t)]} \left[f_r^S(b, t) + f_r^S(a, t) + \int_a^b f_r^V \, \mathrm{d}r + \frac{2}{\sqrt{3}} \int_a^b \sigma_{\mathit{eff}} \frac{1}{r} \, \mathrm{d}r \right]. \tag{7.47}$$

This equation is a differential equation that can be solved numerically when its right-hand side is known. For our case of a perfectly plastic material $\sigma_{eff} = \sigma_{yp}$ at all time instants and Eq. (7.47) becomes

$$\partial_t v_r(a,t) + v_r^2(a,t) \left[\frac{1}{a(t)} + \frac{a^2(t) - b^2(t)}{2a(t)b^2(t) \ln[b(t)/a(t)]} \right] =$$

$$= \frac{1}{\rho_m \, a(t) \ln[b(t)/a(t)]} \left[f_r^S(b,t) + f_r^S(a,t) + \int_a^b f_r^V \, dr + \frac{2}{\sqrt{3}} \sigma_{eff} \ln[b(t)/a(t)] \right].$$
(7.48)

In a real electromagnetic forming process, the boundaries $r = a$ and $r = b$ of the workpiece move during the process, i.e. $a = a(t)$ and $b = b(t)$, and Eq. (7.48) can be numerically solved only if boundaries of the workpiece $r = a(t)$ and $r = b(t)$, and the corresponding values of $f_r^V(r,t)$, $f_r^S(a,t)$ and $f_r^S(b,t)$ are known at each instant of time. We have solved Eq. (7.48) in the assumption that the term $\int_a^b f_r^V(r,t) \, dr$ is calculated using the initial boundaries of the workpiece $r = a(t = 0)$ and $r = b(t = 0)$, and the corresponding values of $f_r^V(r,t)$, $f_r^S(a,t)$ and $f_r^S(b,t)$ are the ones calculated in Chapter 4. It means that the radial velocity $v_r(a,t)$ can be calculated at each instant of time from Eq. (7.48). After the substitution of its values in Eq. (7.41), the radial velocity of each point $r \in [a,b]$ inside the workpiece may be calculated using Eq. (7.41).

Further, the radial stress σ_r can be calculated from Eq. (7.45) at each point inside the workpiece and at each instant of time. Subsequently the tangential stress σ_φ and the longitudinal stress σ_z can be calculated from Eqs. (7.24) and (7.30) as

$$\sigma_\varphi = \sigma_r - \frac{2}{\sqrt{3}} \sigma_{eff},$$
(7.49)

$$\sigma_z = \frac{1}{2}(\sigma_r + \sigma_\varphi),$$
(7.50)

for electromagnetic compression, and as

$$\sigma_\varphi = \sigma_r + \frac{2}{\sqrt{3}} \sigma_{eff},$$
(7.51)

$$\sigma_z = \frac{1}{2}(\sigma_r + \sigma_\varphi),$$
(7.52)

for electromagnetic expansion.

The dependence of the terms in Eq. (7.45) on $a(t)$ complicates the calculation of σ_r, and thus of all the stress components, since in reality the boundaries of the workpiece are moving and the values of the electromagnetic force

densities $f_r^V(r,t)$ and $f_r^S(a,t)$ change. Thus, for the dynamic case the stress components cannot be calculated without an iterative procedure that takes into account the motion of the boundaries of the workpiece and at the same time the changes in the electromagnetic force densities $f_r^V(r,t)$, $f_r^S(a,t)$ for the workpiece.

7.4 Method for the calculation of elastoplastic deformation of materials

In the elasto-plastic deformation of the workpiece, three stages can be distinguished, see [105]. In the first stage, the workpiece suffers only elastic deformation. Then, in the second stage of the process, a region with plastic deformation starts to develop. In the third stage, the deformation of the workpiece is entirely plastic and plastic flow occurs. We will analyze here each of these three stages.

1. Only elastic deformation

The workpiece will have an elastic behavior, at each point, as long as the yield stress σ_{yp} is nowhere reached. Since there are three theories for the calculation of yield stress, each of them will be applied for the present. The principal stresses for our case are $\{\sigma_r, \sigma_\varphi, \sigma_z\}$ with $|\sigma_\varphi| > |\sigma_z| > |\sigma_r|$.

The theory of maximum shearing stress in Eq. (7.4) gives that there exists only elastic deformation as long as

$$\sigma_{sh} = |\sigma_r - \sigma_\varphi| < \sigma_{yp}. \tag{7.53}$$

The spatial distribution of the shearing stress σ_{sh} shows that, at all instants of time, its maximum value is reached at $r = a$, both for compression and for expansion.

The theory of maximum distortion energy and the theory of octahedral shearing stress give that there exists only elastic deformation as long as

$$\sigma_{eff} = \frac{\sqrt{3}}{2}|\sigma_r - \sigma_\varphi| < \sigma_{yp}. \tag{7.54}$$

For the case of electromagnetic compression and electromagnetic expansion, the effective stress leads to another expression as the shearing stress, but again it reaches the maximum at $r = a$ at all instants of time.
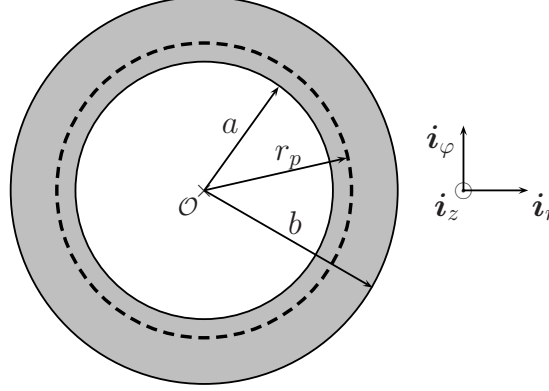
Figure 7.6: Partially yielded cylindrical workpiece.

Thus, all yielding criteria give that the yield stress σ_{yp} will be reached first at $r = a$, at a time instant t_e. So, between $t = 0$ and $t = t_e$, the workpiece presents only elastic deformation, at all points inside it.

2. Elastic and plastic deformation

When $t > t_e$, a so called "elastic-plastic boundary" $r_p(t)$ can be calculated, so that for $a < r < r_p(t)$ the material shows plastic behavior and for $r_p(t) < r < b$ the material shows elastic behavior.

The stresses, strains and radial displacement in the elastic region $r_p(t) < r < b$ are calculated using the equations described in Section 5.2, where r_1 has to be replaced with $r_p(t)$. In the plastic region $a < r < r_p(t)$, the stresses, strains and displacement are calculated using the equations described in Section 7.3, where $r = b$ has to be replaced with $r_p(t)$.

The unknown coefficients in the elastic and plastic regions will be calculated using the boundary conditions. The quantities in the elastic region have the superscript (e), while the quantities in the plastic region have the superscript (p). At each time instant the particle displacement and the normal stress must be continuous at the plastic boundary,

$$\lim_{r \downarrow r_p(t)} u_r^{(e)} - \lim_{r \uparrow r_p(t)} u_r^{(p)} = 0, \tag{7.55}$$

$$\lim_{r \downarrow r_p(t)} \sigma_r^{(e)} - \lim_{r \uparrow r_p(t)} \sigma_r^{(p)} = 0. \tag{7.56}$$

To these conditions, the boundary conditions at outer boundaries of the work-

piece are added

$$\lim_{r\downarrow a} \sigma_r^{(p)} = -f_r^S(a,t), \tag{7.57}$$

$$\lim_{r\uparrow b} \sigma_r^{(e)} = f_r^S(b,t). \tag{7.58}$$

This represents the second stage with elastic and plastic deformations. It lasts until the elastic-plastic boundary reaches the outside radius of the workpiece, at a time instant t_p.

3. Only plastic deformation

When $t > t_p$, the workpiece continues to deform plastically, in accordance to the chosen model. The plastic deformation stops in two cases. Either the workpiece will crash because either stress or strain reaches the ultimate stress σ_u of the workpiece, or the stress increment is negative (unloading of the structure).

7.5 Numerical results

In this section, we present some numerical results for typical electromagnetic forming systems designed for compression and for expansion of hollow circular cylindrical workpieces.

The following types of workpieces subjected to electromagnetic compression are investigated:

- a non-magnetic $(\mu = \mu_0)$ thick workpiece with an inner radius $r = a = 20$ mm and an outer radius $r = b = 22$ mm,

- a hypothetical magnetic $(\mu = 100\,\mu_0)$ thick workpiece with an inner radius $r = a = 20$ mm and an outer radius $r = b = 22$ mm,

- a non-magnetic $(\mu = \mu_0)$ thin workpiece with an inner radius $r = a = 20$ mm and an outer radius $r = b = 20.2$ mm.

For electromagnetic expansion, only a non-magnetic $(\mu = \mu_0)$ thick workpiece with an inner radius $r = a = 20$ mm and an outer radius $r = b = 22$ mm is considered.

In all these cases the workpiece is made of a perfectly plastic behavior with an yield stress $\sigma_{yp} = 105$ MPa. For the calculation of the yielding point, both Tresca (maximum shearing stress) and von Misses (maximum equivalent

stress) yielding criteria are applied, in order to compare the numerical results. Both theories applied at the point $r = a$, will give the time instant t_e when the second stage begins.

For each case, the radial velocity $v_r(r, t)$ is computed at each instant of time with the term $\int_a^b f_r^V(r', t)\, \mathrm{d}r'$ calculated using the initial undeformed boundaries of the workpiece as calculated in Chapter 4. Also, $f_r^S(a, t)$ and $f_r^S(b, t)$ are as calculated in Chapter 4. Further, based on the results for the radial velocity $v_r(r, t)$, the space-time evolution of the conventional strain $\varepsilon_{\varphi;0}(r, t)$ in the material has been calculated.

Non-magnetic thick workpiece in compression

In the non-magnetic ($\mu = \mu_0$) thick ($b - a = 2$ mm) workpiece subjected to compression, the plastic deformation starts at $t = 13\ \mu$s, at the inner boundary $r = a$. At $t = 14\ \mu$s the whole workpiece deforms only plastically. The time interval of progression of the elastoplastic boundary in the workpiece is about $1\ \mu$s, thus it is so small that it can be neglected. Therefore, we may admit that $t = 14\ \mu$s is the onset of the plastic deformation for all points inside the workpiece.

In Fig. 7.7 (a) and (b), we present the space-time evolution of the most important components of the dynamic elastoplastic field i.e., the radial velocity $v_r(r, t)$ and the conventional strain $\varepsilon_{0;\varphi}(r, t)$, respectively. The radial velocity and the conventional strain acquired by the workpiece before the onset of the plastic deformation have been neglected, thus the radial velocity and the conventional strain are zero in the time interval $t \in [0, 16]\ \mu$s.

With the chosen properties of the workpiece, the maximum radial velocity v_r acquired during deformation process is about - 200 m/s. This velocity is reached almost simultaneously by all points inside the workpiece. The maximum conventional strain $\varepsilon_{0;\varphi}$ in absolute value is about 12 %, and it is reached almost simultaneously in all points inside the workpiece.

In order to have a better picture of the real process of deformation, some quantities that characterize the deformation are presented in Fig. 7.8.

We notice that the inside radius of the workpiece $r = a(t)$ deforms more than the outside radius $r = b$, and also that the radial velocity of the inside radius $v_r(a, t)$ is larger than the radial velocity of the outside radius $v_r(b, t)$. This yields a larger conventional strain at $r = a$ than at $r = b$, showing once more that the workpiece becomes thicker during the electromagnetic compression.

Figure 7.7: Radial velocity $v_r(r, t)$ (a) and conventional strain $\varepsilon_{0;\varphi}(r, t)$ (b) in space-time domain for a non-magnetic ($\mu = \mu_0$) thick ($b - a = 2$ mm) workpiece subjected to compression.

Figure 7.8:   Radius $r(t)$, radial velocity $v_r(r,t)$ and conventional strain
$\varepsilon_{0;\varphi}(r,t)$ in time domain at $r = a$ and at $r = b$ for a non-
magnetic ($\mu = \mu_0$) thick ($b - a = 2$ mm) workpiece sub-
jected to compression.

Magnetic thick workpiece in compression

In the magnetic ($\mu = 100\,\mu_0$) thick ($b - a = 2$ mm) workpiece subjected to
compression, the plastic deformation starts at the inner boundary $r = a$ at
$t = 0\ \mu$s, and at $t = 1\ \mu$s the whole workpiece deforms only plastically. The
time interval of progression of the elastoplastic boundary in the workpiece is
so small that is can be neglected, and we can admit that at $t = 1\ \mu$s the plastic
deformation begins at all points inside the workpiece.

Figure 7.9: Radial velocity $v_r(r,t)$ (a) and conventional strain $\varepsilon_{0;\varphi}(r,t)$ (b) in space-time domain for a magnetic ($\mu = 100\,\mu_0$) thick ($b - a = 2$ mm) workpiece subjected to compression.
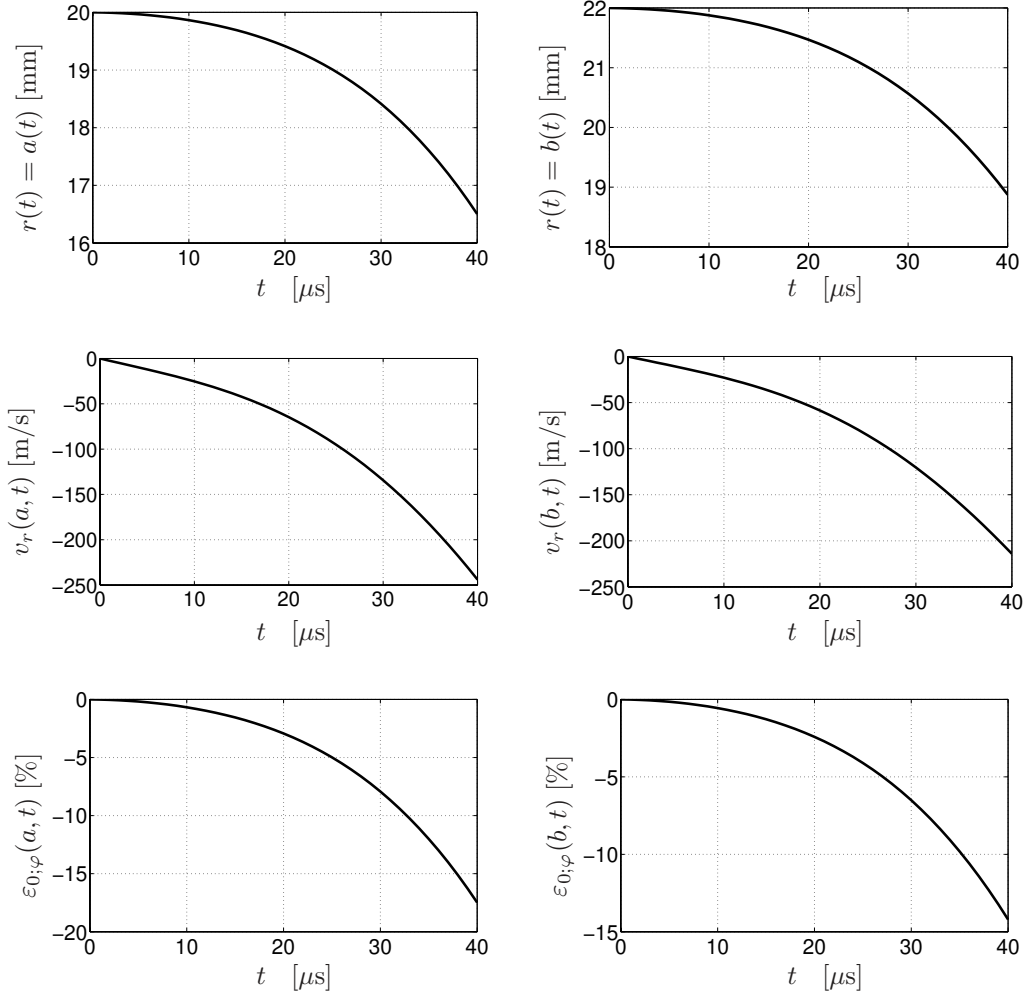
Figure 7.10: Radius $r(t)$, radial velocity $v_r(r,t)$ and conventional strain
$\varepsilon_{0;\varphi}(r,t)$ in time domain at $r = a$ and at $r = b$ for a mag-
netic ($\mu = 100\,\mu_0$) thick ($b - a = 2$ mm) workpiece sub-
jected to compression.

The space-time evolution of the radial velocity v_r and of the conventional strain
$\varepsilon_{0;\varphi}$ are presented in Fig. 7.9 (a) and (b), respectively. The radial velocity and
the conventional strain acquired by the workpiece before the onset of the plastic
deformation have been neglected, thus the radial velocity and the conventional
strain are zero in the time interval $t \in [0,1]\ \mu$s.

With the chosen properties of the workpiece, the maximum radial veloc-
ity v_r acquired during deformation process is about - 250 m/s, and the maxi-

mum conventional strain $\varepsilon_{0;\varphi}$ is about 16 % in absolute value. Both quantities are in the same order of magnitude as for the non-magnetic thick workpiece.

In order to have a better picture of the real process of deformation, some quantities that characterize the deformation are presented in Fig. 7.10. Again, as for the thick non-magnetic workpiece, the inside radius of the workpiece $r = a(t)$ deforms more than the outside radius $r = b$ and the radial velocity of the inside radius $v_r(a, t)$ is larger than the radial velocity of the outside radius $v_r(b, t)$. This yields a larger conventional strain at $r = a$ than at $r = b$.

Non-magnetic thin workpiece in compression

In the non-magnetic $(\mu = \mu_0)$ thin $(b - a = 0.2$ mm) workpiece subjected to compression, the plastic deformation at the inner boundary $r = a$ at $t = 2$ μs, and at $t = 3$ μs the whole workpiece deforms only plastic. Similar with the previous cases, we may admit that $t = 3$ μs represents the instant of time for the onset of the plastic deformation within the whole workpiece.

The space-time evolution of the radial velocity v_r and of the conventional strain $\varepsilon_{0;\varphi}$ are presented in Fig. 7.11 (a) and (b), respectively. The radial velocity and the conventional strain acquired by the workpiece before the onset of the plastic deformation have been neglected, thus the radial velocity and the conventional strain are zero in the time interval $t \in [0, 3]$ μs.

With the chosen properties of the workpiece, the maximum radial velocity v_r acquired during deformation process is about -1200 m/s, thus about 5 times larger than for the non-magnetic thick workpiece. This velocity is reached almost simultaneously by all points inside the workpiece. The maximum conventional strain $\varepsilon_{0;\varphi}$ in absolute value is about 80 %, thus about 6 times larger than in the non-magnetic thick workpiece.

In order to have a better picture of the real process of deformation, some quantities that characterize the deformation are presented in Fig. 7.12. The inside radius of the workpiece $r = a(t)$ deforms slightly more than the outside radius $r = b$ and the radial velocity of the inside radius $v_r(a, t)$ is slightly larger than the radial velocity of the outside radius $v_r(b, t)$.

This time the differences in the radial displacement, radial velocities and conventional strains at $r = a$ and $r = b$ are smaller than for the non-magnetic thick and magnetic thick workpieces. This shows that for a very thin object the thin shell theory may be applied for the calculation of the elastoplastic field.
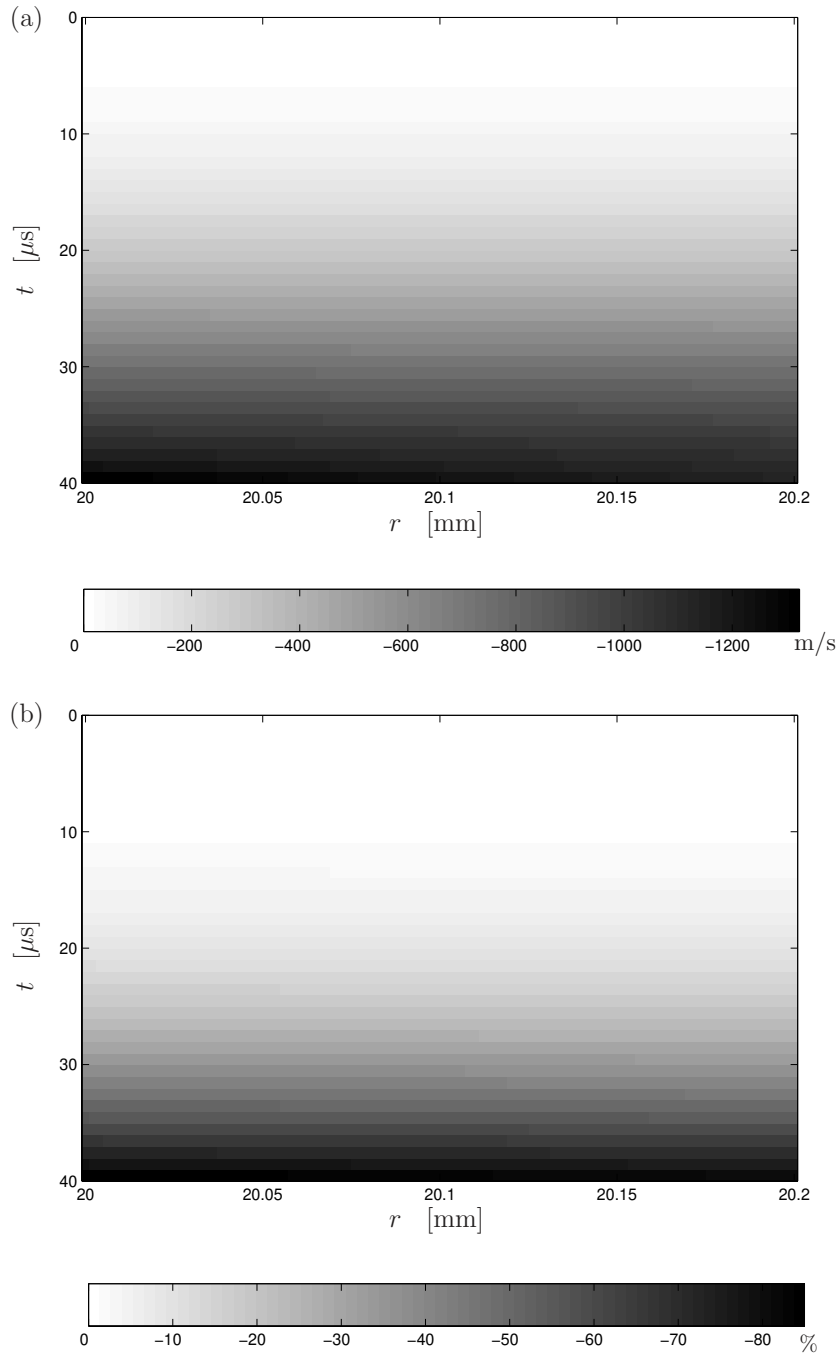
Figure 7.11: Radial velocity $v_r(r,t)$ (a) and conventional strain $\varepsilon_{0;\varphi}(r,t)$
(b) in the space-time domain for a non-magnetic ($\mu = \mu_0$)
thin ($b - a = 0.2$ mm) workpiece subjected to compression.
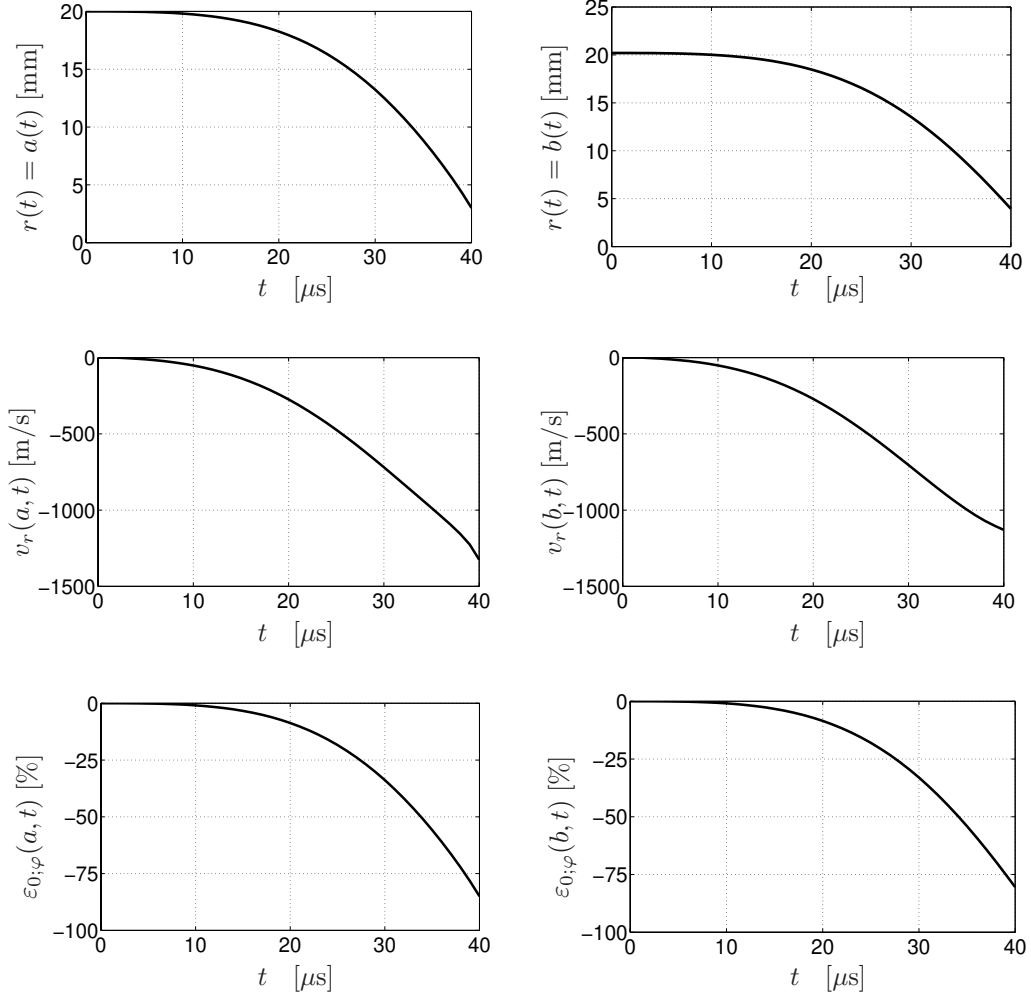
Figure 7.12:   Radius $r(t)$, radial velocity $v_r(r,t)$ and conventional strain $\varepsilon_{0;\varphi}(r,t)$ in time domain at $r = a$ and at $r = b$ for a non-magnetic ($\mu = \mu_0$) thin ($b - a = 0.2$ mm) workpiece subjected to compression.

Non-magnetic thick workpiece in expansion

In the non-magnetic ($\mu = \mu_0$) thick ($b - a = 2$ mm) workpiece subjected to expansion, the plastic deformation starts at the inner boundary $r = a$ at $t = 17\ \mu$s. At $t = 18\ \mu$s the whole workpiece deforms only plastically. The time interval of progression of the elastoplastic boundary in the workpiece is about $1\ \mu$s, thus so small that it can be neglected, and we may admit that $t = 17\ \mu$s is the onset of the plastic deformation for all points inside the workpiece.
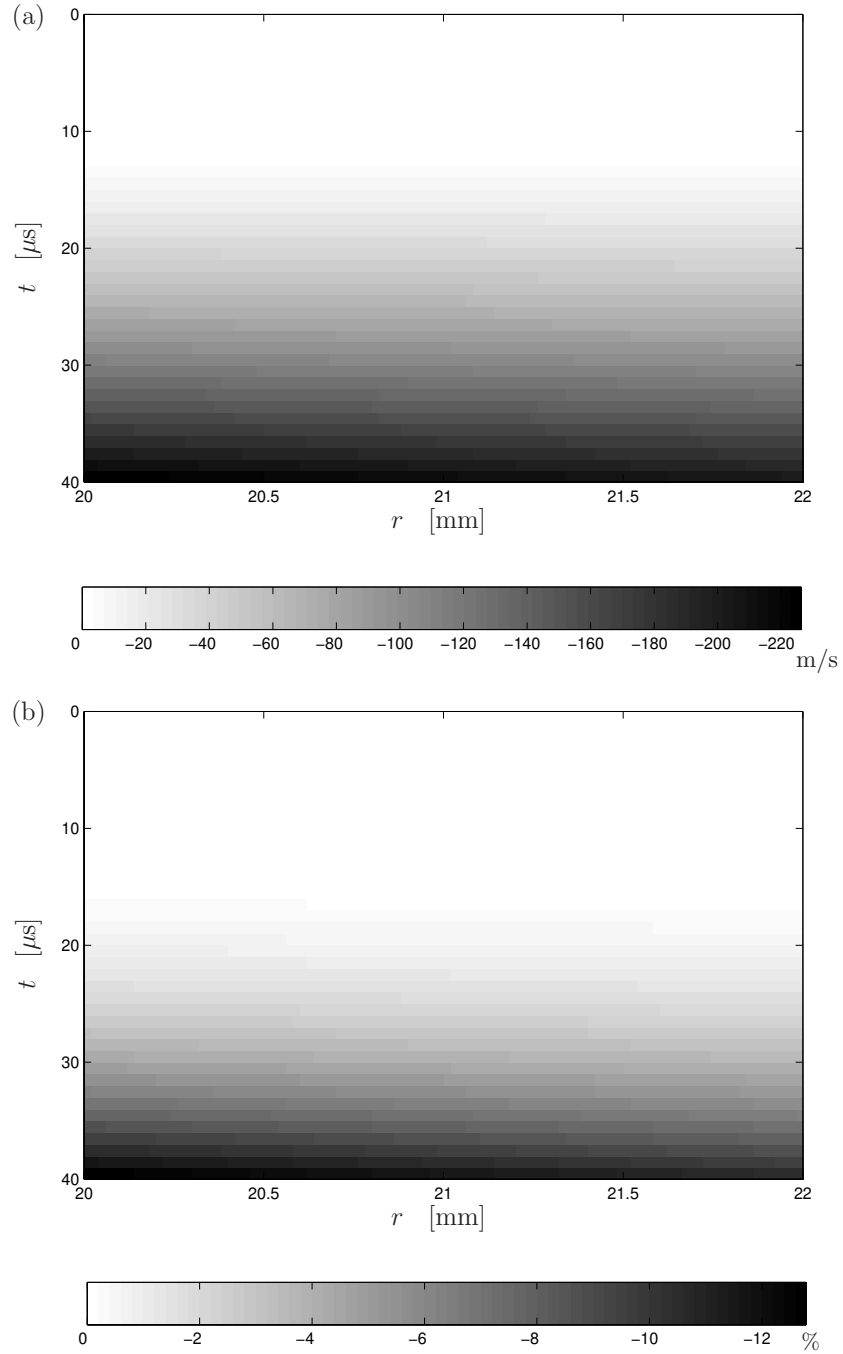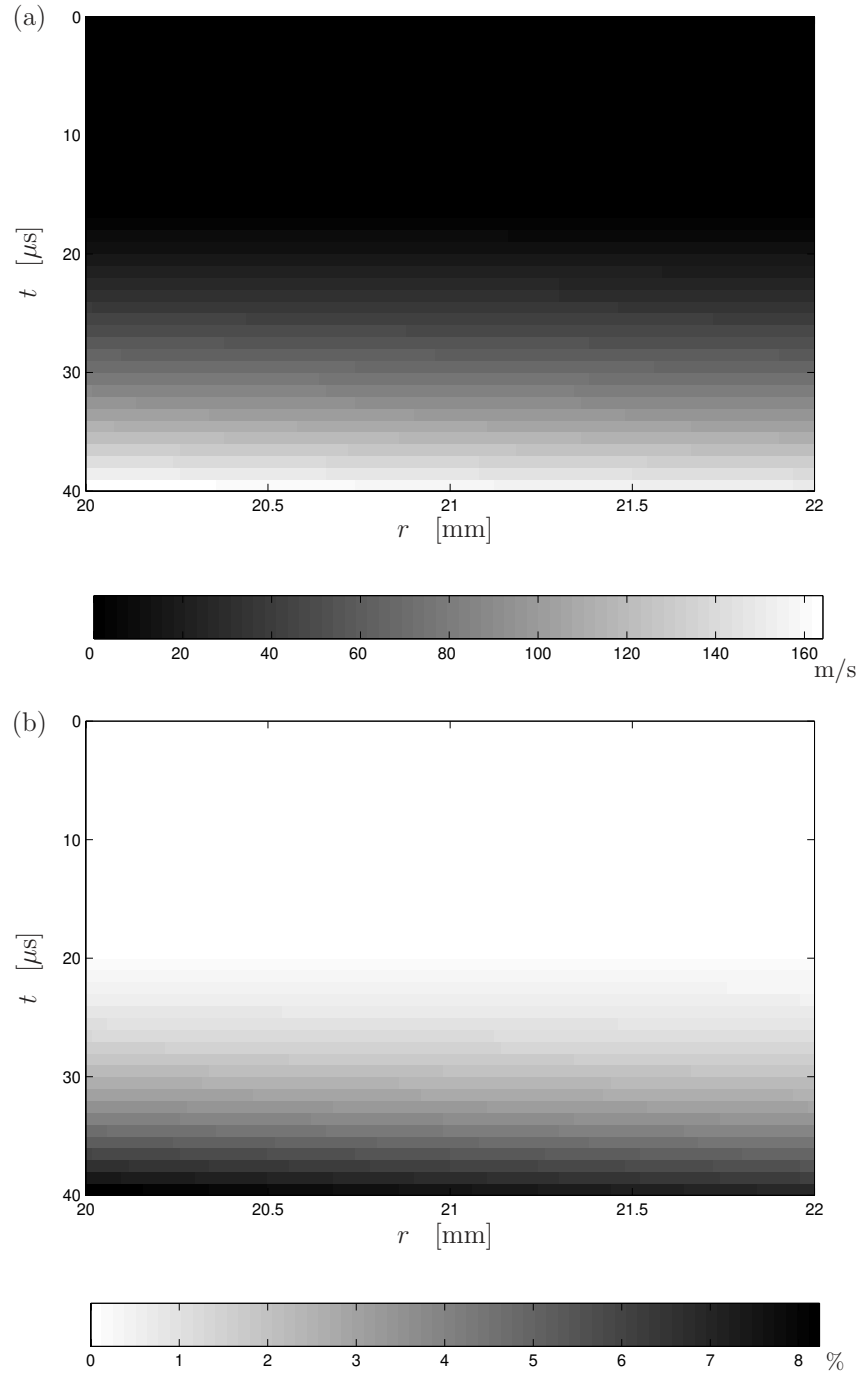
Figure 7.13:   Radial velocity $v_r(r,t)$ (a) and conventional strain $\varepsilon_{0;\varphi}(r,t)$
              (b) in the space-time domain for a non-magnetic ($\mu = \mu_0$)
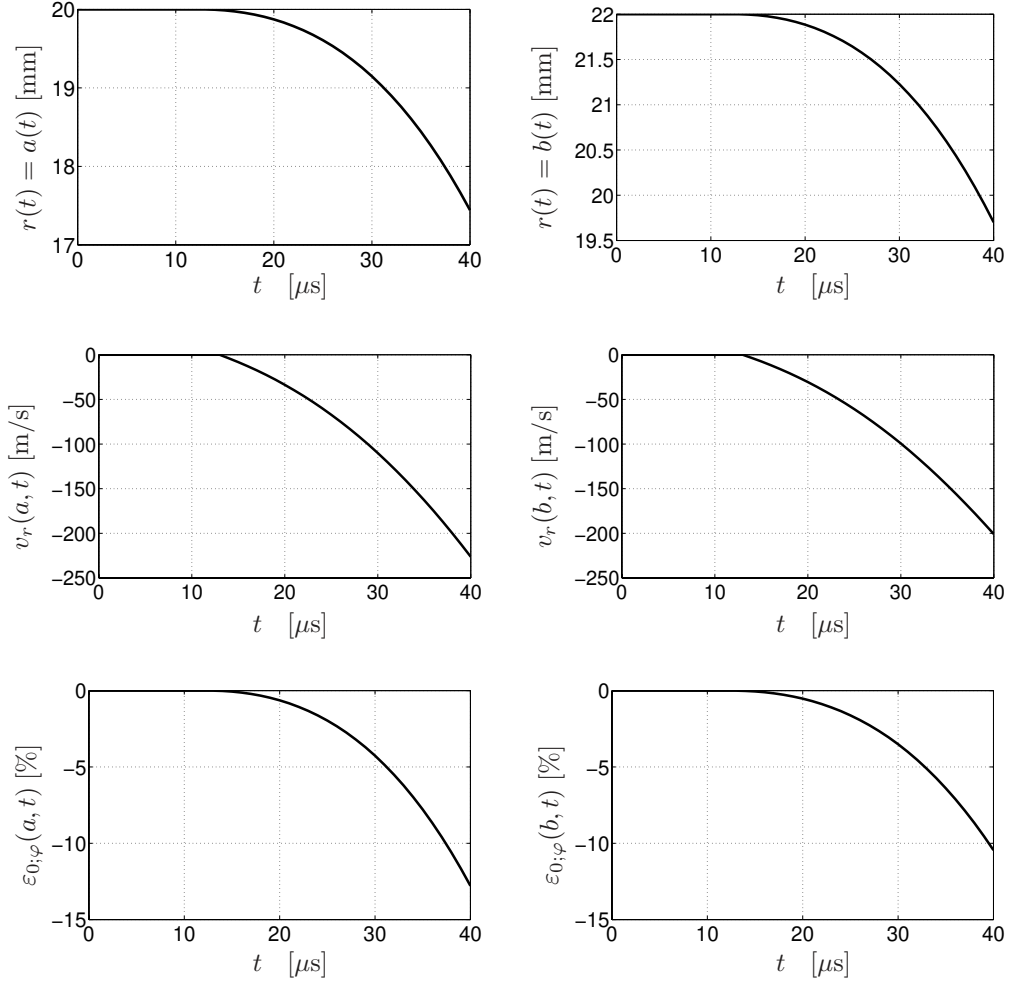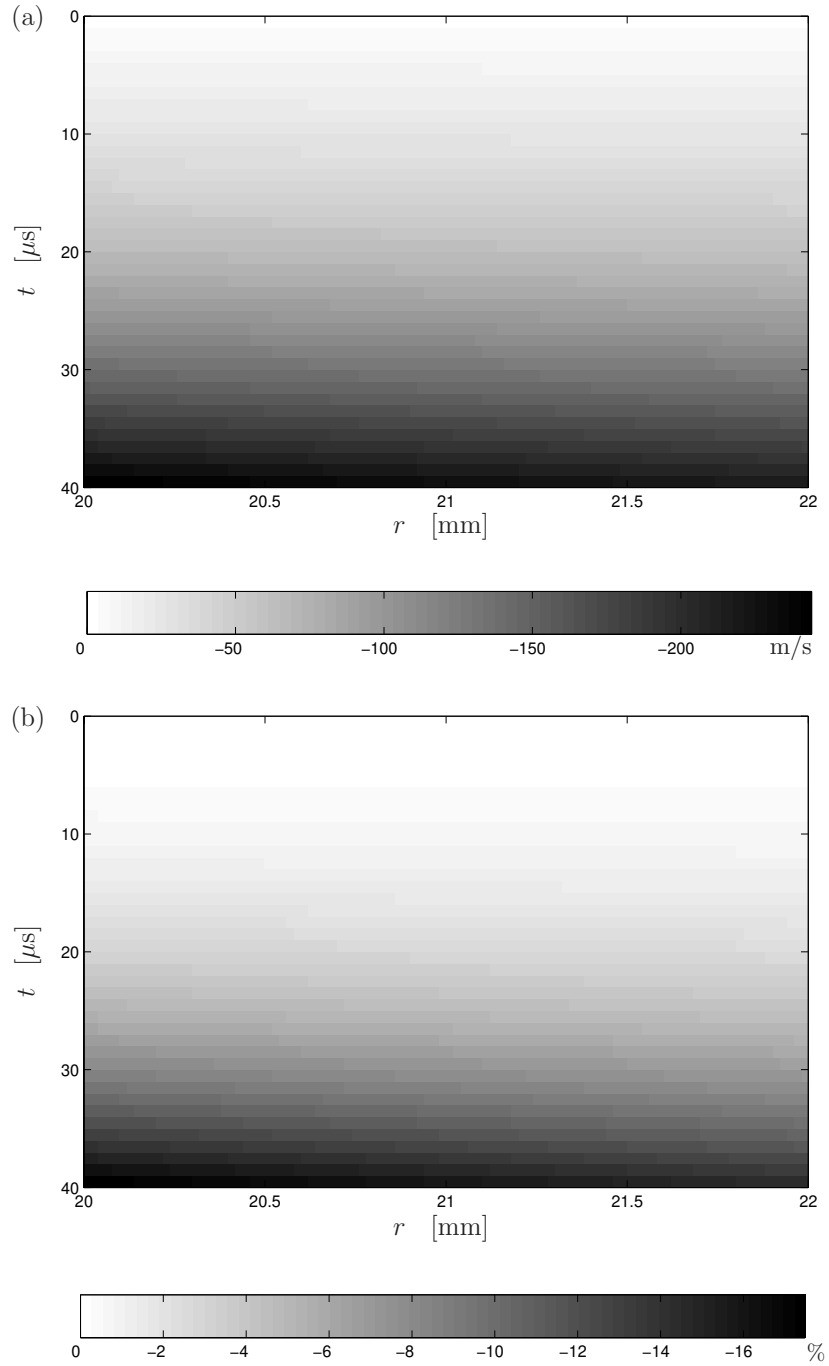   thick ($b - a = 2$ mm) workpiece subjected to expansion.
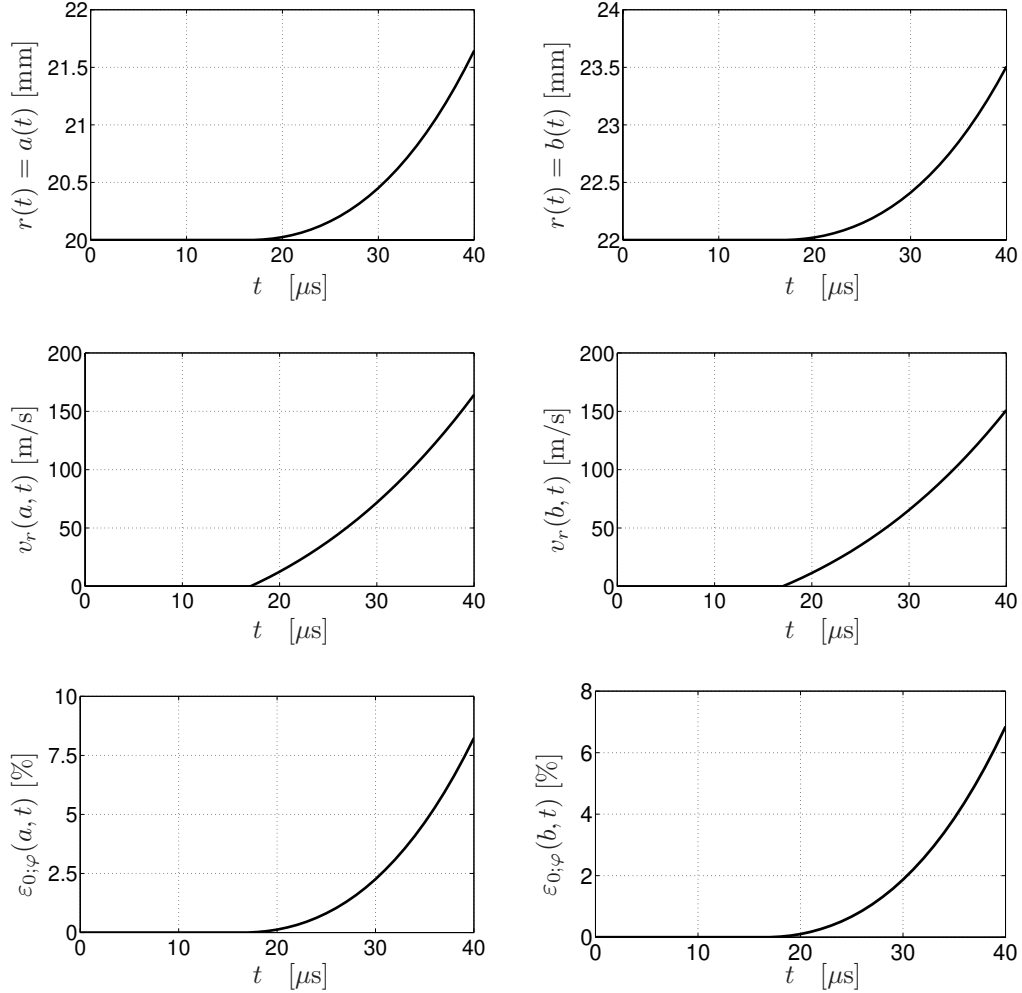
Figure 7.14:   Radius $r(t)$, radial velocity $v_r(r,t)$ and conventional strain
$\varepsilon_{0;\varphi}(r,t)$ in the time domain at $r = a$ and at $r = b$ for
a non-magnetic ($\mu = \mu_0$) thick ($b - a = 2$ mm) workpiece
subjected to expansion.

In Fig. 7.13 (a) and (b), we present the space-time evolution of the most
important components of the dynamic elastoplastic field i.e., the radial velocity
$v_r(r,t)$ and the conventional strain $\varepsilon_{0;\varphi}(r,t)$, respectively. The radial velocity
and the conventional strain acquired by the workpiece before the onset of the
plastic deformation have been neglected, thus the radial velocity and the con-
ventional strain are zero in the time interval $t \in [0, 16]$ μs.

With the chosen properties of the workpiece, the maximum radial veloc-

ity v_r acquired during deformation process is about 200 m/s. This velocity is reached almost simultaneously by all points inside the workpiece. The maximum conventional strain $\varepsilon_{0;\varphi}$ in absolute value is about 12 %, and it is reached almost simultaneously in all points inside the workpiece.

In order to have a better picture of the real process of deformation, some quantities that characterize the deformation are presented in Fig. 7.14. We notice that the inside radius of the workpiece $r = a(t)$ deforms more than the outside radius $r = b$, and also that the radial velocity of the inside radius $v_r(a, t)$ is larger than the radial velocity of the outside radius $v_r(b, t)$. This yields a larger conventional strain at $r = a$ than at $r = b$. This fact confirms once more that the workpiece becomes thinner during the electromagnetic expansion.

7.6 Conclusions

The evaluation of the inelastic deformation in the case of elastic-perfectly plastic materials used in electromagnetic compression and expansion has been discussed, within the plane strain assumption. The elastic deformation and the radial velocity that were reached before the plastic deformation has been neglected. The electromagnetic volume and surface force densities calculated in Chapter 4 have been taken as the source of the inelastic deformation.

In all considered cases, the plastic boundary described in Section 7.4 progresses very rapidly inside the workpiece, so that the intermediary calculations may be avoided. Therefore we may consider that the whole workpiece starts to deform plastically at a certain instant of time, namely when the flow condition is reached in the whole workpiece. It has been shown that both the magnetic thick workpiece and the non-magnetic thin workpieces start to deform plastically after a very short episode of negligible elastic deformations at the beginning of the process. In the non-magnetic thick workpiece subjected both to compression and to expansion, the elastic episodes lasts longer, but the associated deformations are still negligible.

The actual deformation of the workpiece has been calculated using the dynamic equation of motion. It has been shown that the thickness of the workpieces increases during electromagnetic compression, and it decreases during electromagnetic expansion. In a non-magnetic thick and a magnetic thick workpiece, the radial displacement of the inside and outside radius of the workpiece shows to be small, while the radial displacement is considerable in the non-magnetic thin workpiece subjected to compression.

The radial velocity of the inside radius $v_r(a, t)$ is larger in absolute value than the radial velocity of the outside radius $v_r(b, t)$, for all the considered cases. In the non-magnetic thick or magnetic thick workpieces this difference in velocities is larger, while in a non-magnetic thin workpiece the difference in velocities is smaller. Anyhow, $|v_r(a, t)| > |v_r(b, t)|$ and this also shows that the thickness of the workpiece increases during electromagnetic compression and decreases during electromagnetic expansion under the plane strain assumption. For the considered case the change in thickness is not so large, but in other applications it may become significant.

Inside the workpiece the distribution of the conventional strain is almost linear. For a non-magnetic thick workpiece, in the same interval of time, the variation of the thickness is smaller than for the case of a magnetic thick workpiece. This is due to different volume source densities in each point inside the workpiece while for reason of comparison we considered the magnetic workpiece to have the same properties as the non-magnetic one, except for the magnetic permeability. In reality, the yield stress of magnetic materials is much larger that the value we assumed ($\sigma_{yp} = 105$ MPa) and also the elastoplastic behavior of real magnetic materials is not a perfectly plastic one.

It has been shown that the thickness of the workpiece decreases during electromagnetic expansion under the plane strain assumption. This must be kept in mind certainly in some application where the thickness of the workpiece may not be under a given value, for the safety of operation, e.g. vessels under pressure, etc.

Chapter 8

Experimental investigation of electromagnetic forming of steel beverage cans

This chapter presents the design of a set-up for an experimental investigation of electromagnetic expansion of steel beverage cans. In the beginning, this experimental set-up was intended as a practical verification of the electromagnetic forming theory described in this thesis with regard to the assumptions and approximations that have been made. However, through circumstances is was only possible to perform a limited set of experiments for the electromagnetic expansion of very thin, hardened steel beverage cans as shown in Fig. 3.1, where we could assume the deformation to take place under magnetic saturation. Since the thickness of the workpiece became so small that the previously developed theory would no longer be effective, an approximate approach was used. This approximate approach will be discussed here, as well as the results of a set of experiments obtained with the designed experimental set-up.

The original demand from Corus was to be able to expand standard beverage cans, with a coil that could pass through the neck of the can, as shown in Fig. 3.1. The limited diameter of the coil is a serious limitation and it was anticipated that expansion can only be obtained with a set-up that uses a capacity bank having a large capacity.

Initially, the construction of a complete experimental set-up including a clamp diode was intended by Corus in the project. However, the cost of such equipment could not be justified in view of the financial situation of Corus at

that time. So it was decided to use existing equipment as much as possible, and to omit the clamp diode. Only the coil had to be constructed by Corus.

Eventually, the experiments have been carried out at KEMA High Voltage Laboratory, where the number of capacitances of the capacitor bank that may be obtained with the existent units was limited. The maximum capacitance that could be obtained was insufficient to expand wide beverage cans. Some preliminary calculations however showed that, with this equipment, the original coil design could still be used if the beverage can diameter could be reduced sufficiently. So, the verification tests have been carried out using standard aerosol cans.

8.1   Description of the workpiece

The experimental set-up that had to be designed for the practical validation of the electromagnetic forming, is presented schematically in Fig. 8.1.
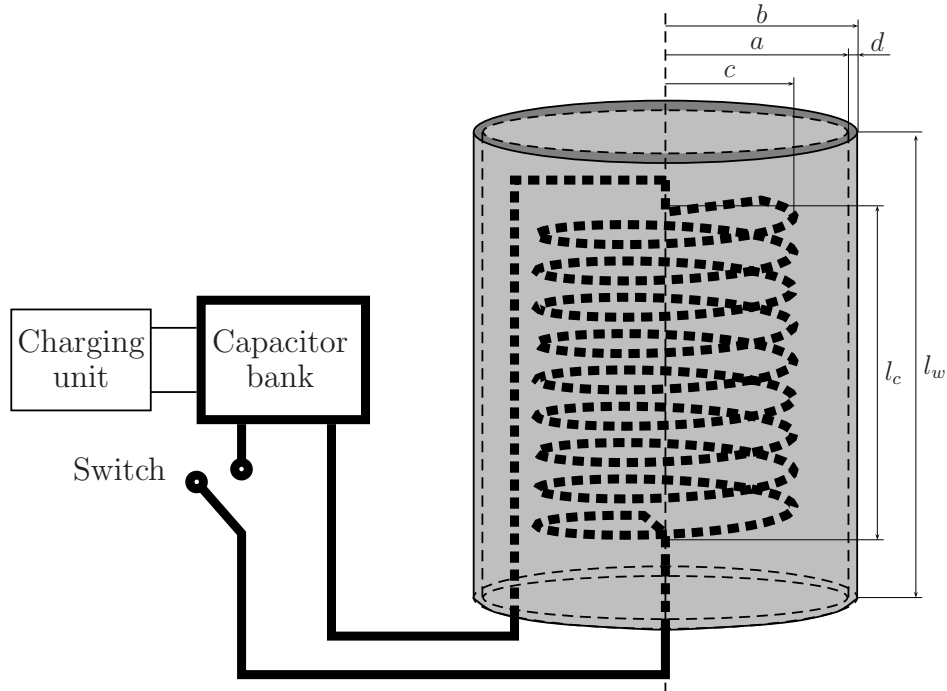
Figure 8.1:   The schematic representation of the experimental set-up for electromagnetic forming of thin steel beverage cans.

The workpiece is a circular cylindrical mild steel tube, that should reach a final deformation of at least 15% without failure by rupture. Its dimensions and properties are presented in Table 8.1. During the actual design process, more types of materials have been considered, and each time the characteristic parameters of the optimal forming systems have been determined.

The material of the workpiece is magnetic, with an unknown relative magnetic permeability $\mu_{r;w}$. However, the actual currents during the larger part of the current pulse are so high that the workpiece is magnetically saturated. Therefore, in all following calculations we have taken $\mu_{r;w} = 1$. The thickness of the workpiece to be considered was in the order of 200 μm, although for some types of beverage cans the thickness was even smaller than 100 μm.

Table 8.1: Dimensions and properties of the workpiece for expansion.

Symbol	Chosen value	Description
$r_{mean}^{(0)}$	26 mm	initial (undeformed) mean radius
d	78, 80 μm	thickness 2-piece can
	186, 200 μm	thickness 3-piece can
l_w	100 mm	length
a	$r_{mean} - d/2$	inside radius
b	$r_{mean} + d/2$	outside radius
σ_w	$8.3 \cdot 10^7$ S/m	electrical conductivity
$\mu_{r;w}$	1	relative magnetic permeability (in saturation regime)
μ_w	$\mu_{r;w}\mu_0$	magnetic permeability
B_{sat}	2 T	magnetic flux at saturation
$\rho_{m;w}$	$7.9 \cdot 10^3$ kg/m^3	mass density
λ_L	140 GPa	Lamé's coefficient of elasticity
μ_L	80 GPa	Lamé's coefficient of rigidity
$\varepsilon_{limit;w}$	0.0011927	limit strain
$\sigma_{yp;w}$	840 MPa	yielding stress 2-piece can
	250 MPa	yielding stress 3-piece can
$c_{T;w}$	472 J/kg K	mass specific heat
$\alpha_{T;w}$	$12.6 \cdot 10^{-6}$ K^{-1}	coefficient of linear thermal expansion
$k_{th;\tau}$	$400 \cdot 10^{-5}$ K^{-1}	coefficient of variation with temperature of electrical conductivity
κ_w	49.8 W/(m K)	thermal conductivity

In Chapter 4, numerical results have been generated for the case of compression and expansion of a non-magnetic $\mu = \mu_0$ thin workpiece with a thickness of 200 μm, thus in the order of the thicknesses of the beverage cans used in electromagnetic expansion. The current in the workpiece was almost similar to the one in the real experimental set-up. We noticed then that the electric field is almost constant along the thickness of the workpiece and the magnetic field shows a linear dependence on the radius. As a consequence, the electromagnetic volume force density has also a linear dependence on the radius. Even for a thin workpiece, the computational effort required to obtain these results was considerable. When integrating the electromagnetic volume force density along the thickness of the workpiece and adding the surface forces, we obtain the total equivalent force acting on the surface of the workpiece, or the equivalent pressure p_{work} exerted on the workpiece.

When analyzing the equivalent pressure for a highly conducting thin workpiece, we notice that we have in fact, $p_{work} = \frac{1}{2}\mu_0 I_S^2$. Since I_S is I_{work} as has been shown in Section 3.2, we see that the total force acting on the surface of the workpiece in this case may be determined equally well using the network model, which is much faster.

Under the given circumstances, we assume that the electromagnetic forces on the whole workpiece will act as an equivalent surface pressure p_{work} on the outside surface of the workpiece. In the beginning of the forming process, this equivalent pressure should built up to the yielding pressure and then exceed it with such an amount that the final deformation of about 15% is obtained.

From the initial mean radius of the workpiece $r_{mean}^{(0)}$ and the final strain $\varepsilon_{0;\varphi} = 0.15$ we want to achieve, the final radius of the workpiece may be calculated as

$$r_{mean} = r_{mean}^{(0)}(\varepsilon_{0;\varphi} + 1). \tag{8.1}$$

The true strain that has to be reached is $\varepsilon_\varphi = \ln(\varepsilon_{0;\varphi} + 1)$. In the plane strain situation for expansion, the corresponding effective strain is

$$\varepsilon_{eff} = \left(2/\sqrt{3}\right)\varepsilon_\varphi = -\left(2/\sqrt{3}\right)\varepsilon_r. \tag{8.2}$$

The total work done by stresses, as mentioned in Chapter 7, results in the plastic (permanent) deformation, in our case $\varepsilon_{eff;max}$. The total work per volume unit done during deformation by stresses, and required to achieve the strain $\varepsilon_{eff;max}$ is

$$w_{def} = \int_{\varepsilon_{eff}=0}^{\varepsilon_{eff;max}} \sigma_{eff}\, d\varepsilon. \tag{8.3}$$

For the case of a thin shell, $\sigma_r \approx 0$ and the effective stress is

$$\sigma_{\textit{eff}} = (\sqrt{3}/2)\ \sigma_\varphi. \tag{8.4}$$

We may assume any convenient type of static stress-strain relation that fits best the experimental results obtained from typical tensile tests on specimens of the given workpiece. Here, for one material, we have assumed that the required yield strength depends on the strain as

$$\sigma_{\textit{eff}} = 1100 \cdot 10^6 + 120 \cdot 10^6 \varepsilon_{\textit{eff}}\ \text{N/m}^2 \qquad \text{(linear hardening),} \tag{8.5}$$

$$\sigma_{\textit{eff}} = 1109 \cdot 10^6\ \text{N/m}^2 \qquad \text{(perfectly plastic).} \tag{8.6}$$

The application of these static stress-strain relations to Eq. (8.3) yields for both models

$$w_{def} = 166.35 \cdot 10^6\ \text{J/m}^3. \tag{8.7}$$

When we assume further that the deformation energy is conveyed entirely by the kinetic energy, the energy balance per volume unit of the workpiece is

$$\frac{1}{2}\rho_{m;w}v_{r;max}^2 = w_{def}. \tag{8.8}$$

where $v_{r;max}$ is the maximum velocity that may be reached by the workpiece. With the above examples this velocity is

$$v_{r;max} = 205.28\ \text{m/s}. \tag{8.9}$$

This maximum velocity is acquired by the workpiece due to the impulsive electromagnetic pressure exerted on it. In reality these velocities will not be reached since the deformation will start while the pressure pulse is not over, i.e. not all required deformation energy will be obtained entirely from the kinetic energy.

In a practical situation, three stages may be described during the electromagnetic forming of the workpiece, see [105] and Section 7.4 .

First, p_{work} increases until the yielding pressure p_{yp}, required to begin the plastic deformation of the workpiece, is reached. In this stage, the workpiece only deforms elastically and the value of this deformation is negligible. If the equivalent surface pressure on the workpiece never reaches p_{yp}, the final deformation of the workpiece is zero at the end of the process.

The second stage of the forming process takes place as long as $p_{work} > p_{yp}$. During this stage the workpiece deforms plastically. The third stage of the
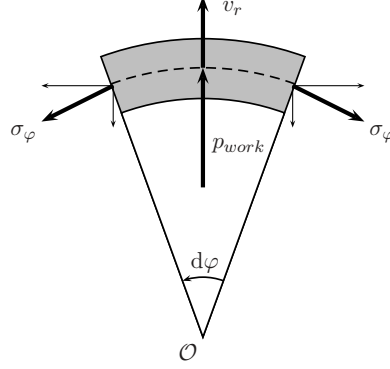
Figure 8.2: Detail of a small element of the workpiece during deformation.

forming process occurs if p_{work} has fallen below p_{yp}. Only for perfectly plastic materials, this new value p_{yp} is the same as the value of the yielding pressure from the beginning of deformation. For materials with strain hardening, the yielding pressure increases during the deformation process. At the time instant when the third stage begins we assume that the radial velocity v_r becomes zero. Now the workpiece again deforms elastically and this deformation will not affect the final deformation of the workpiece.

Using the thin-shell assumption, for a small element of the workpiece as shown in Fig. 8.2 ($d\varphi \to 0$), the following equation of motion is valid at each time instant

$$\rho_{m;w}d \ \partial_t v_r = \ p_{work} - \frac{d}{r_{mean}} \ \sigma_\varphi. \tag{8.10}$$

In the first stage of the forming process, there is no motion and the radial velocity is thus zero. The deformation starts when the yielding pressure is reached

$$p_{work} = p_{yp} = \sigma_{yp} \frac{d}{r_{mean}^{(0)}}. \tag{8.11}$$

The maximum radial velocity that can be reached during the second stage of the process, may be calculated as

$$\rho_{m;w}v_{r;max}d = \int_{t=t_{yp}}^{t_{fin}} (p_{work} - p_{yp}) \, dt, \tag{8.12}$$

where t_{yp} is the instant of time when $p_{work} = p_{yp}$ (yielding begins) and t_{fin} is the instant of time when the pressure reaches again $p_{work} = p_{yp}$, as in Fig. 8.3.
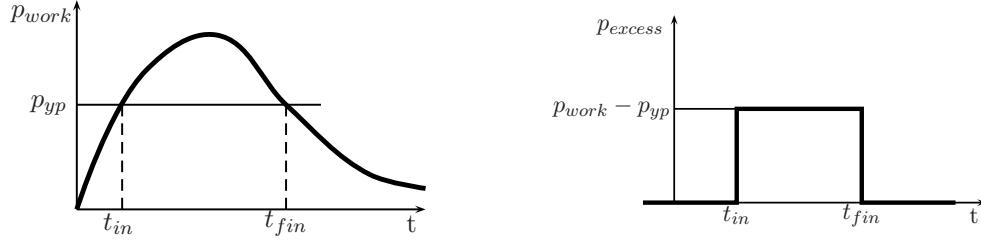
Figure 8.3:   Typical shape of the pressure pulse exerted on the work-
piece during electromagnetic forming.

In Eq. (8.12), we assumed that the material is a perfectly plastic one,
with $\sigma_\varphi = \sigma_{yp}$ and $(d/r_{mean})\,\sigma_\varphi = p_{yp}$ within the whole range of plastic
deformation. For the sake of simplicity, we assume that $p_{excess} = p_{work} - p_{yp}$
is a short rectangular pulse of constant amplitude acting over a time-interval
Δt. In this assumption, Eq.(8.12) becomes

$$\rho_{m;w} v_{r;max} d = p_{excess} \Delta t. \tag{8.13}$$

Some numerical results obtained for the required approximate excess pressure
are presented in Table 8.2.

Now, the total pressure required to deform the workpiece and to obtain
the 15% deformation is

$$p_{work} = p_{yp} + p_{excess}. \tag{8.14}$$

If the stress in the material is a function of strain or of deformation velocity, e.g.
$\sigma_{eff} = \sigma_{eff}(\varepsilon_{eff}, \dot{\varepsilon}_{eff})$, p_{yp} in Eq. (8.12) has to be replaced by the appropriate
value given by $(d/r_{mean})\,\sigma_\varphi$. The actual value of σ_φ is then a function of
actual strain and actual deformation velocity inferred from the relation between
effective stress and effective strain $\sigma_{eff} = \sigma_{eff}(\varepsilon_{eff}, \dot{\varepsilon}_{eff})$.

We have assumed that we are working in the deep magnetic saturation
region, so $\mu_{r;w} = 1$ for the workpiece, and then the pressure acting on the

Table 8.2:   Excess pressure required for obtaining 15% deformation
with different time-intervals of pulse pressure.

Δt	10 μs	20 μs	40 μs	50 μs	80 μs
p_{excess}	12.97 MPa	6.48 MPa	3.24 MPa	2.59 MPa	1.62 MPa

workpiece may be calculated as the pressure on a non-magnetic workpiece

$$p_{work}^{(old)} = \frac{1}{2}\mu_0 I_{work}^2, \tag{8.15}$$

where $I_{work} = I_2$ is the current per unit length in the workpiece calculated from the network model.

Then we re-considered this formula, since in the deep-saturation regime $\mu_{r;w} = 1$, but the magnetic flux density is $B_{sat} \neq \mu_0\mu_r I_{work}$. The saturation flux density $B_{sat} = \mu_0 M_{sat}$ varies in the range 1.5 T – 2.2 T for mild steel. So, the pressure exerted on the workpiece has been subsequently calculated as

$$p_{work}^{(new)} = \frac{1}{2}\mu_0 I_{work}^2 + I_{work}B_{sat}. \tag{8.16}$$

Using the above procedure, the value of the current in the workpiece required to reach the 15% deformation may be deduced. Of course, many combinations of parameters in the primary part of the network model may lead to the same current in the workpiece giving finally the desired deformation of the workpiece.

Thus, we have to find the optimum combination of parameters of the forming system in order to obtain a current per unit length I_{work} able to lead to a final deformation of the workpiece of about 15%.

8.2   The equipment needed for the experiments

As shown in Fig. 8.1, the most important parts of the experimental set-up are: the capacitor bank, the charging unit for the capacitor bank, the high-voltage, high-current switch and the forming coil. Apart from the forming coil, these components could be found on the market. The forming coil had to be designed. Further, some requirements for the each component are given, in order to choose the optimum combination.

A. The capacitor bank

This part of the forming system is sometimes the most expensive one if it has to be purchased. It should have a given capacitance and allow for a sufficiently large charge voltage. Further it should allow a sufficient number of pulse discharges without deterioration. The self inductance and resistance of the capacitor bank should be very small, as assumed implicitly in the equivalent circuit. It will be very convenient if the capacitor bank allows parallel and/or series connections to be made between small units, so that a large range of capacitances can be obtained during experimental verifications.

B. The charging unit for the capacitor bank

The charging unit should be able to load the capacitor bank at the required initial charge voltage V_0 in the range $10 - 20$ kV in steps of a few hundred volts. Also, the charging unit should re-charge the capacitor bank in a reasonable amount of time (in the order of minutes).

C. The switch

The switch should be able to switch currents in the order of hundreds of kA in a very short time, in the order of μs. The self inductance and resistance of the high-voltage, high-current switch should be very small, as assumed implicitly in the equivalent circuit.

D. The measuring equipment

Some measuring equipment is necessary in the experimental set-up, for measuring the discharge current, the temperature rise and also the deformation of the workpiece. This equipment should be able to measure with good accuracy the desired parameters an also to have very small self-inductance and resistance.

E. The forming coil

The forming coil had to be designed specially for this application of electromagnetic forming, since it is not available on the market. This design process is explained in the remainder of this section.

The forming coil may be made of copper wire (circular cross-section) or made of thin copper strips (rectangular cross-section), both choices allowing multiple layers of windings. The conductor with rectangular cross-section is preferred in case of multiple layers of windings. Some geometrical dimensions
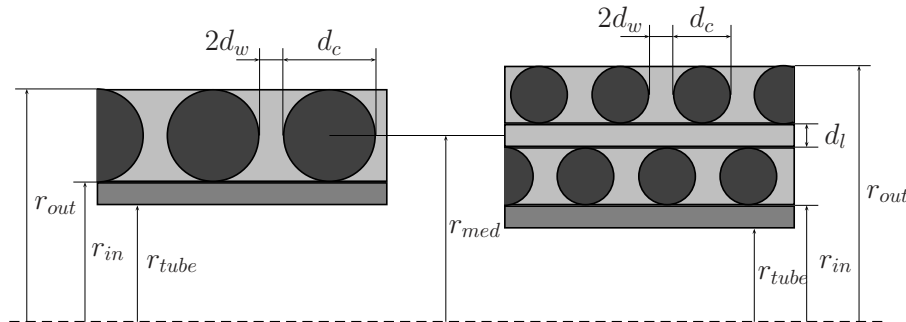
Figure 8.4:   Longitudinal section of the forming coil with windings (black) made of round conductor.
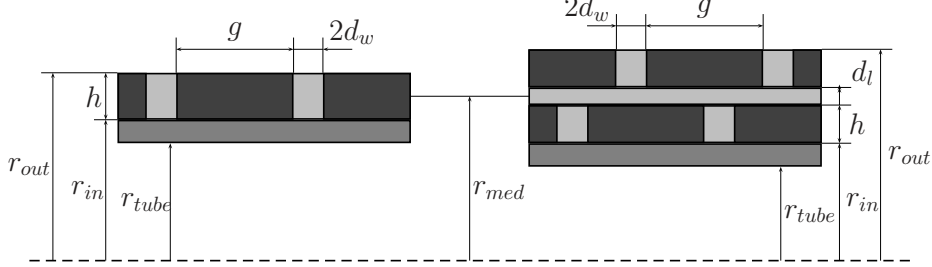
Figure 8.5:   Longitudinal section of the forming coil with windings
               (black) made of rectangular conductor.

required to design the forming coil are presented in Figs. 3.8, 8.4 and 8.5.

Numerical simulations have shown that the performances of forming coils made of one or two layers of windings with rectangular cross-section are very close to the performances obtained for windings with circular cross-section, when both conductors have the same area of cross-section. After many numerical trials with both types of conductors, finally a forming coil with one layer of windings with rectangular cross-section has been chosen.

The copper wire is machined on the surface of a plastic tube, and a layer of insulation has to be applied on the forming coil. The final maximum radius r_{max} of the forming coil after the application of the insulation layer, is such that the forming coil still fits inside the workpiece, thus inside the beverage can. The final dimensions and properties of the forming coil made of one layer of windings of rectangular copper strip are presented in Table 8.3.

The numerical results have shown that, in general, the forming coil is subjected to higher pressure than the workpiece. The heat production in the coil cannot be neglected, since all the parameters of the coil can change with temperature, including its geometry. It follows that a good cooling of the whole configuration should be provided. The manufacturer of the forming coil had ensured the mechanical strength of the forming coil by performing mechanical simulations relating to its strength.

With the prescribed dimensions, the resistance and the self-inductance of the forming coil can be calculated as

$$R_c = 8 \ c \ l_c / (\sigma_c \ d_c^2), \qquad (8.17)$$

$$L_c = \mu_0 \ \pi \ c^2 \ n^2 \ l_c, \qquad (8.18)$$

where $c = r_{out} - \dfrac{1}{2} d_c$ is the mean radius of the coil.

Table 8.3: Dimensions and properties of the forming coil for expansion.

Symbol	Chosen value	Description
n	130 m^{-1}	turns per unit length (1 layer of windings)
g	5.7 mm	width of rectangular conductor
h	3 mm	thickness of rectangular conductor
d_w	1 mm	insulation individual conductor
d_c	2.5 mm	diameter of round conductor
d_{over}	2 mm	overall insulation
r_{min}	20 mm	minimum radius
r_{max}	25 mm	maximum radius
c	22.5 mm	mean radius
l_c	80 mm	length
σ_c	$5.6 \cdot 10^7$ S/m	electrical conductivity
$\mu_{r;c}$	1	relative magnetic permeability
μ_c	$\mu_{r;c}\mu_0$	magnetic permeability
$\rho_{m;c}$	$8.96 \cdot 10^3$ kg/m^3	mass density
$c_{T;c}$	385 J/kg K	mass specific heat
$\alpha_{T;c}$	$16.4 \cdot 10^{-6}$ 1/^{o}C	coefficient of linear thermal expansion
$k_{th;\tau}$	$393 \cdot 10^{-5}(1/^o$C)	coefficient of variation of electrical conductivity with temperature
κ_c	385 W/(m K)	thermal conductivity

Further, the mutual inductance between the forming coil and the workpiece can be approximated with

$$M_{cw} = k_c(L_c \ L_w)^{1/2}, \tag{8.19}$$

where the coupling coefficient between the forming coil and the workpiece k_c is

$$k_c = \left(\frac{2\ c}{a+b}\right)^2. \tag{8.20}$$

It is important also to calculate the total pressure exerted on the forming coil. On the inside surface of the forming coil, the pressure

$$p_{in} = \frac{1}{2}\mu_0(I_{coil} - I_{work})^2, \tag{8.21}$$

will act, while on the outside surface of the forming coil, the pressure

$$p_{out} = \frac{1}{2}\mu_0 I_{work}^2, \qquad (8.22)$$

will act, where I_{coil} and I_{work} are the currents per unit length in the forming coil and in the workpiece, respectively. So, the total pressure acting on the forming coil will be

$$p_{coil} = p_{out} - p_{in} = \frac{1}{2}\mu_0 I_{coil}(2I_{work} - I_{coil}). \qquad (8.23)$$

The pressure exerted on the forming coil is larger than the pressure on the workpiece and it is directed radially inward, thus subjecting the forming coil to compression. As can be seen from Eq. (8.23), when both I_{coil} and I_{work} are oscillating currents with different phase, it is possible that the forming coil is subjected to expansion for some time. This may lead to failure of the forming coil if it is not designed properly.

The problem of alternating loading on the forming coil may be avoided by using a clamp diode, as suggested in Chapter 3. The clamp diode that fit best our requirements showed to be too expensive for the purpose of these experiments and finally it has not been applied, with disastrous effects.

8.3   Numerical simulations and favored choice of parameters

For each type of mild steel that has been considered, many combinations of parameters have been simulated in order to find the optimum combination to obtain the required deformation of 15% .

Further, in the simulations it has been assumed that the forming coil will not deform during the whole process. It has also been assumed that the parameters of the network model do not change during the electromagnetic forming process.

During the first stages of the design process of the set-up a damped current pulse has been considered, since the presence of a clamp diode has been assumed. Such a typical damped current pulse is presented in Fig. 3.5 (b) with dashed line and 8.7 (b).

Since the resistance and self inductance of all other parts in the forming system are not known in the beginning of the designing process, we estimate

them to be in accordance to the values of comparable experimental set-up in the literature, see [140, 191]

$$R_{ext} = 2 \text{ m}\Omega, \tag{8.24}$$

$$L_{ext} = 0.2 \text{ } \mu\text{H}. \tag{8.25}$$

In the circuit, we have assumed that

$$R_{diode} = 0 \text{ }\Omega, \tag{8.26}$$

and because the clamp diode is supposed to be positioned very close to the forming coil, we have assumed that

$$R_{int} = 0 \text{ }\Omega, \tag{8.27}$$

$$L_{int} = 0 \text{ H}. \tag{8.28}$$

When applying the theory presented in Section 8.1, we may construct some diagrams from where we may find a favorite choice of parameters for the experimental set-up. These diagrams are presented in Fig. 8.6.
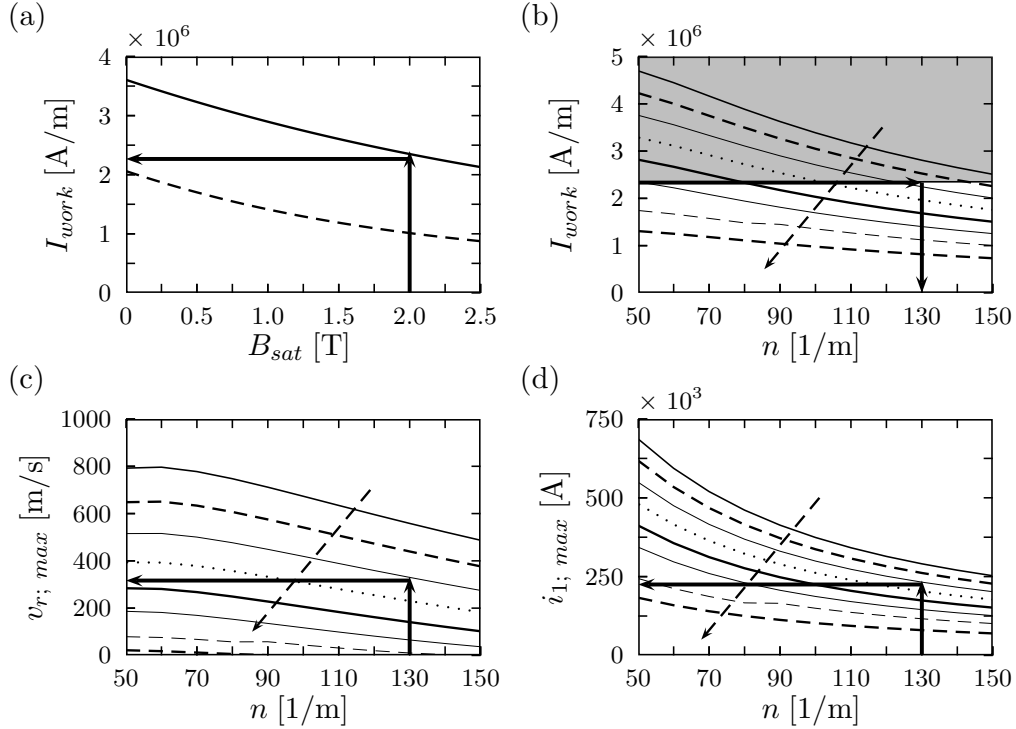
Figure 8.6: Diagrams for the choices of the optimal parameters for obtaining a final deformation of 15% with a 3-piece (blank) can.

In Fig. 8.6 (a), the maximum current in the workpiece required to reach the yielding point (dashed line) and to reach the final deformation (thick line) as a function of B_{sat} is shown. In panels Fig. 8.6(b), (c) and (d), the parameters, as a function of the number of turns per unit length n, for $C = 800\ \mu$F and $B_{sat} = 2$ T are shown. The subsequent curves in the sequence of the dashed arrow refer to $V_0 = \{20,\ 18,\ 16,\ 14,\ 12\ 10,\ 8,\ 6\}$ kV, respectively.

When B_{sat} is chosen, e.g. $B_{sat} = 2$ T, the maximum current per unit length I_{work} in the workpiece to be acquired is easily found in Fig. 8.6 (a) by following the thick lines in the sense indicated by the arrows. The current I_{work} so found is the current with which the final deformation is reached, when a static force is applied on the workpiece, thus without taking into account the temporal changes of the total pressure exerted on the workpiece.

Subsequently, we have chosen some values for the capacitance C of the capacitor bank so that the same I_{work} as in Fig. 8.6 (a) may be reached. For each capacitance the same diagrams are constructed, see Fig. 8.6 (b). For the given capacitance, e.g. $C = 800\ \mu$F, the final deformation may be theoretically reached for all combinations of voltage V_0 and number of turns per unit length n of the forming coil in the shaded region of Fig. 8.6 (b).

We have chosen the charge voltage $V_0 = 10$ kV, and following the sense indicated with arrows in Fig. 8.6 (b), the required number of turns per unit length n in the forming coil is $n = 130$ m^{-1}. Using this number of turns, we find following the sense indicated with arrows in Fig. 8.6 (c) the maximum radial velocity that may be acquired by the workpiece. Further, from Fig. 8.6 (d) we have the maximum current in the forming coil, thus the current that has to be used in choosing the high-voltage high-current switch.

Based on these diagrams a favored combination of number of turns per unit length in the forming coil $n = 130$ m^{-1}, capacitance $C = 800\ \mu$F and charge voltage $V_0 = 10$ kV is chosen. For this combination of parameters the required 15% final deformation of the workpiece may be reached, in normal circumstances.

During the forming process, the total pressure applied on the workpiece will no longer be a static one and other unknown material parameters may play a role in the deformation process. For this reason we finally decided to chose a slightly higher voltage $V_0 = 12$ kV instead of $V_0 = 10$ kV. For the favored combination, with $n = 130$ m^{-1} turns per unit length, capacitance $C = 800\ \mu$F and charge voltage $V_0 = 12$ kV, the temporal behavior of some quantities has been investigated in order to see if the chosen combination is the right one, since we want to have rapid deformation that occurs at early stages of the

current pulse, see Fig. 8.7. These results were obtained using a clamp diode, and therefore the pressure on the coil p_{coil}, see Fig. 8.7 (e) has only negative values, while the currents in the forming coil $i_1(t)$ and in the workpiece $i_2(t)$ are damped current pulses. The deformation energy w_{def} required to obtain the 15% deformation of the workpiece is acquired in a very short interval of time, due to the excess pressure exerted on the workpiece, see the hatched area
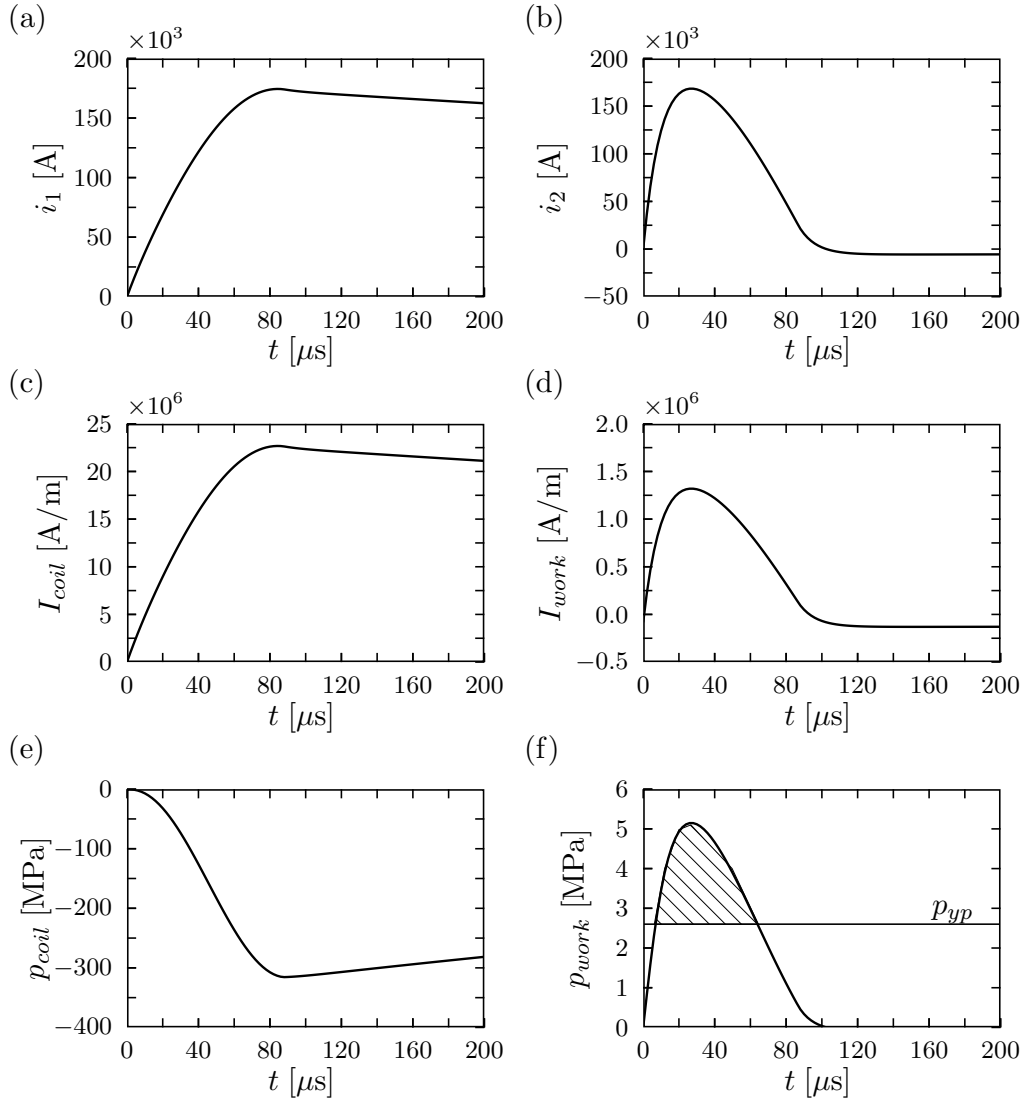
Figure 8.7:   Various quantities of the forming system obtained with the favored combination of parameters $C = 800$ μF, $V_0 = 12$ kV and $n = 130$ m^{-1} when a clamp diode is applied, for a 3-piece (blank) can.

on Fig. 8.7 (f), where the yielding pressure is $p_{yp} = 2.7$ MPa.

Despite some changes in the given properties of the workpiece, motivated by mechanical tests on the materials of the beverage cans at Corus, we finally ended up with a forming coil as presented in the previous section. This coil was then fabricated. Besides, it was decided not to use a clamp diode, so further on, the current pulses in the forming coil and workpiece will be oscillating ones.

At this stage, an intricate stress-strain relation for the materials was provided by Corus. This relation gave the dependence of the stress on strain and deformation velocity, thus it was of the form $\sigma_{eff} = \sigma_{eff}(\varepsilon_{eff}, \dot{\varepsilon}_{eff})$.

Now, the design process had to be changed. The main question had become: given the forming coil, what is the best combination of the remaining parameters, capacitance C and charge voltage V_0, in order to reach a deformation of i.e. 15% without damaging the forming coil?

The choice of the capacitance C was limited to combinations that may be obtained with 10 legs that can be adjusted with capacitors of $3\mu F$, $13.5\mu F$, $21.5\mu F$ and $37.5\mu F$. For each type of material, diagrams similar to those in Fig. 8.8 have been constructed. In this figure, the subsequent curves in the sequence of the arrow refer to $C = \{81,\ 60,\ 43,\ 35,\ 27,\ 21\}\ \mu F$, respectively.

Using the diagrams in Fig. 8.8, for simplicity of construction of the experimental set-up we have chosen one capacitance, namely $C = 60\ \mu F$, so that the only free parameter in the process is the voltage V_0. Further it has been supposed that the high-voltage, high-current switch may operate on a large range of voltages and that the charging unit may be easily adjustable to the
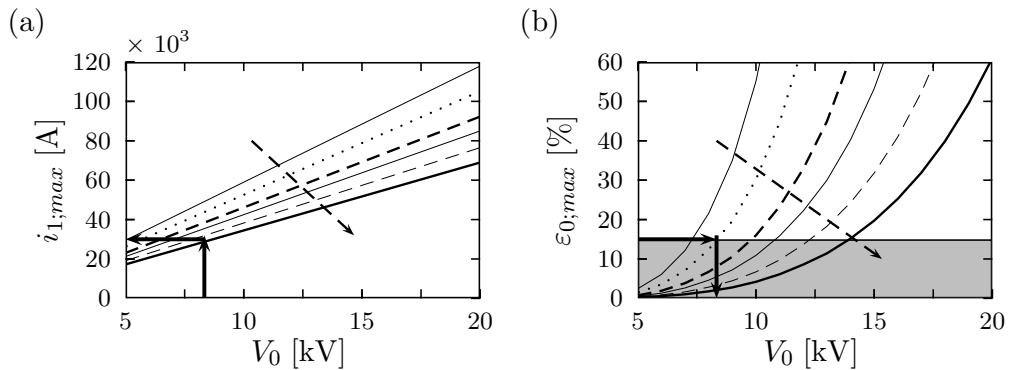
Figure 8.8:   Maximum current in the forming coil (a) and conventional strain (deformation) (b) acquired with various combinations of capacity C and voltage V_0 and with the constructed forming coil with $n = 130$ m^{-1}, for a 3-piece (blank) can.

desired charge voltage V_0.

Finally, with the chosen capacitance, for each type of can, the charge voltage that will yield a plastic deformation of 15% has been determined. For each type of can, similar diagrams have been constructed to show the temporal behavior of some parameters during the plastic deformation. Examples of such diagrams for a 3-piece (blank) can are given in Figs. 8.9 and 8.10.
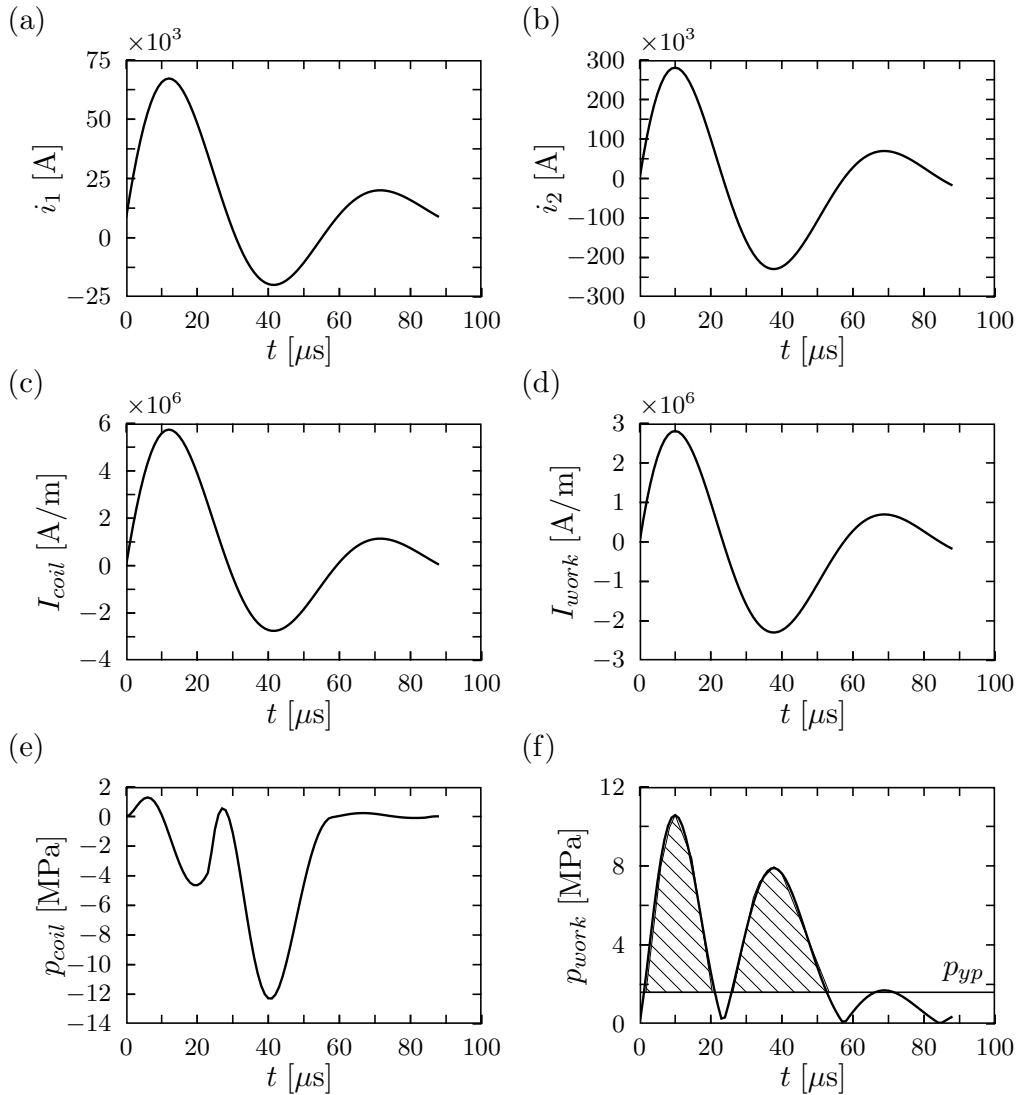
Figure 8.9:   Various quantities of the forming system obtained with the final combination of parameters $C = 60$ μF, $V_0 = 8.4$ kV and $n = 130$ m^{-1} in the constructed forming coil, when a clamp diode is not applied, for a 3-piece (blank) can.

(a)

(b)

(c)

(d)

Figure 8.10: Various quantities of the forming system obtained with the
final combination of parameters $C = 60\ \mu\text{F}$, $V_0 = 8.4$ kV
and $n = 130$ m $^{-1}$ in the constructed forming coil, when a
clamp diode is not applied, for a 3-piece (blank) can.

For a 3-piece (blank) can, at least 15% deformation of the workpiece will
be acquired with the final combination of parameters a capacitance $C = 60\ \mu\text{F}$
and charge voltage $V_0 = 8.4$ kV in a forming system that uses the constructed
forming coil and without the application of a clamp diode.

The temporal behavior of some quantities in this forming system have
been investigated in order to show that the chosen combination is the right one
for obtaining at least 15% final deformation of the workpiece. These results
were obtained without a clamp diode, and therefore the currents in the forming
coil $i_1(t)$ and in the workpiece $i_2(t)$ are underdamped current pulses.

The deformation energy w_{def} required to obtain the 15% deformation of
the workpiece is acquired in a very short interval of time, due to the excess
pressure exerted on the workpiece, see the hatched area on Fig. 8.9 (f), where
the yielding pressure is $p_{yp} = 1.8$ MPa. We notice also that the forming coil
is subjected for a while to expansion, since the pressure on the forming coil

p_{coil} in Fig. 8.9 (e), calculated with Eq. (8.23) reaches positive values when $t < 10$ μs. When $t > 10$ μs, the forming coil is subjected to compression most of the time, since the pressure p_{coil} has then only negative values.

When a clamp diode has been applied, see Fig. 8.7 (e) the pressure on the coil has only negative values. However, the values of the corresponding quantities in Figs. 8.7 and 8.9 cannot be compared with each other since the capacitance C, the charge voltage V_0 and the material properties of the work-piece differ very much.

8.4 Experimental results

Experimental results obtained from the experimental set-up in Fig. 8.11 are presented here. The experiments have been performed with the equipment provided by KEMA High Voltage Laboratory, at their location in Arnhem.
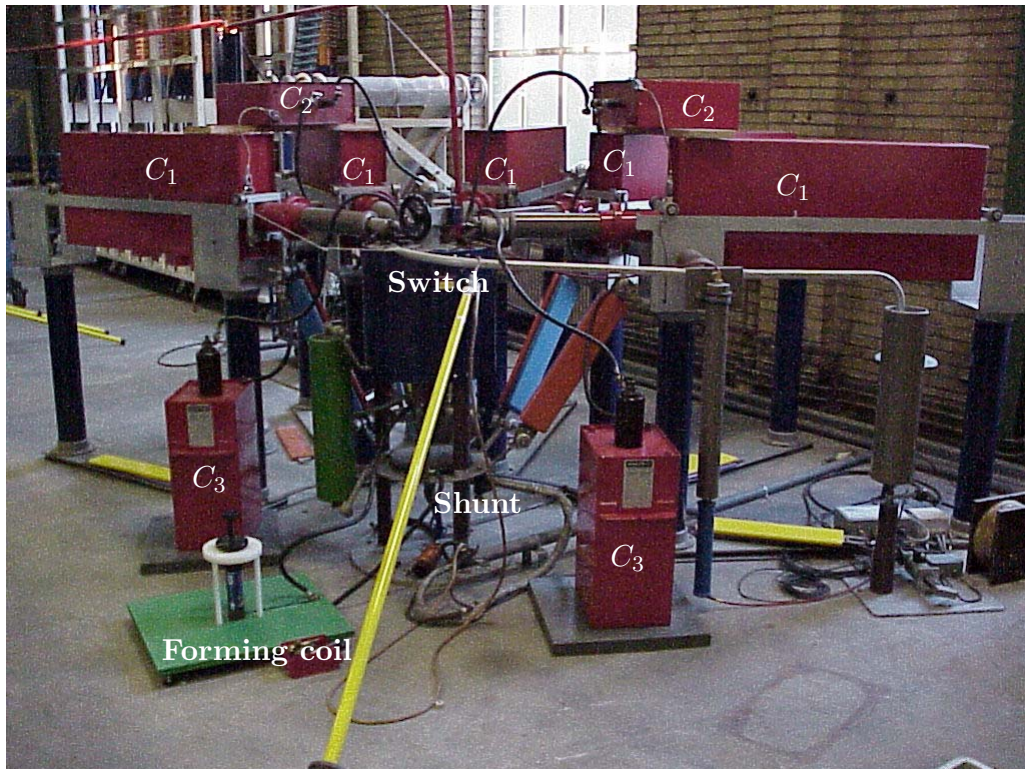
Figure 8.11: Experimental set-up for electromagnetic forming con-
structed at KEMA.

The experimental set-up consisted of:

- a capacitor bank with a measured capacitance $C = 60.25\ \mu\text{F}$ (being a parallel connection of 5 capacitors of $C_1 = 2.5\ \mu\text{F}$, 2 capacitors of $C_2 = 3\ \mu\text{F}$ and 2 capacitors of $C_3 = 21.5\ \mu\text{F}$)

- a charging unit of the capacitor bank, able to charge the capacitor bank at voltages up to 100 kV; the required range of charge voltage for the experiments was 6 - 20 kV

- a shunt (500 V @ 100 kA) for measuring the discharge voltage and the discharge current

- a high-voltage, high-current spark-gap switch

- connecting cables with a transversal cross section of about 70 mm^2

- measuring equipment.

In Fig. 8.12, the forming coil, manufactured by Corus, together with one of the beverage cans is presented before deformation.

Three sets of cans have been deformed. Two sets are the so-called 3-piece cans where the can wall is basically undeformed thin steel sheet of 0.18 mm thickness. One of these series comes from commercial production and the cans were coated with a blue decorating coating. These cans are labeled 'blue'.

The second series has been manufactured by Corus and the cans were provided with a thin clear coating; these cans are labeled 'blank'. The first

Figure 8.12:   Detail of the forming coil with the thin beverage can on top
of it (left) and after the failure (right).

Figure 8.13: Set of 3-piece (blank) and 2-piece (white) cans after elec-
tromagnetic expansion.

set of blue (3-piece) cans had similar properties with the second set of 3-piece
(blank) cans, except for the fact that a thin layer of paint was present on the
first set of cans.

The third series of cans are from a commercial production of so-called
2-piece cans. The can walls of 0.09 mm thickness is obtained by heavy cold
working of steel sheet and has a very high yield stress due to work hardening.
The cans are provided with a standard white base coat and labeled 'white'.

The deformations obtained with the set of blue cans were similar to the
deformations of the set of blank cans, but the paint layer has been damaged
during deformation, due to the temperature rise of the workpiece. The defor-
mations obtained with the third set of 2-piece (white) cans were very small
since the material is a prestrained one with very large yielding stress, and the
layer of white pain present on them was also partially damaged due to the
temperature rise of the workpiece.

In Fig. 8.13, two sets of cans after electromagnetic forming at different
voltages are presented. The final deformation of the cans has been measured
as the increase of the workpiece outside circumference after deformation and
the results are presented in Table 8.4.

Finally, the only measurements that could be done at KEMA were:

- the instantaneous value of the discharge current $i_1(t)$

- the instantaneous value of the voltage on the forming coil $u_{coil}(t)$

- the outside circumference of the workpiece before and after deformation.

Table 8.4:   Increase of the circumference of the beverage cans (in mm) after deformation at various charge voltages V_0.

V_0	10 kV	12 kV	13 kV	14 kV	15 kV	16 kV	18 kV
blue	0.5	0.95	1.25	1.6	2.25	no try	no try
blank	0.6	0.9	1.25	1.7	2	no try	no try
white	no try	-	no try	0.3 ± 0.2	0.4 ± 0.2	0.6 ± 0.2	

8.5   Comparison of the predicted results with the experimental results

In this section the measured experimental results are compared with the predicted numerical results.

The only important electrical quantity that has been measured is $i_1(t)$. This is the only quantity that can be compared with our previous simulations, and may give some information about the temporal development of the electromagnetic forming process.

In Fig. 8.14 (a) the measured current (dotted line) is presented together with the predicted current (dashed line) for $C = 60.25$ μF and $V_0 = 14$ kV. Clearly, the experimental results show no agreement with the numerical simulations. Among the possible causes for such a big discrepancy between the numerical results and the experimental ones, we have considered the following possibilities:

- different parameters in the network model

- different formula for the pressure on the workpiece

- other saturation flux density B_{sat}

- changes of properties due to temperature rise.

In order to understand which combination of parameters could bring the predicted current $i_1(t)$ closer to the measured current, we performed several computations while changing the various parameters of the model.

Our suspicion was that the values we proposed for the external resistance and self-inductance, $R_{ext} = 2$ mΩ and $L_{ext} = 0.2$ μH, respectively, were not achieved in the experimental set-up, see for example the long connecting wires

in Fig. 8.11. However, with

$$R_{ext} = 15 \text{ m}\Omega, \tag{8.29}$$

$$L_{ext} = 2.5 \text{ }\mu\text{H}, \tag{8.30}$$

we got almost the same discharge current with our model, see Fig. 8.14 (a). Using these new parameters, we obtained an equally good match between the modelled current and the measured current for all types of cans and all charge voltages, for which the experiments have been carried out.

Just for comparison, the numerical results obtained with the former values of R_{ext} and L_{ext} are indicated with dashed thick lines in Figs. 8.14 and 8.15.

With the new parameters R_{ext} and L_{ext} and using the pressure on the workpiece as calculated in Eq. (8.16), we have not obtained the same deformation as the measured ones, see the graphs with thin solid lines in Figs. 8.14 and 8.15. When the pressure on the workpiece is calculated with Eq. (8.15) and the new parameters R_{ext} and L_{ext} are used, our theoretical model gives the same final deformation as the measured ones, see the graphs with thick solid lines in Figs. 8.14 and 8.15.

The measured values of the increase in the circumference of the workpiece, as compared with the ones obtained for the model with the new parameters from Eqs. (8.29) and (8.30) and pressure formula from Eq. (8.15), are given in Tables 8.5 and 8.6.

Table 8.5: Comparison of the measured increase of the circumference of the workpiece (in mm) with the re-calculated values with the new parameters for the blank cans.

V_0	10 kV	12 kV	13 kV	14 kV	15 kV
measured	0.5-0.6	0.9-0.95	1.25	1.6-1.7	2-2.25
calculated	0.38	0.8	1.17	1.78	2.45

Table 8.6: Comparison of the measured increase of the circumference of the workpiece (in mm) with the re-calculated values with the new parameters for the white cans.

V_0	12 kV	14 kV	15 kV	16 kV	18 kV
measured	-	0.3 ± 0.2	0.4 ± 0.2	0.6 ± 0.2	collapse coil
calculated	0	0.76	0.87	1.04	1.63

(a)

(b)

(c)

(d)

(e)

(f)
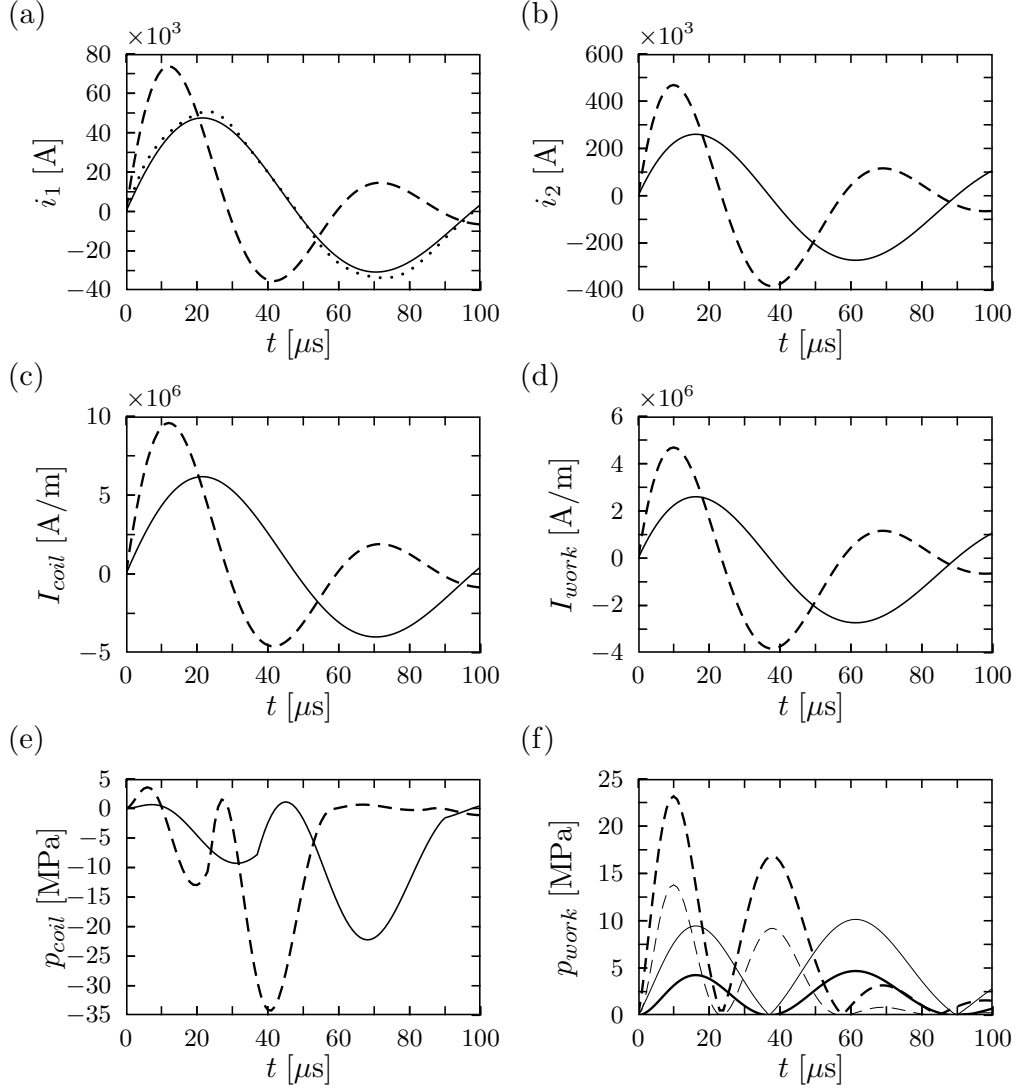
Figure 8.14:   Comparison of the initial numerical results with the recal-
culated numerical results for $C = 60.25$ μF and $V_0 = 14$
kV, for a 3-piece can. In panel (a) the measured current is
also shown (dotted line). In panels (b, c, d, e, f) are pre-
sented the values obtained with the former R_{ext} and L_{ext}
when $p_{work}^{(old)}$ (thin dashed line) or $p_{work}^{(new)}$ (thick dashed line)
is applied, and the values obtained with the new R_{ext} and
L_{ext} when $p_{work}^{(old)}$ (thick solid line) or $p_{work}^{(new)}$ (thin solid line)
is applied.
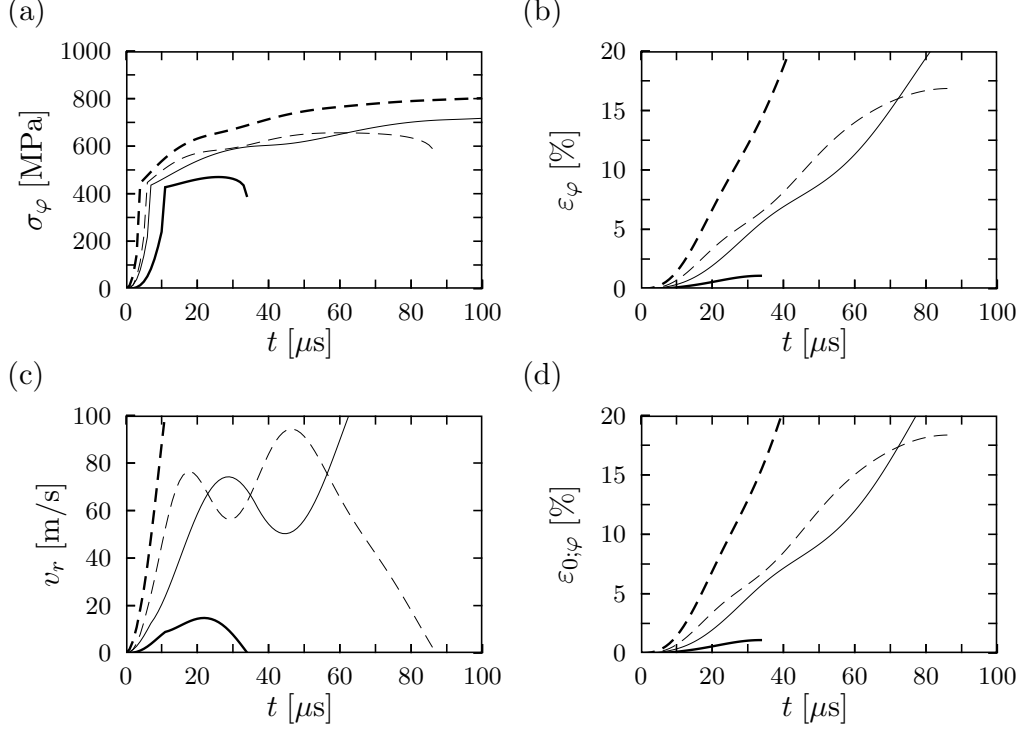
Figure 8.15: Comparison of the initial numerical results (dashed line) with the recalculated numerical results (thick line) for $C = 60.25$ μF and $V_0 = 14$ kV, for a 3-piece can. In panels (a, b, c, d) are presented the values obtained with the former R_{ext} and L_{ext} when $p_{work}^{(old)}$ (thin dashed line) or $p_{work}^{(new)}$ (thick dashed line) is applied, and the values obtained with the new R_{ext} and L_{ext} when $p_{work}^{(old)}$ (thick solid line) or $p_{work}^{(new)}$ (thin solid line) is applied.

Due to the better agreement of the new numerical results with the measured ones, we may conclude that, using the new parameters R_{ext} and L_{ext}, we can calculate the deformation to be obtained in this electromagnetic forming system.

We notice, that the maximum radial velocity acquired by the workpiece during the deformation process is not very high, so the influence of the strain rate term in the stress expression $\sigma_{eff} = \sigma_{eff}(\varepsilon_{eff}, \dot{\varepsilon}_{eff})$ is very small. Due to the larger values of R_{ext} and L_{ext} in the primary circuit, the currents $i_1(t)$ and $i_2(t)$ stay below their originally predicted values. Therefore, the acquired deformation will be much (ten times) smaller that the one calculated before.

(a)   (b)
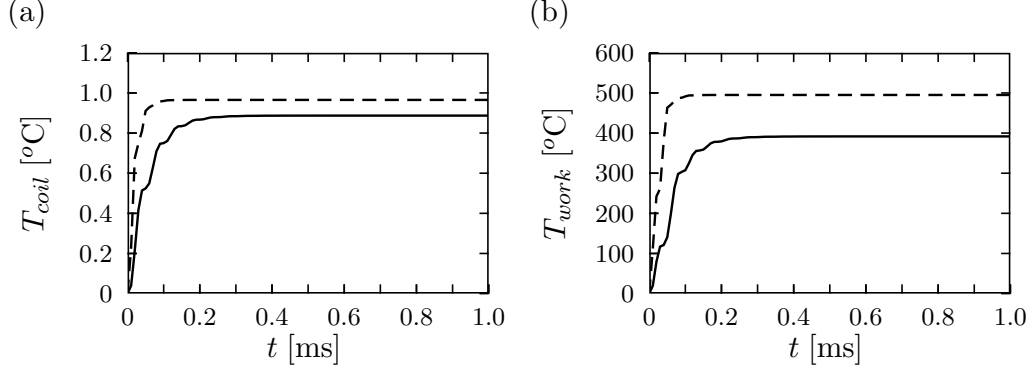
Figure 8.16:   Temperature rise T in the forming coil (a) and in the work-
                piece (b) with the initial parameters (dashed line) and with
                the recalculated parameters (full line) for $C = 60.25$ μF and
                $V_0 = 14$ kV without considering the heat exchange.

In these new calculations, the temperature rise in the forming coil and workpiece has not been taken into account. The temperature rise in the work-piece has been calculated from Eq. (6.33) with the isothermal assumption for a thin workpiece. The temperature rise in the forming coil has been calculated in a similar manner, using the isothermal assumption for a thin object. It has been also assumed that there is no heat exchange between the forming coil and the workpiece, see Fig. (8.16).

We notice that the temperature continues to rise significantly after the deformation, because the current remains to flow both in the forming coil and in the workpiece a long while after the deformation.

8.6   Conclusions from the experimental results

With the new parameters R_{ext} and L_{ext} of the network model, there seems to be a good agreement between the numerical and the experimental results for the current in the forming coil $i_1(t)$, and there is also a good agreement between the numerical and experimental results for the deformation. It means that, with the same design procedure presented here, a better experimental set-up may be designed, so that the actual deformation of the beverage cans will be the desired one.

Upon adapting the model accordingly, the required final deformation of about 15% will be reached in the unchanged configuration with $V_0 = 19$ kV for

the blank cans and with $V_0 = 26.5$ kV for the white cans. With these values, the forming coil has to be dimensioned so that is allows a maximum current $i_{1;max} = 65$ kA for the blank cans and $i_{1;max} = 83$ kA for the white cans, respectively.

In future experimental work, the resistance and self-inductance of the other components than the forming coil and the workpiece have to be controlled. Particular attention should be paid to the temperature rise of the forming coil and the workpiece. The use of a clamp diode will improve an eventual experimental set-up as regarding the pressure exerted on the forming coil.

Chapter 9

Steps towards a more complex model of the problem

This chapter presents some steps that may lead to the improvement of both theoretical and experimental models developed in the previous chapters. With a more complex model we will get closer to a realistic model, and it is possible to obtain a better accordance between the numerical simulations and the experimental results.

Since the analysis of all parts of the forming system is too complex we will investigate only the forming coil and the workpiece. The other parts of the forming system are assumed to be invariant in their properties and behavior.

In the previous chapters two models have been developed based on the assumption that the geometry and the parameters that characterize the forming system are time, temperature and deformation invariant. This is not the case in a real forming system, so we will describe here the changes induced by temperature rise, and by deformation in the geometry and parameters of the configuration. Further, all influences are integrated in a complex model.

The computational effort being significantly smaller for the experimental model, numerical results related to the final network model described in Chapter 8, i.e., with R_{ext}, L_{ext} and p_{work} as defined in Eqs. (8.29), (8.29) and (8.15), respectively, are presented. For the theoretical model, similar steps may be followed, but with the reservation that up till now the results couldn't be verified.

9.1   Changes due to deformation

The geometry of both the forming coil and workpiece changes within the forming process. At the end of an ideal electromagnetic forming process, we may obtain a certain permanent deformation of the workpiece, while the forming coil remains unchanged, not damaged and able to be used in a large number of subsequent forming steps. We will consider here such an ideal case, where the forming coil is undeformed and only the workpiece deforms.

The deformation of the workpiece during the forming process means changes of its linear dimensions, surface area and volume, but only one type of geometrical changes is predominant in each configuration. Moreover, there exists a certain dependence on deformation state for the electromagnetic, elastic and thermal properties of the workpiece, especially when the deformation takes place with large velocity, but this dependence will not be investigated here.
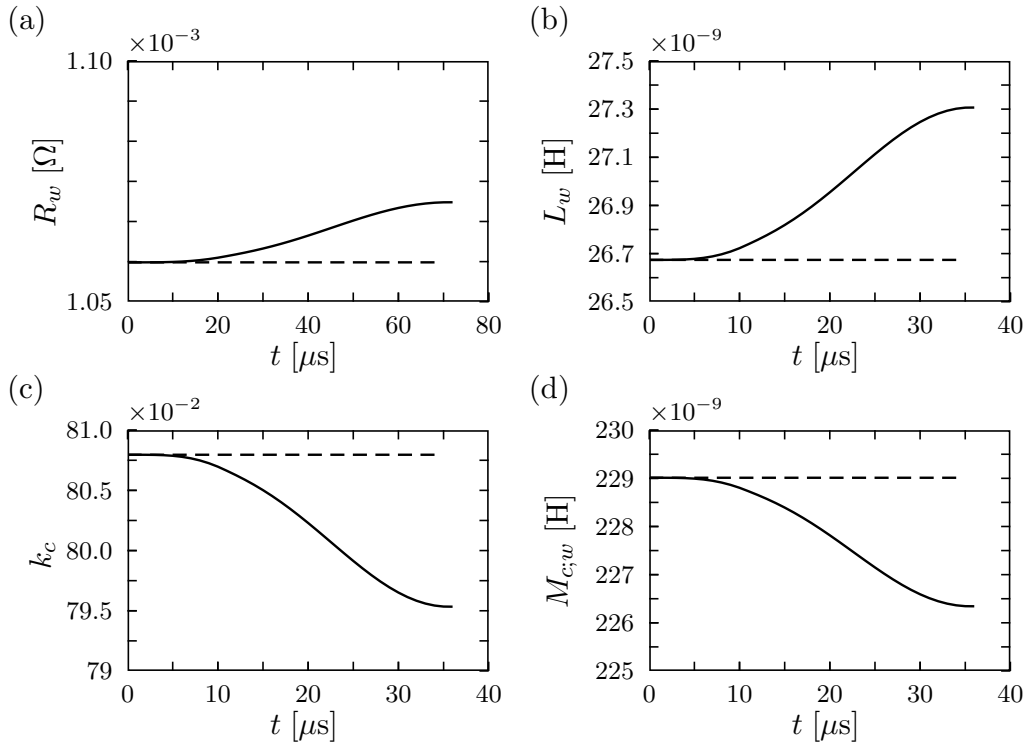
Figure 9.1:   Elements of the network model with (solid line) and without (dashed line) considering the changes of the geometry due to deformation.
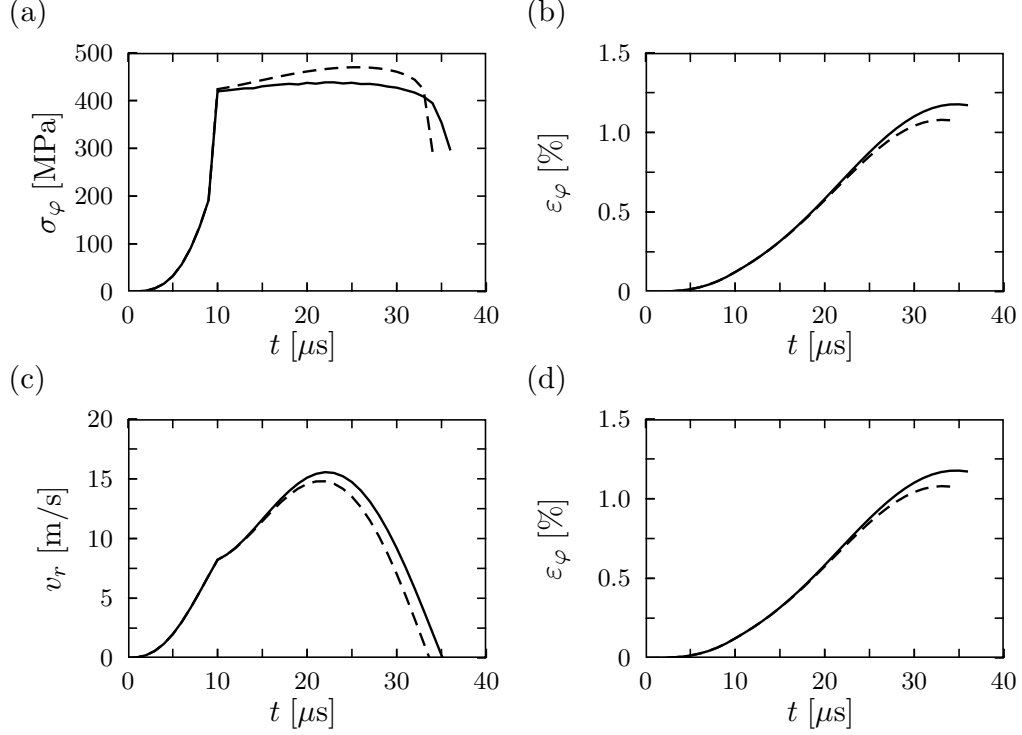
Figure 9.2: Various quantities of the forming system with (solid line) and without (dashed line) considering the changes of the geometry due to deformation.

We focus in this section only on the changes brought by the deformation of the workpiece on the forming process in general. Thus, only the geometry of the workpiece changes.

In principle, at each instant of time, based on the parameters of the forming system at the previous instant of time, the new geometry of the forming system may be calculated. Using this new geometry, the new parameters of the equivalent network model may be re-calculated and subsequently new currents within the forming coil and workpiece, new deformation of the forming coil and workpiece, etc., may be obtained in an iterative manner.

Since we have assumed here that only the workpiece deforms during the forming process, the only elements of the network model, see Chapter 3 are R_w, L_w, k_c and M_{cw}, in accordance to their definitions in Eqs. (3.10), (3.11), (3.14) and (3.15), respectively.

In Fig. 9.1 we present the temporal evolution of these elements of the

network model during deformation, as compared with the values of the same elements when the invariant geometry is assumed, see Chapter 8. The changes in the values of these elements of the network model yield changes in the values of the currents and further in the stress and strain.

In Fig. 9.2, we present the temporal evolution of some quantities related to the forming system discussed in the previous chapter, when the changes of the geometry due to the deformation are taken into account. For the considered case, the absolute changes of the corresponding quantities are not major because the deformation of the workpiece is not very large, but in view of their relative size these changes have to be taken into account within a realistic model of the forming process.

9.2   The heat exchange between the forming coil and the workpiece

Beside the temperature rise in the configuration and the quasistatic thermoelastic field as they have been calculated in Chapter 6, the heat exchange between the components of the forming system and the environment may also be calculated. In any configuration, there exist three ways to transfer the heat between two solid bodies, namely by conduction, by convection and by radiation. For the forming systems described in this thesis, except for the heat conduction that has been analyzed in Chapter 6, we have only heat radiation. The heat radiation occurs when a layer of air or vacuum exists between two solid bodies at different temperatures, or when there is only a body that radiates heat into the environment. The thermal radiation of a body is characterized by the black-body emissive power density E_b

$$E_b = k_{S-B}T^4 \tag{9.1}$$

where $k_{S-B} = 5.6697 \cdot 10^{-8}$ W/m^{2}K^4 is the Stefan-Boltzmann constant and T is the absolute temperature of the body. In general, the radiation heat transfer between two bodies with absolute temperatures T_1 and T_2 is

$$q_R = F_{1;2}k_{S-B}(T_1^4 - T_2^4), \tag{9.2}$$

where $F_{1;2}$ is a correction factor (view factor) depending on the type of surface and on the relative position of the two surfaces. The main property of the view factor is that for an enclosure made of N surfaces, for each surface i the

summation rule

$$\sum_{j=1}^{N} F_{i;j} = 1, \qquad (9.3)$$

is valid, where $F_{i;i}$ is the fraction of the radiation leaving the surface i and intercepted by itself, with $F_{i;i} = 0$ if the surface i is flat or convex and $F_{i;i} \neq 0$ if the surface is concave.

The easiest way to solve the heat transfer problem in our case is to use an electrical analogy, see [5]. Each surface i, having the surface area A_i, is characterized by a surface (color) resistance, $(1-e_i)/A_i e_i$ and a view resistance, $1/A_i F_{i;j}$, where e_i is the emissivity of the surface. The surfaces with known temperatures are represented as sources of radiation heat $E_{b;i}$, while the air is represented as a black surface, $E_{b;\infty}$.

First, we consider the workpiece as a separate system located in air, and without heat exchange between it and the forming coil. With such a condition, the equivalent electric representation in Fig. 9.3 is obtained. The equations corresponding to the equivalent circuit in Fig. 9.3 are

$$E_{b;out} - E_{b;\infty} = \dot{Q}_{out} \left(\frac{1}{F_{w;\infty}^{out} A_{out}} + \frac{1-e}{e\,A_{out}} \right), \qquad (9.4)$$

$$E_{b;in} - E_{b;\infty} = \dot{Q}_{in} \left(\frac{1}{F_{\infty;w}^{in} A_{\infty}} + \frac{1-e}{e\,A_{in}} \right). \qquad (9.5)$$
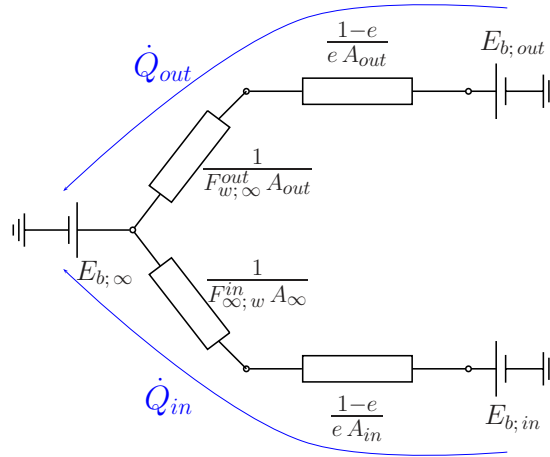
Figure 9.3: The equivalent electric network representation of the workpiece in thermodynamics.

With

$$F_{w;\infty}^{out} = 1, \quad F_{\infty;w}^{in} = 1, \tag{9.6}$$

$$A_\infty = 2\pi r_1^2, \quad A_{out} = 2\pi r_2 l_w, \quad A_{in} = 2\pi r_1 l_w, \tag{9.7}$$

the following radiation losses per surface unit of the workpiece are obtained

$$q_{in} = \frac{\dot{Q}_{in}}{A_{in}} = k_{S-B}\frac{r_1 e}{(l_w - r_1)e + r_1}(T_{in}^4 - T_\infty^4), \tag{9.8}$$

$$q_{out} = \frac{\dot{Q}_{in}}{A_{in}} = k_{S-B}e(T_{out}^4 - T_\infty^4), \tag{9.9}$$

where T_{in} is the absolute temperature of the inside surface of the workpiece, T_{out} is the absolute temperature of the outside surface of the workpiece and T_∞ is the absolute temperature of the environment.

In Fig. 9.4, the equivalent electric circuit of the system workpiece-forming coil obtained for a forming system for expansion as the one described in Chapter 8, is presented. The equations corresponding to the equivalent circuit in Fig. 9.4 are

$$E_{b;w} - E_{b;c} = (\dot{Q}_{w;c} + \dot{Q}_{w;\infty})\frac{1 - e_w}{e_w A_w} + \dot{Q}_{w;c}\frac{1}{F_{w;c}A_w} + (\dot{Q}_{w;c} - \dot{Q}_{c;\infty})\frac{1 - e_c}{e_c A_c}, \tag{9.10}$$

$$E_{b;w} - E_{b;\infty} = (\dot{Q}_{w;c} + \dot{Q}_{w;\infty})\frac{1 - e_w}{e_w A_w} + \dot{Q}_{w;\infty}\frac{1}{F_{w;\infty}A_w}, \tag{9.11}$$

$$E_{b;c} - E_{b;\infty} = (\dot{Q}_{c;\infty} - \dot{Q}_{w;c})\frac{1 - e_c}{e_c A_c} + \dot{Q}_{c;\infty}\frac{1}{F_{\infty;c}A_\infty}. \tag{9.12}$$
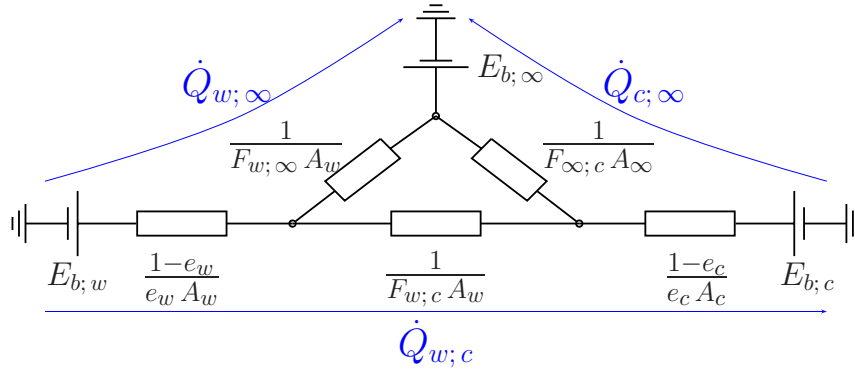
Figure 9.4:   The equivalent electric representation of the system coil-workpiece in thermodynamics.

Since the whole configuration has been assumed very long, there is no heat exchange from the inside part of the forming coil and

$$\dot{Q}_{c;\infty} = 0. \tag{9.13}$$

The view factors $F_{c;w}$, $F_{w;c}$ and $F_{w;\infty}$ are defined for long cylinders as, see [5]

$$F_{c;w} = 1, \quad F_{w;c} = \frac{A_c}{A_w}, \quad F_{w;\infty} = 1 - \frac{A_c}{A_w}, \tag{9.14}$$

and we have

$$A_w = 2\pi r_{mean} l_w, \quad A_c = 2\pi c l_c, \quad A_\infty = 2\pi r_{mean}^2. \tag{9.15}$$

After solving the system of equations given by Eqs. (9.10) - (9.12), the radiation losses per surface unit of the workpiece and coil are obtained as

$$q_{c;rad} = \frac{\dot{Q}_{w;c}}{A_c} = \{A_w - (1 - e_w)(1 - e_c)A_c\}^{-1}\{E_{b;w}e_w e_c A_w +$$
$$E_{b;\infty}e_c(1 - e_w)(A_w - A_c) - E_{b;c}e_c[A_w - (1 - e_w)A_c]\}, \tag{9.16}$$

$$q_{w;rad} = \frac{\dot{Q}_{w;c} + \dot{Q}_{w;\infty}}{A_w} = \{A_w - (1 - e_w)(1 - e_c)A_c\}^{-1}\{E_{b;w}e_w[A_w -$$
$$(1 - e_c)A_c] - E_{b;\infty}e_w(A_w - A_c) - E_{b;c}e_c e_w A_c\}. \tag{9.17}$$

When the forming system designed for compression is analyzed, the same equations hold with the interchanged subscripts c and w.

If we assume that the workpiece is so thin that $T_{in} = T_{out} = T_{work}$ we have then

$$\frac{\dot{Q}_{w;\infty}}{A_w} = F_{w;\infty}k_{S-B}(T_{work}^4 - T_\infty^4), \tag{9.18}$$

$$\frac{\dot{Q}_{w;c}}{A_c} = F_{c;w}k_{S-B}(T_{coil}^4 - T_{work}^4), \tag{9.19}$$

$$\frac{\dot{Q}_{w;c}}{A_w} = F_{w;c}k_{S-B}(T_{work}^4 - T_{coil}^4). \tag{9.20}$$

Then, the actual absolute temperature of the forming coil and the actual ab-

solute temperature of the workpiece may be calculated yield as

$$T_{work} = T_{\infty}^4 + \frac{1}{k_{S-B}} \left[\frac{A_w}{A_w - A_c} q_{w;rad} - \frac{A_c}{A_w - A_c} q_{c;rad} \right], \qquad (9.21)$$

$$T_{coil} = T_{\infty}^4 + \frac{1}{k_{S-B}} \left[\frac{A_w}{A_w - A_c} q_{w;rad} + \frac{A_w - 2\,A_c}{A_w - A_c} q_{c;rad} \right], \qquad (9.22)$$

or

$$T_{coil} = T_{\infty}^4 + \frac{1}{k_{S-B}} \left[\frac{A_w}{A_w - A_c} q_{w;rad} - \frac{A_w}{A_w - A_c} q_{c;rad} \right]. \qquad (9.23)$$

As shown in the previous chapter, the temperature rise in the forming coil is very small and then $q_{c;rad}$ has a negligible value as compared with $q_{w;rad}$. It means that we may neglect $q_{c;rad}$ in Eqs. (9.21) - (9.23). Then the problem is completely solved and the actual temperature in both the forming coil and the workpiece may be calculated.

We will apply this model for the calculation of the actual temperature of the forming coil and workpiece for the forming system with $C = 60\ \mu F$, $V_0 = 14$ kV and with the constructed forming coil with $n = 130\ \text{m}^{-1}$, for a 3-piece (blank) can, as considered in the previous section. Thus, for the numerical results in this section, besides the heat exchange model, the changes of the geometry due to the deformation are also taken into account, see Section 9.1.

The temporal evolution of the temperature of the forming coil and of the workpiece in this forming system are presented in Fig. 9.5.
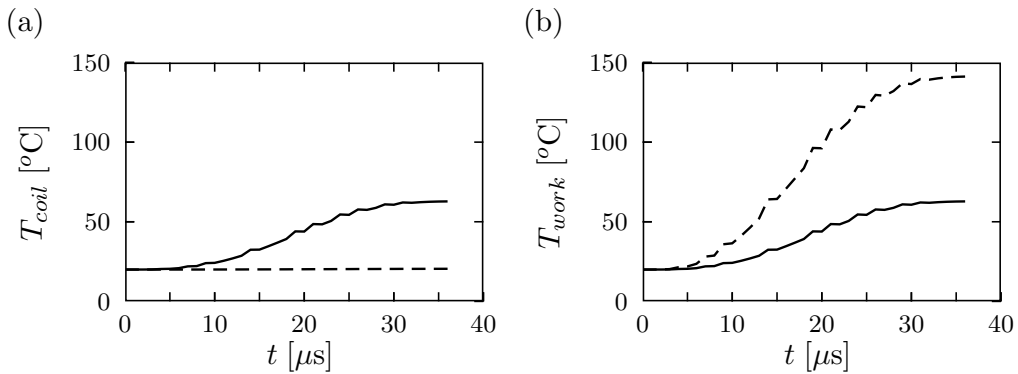
Figure 9.5:   Temperature T of the forming coil (a) and of the workpiece (b) in time domain including the changes of the geometry due to deformation, with (solid lines) and without (dashed lines) considering the heat exchange between the forming coil and the workpiece.

We notice that, when the heat exchange between the forming coil and the workpiece is not taken into account (dashed line in Fig. 9.5), the temperature rise in the forming coil is very small, while the temperature rise in the workpiece is quite large. After the heat exchange, both the forming coil and the workpiece reach the same temperature (solid line in Fig. 9.5), calculated with the model presented in this section.

9.3   Changes due to the temperature rise

The temperature rise in the forming coil and in the workpiece may lead to changes in the geometry of the forming coil and of the workpiece and also to changes in the material properties of the forming coil and of the workpiece.

The geometry of both the forming coil and workpiece changes within the forming process, not only due to the influence of electromagnetic forces, but also due to the temperature rise in the configuration. These changes in geometry due to a temperature rise concern linear dimensions, surface area and volume, but only one type of geometric changes is predominant in each configuration. We will consider here the case where the geometry of both the forming coil and the workpiece changes due to the temperature rise.

The changes with the temperature of the linear dimensions of both the forming coil and of the workpiece , over a reasonable temperature range $T \in [0, 200]$ ^{o}C, may be calculated with the simplified formula

$$x(T) = x(T_0)[1 + \alpha_T(T - T_0)], \tag{9.24}$$

where x is any linear dimension that characterizes the geometry of the configuration, α_T is the coefficient of linear thermal expansion, $2\alpha_T$ is the coefficient for changes in the superficial area and $3\alpha_T$ is the coefficient for volume changes.

These changes have not been taken into account in this way, but they are enclosed in the model via the changes in the material properties due to temperature rise. The changes in the material properties affect further the values of the elements of the network model and the value of the final plastic deformation of the workpiece.

In this section, we focus on some of the changes in the material properties related to the forming coil and to the workpiece, in the same forming system as considered in the previous sections. Thus, we have a forming system with $C = 60$ μF, $V_0 = 14$ kV and with the constructed forming coil with $n = 130$ m^{-1}, while the workpiece is a 3-piece (blank) can.

1. The electrical and magnetic properties of the materials

As mentioned in Section 3.4, the electrical properties of highly conducting materials have a strong dependence on the temperature. For the electrical conductivity, a linear dependence of conductivity with the temperature can be established for many metals at temperatures lower than the Curie temperature,

$$\sigma(T) = \frac{\sigma(T_0)}{1 + k_{th;\sigma}(T - T_0)}, \qquad (9.25)$$

where T_0 is the initial temperature, T is the actual temperature and $k_{th;\sigma}$ is the temperature coefficient of conductivity. This coefficient is equal to the temperature coefficient of the electrical resistance.

We notice that the electrical conductivity shows an important decrease in both the forming coil and the workpiece in the temperature range considered in Fig. 9.6. This decrease may have important effects in the entire model of the process and it has to be taken into account for a complex model of the electromagnetic forming system. The permeability also depends on the temperature, but further we assume that it is temperature invariant.

2. The elastoplastic properties of the materials

There exist a certain influence on the elastoplastic properties due to the temperature rise. In principle, for each material there exist a so-called "critical temperature" T_{cr}, obtained at the intersection of the curves of yielding and fracture. As the temperature rises, the material yields easily. It means that
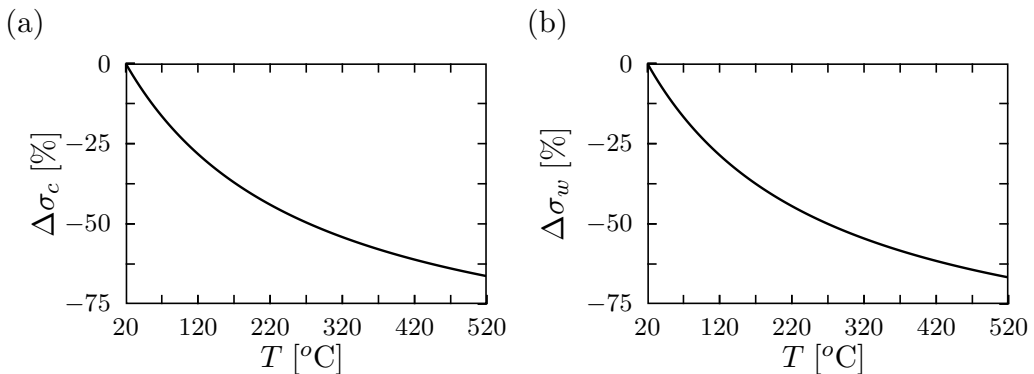
Figure 9.6:   Relative variation of the electrical conductivity with temperature for the forming coil σ_c and for the workpiece σ_w.

both the yielding stress and the ultimate stress decrease when the temperature rises.

The temperature rise has also a great influence on the strain hardening. For each material the stress-strain diagram, $\sigma(\varepsilon, \dot{\varepsilon})$ is obtained experimentally at a given constant temperature T_{exp}, and we will denote the stress-strain relation as $\sigma(\varepsilon^{(T_{exp})}, \dot{\varepsilon}^{(T_{exp})})$. The effect of a certain strain rate $\dot{\varepsilon}(T_1)$ at a certain temperature T_1 has to be converted to an equivalent strain rate at temperature T_{exp} in order to have the actual stress in the material from the diagram $\sigma(\varepsilon^{(T_{exp})}, \dot{\varepsilon}^{(T_{exp})})$. This equivalent strain rate is obtained as

$$\log \dot{\varepsilon}^{(T_{exp})} = \alpha + \frac{T_1}{T_{exp}} \left(\log \dot{\varepsilon}^{(T_1)} - \alpha \right), \tag{9.26}$$

with α a constant that depends on the actual amount of strain and has to be determined experimentally. For the numerical results we have assumed that $\alpha = 8.3$.

The mass density changes with the temperature, and this change can be calculated taking into account the mass invariance

$$\rho_m(T) = \frac{\rho_m(T_0)}{1 + k_{te;vol}(T - T_0)}, \tag{9.27}$$

where θ_0 is the initial temperature, θ is the actual temperature and $k_{te;vol}$ is the coefficient of volumetric thermal expansion. For relatively small changes in temperature the value of this coefficient is $k_{te;vol} = 3k_{te}$. For a large range of temperature, the mass density of both the forming coil and the workpiece varies very little with the temperature, see Fig. 9.7.

(a)   (b)
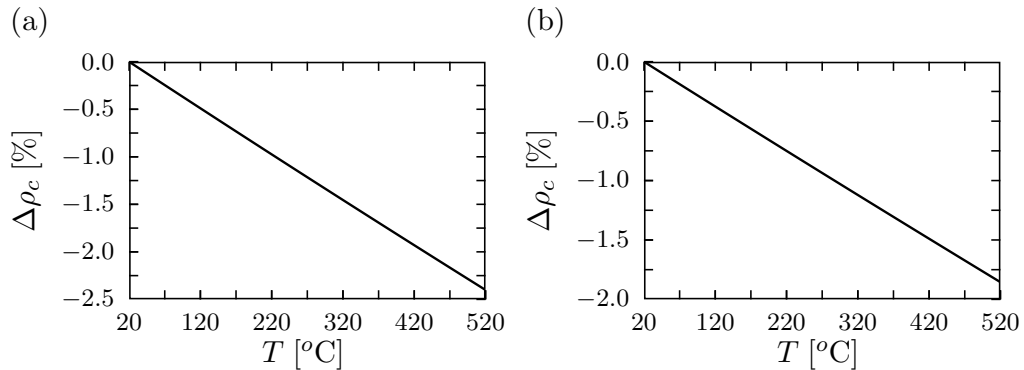
Figure 9.7:   Relative variation of the mass density with temperature for the forming coil $\rho_{m;c}$ and for the workpiece $\rho_{m;w}$.

3. The thermal properties of the materials

The thermal conductivity and the specific heat are the main thermal properties described in Section 3.4 and they change with the temperature. For most of the highly conducting materials, the thermal conductivity increases in a reasonably linear manner as the temperature rises.

Regarding the changes in specific heat with temperature, sometimes the product between specific heat and mass density is considered in itself a parameter of the material. This product shows also a reasonably linear behavior for most of the highly conductive materials. In our case we assumed that the thermal properties of the materials are invariant.

We will apply all the changes due to the temperature rise presented in this section to the experimental model of the forming system with $C = 60\ \mu\mathrm{F}$,
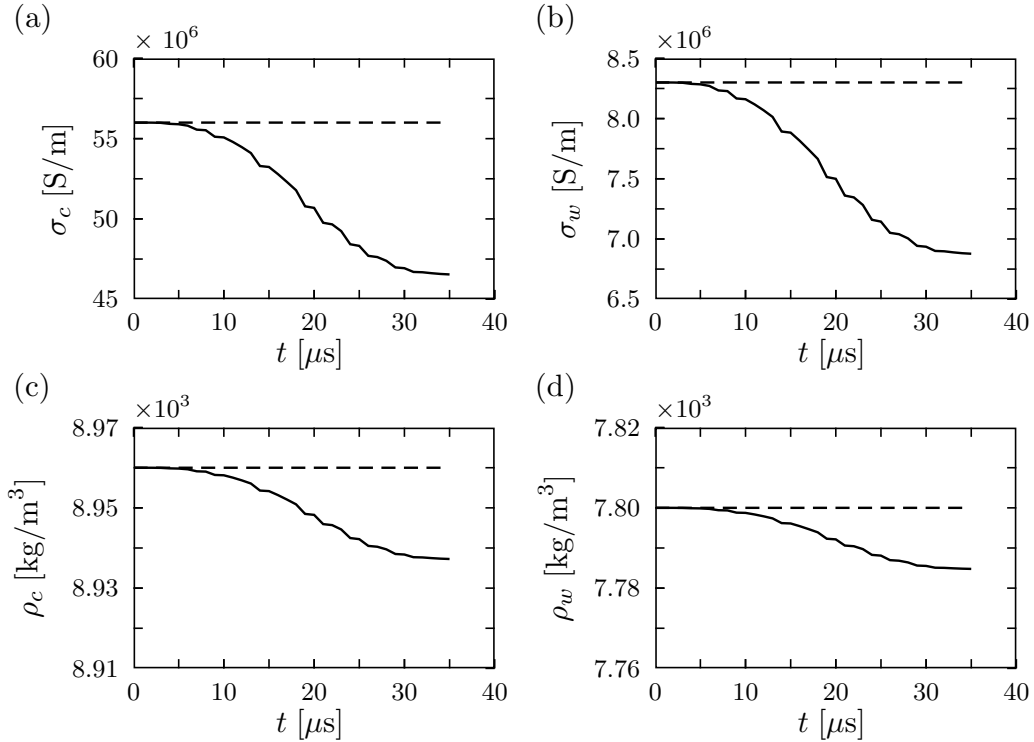
Figure 9.8:   Electrical conductivity σ and mass density ρ_m in time domain for the forming coil and for the workpiece, with (solid line) and without (dashed line) considering the changes due to deformation and due to temperature rise.

(a)

(b)

(c)

(d)
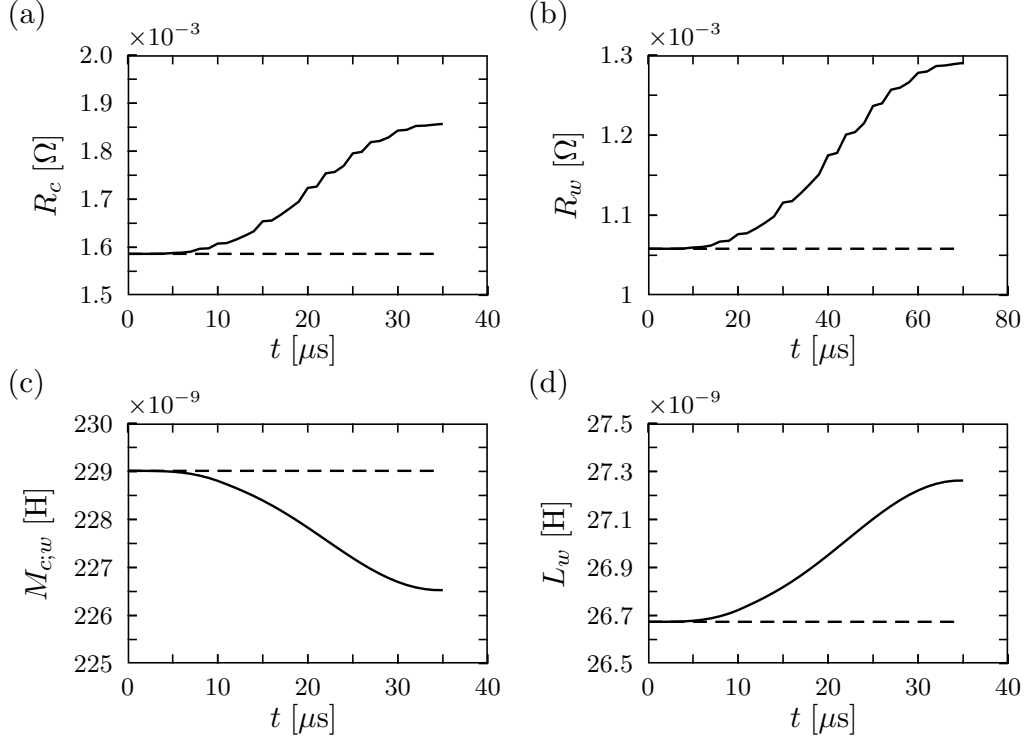
Figure 9.9:   Temporal evolution of some parameters of the network
model with (solid line) and without (dashed line) consider-
ing the changes due to deformation and due to temperature
rise.

$V_0 = 14$ kV and with the constructed forming coil with $n = 130$ m^{-1}, for
a 3-piece (blank) can, as considered in the previous section. Thus, for the
numerical results in this section, all mentioned effects due to deformation and
temperature rise are taken into account. The numerical results obtained with
this complex experimental model will be compared with the corresponding
numerical results obtained with the initial experimental model, as given in
Chapter 8.

The temporal evolution of the material properties of the forming coil and
workpiece is presented in Fig. 9.8, while the temporal evolution of the network
elements is presented in Fig. 9.9.

In Figs. 9.10 and 9.11, some quantities of the forming system are pre-
sented. The results do not vary significantly from the results obtained in the
previous chapter due to the fact that only small radial displacement is reached

(a)

(b)

(c)

(d)

(e)

(f)
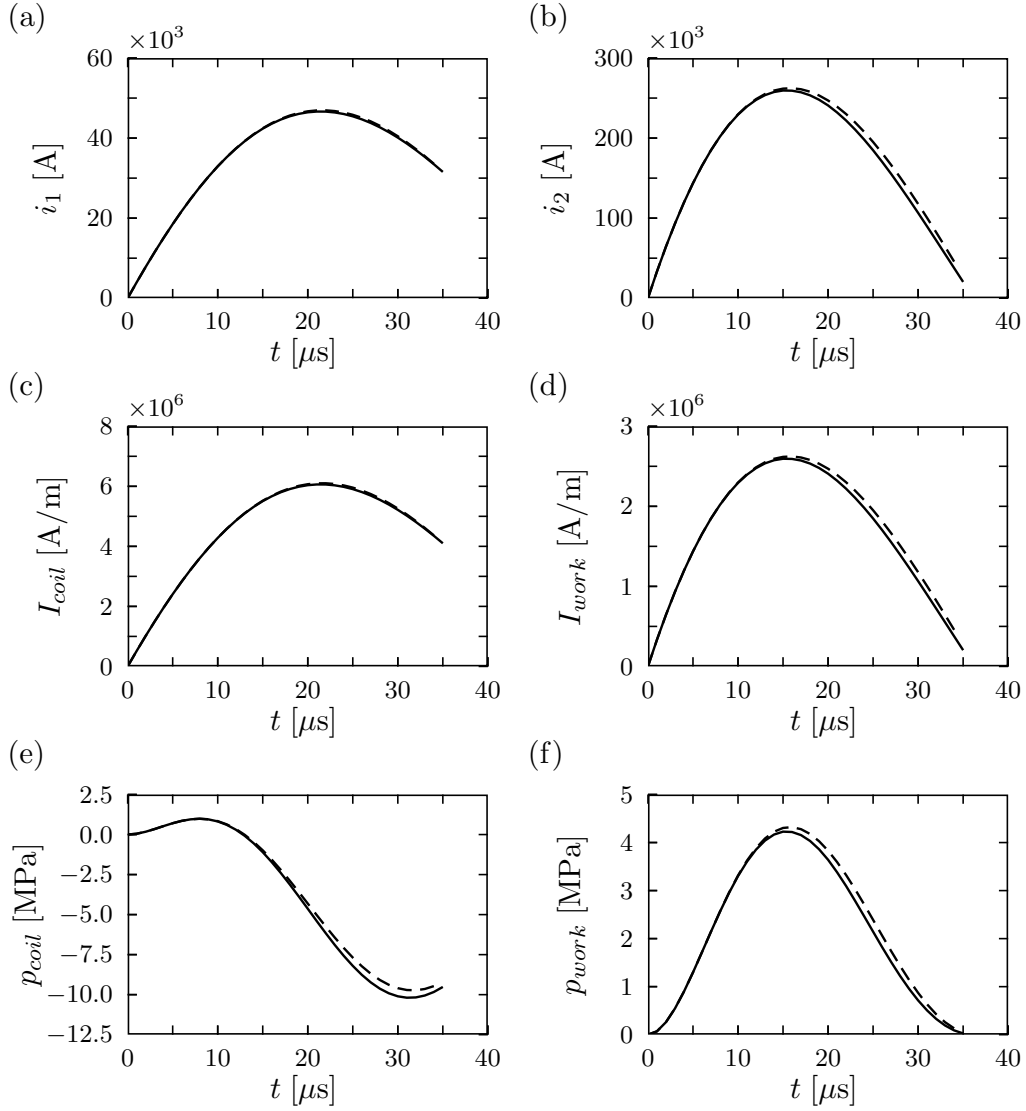
Figure 9.10: Various quantities of the forming system obtained with (solid line) and without (dashed line) considering the changes due to deformation and due to temperature rise.

in the configuration. The obtained deformations are comparable to the ones calculated in the previous chapter, due to the fact that the radial velocity is not significant and also the radial displacement and the actual temperature increase in the configuration remain small.

The shape of the curves in Fig. 9.11 (d) shows that the temperature rise

(a)

(b)

(c)

(d)

(e)

(f)
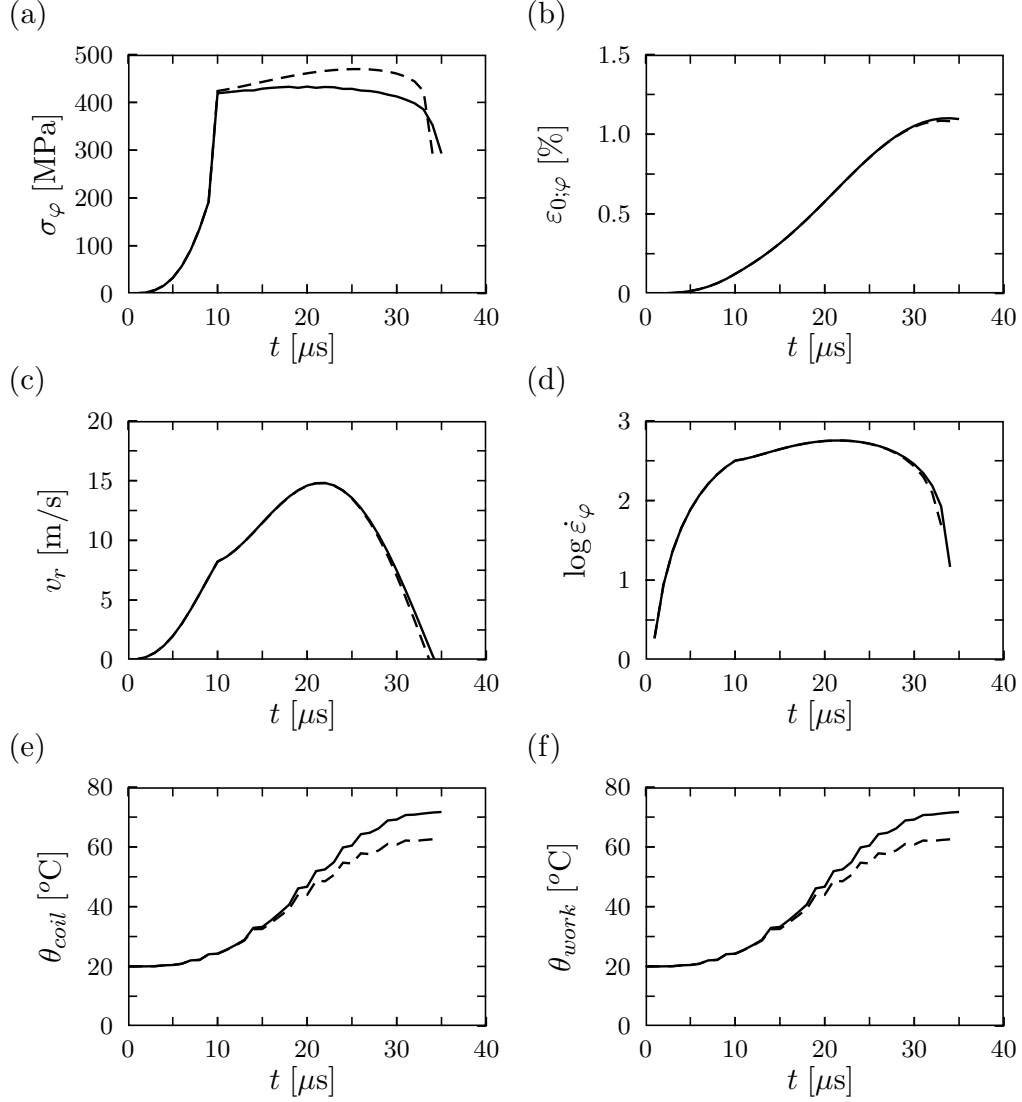
Figure 9.11: Various quantities of the forming system obtained with (solid line) and without (dashed line) considering the changes due to deformation and due to temperature rise.

causes indeed a decrease in the equivalent strain rate. This will yield lower stresses in the material and will contribute further to smaller final deformations of the workpiece. When all the changes due to deformation and due to temperature rise are taken into account, the actual temperature in the forming coil and workpiece is smaller than when these changes are not considered, see Fig. 9.11 (e) and (f).

9.4   Conclusions

In this chapter few ideas that may lead to a complex, realistic experimental model for the electromagnetic forming process described in Chapter 8 have been presented.

The numerical results obtained with the realistic model show that the evolution of the network model elements is strongly influenced by deformation, when these deformations have significant values. Also, the changes in material properties due to the temperature rise in the configuration play an important role. For the typical materials used in electromagnetic forming, the material properties most affected by the temperature rise are the mass density and the electrical conductivity. The variation of these parameters with temperature is quite large and this variation has effects on the whole electromagnetic forming process. The temperature rise in the configuration affects the final deformation in the sense that at higher temperature the obtained deformation will be smaller. For the considered case, we notice that the geometrical influences and temperature influences almost cancel each others effect, see Figs. 9.1 (b) and 9.11 (b).

The same iterative steps presented in this chapter may be used to obtain a complex, realistic theoretical model of the electromagnetic forming process as presented in Chapters 4, 5, 6 and 7. Such a complex theoretical model is not trivial and it requires high computational efforts. Moreover, the experimental verification of the resulting complex theoretical numerical results is difficult since these results describe the evolution of each point inside the workpiece.

Chapter 10

Conclusions and future research

This chapter presents some conclusions based on the work presented in this monograph. Besides, a few possible directions for future research are given.

10.1   Conclusions

The proposed goal of this is work was to calculate the spatial and temporal behavior of a conducting, electromagnetically stationary and mechanically deformable hollow circular cylinder (the workpiece) subjected to an intense transient electromagnetic field, as stated in Section 1.3. This is a typical problem of electromagnetic forming.

In order to achieve the proposed goal, the evolution of all quantities that characterize the process should be investigated during the deformation process. The number of these parameters/quantities is rather large and besides there is a strong interdependence between them. This was the reason to make some initial assumptions in order to have an accurate semi-analytical model that can easily be computed.

In our present situation the deformation of the matter is due to the electromagnetic force density and may occur for both magnetic and non-magnetic media. The literature on electromagnetic force distribution in magnetic media is confusing because various contradicting expressions are reported. This was the reason to analyze in detail the electromagnetic force densities in Chapter 2.

The workpiece was assumed to be electromagnetically stationary though the workpiece will have to move in order to deform. Although there are many phenomena related to the motion of the matter, the velocity of the material will be much smaller than the velocity of the electromagnetic field, i.e., the light speed. In this case it is sufficient that only stationary matter is considered in the analysis of the electromagnetic field, see [123].

As stated from the beginning, the workpiece may be made of magnetic or non-magnetic material. In Chapter 2, a general theory about the electromechanical force densities associated with pulsed electromagnetic fields in piecewise homogeneous, isotropic, linear media with conductive losses has been presented. In has been shown that the conductivity and the gradients in permittivity and permeability lead to volume force densities, while jump discontinuities in permittivity and permeability lead to surface force densities. These force densities act as impressed external mechanical volume and surface forces, respectively, and thus generate an elastodynamic wave field in the object. In this chapter we have also discussed the basic equations of linear, elastodynamic deformation.

As mentioned above, the number of quantities involved in an electromagnetic forming process is large and they are interdependent. In Chapter 3, some initial simplifications and approximations have been presented that have been used to develop a comprehensive semi-analytical model of the electromagnetic forming process.

These simplifications and approximations were related to the geometry, parameters and fields that are characteristic for a typical electromagnetic forming system, and they may be applied both to electromagnetic compression and to electromagnetic expansion.

Further, a theoretical model for the electromagnetic compression and expansion of hollow circular cylindrical objects (workpieces), based on these assumptions, has been developed and discussed in detail. At each step in the development of this theoretical model, numerical results were presented for three types of workpieces, namely for a non-magnetic thick workpiece, for a magnetic thick workpiece and for a non-magnetic thin workpiece.

The first step in the construction of our model was to calculate in Chapter 4 the transient diffusive electromagnetic field in the cylindrical configuration related to the discussed electromagnetic forming system for compression of hollow circular cylindrical objects. The axially symmetric configuration with infinite length in which the electromagnetic field and the electromagnetic force densities had to be calculated consisted of a hollow cylindrical domain with a

high electrical conductivity and a given permeability placed inside (for compression) or outside (for expansion) a cylindrical sheet antenna carrying a given electric current per unit length.

The electromagnetic field components and electromagnetic volume force have been computed in the frequency domain and the results were then transformed to the time domain. It has been shown that, inside the workpiece, for sufficiently low frequencies, the electromagnetic field components have almost a linear dependence as function of the radial position, while at higher frequencies the electromagnetic field is concentrated near the interface closest to the sheet antenna.

The numerical results for the presented cases have shown that the values of the electromagnetic volume force density are much larger in a magnetic thick material and in a non-magnetic thin material than in a non-magnetic thick one. In all cases the electromagnetic force density has large values near the interface close to the source and it decays rapidly in time and space. In the magnetic thick material, the electromagnetic surface force density has also been calculated. Its values are much smaller that the average value of the electromagnetic volume force density along the thickness of the workpiece, but they are not negligible.

The electromagnetic volume force and the electromagnetic surface force calculated in Chapter 4 have been used as source terms for the calculation of the elastic field in the considered cylindrical configuration in Chapter 5. The complete elastodynamic problem for the case of plane strain has been considered for the calculation of the elastic field in the circular cylindrical workpiece used in electromagnetic compression and expansion. The solution of the equation of radial motion has been found as the sum of the general solution of the homogeneous equation of motion with a particular solution of the inhomogeneous equation of motion, where the particular solution has been calculated using a source type of integral representation.

The numerical results obtained for the elastic field in the cylindrical configuration have shown that the particle radial displacement has smaller values in a non-magnetic thick workpiece and in a magnetic thick than in a non-magnetic thin workpiece. In all the considered cases, the radial displacement at the inner boundary the workpiece is slightly larger in absolute value than the one at the outer boundary. It means that the workpiece becomes slightly thicker during electromagnetic compression, and thinner during electromagnetic expansion. The sign of tangential stress is consistent with the sign of the particle displacement. Also, the radial stresses have small, negligible values as

compared with the values of the tangential stresses at the same instant of time.

The results for the elastic field components have also been calculated with the theory of equivalent surface forces and they differ from the results obtained with our theory. For the case of a non-magnetic thick and non-magnetic thin workpiece the results are almost the same. When a magnetic thick workpiece is considered, the results given by the two methods are very different. These considerable differences are due to the fact that the Maxwell stress tensor used for the calculation of the equivalent surface forces does not take into account the magnetic nature of the workpiece, since it is calculated in the air where only the permeability of vacuum is used and not the actual permeability of the considered magnetic material.

In Chapter 6 some considerations regarding the temperature effects in the electromagnetic forming system were discussed. The temperature rise in the workpiece was only attributed to dissipation of electromagnetic energy in the forming process.

The solution of the equation of heat flow has been found as the sum of the general solution of the homogeneous equation of heat flow with a particular solution of the inhomogeneous equation of heat flow. The particular solution has been calculated using a source type of integral representation.

Then, the mean temperature of the workpiece has been estimated based on the temperature field previously calculated. It has been shown that a simplified formula that does not account for the heat conduction in the workpiece may not be used for the computation of the mean temperature in the workpiece.

It has been also shown that the resulting temperature rise in the configuration leads to some supplementary thermoelastic strains. These have been computed and then compared with the results obtained without taking into account the temperature effects. For the electromagntic compression, the temperature rise has negative consequences for the deformation process, because a significant undesired expansion of the workpiece is obtained in all cases. This undesired expansion of the workpiece is sometimes larger than the desired compression of the workpiece. For the electromagntic expansion, the temperature rise has positive consequences for the deformation process, because a suplementary expansion of the workpiece is obtained.

The plastic deformation of an infinite, hollow, cylindrical object has been investigated in Chapter 7. The evaluation of the inelastic deformation in the case of elastic-perfectly plastic materials under plane strain assumption has been considered. To simplify the calculations, the elastic deformation has

been neglected, as well as the influence of the radial velocity acquired by the workpiece during the elastic deformation. In all the considered cases for the numerical results, the plastic boundary, that delimits regions with elastic and plastic deformation, see Section 7.4 moves very rapidly inside the workpiece, so intermediary calculations may be avoided and we may consider that the entire workpiece starts to deform plastically at a certain instant of time. It has been shown that both the magnetic thick workpiece and the non-magnetic thin workpieces start to deform plastically short after the beginning of the process. In the non-magnetic workpiece subjected either to compression or to expansion, the onset of the plastic deformations takes place after a longer interval of time from the beginning of the process.

The actual deformation of the workpiece has been calculated using the dynamic equation of motion. It has been shown that in electromagnetic compression the thickness of the workpieces increases, while in electromagntic expansion the thickness of the workpieces decreases. The velocities reached by a non-magnetic thin workpiece are the largest from all the considered cases.

In Chapter 8, the experimental investigation of electromagnetic forming of very thin steel beverage cans has been presented. All steps required, in general, for designing an optimal experimental set-up for electromagnetic forming have been presented. An experimental model based on the equivalent network model of the electromagnetic forming system has been developed, under the assumption that the workpiece is a cylindrical thin shell.

The whole design procedure has been applied for designing an optimal experimental set-up for electromagnetic expansion of thin steel beverage cans. Some experimental results obtained with the designed experimental set-up have been given and they have been compared with the numerical simulations. The discrepancy between the numerical and experimental results has been explained and an improved experimental set-up has been proposed.

At the end of this thesis, in Chapter 9 some ideas that may lead to a more complex, realistic experimental model for the electromagnetic forming process, as described in Chapter 8, have been presented. The calculation of the actual temperature in the configuration after the heat exchange between the forming coil and the workpiece has been investigated with the use of an electrical network analogy. The numerical results showed that the evolution of the network model elements used for designing the experimental set-up is significantly influenced by deformation and also that the changes in material properties due to the temperature rise in the configuration play an important role in the electromagnetic forming process. For the typical materials used

in electromagnetic forming, the material properties most affected by the temperature rise are the mass density and the electrical conductivity, since the variation of these parameters with temperature is quite large and this variation has effects on the whole electromagnetic forming process. The temperature rise, when significant, affects the final deformation in the sense that at higher temperature the obtained deformation will be smaller.

10.2   Future research

In this thesis, the theoretical model of the electromagnetic compression and expansion in the assumption of infinite length of the axially symmetric cylindrical configuration has been presented. This resulted in an one-dimensional model. Both for electromagnetic compression and for electromagnetic expansion it would be interesting to develop a two-dimensional model, based on a finite length of the axially symmetric cylindrical configuration. Within such a model the end effects of the forming coil and of the workpiece can be taken into account.

Another possible idea of future research related to the electromagnetic compression of hollow circular cylindrical objects may be the development of a complex theoretical model that takes into account in an iterative manner the changes in geometry, parameters, properties and fields, as induced by the high velocity, temperature rise and other possible effects such as defects in materials, hysteresis losses and inhomogeneity of the workpiece. Such a model should take into account not only the behavior of the workpiece, but of all the components of the electromagnetic forming system.

The development of such a theoretical model is not trivial and it may require high computational efforts. A major inconvenience of such a model is that it cannot be experimentally verified with a simple experimental setup, since it requires the measurement of the properties and the behavior of the workpiece at each point inside the material, since these quantities are supposed to change at each instant of time.

Another idea of future research is to analyze the possible effects on the electromagnetic forming process due to the presence of thin layers of other types of materials, e.g. paints and plastic coatings applied on the workpiece. In a practical application, e.g. electromagnetic expansion of very thin steel beverage cans as described in Chapter 8, the workpieces subjected to electromagnetic forming have layers of paints, plastics, etc. applied on them. These layers have different properties and behavior as compared with the material of the

workpiece and it is desirable that these layers will not be damaged during electromagnetic forming. Therefore, a study of the influence and vulnerability of thin layers of materials applied on the workpiece before electromagnetic forming is another possibility of future research.

It is also possible to investigate the same aspects for the electromagnetic forming of plane objects with the use of pancake coils. In this case, when all aspects are considered, the problem may become a three-dimensional one, if the coil is not radially symmetric.

Appendix A

List of common quantities and symbols
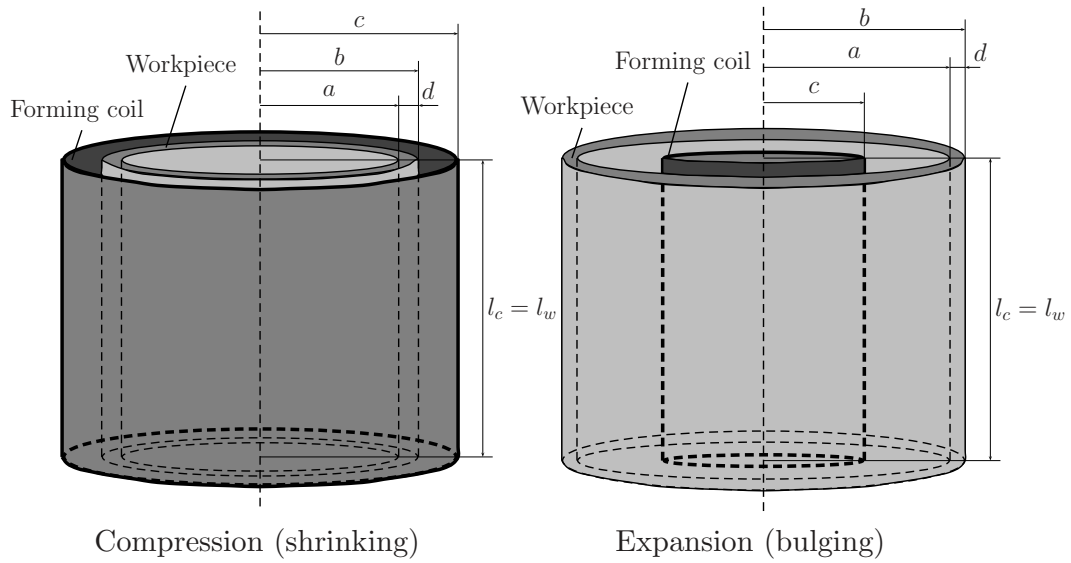
Figure A.1: The modeled configurations.

A, B	-	strain-hardening coefficients
a	-	inside radius workpiece (m)
B_{sat}	-	saturation flux density (T)
b	-	outside radius workpiece (m)
c	-	mean radius forming coil (m)
c	-	light speed in vacuum (m/s)

$$
\begin{array}{lll}
c_P & - & \text{compressional or P-wave speed (m/s)} \\
c_T & - & \text{mass specific heat (J/kg K)} \\
C_{p,q,i,j} & - & \text{elastic stiffness tensor} \\
C & - & \text{capacitance of the capacitor bank (F)} \\
\mathcal{D} & - & \text{domain in the configuration} \\
\partial\mathcal{D} & - & \text{boundary of domain } \mathcal{D} \text{ in the configuration} \\
d & - & \text{thickness of the workpiece (m)} \\
d_c & - & \text{diameter of a round conductor (m)} \\
d_{gap} & - & \text{air-gap in between forming coil and workpiece (m)} \\
d_l & - & \text{insulation between layers of windings (m)} \\
d_{over} & - & \text{overall insulation of the forming coil(m)} \\
d_w & - & \text{insulation between consecutive windings (m)} \\
\boldsymbol{E} & - & \text{electric field strength} \\
E & - & \text{total energy stored in the capacitor bank (J)} \\
E & - & \text{Young's modulus of elasticity (N/m}^2) \\
E_s & - & \text{modulus of plasticity(secant modulus) (N/m}^2) \\
e_{i,j} & - & \text{strain tensor} \\
\boldsymbol{F}_V^{ext} & - & \text{volume force exerted by external currents and charges} \\
\boldsymbol{F}_V^{ind} & - & \text{volume force exerted on induced volume density of} \\
& & \text{electric current} \\
\boldsymbol{F}_V^{ext} & - & \text{volume force exerted on gradients of permittivity and} \\
& & \text{permeability} \\
\boldsymbol{F}_S^M & - & \text{surface force due to a jump in Maxwell stress tensor} \\
\boldsymbol{F}_S^{M,\infty} & - & \text{surface force due to a jump in Maxwell stress tensor} \\
F_j & - & \text{coefficient in the polynomial approximation of the} \\
& & \text{electromagnetic volume force density} \\
f & - & \text{frequency of operation (Hz)} \\
f_r^V & - & \text{electromagnetic volume force density (N/m}^3) \\
f_r^S & - & \text{electromagnetic surface force density (N/m}^2) \\
\boldsymbol{G} & - & \text{electromagnetic momentum} \\
G^T & - & \text{time domain Green function } G^T(z, z'; t, t') \\
g & - & \text{width of the rectangular conductor (m)} \\
\boldsymbol{H} & - & \text{magnetic field strength} \\
h & - & \text{thickness of the rectangular conductor (m)} \\
\mathcal{I} & - & \text{unit tensor of rank two} \\
I_1 & - & \text{current per unit length in the forming coil (A/m)} \\
I_2 & - & \text{current per unit length in the workpiece (A/m)} \\
I_{coil} & - & \text{current per unit length in the forming coil (A/m)} \\
I_{work} & - & \text{current per unit length in the workpiece (A/m)} \\
I_S(t) & - & \text{current per unit length flowing in the sheet antenna (A/m)}
\end{array}
$$

$i_1(t)$	-	current pulse in the forming coil (A)
$i_2(t)$	-	current pulse in the workpiece (A)
$i_{1;max}$	-	maximum current in the forming coil (A)
$\boldsymbol{J}_S$	-	source density of electric current
$\boldsymbol{J}^{ext}$	-	external current density
$\boldsymbol{J}^{ind}$	-	induced current density
K	-	strength coefficient in a static stress-strain relation
k	-	ω/c_P wavenumber
k_{geom}	-	geometric factor for the planar approximation
k_{te}	-	coefficient of linear thermal expansion (1/^{o}C)
k_{th}	-	temperature coefficient of resistance (1/^{o}C)
$k_{th;\tau}$	-	coefficient of variation with temperature of electrical conductivity (1/^{o}C)
L_c	-	self-inductance of the forming coil (H)
L_{ext}	-	equivalent inductance of other components before the clamp diode (H)
L_{int}	-	equivalent inductance of other components after the clamp diode (H)
L_w	-	self-inductance of the workpiece (H)
l_c	-	length of the forming coil (m)
l_w	-	length of the workpiece (m)
M_{cw}	-	mutual inductance between coil and workpiece (H)
n	-	turns per unit length in the forming coil (m^{-1})
n	-	strain-hardening index in a static elastoplastic model
p_{coil}	-	instantaneous pressure exerted on the forming coil (N/m^2)
p_{excess}	-	excess pressure to be exerted for the workpiece (N/m^2)
p_{max}	-	maximum pressure exerted on the workpiece (N/m^2)
p_{work}	-	instantaneous pressure exerted on the workpiece (N/m^2)
p_{yp}	-	yielding pressure for the workpiece (N/m^2)
q	-	heat flow density (heat flux) (W/m^2)
R_c	-	resistance of the forming coil (Ω)
R_{diode}	-	equivalent resistance of the clamp diode (Ω)
R_{ext}	-	equivalent resistance of other components before clamp diode (Ω)
R_{int}	-	equivalent resistance of other components after clamp diode (Ω)
R_w	-	resistance of the workpiece (Ω)
r_{in}	-	inside radius of the forming coil (m)
r_{mean}	-	mean radius of the workpiece (m)
r_{min}	-	minimum radius of the constructed forming coil (m)

r_{max}	-	maximum radius of the constructed forming coil (m)
r_{out}	-	outside radius of the forming coil (m)
r_p	-	elastic-plastic boundary (m)
r_{tube}	-	outside radius of the plastic tube (m)
T	-	temperature (rise) (^{o}C)
$\mathcal{T}^M$	-	Maxwell stress tensor
T_0	-	initial temperature in the configuration (^{o}C)
T_m	-	mean temperature (^{o}C)
t_{cross}	-	crossover time (s)
t_e	-	initiation plastic boundary in the workpiece (s)
t_{fin}	-	time instant when deformation stops (s)
t_p	-	the whole workpiece shows plastic deformation (s)
t_w	-	current pulse time width (s)
t_{yp}	-	instant of time when yielding begins
u_{coil}	-	voltage across the forming coil (V)
u_r	-	particle radial displacement (m)
u_z	-	particle longitudinal displacement (m)
V_0	-	charged voltage on the capacitor bank (V)
$\boldsymbol{v}$, v_r	-	particle velocity (m/s)
$v_{r;max}$	-	maximum radial velocity during deformation (m/s)
$\dot{w}_h$	-	volume density of Joule losses (W/m^3)
α	-	thermal diffusivity of the workpiece (m^2/s)
α_T	-	coefficient of linear thermal expansion (1/K)
β	-	$\alpha_T(3\lambda_L + 2\mu_L)$ for the calculation of thermoelastic field
γ	-	$\sqrt{s\sigma\mu}$ for the electromagnetic field calculation
γ	-	$\sqrt{s\rho_m c_T/\kappa}$ for the temperature field calculation
κ	-	thermal conductivity (W/(m K))
δ	-	experimental coefficient in the conventional stress
ε_0	-	conventional strain (%)
ε	-	normal true strain (%)
ε_0	-	electrical permittivity of vacuum (F/m)
ε_{limit}	-	limit strain (%)
ε_{eff}	-	effective strain (%)
λ	-	consolidation coefficient in the viscoplastic model
λ_L	-	Lamé's coefficient of elasticity (N/m^2)
μ_L	-	Lamé's coefficient of rigidity (N/m^2)
μ_0	-	permeability of vacuum (H/m)
μ_r	-	relative magnetic permeability (-)
μ	-	magnetic permeability (H/m)
$\boldsymbol{\nu}$	-	normal unit vector

ν	-	Poisson's ratio
ν	-	coefficient of viscosity in the viscoplastic model
ω	-	$2\pi f$ radial frequency
ρ^{ext}	-	external charge density (C/m^3)
ρ_m	-	mass density (kg/m^3)
σ	-	electrical conductivity(S/m)
σ	-	normal true stress (N/m^2)
σ_0	-	normal conventional stress (N/m^2)
$\sigma_{0;u}$	-	ultimate tensile stress (N/m^2)
$\sigma_{0;r}$	-	rupture stress (N/m^2)
σ_{eff}	-	effective stress (N/m^2)
σ_{oct}	-	octahedral stress (N/m^2)
σ_{sh}	-	shearing stress in simple tension (N/m^2)
σ_{yp}	-	yielding stress (N/m^2)
$\tau_{p,q}$	-	component of the dynamic stress (N/m^2)
τ	-	true stress (N/m^2)
τ_0	-	conventional stress (N/m^2)
τ_e	-	effective stress (N/m^2)
τ_{oct}	-	octahedral stress (N/m^2)
τ_r	-	rupture stress (N/m^2)
τ_{sh}	-	shearing stress (N/m^2)
τ_u	-	ultimate tensile strength (N/m^2)
τ_{yp}	-	yielding stress (N/m^2)

Appendix B

Typical parameters in electromagnetic forming obtained from the literature

The symbols E, C and F in the next tables represent the type of electromagnetic forming used by the respective authors (in chronological order) :

E − expansion (bulging) of hollow circular cylindrical workpieces,

C − compression (shrinking) of hollow circular cylindrical workpieces,

F − deformation of flat workpieces (metal sheets).

The materials used for the workpiece have the following symbols:

Al − pure aluminum or an aluminum alloy,

Co − pure copper or a copper alloy,

Fe − low carbon mild steel.

Table B.1: Typical parameters for the EMF obtained from the literature.

Author	type	R mΩ	L µH	C µF	V_0 kV	E kJ	n m^{-1}	d_c mm	l_c mm	c mm	$i_{1,max}$ kA	p_{max} MPa
Baines [9]	E	31	4.2	21-65	11,20	16	210	3.2	76	43.2	56.24	82.68
Lal [105]	E	50	0.05			12.5	98		152	25	135	268.7
Jansen [96]	E	47	2.45	180	1.9		164		73	22.25	15.4	
			2.22	60	1.9						9.4	
Fluerasu [62]	E			40	8	1.28	300	0.9	40	12.4	38.1	28
Lal [106]	E	47	0.9	60,180	5-10		216		54	22		20.5
Al-Hassani [3]	E			42.56	11		212.8		49	23,24	50	48.2
King [100]	E			240		12	214					
Sasu [160]				200	8,10						300	
Rioux [152]	F					5						
Schley [163]	E		0.195	360		12						357
Galizzi [68]	C			80.80	2,6,14			1.2				
Takatsu [181]	F	25.5	2	40	6						20	
Murata [140]	E			215	10	10	300	3	150			
Hwang [92]	C					4-16			100	50.8		
Lee [110]	E					2		2	80	42	7.5	2.9
Zhang [191]	E			20-800		1	330	2	200	18.5-10	15	15-4
Bendjima [16]	E								40	11.65	9.9	28.5
Fenton [61]	E											
Hashimoto [81]	C	17.2	1.2	400	5.5							26
Beerwald [19]	C	5	0.1	100		2		2			15	140

Table B.2: Typical parameters for the EMF obtained from the literature.

Author		d mm	a mm	b mm	d_{gap} mm	l_w mm	σ_w $\cdot 10^7$ S/m	t_{fin} μs	$v_{r,max}$ m/s	τ_{yp} MPa	e_{max} %
Baines [9]	Al	1.2	24.3	25.5	3.9	76.2		60	234.7	137.8	
Lal [105]		3	29	32	7	152			286.5	15.4	
Jansen [96]		1.25	24.15	25.4	1.9	54			180	3.72	15
Fluerasu [62]	Al	1	15	16	2.6	40			87	76	20
Lal [106]		1.25	25.4			54		74-109	84-134	216.3	7-19
Al-Hassani [3]	Al,Co,Fe	1.6	24			82.5	3.5;5.6;0.76	70	100.6	189-655	
King [100]	Al	1.66	34.8		0.24	95.25				32.2	10
Sasu [160]											
Rioux [152]	Al,Co,Fe	1-5					3.7;5.5;0.67		140-150		
Schley [163]		1	10	11					700		25
Galizzi [68]		0.45	3.28	3.73					600		183
Takatsu [181]	Al	0.5			1.6		3.6	250		118	
Murata [140]	Al	1	19	20			3.6			76	43
Hwang [92]											
Lee [110]	Al	1	44	45	1	152	3.56	200	47		
Zhang [191]	Al	1		20				135	85		25
Bendjima [16]	Al	1	15	16	2.6	38	3.4	75	88.4	76	
Fenton [61]	Al	0.127		28.3		114.3	3.6	70-80		290	18
Hashimoto [81]	Al	2	25	27		50	3.56				
Beerwald [19]	Al	3	10		1	30	2.5				

Appendix C

Description of the configurations to be simulated

In this thesis, numerical results are presented for two forming systems for electromagnetic forming of hollow, circular cylindrical objects. One forming system is designed for the compression and expansion of hollow circular cylindrical objects. Both for compression and expansion, a theoretical model has been developed. The second forming system is designed for the expansion very thin hollow circular cylindrical objects made of (non)magnetic material. For expansion an experimental model has been elaborated as well. The main characteristics of these forming systems are presented in the next tables.

C.1 Theoretical electromagnetic forming system for compression and expansion of hollow, circular cylindrical objects

		WORKPIECE
r_{mean}	21 mm, 20.1 mm	mean radius
d	2 mm, 0.2 mm	thickness
l_w	100 mm	length
a	20 mm	inside radius
b	22 mm, 20.2 mm	outside radius

σ	$3.6 \cdot 10^7$ S/m	electrical conductivity
μ	μ_0, 100 μ_0	magnetic permeability
ρ_m	$2.7 \cdot 10^3$ kg/m^3	mass density workpiece
λ_L	$17 \cdot 10^{10}$ N/m^2	Lamé's coefficient of elasticity
μ_L	$8 \cdot 10^{10}$	Lamé's coefficient of rigidity
ε_{limit}	0.00150284	limit strain
σ_{yp}	105 MPa	yielding stress
c_T	880 J/(kg K)	mass specific heat
α_T	$24 \cdot 10^{-6}$ K^{-1}	coefficient of linear thermal expansion
$k_{th;\sigma}$	$403 \cdot 10^{-5}(1/^oC)$	coefficient of variation with temperature of electrical conductivity
κ	190 W/(m K)	thermal conductivity
		FORMING COIL
n	100 m^{-1}	turns per unit length (1 layer of windings)
g	8 mm	width of rectangular conductor
h	1 mm	thickness of rectangular conductor
d_w	1 mm	insulation individual conductor
d_{over}	2 mm	overall insulation
r_{min}	28 mm	minimum radius
r_{max}	calculated	maximum radius
c	24 mm	mean radius for compression
c	20 mm	mean radius for expansion
l_c	100 mm	length
σ_c	$5.6 \cdot 10^7$ S/m	electrical conductivity
μ_c	μ_0	magnetic permeability
$\rho_{m;c}$	$8.96 \cdot 10^3$ kg/m^3	mass density
E	$11 \cdot 10^{10}$ N/m^2	Young's modulus of elasticity
ν	0.343	Poisson's ratio
ε_{limit}	0.00203907	limit strain
σ_{yp}	224.3 MPa	yielding stress
c_T	385 J/(kg K)	mass specific heat
α_T	$16.4 \cdot 10^{-6}$ 1/^oC	coefficient of linear thermal expansion
$k_{th;\sigma}$	$393 \cdot 10^{-5}(1/^oC)$	coefficient of variation with temperature of electrical conductivity
κ	385 W/(m K)	thermal conductivity
		NETWORK ELEMENTS
V_0	10 kV	charged voltage on the capacitor bank
C	2000 μF	capacitance of the capacitor bank

R_{ext}	2 mΩ	resistance other parts before diode
L_{ext}	0.2 μH	self-inductance other parts before diode
R_{diode}	0 mΩ	resistance clamp diode
R_{int}	0 mΩ	resistance other parts after diode
L_{int}	0 μH	self-inductance other parts after diode

C.2 Experimental electromagnetic forming system for expansion of thin steel beverage cans

		WORKPIECE
$r_{mean}^{(0)}$	26 mm	initial (undeformed) mean radius
d	78, 80 μm	thickness 2-piece can
	186, 200 μm	thickness 3-piece can
l_w	100 mm	length
a	$r_{mean} - d/2$	inside radius
b	$r_{mean} + d/2$	outside radius
σ_w	$8.3 \cdot 10^7$ S/m	electrical conductivity
$\mu_{r;w}$	1	relative magnetic permeability
μ_w	$\mu_{r;w}\mu_0$	magnetic permeability
B_{sat}	2 T	magnetic flux after saturation
$\rho_{m;w}$	$7.9 \cdot 10^3$ kg/m^3	mass density
λ_L	140 GPa	Lamé's coefficient of elasticity
μ_L	80 GPa	Lamé's coefficient of rigidity
$\varepsilon_{limit;w}$	0.0011927	limit strain
$\sigma_{yp;w}$	840 MPa	yielding stress 2-piece can
	250 MPa	yielding stress 3-piece can
$c_{T;w}$	472 J/kg K	mass specific heat
$\alpha_{T;w}$	$12.6 \cdot 10^{-6}$ 1/^{o}C	coefficient of linear thermal expansion
$k_{th;\tau}$	$400 \cdot 10^{-5}(1/^o$C)	coefficient of variation with temperature of electrical conductivity
κ_w	49.8 W/(m K)	thermal conductivity
		FORMING COIL
n	130 m^{-1}	turns per unit length (1 layer of windings)
g	5.7 mm	width of rectangular conductor
h	3 mm	thickness of rectangular conductor
d_w	calculated	insulation individual conductor
d_l	0 mm	insulation between layers of windings

d_{over}	2 mm	overall insulation
r_{min}	calculated	minimum radius
r_{max}	25 mm	maximum radius
c	calculated	mean radius
l_c	80 mm	length
σ_c	$5.6 \cdot 10^7$ S/m	electrical conductivity
$\mu_{r;c}$	1	relative magnetic permeability
μ_c	$\mu_{r;c}\mu_0$	magnetic permeability
$\rho_{m;c}$	$8.96 \cdot 10^3$ kg/m^3	mass density
$c_{T;c}$	385 J/kg K	mass specific heat
$\alpha_{T;c}$	$16.4 \cdot 10^{-6}$ 1/^{o}C	coefficient of linear thermal expansion
$k_{th;\tau}$	$393 \cdot 10^{-5}(1/^oC)$	coefficient of variation with temperature of electrical conductivity
κ_c	385 W/(m K)	thermal conductivity
		NETWORK ELEMENTS
V_0	8.4 kV, 10 kV	charged voltage on the capacitor bank
C	60 μF	capacitance of the capacitor bank
R_{ext}	2 mΩ	resistance other parts before diode
L_{ext}	0.2 μH	self-inductance other parts before diode
R_{diode}	0 mΩ	resistance clamp diode
R_{int}	0 mΩ	resistance other parts after diode
L_{int}	0 μH	self-inductance other parts after diode

Bibliography

[1] Ablamunets, I.G., "Excitation of electromagnetic waves in uniformly moving media", *Technical Physics*, Vol. 38, No. 6, June 1993, pp. 439 – 446.

[2] Achenbach, J.D., *Wave Propagation in Elastic Solids*, Elsevier, Amsterdam, 1984.

[3] Al-Hassani, S.T.S., Duncan, J.L., Johnson, W., "On the parameters of magnetic forming process", *Journal Mechanical Engineering Science*, Vol. 16, No. 1, 1974, pp. 1 – 9.

[4] Arpaci, V. S., *Conduction Heat Transfer*, Addison-Wesley, 1966.

[5] Arpaci, V. S., *Introduction to Heat Transfer*, Prentice-Hall, Upper Saddle River, 1999.

[6] Atanackovic, T. M., *Theory of Elasticity for Scientists and Engineers*, Birkhuser, Boston, 2000.

[7] Azzouz, F., Bendjima, B., Feliachi, M., "Application of macro-element and finite element coupling for the behavior analysis of magnetoforming systems", *IEEE Transactions on Magnetics*, Vol. 35, No. 3, May 1999, pp. 1845 – 1848.

[8] Baccino, R., Parayre, C., David, R., "Le magnetocompactage de poudres: obtenir des materiaux inedits", *RGE Revue Generale d'Electricité*, No. 9, October 1987, pp. 57 – 61.

[9] Baines, K., Duncan, J.L., Johnson, W., "Electromagnetic metal forming", *Proceedings Instsn. Mechanical Engineers*, Vol. 180, part 1, No. 4, 1965-1966, pp. 93 –104.

[10] Balanethiram, V.S., Daehn G.S., "Hyperplasticity: increased forming limits at high workpiece velocity", *Scripta Metallurgica et Materialia*, Vol. 30, No. 4, 15 February 1994, pp. 515 – 520.

[11] Baldomir, D., *Geometry of Electromagnetic Systems*, Clarendon, Oxford, 1996.

[12] Bartsch, M., Dehler, M., et. co., "Solutions of Maxwell's equations", *Computer Physics Communications*, Vol. 72, 1992, pp. 22 – 39.

[13] Batygin, V.V., Toptygin, I.N., *Problems in Electrodynamics*, Academic Press, London, 1978.

[14] Beck, F.J., Pacholder, A.O., "Energy flow in transformers", *IEEE Summer Power Meeting*, 1966, pp. 248 – 254.

[15] Beck, J. V., *Heat Conduction Using Green's Functions*, Hemisphere Publishing Corporation, Washington, 1992.

[16] Bendjima, B., Feliachi, M., "Finite element analysis of transient pheNomena in electromagnetic forming system", *IEE Computation in Electromagnetics*, 10-12 April 1996, pp. 113 – 116.

[17] Bendjima, B., Srairi, K., Feliachi, M., "A coupling model for analyzing dynamical behaviours of an electromagnetic forming system", *IEEE Transactions on Magnetics*, Vol. 33, No. 2, March 1997, pp. 1638 – 1641.

[18] Bescond, C., Deschamps, M., "Dynamical surface response of a semi-infinite anisotropic elastic medium to an impulsive force", in *Journal of Acoustical Society of America*, Vol. 103, No. 1, January 1998, pp. 114 – 124.

[19] Beerwald, H., "Contribution to the generation of pulsed magnetic fields up to 25 T for industrial applications especially electromagnetic metal forming systems", *Proceedings OPTIM 2000*, 2000, pp. 37 – 40.

[20] Birdsall, D.H., Ford, F.C., Furth, H.P., Riley, R.E., "Magnetic forming", *American Machinist*, Vol. 105, No. 6, March 1961, pp. 117 – 121.

[21] Bladel, J.G. van, "Motion of a conducting loop in a magnetic field", *IEE Proceedings*, Vol. 135, No. 4, April 1988, pp. 212 – 222.

[22] Blok, H., *Electromagnetische Velden in de Energietechniek*, VSSD, Delft, 1975.

[23] Bobbio, S., *Electrodynamics of Materials. Forces, Stresses, and Energies in Solids and Fluids*, Academic Press, San Diego, 2000.

[24] Boichenko, A.N., Bel'ii, I.V., Fertik, S.M., Khimenko, L.T., "Electromagnetic forming", *Russian Engineering Journal*, Vol. 54, No. 11, 1974, pp. 77 – 80.

[25] Booker, H.G., *Energy in Electromagnetism*, Peregrinus, Stevenage, 1982.

[26] Boresi, A. P., *Elasticity in Engineering Mechanics*, Wiley, New York, 2000.

[27] Boyer, T.H., "Understanding the penetration of the electromagnetic velocity fields into conductors", *American Journal of Physics*, Vol. 67, No. 11, 1999, pp. 954 – 958.

[28] Brekovskih L., Goncharov, V., *Mechanics of Continua and Wave Dynamics*, Springer-Verlag, Berlin, 1985.

[29] Bruno, E.J., (Ed.) *High-velocity Forming of Metals*, ASTME, Dearborn, Michigan, 1964.

[30] Bruno, E.J., (Ed.) *High-velocity Forming of Metals*, ASTME, Dearborn, Michigan, 1968.

[31] Byrne, J.V., "Ferrofluid hydrostatics according to classical and recent theories of the stresses", *IEE Proceedings*, Vol. 124, No. 11, November 1977, pp. 1089 – 1097.

[32] Carpenter, C.J., "Surface-integral methods of calculating forces on magnetized iron parts", *The Institution of Electrical Engineers*, Monograph No. 342, August 1959, pp. 19 – 28.

[33] Carpenter, C.J., "Distribution of mechanical forces in magnetized material", *IEE Proceedings*, Vol. 113, No. 4, April 1966, pp. 719 – 720.

[34] Carter, G.W., "Distribution of mechanical forces in magnetized material", *IEE Proceedings*, Vol. 112, No. 9, Sept. 1965, pp. 1771 – 1777.

[35] Charlier, R., Grisard, L., Cescotto, S., "Grandes deformations elastoplastiques et problemes de contact lors du magnetoformage de bielles de trasmission", *RGE Revue Generale d'Electricite*, No. 9, October 1987, pp. 26 – 31.

[36] Childs, T., Maekawa, K., Obikawa, T., Yamane, Y., *Metal Machining : Theory and Applications* Arnold, London, 2000.

[37] Ciric, I.R., "Proximity effect between a wire carrying current and a rotating cylindrical conductor", *IEE Proceedings*, Vol. 130, No. 3, May 1983, pp. 122 – 128.

[38] Conserva, M., *Aluminium and Its Applications*, Edimet, Brescia, 1994.

[39] Cooper, J., "Scattering of electromagnetic fields by a moving boundary: the one-dimensional case", *IEEE Transactions on Antennas and Propagation*, Vol. 28, No. 6, November 1980, pp. 791 – 795.

[40] Cooper, J., "Long-time behavior and energy growth for electromagnetic waves reflected by a moving boundary", *IEEE Transactions on Antennas and Propagation*, Vol. 41, No. 10, October 1993, pp. 1365 – 1370.

[41] Coulomb, J.L., "A methodology for the determination of global electromechanical quantities from a finite element analysis and its application to the evaluation of magnetic forces, torques and stiffness", *IEEE Transactions on Magnetics*, Vol. 19, No. 6, November 1983, pp. 2514 – 2519.

[42] Craik, D.J., *Electricity, Relativity and Magnetism: a Unified text*, Wiley, Chichester, 1999.

[43] Crandall, S.H., *An Introduction to the Mechanics of Solids*, McGraw-Hill, New York, 1978.

[44] Cullwick, E.G., *Electromagnetism and Relativity with Particular Reference to Moving Media and Electromagnetic Induction*, Longman-Green, London, 1957.

[45] Daehn, G.S., AltyNova, M., Balanethiram, V.S., Fenton,G., Padmanabhan, M., Tamhane, A., Winnard, E., "High-velocity metal forming - an old technology addresses new problems", *JOM*, Vol. 47, No. 7, July 1995, pp. 42 – 45.

[46] Davies, G.A.O., *Virtual Work in Structural Analysis*, Wiley, Chichester, 1982.

[47] Davies, E.J., *Conduction and Induction Heating*, Peter Peregrinus, London, 1990.

[48] de Groot, S.R., Suttorp, L.G., *Foundations of Electrodynamics*, North-Holland Publishing Company, Amsterdam, 1972.

[49] de Hoop, A.T., Oristaglio, M.L., "Application of the modified Cagniard technique to transient electromagnetic diffusion problems", *Geophysical Journal*, Vol. 94, 1988, pp. 387 – 397.

[50] de Hoop, A.T., *Handbook of Radiation and Scattering of Waves*, Academic Press, Amsterdam, 1995.

[51] de Hoop, A.T., "Transient diffusive electromagnetic fields in stratified media: Calculation of the two-dimensional E-polarized field", *Radio Science*, Vol. 35, No. 2, 2000, pp. 443 – 453.

[52] Dolinsky, Yu., Elperin, T., "Dynamics of electromagnetic field in imploding conducting shell", *Journal of Applied Physics*, Vol. 83, No. 11, June 1998, pp. 5644 – 5649.

[53] Donnell, L.H., *Beams, Plates and Shells*, McGraw-Hill, New York, 1976.

[54] Dormeval, R., "Le comportement des materiaux: des particularites aux grandes vitesses de deformation", *RGE Revue Generale d'Electricite*, No. 9, October 1987, pp. 19 – 25.

[55] Dunn, D.A., *Models of Particles and Moving Media*, Academic Press, New York, 1971.

[56] Eringen, A.C., Suhubi, E.S., *Elastodynamics*, Academic Press, New York, 1975.

[57] Eringen, A.C., *Elastodynamics of Continua*, Springer, New York, 1990.

[58] Fano, R.M., Chu, L.J., Adler, R.B., *Electromagnetic Fields, Energy and Forces*, Wiley, New York, 1960.

[59] Fawzi, T., "Analytical solutions of transverse electric eddy current problems with rotational symmetry", *IEEE Transactions on Magnetics*, Vol. 31, No. 3, May 1996, pp. 1396 – 1399.

[60] Fellinger, P., Marklein, R., Langenberg, K.J., Klaholtz, S., "Numerical modeling of elastic wave propagation and scattering with EFIT - elastodynamic finite integration technique", *Wave Motion*, No. 21, 1995, pp. 47 – 66.

[61] Fenton, G.K., Daehn, G.S., "Modeling of electromagnetically formed sheet metal", *Journal of Materials Processing TechNology*, Vol. 75, September 1998, pp. 6 – 16.

[62] Fluerasu, C., "Electromagnetic forming of a tubular conductor", *Revue Roumaine des Sciences Techniques, Serie Electrotechnique et Energetique*, Vol. 15, No. 3, 1970, pp. 457 – 488.

[63] Fluerasu, C., "Equivalent schemes of electromagnetic forming", *Revue Roumaine des Sciences Techniques, Serie Electrotechnique et Energetique*, Vol. 16, No. 4, 1971, pp. 593 – 609.

[64] Fluerasu, C., Fluerasu, C., "Numerical simulation of electromagnetic forming of conductors using RESEL program", *Revue Roumaine des Sciences Techniques, Serie Electrotechnique et Energetique*, Vol. 36, No. 4, 1991, pp. 417 – 424.

[65] Franois, D., *Mechanical Behaviour of Materials. Vol. 1. Elasticity and Plasticity*, Kluwer Academic Publishers, Amsterdam, 1998.

[66] Furth, H.P., Waniek, R.W., "Production and use of high transient magnetic fields. I.", *The Review of Scientific Instruments*, Vol. 27, No. 4, April 1956, pp. 195 – 202.

[67] Furth, H.P., Levine, M.A., Waniek, R.W., "Production and use of high transient magnetic fields. II.", *The Review of Scientific Instruments*, Vol. 28, No. 11, November 1957, pp. 949 – 958.

[68] Gallizi, H., Colombe, G., "Soudage par pression magnetique d'elements de gainage en acier inoxydable", *RGE Revue Generale d'Electricite*, No. 9, October 1987, pp. 52 – 57.

[69] Gasiak, G., *Theoretical and Experimental Analysis of Stresses, Strains and Load Capacity of Cylindrical Shells*, VDI Verlag, Dusseldorf, 1994.

[70] Gebhart, B., *Heat Conduction and Mass Diffusion*, McGraw-Hill, New York, 1993.

[71] Gere, J. M., *Mechanics of Materials*, Brooks/Cole,Pacific Grove, 2001.

[72] Gibson, J.E., *Thin Shells*, Pergamon, Oxford, 1980.

[73] Gobl, N., Szalay, A., "Working process for superconductors by means of HERF- technique", *Journal-De-Physique.-IV-:-JP*, Vol. 7, No. 3, August 1997, pp. 39 – 44.

[74] Goldstein, H., *Classical Mechanics*, Addison-Wesley, 1980.

[75] Gopinathan, V., *Plasticity Theory and Its Applications in Metal Forming*, Willey, New York, 1982.

[76] Gould, P.L., *Analysis of Shells and Plates*, Upper Saddle River, Prentice Hal, 1999.

[77] Guillot, M., "La production de champs magnetiques intenses transitoires: les effects secondaires deviennent preponderants", *RGE Revue Generale d'Electricite*, No. 9, October 1987, pp. 37 – 48.

[78] Guo, R.M., Johnson, R.E., "Modeling, simulation and control of metal processing", *Advanced-Materials:-Development,-Characterization-Processing,-and-Mechanical-Behavior-American-Society-of-Mechanical-En*, Vol. 74, 1996, ASME, New York, NY, USA. p. 179.

[79] Hague, B., *Electromagnetic Problems in Electrical Engineering, an Elementary Treatise on the Application of the Principles of Electromagnetism to the Theory of the Magnetic Field and of the Mechanical Forces in Electrical Machinery and Apparatus*, Oxford University Press, London, 1929.

[80] Hammond, P., *Energy Methods in Electromagnetism*, Clarendon, Oxford, 1981.

[81] Hashimoto, Y., Hata, H., Sakai, M., Negishi, H., "Local deformation and buckling of a cylindrical Al tube under magnetic impulsive pressure", *Journal of Materials Processing Technology*, Vol. 85, 1999, pp. 209 – 212.

[82] Haus, H.A., "Electrodynamics of moving media and the force on a current loop", *Applied Physics A*, Vol. 27, 1982, pp. 217 – 222.

[83] Haus, H.A., Melcher, J.R., *Electromagnetic Fields and Energy*, Prentice-Hall, Englewood Cliffs, 1989.

[84] Hemmi, S., "Nodal forces due to the Maxwell's stress tensors in the FEM analysis", *Electromagnetic forces and Applications*, Elsevier Science Publishers, Amsterdam, 1992, pp. 291 – 294.

[85] Hill, R., *The Mathematical Theory of Plasticity* Clarendon, Oxford, 1998.

[86] Hofmann, H., "Die Behandlung von Sprungflachen beim Kraftangriff des stationaren elektromagnetischen Feldes an der Materie", 1956.

[87] Hsieh, K.T., Kim, B.K., "One kind of scaling relations on electromechanical system", *IEEE Transactions on Magnetics*, Vol. 33, No. 1, January 1997, pp. 240 – 244.

[88] Hsu, T.H., *Structural Engineering and Applied Mechanics Data Handbook. Vol. 4. Shells*, Gulf, Houston, 1991.

[89] Huang, S., Chang, Z., Wang, Z., Wang, L., Yang, M., "Finite element analysis of electromagnetic sheet metal expansion process", *Transactions-of-Nonferrous-Metals-Society-of-China- (English-Edition)*, Vol. 8, No. 3, 1998, pp. 490 – 495.

[90] Huo, T., Nakamachi E., "Evaluation of the dynamic explicit/viscoplastic finite-element method in sheet-forming simulation", *Journal of Materials Processing Technology*, Vol. 50, 1995, pp. 180 – 196.

[91] Hutter, K., van de Ven, A.A.F., *Field Matter Interactions in Thermoelastic Solids*, Springer-Verlag, Berlin, 1978.

[92] Hwang, W.S., Lee, J.S., Kim, N.H., Sohn, H.S., "Joining of copper tube to polyurethane tube by electromagnetic pulse forming", *Journal of Materials Processing Technology*, Vol. 37, No. 1-4, February 1993, pp. 83 – 93.

[93] Iesan, D., Scalia, A., *Thermoelastic Deformations*, Kluwer Academic Publishers, Dordrecht, 1996.

[94] Jablonski, J., Winkler, R., "Analysis of the electromagnetic forming process", *International Journal of Mechanical Science*, Vol. 20, 1978, pp. 315 – 325.

[95] Jackson, J.D., *Classical Electrodynamics*, Willey, New York, 1975.

[96] Jansen, H., "Some measurements of the expansion of a metallic cylinder with electromagnetic pulses", *IEEE Transactions on Industry Applications*, Vol. IGA-4, No. 4, July-August 1968, pp. 428 – 440.

[97] Johnson, W., *Engineering Plasticity*, Horwood, Chicester, 1983.

[98] Kameerbeek, E.M.H., "On the Theoretical and Experimental Determination of the Electromagnetic Torque in Electrical Machines" (PhD- thesis), TU Eindhoven, 1970.

[99] Kawata, K., Shioiri, J., (Ed.) *High-velocity Deformation of Solids*, Symposium, Tokyo, Aug. 1977.

[100] King, R.J., Thorp, J.M., "A study of process variables in the electromagnetic bulging of tubes", *International Journal of Engineering Science*, Vol. 16, No. 6, 1978, pp. 365 – 378.

[101] Kitahara, H., Kotera, H., Shima, S., "3-D particulate modelling for simulation of compaction in magnetic field", *IEEE Transactions on Magnetics*, Vol. 36, No. 4, July 2000, pp. 1519 – 1522.

[102] Koelsch, J.R., "Noncontact forming: fact of fiction?", *Machine and Tool Blue Book*, Vol. 83, No. 6, June 1988, pp. 50 – 52.

[103] Kunerth, D.C., Lassahn, G.D., "Search for electromagnetic forming process control", *JOM*, Vol. 41, No. 3, March 1989, pp. 54 – 56.

[104] Kunz, K.S., "Plane electromagnetic waves in moving media and reflections from moving interfaces", *Journal of Applied Physics*, Vol. 51, No. 2, February 1980, pp. 873 – 884.

[105] Lal, G.K., Hillier, M.J., "The electrodynamics of electromagnetic forming", *International Journal of Mechanical Science*, Vol. 10, 1968, pp. 491 – 498.

[106] Lal, G.K., "Electromagnetic metal forming", *IEEE Transactions on Industry Applications*, Vol. IA-8, No. 4, July-August 1972, pp. 425 – 429.

[107] Landau, L.D., Lifschitz, E.M., *Electrodynamics of Continuous Media*, Pergamon Press, Oxford, 1960.

[108] Langlois, A.P., "Metal forming with electromagnetics", *american Society of Tool and Manufacturing Engineers*, Creative Manufacturing Seminars, 1960-1961.

[109] Lax, M., Nelson, D.F., "Maxwell equations in material form", *Physical Review B*, Vol.13, No. 4, February 1976, pp. 1188 – 1195.

[110] Lee, S.H., Lee, D.N., "Finite element analysis of electromagnetic forming for tube expansion", *Journal of Engineering Materials and Technology, Transactions of the ASM*, Vol. 116, No. 2, April 1994, pp. 250 – 254.

[111] Lee, S.H., Lee, D.N., "Estimation of the magnetic pressure in tube expansion by electromagnetic forming", *Journal of Materials Processing Technology*, Vol. 57, 1996, pp. 311 – 315.

[112] Lehner, G., "Electromagnetic field diffusion, T-functions, and image solutions", *Electrical engineering*, Vol. 78, 1995, pp. 209 – 217.

[113] Lehner, G., "One-dimensional cylindrical diffusion of electromagnetic fields. Part I", *Electrical engineering*, Vol. 79, 1996, pp. 393 – 406.

[114] Lehner, G., "One-dimensional cylindrical diffusion of electromagnetic fields. Part II", *Electrical engineering*, Vol. 80, 1997, pp. 155 – 161.

[115] Levich, B.G., *Theoretical Physics. Vol. I Theory of the Electromagnetic Field, Theory and Relativity*, North-Holland, Amsterdam, 1970.

[116] Libai, A., *The Non-linear Theory of Elastic Shells*, UK Cambridge University Press, Cambridge, 1998.

[117] Mann, R.A., *The Classical Dynamics of Particles, Galilean and Lorentz relativity*, Academic Press, New York, 1974.

[118] Manea, T.E., Verweij, M.D., Blok, H., "Is there a discrepancy in the calculation of the total magnetic force?" - Conference on Optimization of Electrical and Electronic Equipments OPTIM'2000, Brasov, Romania, May 2000.

[119] Manea, T.E., Verweij, M.D., Blok, H., "The approximate elastic field in a conducting non-magnetic cylindrical shell in an electromagnetic field", internal report, ITS/EM 2001-08, Delft University of Technology, 2001.

[120] Manea, T.E., Verweij, M.D., Blok, H., "Experimental set-up for electromagnetic expansion (deformation) of hollow circular cylindrical workpieces", internal report, ITS/EM 2002-02, Delft University of Technology, 2002.

[121] Manea, T.E., Verweij, M.D., Blok, H., "Experimental set-up for electromagnetic deformation of hollow circular cylindrical workpieces", internal report, ITS/EM 2002-06, Delft University of Technology, 2002.

[122] Manea, T.E., Verweij, M.D., Blok, H., "Electrodynamics in deformable solids for electromagnetic forming (deformation of thin cylindrical shells)" -Conference on advanced computational methods in engineering ACOMEN2002, Liege, Belgium, May 2002.

[123] Manea, T.E., Verweij, M.D., Blok, H., "The importance of the velocity term in the electromagnetic forming process" - The 27-th triennial General Assembly of the International Union of Radio Science URSI2002, Maastricht, The Netherlands, August 2002.

[124] Manea, T.E., Verweij, M.D., "Electromagnetic forming of thin steel beverage cans" - The 11-th International Conference on Computational Methods and Experimental Measurements CMEM2003, Sani, Greece, May 2003.

[125] Maouche, B., Feliachi, M., "A discretized integral method for eddy current computation in moving objects with the coexistence of the velocity and time terms", *IEEE Transactions on Magnetics*, Vol. 34, No. 5, September 1998, pp. 2567 – 2569.

[126] Mayergoyz, I., *Nonlinear Diffusion of Electromagnetic Fields: with Applications to Eddy Currents and Superconductivity*, Academic Press, San Diego, 1998.

[127] Maugin, G., *Continuum Mechanics of Electromagnetic Solids*, North-Holland, Amsterdam, 1988.

[128] McFee, S., "A classical virtual work force method for time-harmonic eddy-currents analysis", *IEEE Transactions on Magnetics*, Vol. 32, No. 3, May 1996, pp. 1673 – 1676.

[129] Medeiros, L.H., Reyne, G., Meunier, G., "About the distribution of forces in permanent magnets", *IEEE Transactions on Magnetics*, Vol. 35, No. 3, May 1999, pp. 1215 – 1218.

[130] Melcher, J.R., "Electric fields and moving media", *IEEE Transactions on Education*, Vol. 17, No. 2, May 1974, pp. 100 – 110.

[131] Melcher, J.R., *Continuum Electro-mechanics*, MIT Press, Cambridge, Massachusetts, 1981.

[132] Meriched, A., Feliachi, M., "Electromagnetic forming modelling of thin metal sheets", *IEEE Transactions on Magnetics*, Vol. 36, No. 4, July 2000, pp. 852 – 853.

[133] Moon, F.C., Pao, Y.H., "Magnetoelastic Buckling of a Thin Plate", *Journal of Applied Mechanics*, March 1968, pp. 53 – 58.

[134] Moon, F.C., Chattopadhyay, S., "Magnetically induced stress waves in a conducting solid-theory and experiment", *Transactions of the ASME. Series E, Journal of Applied Mechanics*, Vol. 41, No. 3, Sept. 1974, pp. 641 – 646.

[135] Moon, F.C., *Magneto-Solid Mechanics*, Wiley, New York, 1984.

[136] Mor, A., Gavril, S., "Electromagnetic energy absorption by a moving conductor plane", *International Journal of Electronics*, Vol. 63, No. 5, April 1988, pp. 643 – 653.

[137] Morita, K., *Applied Fourier Transform*, Ohmsha, Tokyo, 1995.

[138] Morse, P.M., Feshbach, H., *Methods of Theoretical Physics*, McGraw-Hill, New York, 1953.

[139] Murakoshi, Y., Takahashi, M., SaNo, T., Hanada, K., Negishi, H., "Inside bead forming of aluminum tube by electro-magnetic forming", *Journal of Materials processing TechNology*, Vol. 80 –81, 1998, pp. 695 – 699.

[140] Murata, M., Suzuki, H., "Profile Control in tube flaring by electromagnetic forming", *Journal of Material Processing Technology*, Vol. 22, 1990, pp. 75 – 90.

[141] Ozisik, M. N., *Heat Conduction*, Wiley, New York, 1993.

[142] Padmanabhan, K.A., *Superplasticity: Mechanical and Structural Aspects, Environmental Effects, Fundamentals and Applications*, Springer-Verlag, Berlin, 1980.

[143] Peiffer, A., Kohler, B., "The acoustic finite integration technique for waves of cylindrical symmetry", *Journal of Acoustic Society of America*, Vol. 102, No. 2, August 1997, pp. 697 – 706.

[144] Penfield, P., Haus, H.A., *Electrodynamics of Moving Media*, MIT Press, Cambridge, Massachusetts, 1967.

[145] Poruchikov, V.B., *Methods of the Classical Theory of Elastodynamics*, Springer-Verlag, Berlin, 1993.

[146] Puzrin, A.M., Houlsby, G.T., "Fundamentals of kinematic hardening hyperplasticity", *International-Journal-of-Solids-and-Structures*, Vol. 38, No. 21, May 2001, pp. 3771 – 3794.

[147] Ren, Z., Razek, A., "A coupled electromagnetic-mechanical model for thin conductive plate deflection analysis", *IEEE Transactions on Magnetics*, Vol. 26, No. 5, September 1990, pp. 1650 – 1652.

[148] Ren, Z., Razek, A., "Local force computation in deformable bodies using edge elements", *IEEE Transactions on Magnetics*, Vol. 28, No. 2, March 1992, pp. 1212 – 1215.

[149] Ren, Z., Razek, A., "A strong coupled model for analyzing dynamic behaviours of Non-linear electromechanical systems ", *IEEE Transactions on Magnetics*, Vol. 30, No. 5, September 1994, pp. 3252 – 3255.

[150] Ren, Z., Ionescu, B., Besbes, M., Razek, A., "Calculation of mechanical deformation of magnetic materials in electromagnetic devices", *IEEE Transactions on Magnetics*, Vol. 31, No. 3, May 1995, pp. 1873 – 1876.

[151] Reyne, G., Sabonnadiere, J.C., Coulomb, J.L., Brisonneau, P., "A survey of the main aspects of magnetic forces and mechanical behaviour of ferromagnetic materials under magnetization", *IEEE Transactions on Magnetics*, Vol. 23, No. 5, September 1987, pp. 3765 – 3767.

[152] Rioux, C., Rioux-Damidau, F., "Energetic aspects of magnetic forming", *Revue de Physique Appliquee*, Vol. 22, No. 4, April 1987, pp. 253 – 259.

[153] Rioux, C., Rioux-Damidau, F., Sultanem, F., "Les sources impulsionnelles a base de stockage cinetique: une voi de recherches pour les tres fortes

energies", *RGE Revue Generale d'Electricite*, No. 9, Oct 1987, pp. 32 – 36.

[154] Rodger, D., Karaguler, T., Leonard, P.J., "A formulation for 3D moving conductor eddy-current problems", *IEEE Transactions on Magnetics*, Vol. 25, No. 5, September 1989, pp. 4147 – 4149.

[155] Rosser, W.G.V., *An Introduction to the Theory of Relativity*, Butterworths, London, 1964.

[156] Rosser, W.G.V., *Classical Electromagnetism Via Relativity*, Butterworth, London, 1968.

[157] Rosser, W.G.V., *Interpretation of Classical Electromagnetism*, Kluwer Academic Publishers, 1997.

[158] Russakoff, G., "A derivation of the macroscopic Maxwell equations", *American Journal of Physics*, Vol. 38, No. 10, October 1970, pp. 1188 – 1195.

[159] SaNo, T., Takahashi, M., Murakoshi, Y., MatsuNo, K., "Impulsive forming of tube ends by electromagnetic force", *Advanced Technology of Plasticity*, Vol. I, 1984, pp. 373 – 378.

[160] Sasu, M., "Magnetoforming machines. Nonlinear electric circuit functioning analysis", *Acta Technica CSAV*, Vol. 25, No. 4, 1980, pp. 448 – 464.

[161] Save, M.A., Massonnet, C.E., de Saxce, G., *Plastic Limit Analysis of Plates, Shells and Disks*, Elsevier, Amsterdam, 1997.

[162] Schinke, M., Reiss, K., "Kanonische Zeitbereichlosung der Maxwellgleichungen in verlustbehafteter Materie", *Electrical Engineering*, Vol. 78, 1995, pp. 69 – 77.

[163] Schley, R., "Le soudage par pression magnetique des metaux non ferreux", *RGE Revue Generale d'Electricite*, No. 9, October 1987, pp. 49 – 51.

[164] Schubert, F., Peiffer, A., Kohler, B., "The elastodynamic finite integration technique for waves in cylindrical geometries", *Journal of Acoustical Society of America*, Vol. 104, No. 5, November 1998, pp. 2604 – 2614.

[165] Shen, J., Li, J., Fu, H., Su, J., "Electromagnetic confinement and shaping for plate-form part", *Journal-of-Materials-Science-and-Technology*, Vol. 16, No. 1, 2000, pp. 27 – 32.

[166] Shen, Y., Drugan, W.J., "Constraints on moving strong discontinuity surfaces in dynamic plane-stress or plane-strain deformations of stable elastic-ideally plastic materials", *Journal of Applied Mechanics,Transactions of the ASME*, Vol. 57, 1990, pp. 569 – 576.

[167] Shvartsburg, A.B., *Impulse Time-domain Electromagnetics of Continuous Media*, Birkahusen, Boston, 1999.

[168] Silhavy, M.,, *The Mechanics and Thermodynamics of Continuous Media*, Springer, Berlin, 1997.

[169] Singer, J., *Buckling Experiments: Experimental Methods in Buckling of Thin-walled Structures. Vol.1*, Wiley, Chichester, 1998.

[170] Smith, M.T., McVay, G.L., "Optimization of light metal forming methods for automotive applications", *Light-Metal-Age*, Vol. 55, No. 9-10, Oct. 1997, pp. 24 – 28.

[171] Sommerfeld, A., *Encyclopaedie der Mathemetischeen Wissenschaften*, Leipzig, 1905.

[172] Sommerfeld, A., *Electrodynamics*, Academic press, New York, 1964.

[173] Spencer, A.J.M., *Continuum Mechanics*, Longman, New York,1980.

[174] Stakgold, I., *Green's Functions and Boundary Value Problems*, Willey, New York, 1979.

[175] Steiner, K.H., *Interactions Between Electromagnetic Field and Matter*, Vieweg, Braunschweig, 1973.

[176] Stouffer, D.C., Dame, L.T., *Inelastic Deformation of Metals, Models, Mechanical Properties, and Metallurgy*, John Willey, New York, 1996.

[177] Stratton, J.A., *Electromagnetic Theory*, McGraw-Hill, New York, 1941.

[178] Suzuki, H., Yokouchi, Y., Murata, M., Neghishi, H., "Finite element analysis of tube deformation under impulsive internal pressure", *Advanced Technology of Plasticity*, Vol. I, 1984, pp. 367 – 372.

[179] Suzuki, H., Murata, M., Neghishi, H., "The effect of a field shaper in electromagnetic tube bulging", *Journal of Mechanical Working Technology*, Vol. 15, 1987, pp. 229 – 240.

[180] Tai, C.T., "Transient radiation in a moving isotropic medium", *Journal of electromagnetic waves and applications*, Vol. 7, No. 1, 1993, pp. 1 – 11.

[181] Takatsu, N., Kato, M., Sato, K., Tobe, T., "High-speed forming of metal sheets by electromagnetic force", *JSME International Journal*, series III, Vol. 31, No. 1, 1988, pp. 142 – 148.

[182] Tamhane, A.A., AltyNova, M.M., Daehn, G.S., "Effect of sample size on ductility in electromagnetic ring expansion", *Scripta Materialia*, Vol. 34, No. 8, April 1996, pp. 1345 – 1350.

[183] Teodorescu, P.P., *Dynamics of Linear Elastic Bodies*, Abacus Press, Tunbridge Wells, 1975.

[184] Ugural, A.C., Fenster, S.K., *Advanced Strength and Applied Elasticity*, Prentice Hall, Englewood Cliffs, 1995.

[185] Ugural, A.C., *Stresses in Plates and Shells*, McGraw-Hill, Boston, 1999.

[186] Verweij, M.D., "Four ways of deducing Maxwells equations from their microscopic counterparts - Lorentzs theory of electronics revised" - Proceedings XXVIIth General Assembly of the URSI International Union of Radio Science URSI2002, 17-24 August 2002, Maastricht, The Netherlands, 4 pp. (CD-ROM).

[187] Vinson, J.R., *The Behavior of Thin Walled Structures: Beams, Plates, and Shells*, Kluwer Academic Publisher, Dordrecht, 1989.

[188] Wilmanski, K., *Thermomechanics of Continua*, Springer, Berlin, 1998.

[189] Winkler, R., *Hochgeschwindigkeitsbearbeitung*, VEB Verlag Technik, Berlin, 1973.

[190] Woodson, H.H., Melcher, J.R., *Electromechanical Dynamics*, Wiley, New York, 1990.

[191] Zhang, H., Murata, M., Suzuki, H., "Effects of various working conditions on tube bulging by electromagnetic forming", *Journal of Materials Processing Technology*, Vol. 48, 1995, pp. 113 – 121.

[192] "Discussion on distribution of mechanical forces in magnetised material and evaluation of magnetic energy density in magnetized matter", *IEE Proceedings*, Vol. 113, No. 12, Dec. 1966, pp. 2095 – 2098.

Summary

Electrodynamics in Deformable Solids
for Electromagnetic Forming

by Teodora-Emilia MOTOAŞCĂ

The behaviour of matter in an electromagnetic field represents a very complex problem, involving not only electromagnetism but also mechanics and thermodynamics. The interaction field-matter is not simple even for a rigid body, and it becomes more complicated for a deforming body, as long as all the physical quantities that characterize the process are changing both in time and space and also in their interdependence. Conducting bodies can move and/or can be deformed when they are subjected to strong electromagnetic fields. One of the practical applications of these phenomena is the electromagnetic forming, i.e. shaping objects using strong electromagnetic fields. Since the early 20-th century this has been used at an industrial level, though without a well developed theory about all the phenomena involved in the process.

The electromagnetic forming system has many advantages that make it an attractive alternative to conventional forming systems or even to other high-velocity forming systems. During the deformation process, a process with a duration in the order of microseconds, there is no mechanical contact with the workpiece as in most conventional forming systems. A principal advantage is its controllability and repeatability, as most of the high-velocity procedures, while the required equipment is relatively simple. Electromagnetic forming has also some disadvantages because it needs special safety precautions and the required equipment is still expensive and physically large. In practice, its application is restricted to rather simple shapes (unless forming dies are used), and there are size limitations for workpieces to be shaped. During the last few decades, an

increasing need to produce high-strength components more economically than by conventional forming caused renewed interest in electromagnetic forming. Due to its complexity, the approach of this subject is still not a trivial problem.

In this thesis, we have developed a simple analytical model of the electromagnetic forming process performed for shaping of hollow circular cylindrical objects, both for compression and expansion. Additionally, for expansion, an experimental model has been developed to design an experimental set-up, which is used for verification of the various aspects of our theoretical model. In order to have as much as possible an analytical model of the electromagnetic forming process, some assumptions and approximations related to geometry, parameters, properties and fields characteristic to a typical electromagnetic forming system for hollow circular cylindrical objects (workpieces) have been made. Based on these assumptions, the theoretical model of electromagnetic compression has been elaborated in sequential steps. At each step in model development, numerical results have been given for three types of objects to be compressed: a non-magnetic thick workpiece, a magnetic thick workpiece and a non-magnetic thin workpiece. For expansion we suffice to present results for the magnetic thick workpiece.

First, the transient diffusive electromagnetic field in the cylindrical configuration related to the discussed electromagnetic forming system for compression and expansion of hollow circular cylindrical objects has been calculated. The axially symmetric workpiece of infinite length with a high electrical conductivity is placed either inside (for compression) or outside (for expansion) a cylindrical sheet coil. The electromagnetic field components have been computed in the frequency domain and the results were then transformed to the time domain. The electromechanical force densities associated with our pulsed electromagnetic fields are investigated, since these forces are the driving forces that will produce the final deformation of the object to be deformed during electromagnetic compression and expansion. In all cases the electromagnetic force density had large values near the interface close to the source and it decayed rapidly in time and space. Non-zero electromagnetic surface forces are present only in the magnetic workpiece and they are smaller than the average value of the electromagnetic volume force density along the thickness of the workpiece, but still not negligible in further calculations.

The electromagnetic volume force and the electromagnetic surface force previously calculated have been used as source terms for the calculation of the elastic field in the workpiece. The complete elastodynamic problem for the case of plane strain has been considered. The solution of the equation of radial motion to be solved has been found as the sum of the general solution of the

homogeneous equation of motion with a particular solution of the equation of motion, where the particular solution has been calculated using a source type of integral representation. The numerical results obtained for the elastic field in the compressed configuration have shown that the radial displacement at the inner boundary the workpiece is slightly larger than the one at the outer boundary, thus the workpiece becomes slightly thicker during electromagnetic compression. For expansion the workpiece becomes slightly thinner. Also, the particle radial displacement has smaller values in a non-magnetic thick workpiece than in a magnetic thick or in a non-magnetic thin workpiece. In all cases the radial stress had small, negligible values as compared with the values of the tangential stress at the same instant of time. The results for the elastic field components have also been calculated with the approximation of equivalent surface forces assuming zero volume forces. The maximum values are the roughly the same, but their space-time evolution is different.

The results obtained for the transient diffusive electromagnetic field have been used to calculate the evolution of the temperature in the workpiece due to dissipation of electromagnetic energy in the forming process. The solution of the equation of heat flow has been found as the sum of the general solution of the homogeneous equation of heat flow with a particular solution of the equation of heat flow, while the particular solution has been calculated using a source type of integral representation. Then, the temperature effects in the thermoelastic strains have been taken further into account for computing the thermoelastic field in the same manner as the elastic field. It has been shown that the temperature rise has negative consequences for the electromagnetic compression, because a significant expansion of the workpiece is obtained in all cases. This expansion of the workpiece is sometimes larger than the desired compression of the workpiece. For expansion the temperature effects contribute to the expansion of the workpiece.

Since the final deformation of the workpiece had to be a permanent one, the plastic deformations have also been discussed in an inelastic-perfectly plastic material within the plane strain assumption. The elastic deformation has been neglected, as well as the influence of the radial velocity acquired by the workpiece during the elastic deformation. In all the considered cases, a plastic boundary, separating the elastic and the plastic types of deformations, develops in the workpiece starting from the inner boundary of the workpiece. This plastic boundary moves very rapidly inside the workpiece, so the intermediary calculations with two regions inside the workpiece, one with elastic deformations and the other with plastic deformations, may be avoided and we may consider that the entire workpiece starts to deform plastically at a certain in-

stant of time. The actual deformation of the workpiece has been calculated using the dynamic equations of motion. For each type of workpiece, it has been shown that for compression in all three types of workpieces there exist an increase in the thickness of the workpieces during plastic deformations, while for expansion, a decrease of the thickness of the workpiece takes place. The modification in thickness is shown to be smaller for a non-magnetic thick workpiece than for a non-magnetic thin workpiece subjected to compression, due to different force density distributions and consequently different velocities of each point inside the workpiece.

A particular attention has been given to the design of a set-up for an experimental investigation of electromagnetic forming of steel beverage cans. The design of the set-up has been done in cooperation with Corus Research Development and Technology from IJmuiden. A limited set of experiments have been performed at KEMA High Voltage Laboratory in Arnhem. Smaller deformations have been obtained, but with a small adjustment of the model, these results could be perfectly justified with the developed experimental model.

As a concluding chapter, various ways to improve the given experimental model have been presented, together with some numerical results. The calculation of the actual temperature in the configuration after the heat exchange between the forming coil and the workpiece has been investigated with the use of an electrical analogy. The numerical results showed that both deformation and temperature rise within the electromagnetic forming system have considerable influence in the evolution of the whole electromagnetic forming process. The numerical results obtained with the complex model have shown that there is still room for more investigation of the electromagnetic forming process and that the electromagnetic forming is a promising technology that can be applied at industrial level after a good optimization of the whole process, based on a better understanding of all phenomena involved in it.

Samenvatting

Elektrodynamica van het elektromagnetisch vervormen

Teodora-Emilia MOTOAŞCĂ

Het gedrag van materie onder invloed van een elektromagnetisch veld is een zeer complex probleem, waarbij niet alleen elektromagnetisme maar ook mechanica en thermodynamica een rol spelen. Voor een stijf lichaam is de interactie tussen veld en materie al niet eenvoudig te beschrijven en deze interactie wordt zeer gecompliceerd voor een lichaam dat ook nog kan vervormen. Het is bekend dat geleidende objecten kunnen bewegen en daarbij ook van vorm veranderen onder invloed van sterke elektromagnetische velden. Met name dat laatste heeft toepassing gevonden in het zogenaamde elektromagnetisch vervormen, waarbij met behulp van sterke elektromagnetische velden aan objecten een bepaalde vorm wordt gegeven. Alhoewel deze vervormingsmethode sinds het begin van de 20-ste eeuw industrieel wordt toegepast, is de theorievorming eromheen en daarmee het optimaliseren van het vervormingsproces achtergebleven.

De elektromagnetische vervormingstechniek heeft een aantal voordelen als een aantrekkelijk alternatief voor conventionele en zelfs hogesnelheidsvervormingstechnieken. Genoemd kunnen worden: het ontbreken van mechanisch contact tussen werkstuk en vervormingspoel, regelbaarheid en herhalingssnelheid en dat met relatief eenvoudige technische voorzieningen. Als nadelen kunnen genoemd worden: speciale veiligheidsvoorzieningen door het gebruik van hoge elektrische spanningen (10 kV), optredende opwarmingseffecten en tamelijk dure componenten. Verder was de toepassing beperkt tot tamelijk eenvoudige vormen en werkstukken van beperkte afmetingen. Meer recentelijk is er een hernieuwde belangstelling voor elektromagnetische vervormingstechnieken. De ontwikkelingen in de elektromagnetische vermogenstechniek en ver-

mogenselektronica maken het optimaal ontwerpen van een elektromagnetisch vervormingsysteem nu mogelijk. Door de al eerder genoemde gecompliceerdheid is de theorievorming eromheen en de wiskundige modelering geen triviaal probleem.

In dit proefschrift wordt dit probleem aangepakt door een zo'n eenvoudig mogelijk analytisch model voor het elektromagnetisch vervormen van holle, cilindrische objecten te ontwikkelen. Het ontwikkelde theoretische model beschrijft zowel compressie als expansie van de holle cilinders. Voor expansie is daarnaast een benaderend model ontwikkeld, dat gebruikt is om in een experiment verschillende aspecten van de modelvorming te verifiëren. Teneinde de modelvorming niet te gecompliceerd te maken, zijn een aantal aannames en benaderingen met betrekking tot geometrie, parameters en eigenschappen voor holle cilindrische werkstukken gemaakt. Op basis van deze aannames is het theoretische model in opeenvolgende stappen opgezet. In iedere stap worden numerieke resultaten gegeven voor drie soorten objecten: een dik niet-magnetisch werkstuk, een dik magnetisch werkstuk en een dun niet-magnetisch werkstuk. Dit eerst voor compressie, daarna worden ook voor expansie een aantal stappen met numerieke resultaten toegelicht.

Eerst wordt het elektromagnetische veld in de diffusiebenadering berekend voor het geval van compressie en expansie van holle cilindrische werkstukken. In beide gevallen is de configuratie zowel oneindig lang als axiaal symmetrisch ondersteld. Het werkstuk is sterk elektrisch geleidend en al of niet magnetisch. Voor compressie is het werkstuk coaxiaal binnen een cilindrische plaatspoel geplaatst, terwijl voor expansie het werkstuk buiten een cilindrische plaatspoel is geplaatst. De componenten van het elektromagnetische veld zijn berekend in het frequentiedomein en vervolgens getransformeerd naar het tijddomein. Vervolgens zijn de elektromagnetische krachtdichtheden, die optreden als gevolg van een gepulst elektromagnetisch veld in een stuksgewijs homogeen, isotroop, lineair medium met geleidingsverliezen, onderzocht. Dit zijn de drijvende krachten, die de uiteindelijk vervorming van het werkstuk gedurende het compressie- of expansieprocess veroorzaken. In alle gevallen vertoont de elektromagnetische krachtdichtheid hoge waarden in de nabijheid van het scheidingsvlak dichtbij de bron en neemt vervolgens snel af in tijd en plaats. Elektromagnetische oppervlaktekrachten treden alleen op in magnetische werkstukken; hoewel zij kleiner zijn dan de gemiddelde waarde van de volumekrachtdichtheden over de dikte van het werkstuk, zijn zij niet verwaarloosbaar in verdere berekeningen.

De op bovenstaande wijze berekende, elektromagnetische volume- en oppervlaktekrachten worden vervolgens gebruikt als brontermen voor de bereke-

ning van het elastische veld in het werkstuk. Daarbij is het complete elastody-namische probleem voor het geval van "plane strain" beschouwd. De oplossing van de resulterende vergelijking voor de radiale beweging wordt gevonden als de som van de algemene oplossing van de homogene vergelijking en een particuliere oplossing gebaseerd op een integraalrepresentatie van het brontype. De numerieke resultaten laten zien dat de radiale deeltjesverplaatsing in een dik niet-magnetisch werkstuk lagere waarden heeft dan in een dik magnetisch en in een dun niet-magnetisch werkstuk. Bovendien blijkt in alle gevallen dat de radiale spanning verwaarloosbaar klein is ten opzichte van de tangentiële spanning op hetzelfde moment. In overeenstemming met de verwachting wordt bij compressie het werkstuk iets dikker en bij expansie iets dunner. De resultaten voor het elastische veld zijn ook berekend met behulp van een benadering met equivalente oppervlaktekrachten, terwijl de volumekrachten nul verondersteld worden. In deze resultaten zijn de maximum amplitudes ongeveer hetzelfde, maar het transiente gedrag binnen het werkstuk is tamelijk verschillend.

De verkregen resultaten met betrekking tot het transiente elektromag-netische veld in de diffusiebenadering zijn vervolgens gebruikt om de temperatuurontwikkeling in het werkstuk gedurende het vervormingsproces te berekenen. Tijdens dit process vindt dissipatie van elektromagnetische energie plaats. De oplossing van het onderhavige warmtegeleidingsprobleem wordt gevonden als de som van de algemene oplossing van de homogene diffusie-vergelijking en een particuliere oplossing gebaseerd op een integraalrepresen-tatie van het brontype. Vervolgens zijn de temperatuureffecten in de thermo-elastische rek gebruikt om het thermoelastische veld te berekenen. Dit gebeurt op bijna dezelfde wijze als de berekening van het elastische veld. Het blijkt dat bij compressie het werkstuk uitzet, soms zoveel dat het de gewenste compressie compenseert. Bij expansie kan het thermodynamische effect het uitzetten van het werkstuk aanzienlijk versterken.

Het doel van elektromagnetische vervormen is dat de uiteindelijke vorm permanent is. Daarom wordt de theorie van het plastisch vervormen in een inelastisch perfect plastisch materiaal in de situatie van "plain strain" be-sproken. Twee verschillende gevallen zijn hierbij opgelost. Daarbij zijn zowel de elastische vervorming als de invloed van de kleine radiale snelheid, die in het elastische vervormingsproces kan optreden, verwaarloosd. In alle gevallen treedt een plastisch grensvlak op in het werkstuk, dat de elastische van de plastische vervorming scheidt. Bij compressie (en ook bij expansie) start dit plastische grensvlak bij de binnenrand van het werkstuk en beweegt dan zeer snel naar de buitenrand. Extra berekeningen van de velden in twee aaneen-grenzende gebieden, waar in het ene gebied een elastische vervorming en in

het andere gebied een plastische vervorming plaats vindt, mogen dan worden vermeden door aan te nemen dat het gehele werkstuk vanaf het moment, dat het plastisch grensvlak de buitenrand bereikt, plastisch aan het vervormen is. De werkelijke (plastische) vervorming wordt berekend met de dynamische bewegingsvergelijkingen. Voor ieder type werkstuk blijken de radiale, tangentiële en longitudinale spanningen eenzelfde gedrag te vertonen, maar met verschillende amplitudes. In het algemeen blijken de spanningen in dikke magnetische en dunne niet-magnetische werkstukken groter dan in dikke niet-magnetische werkstukken. Verder blijkt dat bij compressie, in alle drie typen werkstukken, de dikte bij het plastisch vervormen toeneeemt. Voor een dik niet-magnetisch werkstuk is deze vervorming kleiner dan voor een dik magnetisch werkstuk.

Speciale aandacht is gegeven aan het ontwerp voor een laboratorium-opstelling voor een experimenteel onderzoek aan het elektromagnetisch vervormen van drankblikjes. Het ontwerpen van deze opstelling is in samenwerking gebeurd met Corus Research Development and Technology van IJmuiden. Met de uiteindelijke opstelling is een beperkt aantal experimenten gedaan bij het Hoogspanningslaboratorium van KEMA te Arnhem. De gemeten vervormingen bleken kleiner dan verwacht. Een analyse van de beperkte resultaten heeft echter aangetoond dat, met kleine aanpassingen van het model, de gevonden resultaten toch met de verwachtingen in overeenstemming gebracht kunnen worden.

Tenslotte wordt in een afsluitend hoofdstuk een aantal mogelijkheden voorgesteld om het experimentele model te verbeteren en een aantal numerieke resultaten gepresenteerd. De berekening van de actuele temperatuurveranderingen door de warmteuitwisseling tussen de spoel en het werkstuk zijn onderzocht met een elektrisch analogon. Enerzijds blijkt het dat zowel de vervorming als de temperatuurstijging in het elektromagnetische vervormingssysteem een belangrijke invloed heeft, maar anderzijds blijkt het dat de modelvorming rondom het elektromagnetische vervormen zodanig uitbreidbaar is dat een beter ontwerp voor een vervormingssysteem kan worden verkregen.

Acknowledgements

First of all I would like to thank my parents for their support and encouragement during the years. Even the geographical distance between us is quite large, I felt them all time besides me, in good and bad times. I would like also to thank my brother who helped me with the design of the thesis cover and supported me with encouraging emails through the years. Then my thanks go to Roger, my dear friend, with whom I shared all the ups and downs in my "Delft-years" and with whom the life become worth living and "gezellig".

I would like also to thank to Professor Hans Blok, Professor Peter van den Berg and to Doctor Martin Verweij for their guidance throughout the preparation of this thesis. Even it was for a short period of time, I would like also to thank to Professor A.T. de Hoop for his constructive ideas regarding the electromagnetic forces and in general for its kindness in explaining electromagnetic subjects that I didn't know at that time. Many thanks to my roommates, Pieter and Bilal, to Toke and to all my colleagues from the Electromagnetic Research Group.

During the last three years, the steel manufacturing company Corus was involved in this research. Through all our collaboration I would like to thank them for the opportunity to perform a set of experiments relating to the subject of my thesis and for the financial support of my research between January 2003 and July 2003. Also, many thanks to the people from KEMA High Voltage Laboratory where the experiments were performed.

I would like to thank all my friends from Delft or from elsewhere for the nice time together. Many thanks to Delia, Oana, Cristina, Ioana, Adela and Carmen for their friendship and good advice and I hope we will still be friends despite the geographical distances between us.

Many thanks to all who directly or indirectly contributed to this thesis and who brought something into my life.

About the author

Teodora-Emilia MOTOAŞCĂ was born in Brasov, Romania on the 3-rd of November 1971. She received her BS and MS degrees in Electrical Engineering from the "Transilvania" University of Brasov in 1996 and 1997, respectively, and also a BS degree in Economy from the "Transilvania" University of Brasov in 1997. After graduation she was research assistant at the Faculty of Electrical Engineering, "Transilvania" University of Brasov in the Department of Electrical Engineering, in the group of professors Andrei Nicolaide and Elena Helerea.

Since January 1999 she has been a PhD-student at Delft University of Technology, Faculty of Information, Technology and Systems with the Laboratory of Electromagnetic Research. The results of her research are presented in this thesis.